THERMAL DEGRADATION OF PC AND PA6 DURING LASER TRANSMISSION WELDING (LTW)

by

Tasie B. Okoro

A thesis submitted to the Department of Chemical Engineering

In conformity with the requirements for

the degree of Master of Applied Science

Queen's University

Kingston, Ontario, Canada

(September, 2013)

Abstract

In laser transmission welding (LTW), a laser beam passes through the laser-transparent part and is absorbed by carbon black (CB) in the laser-absorbent part. This causes a temperature rise at the interface between the parts which leads to melting, diffusion and ultimately joining of the two components. Weld temperatures increase with laser power at a given scan speed. However at higher temperatures, it has been observed that weld strength of LTW starts to decline due to material thermal degradation.

Thermal degradation of materials is a kinetic phenomenon which depends on both temperature and time. Therefore there is no specific temperature for thermal degradation. Thermal gravimetric analysis (TGA) is used to study the thermal degradation of two commonly used thermoplastic materials: polycarbonate (PC) and polyamide 6 (PA6). Each material was studied at two levels of CB. It is shown in this work that increasing the carbon black (CB) level from 0.05 to 0.2wt% has no significant effect on the thermal stability of PA6. However, it is observed that increasing the CB level from 0.05 to 0.2wt% has a noticeable effect on the thermal stability of PC.

The TGA data were then used to obtain the kinetic triplets (frequency factor (k_0), activation energy (E), and reaction model ($f(\alpha)$)) of the materials using a non-linear model-fitting method. These kinetic triplets were combined with temperature-time data obtained from a Finite Element Method (FEM) simulation of the LTW process to predict material degradation during LTW. The predicted degradation was then compared with experimental

data. It is found that the predicted onset of material degradation is in good agreement with experimentally observed thermal degradation (of both visually observed degradation onset and weld strength decline) for PC and PA6.

A semi-empirical model based on the FEM temperature data is also developed in this work as a simpler alternative for obtaining LTW maximum temperature-time profiles for prediction of material thermal degradation during LTW. Comparison of the predicted material conversion using temperature-time profile obtained by FEM and the semi-empirical model shows good agreement.

Acknowledgements

I wish to express my gratitude to my supervisor, Dr Philip Bates, Professor at the Royal Military College of Canada (RMCC) whose immense grasp of and enthusiasm for the subject formed a source of guidance, support and encouragement for me in conducting and carrying out this research.

I am grateful to Dr Mingliang Chen whose thesis provided the background for mine. He helped me to understand the Comsol® FEM program used in this work. I am thankful to my friend Chinedu Onwugbufor, a graduate of Queen's university, for all his encouragement and for helping me to understand Matlab programing better. I am also grateful to Andrea Liskova then from Queen's university who was of immense assistance to me while I was conducting the TGA experiments used in this thesis.

My unreserved gratitude goes to my family and friends who stood solidly behind me in patience as I was working on my research. I am grateful to Queen's Society of Graduate Students (SGPS) for all their support to me. I am also grateful to NSERC for funding my research.

Table of Contents

Abstract ii

Acknowledgements iv

Table of Contents v

List of Figures ix

List of Tables xxiv

Abbreviations xxvi

Chapter 1 Introduction 1

1.1 Plastic Joining 1

1.1.1 Plastic Joining Techniques 2

1.2 Laser transmission welding (LTW) 3

1.2.1 Introduction and history 3

1.2.2 Advantages of LTW 5

1.2.3 Laser beam delivery techniques 6

1.3 Objective 7

1.3.1 Thermo-gravimetric analysis (TGA) 9

1.3.2 Degradation kinetics model 9

1.3.3 Temperature-time profile 9

1.3.4 Thermal degradation in LTW 10

1.3.5 Semi-empirical model for temperature-time profiles 10

Chapter 2 Literature Review 11

2.1 Thermal degradation kinetics of polymers 11

2.1.1 Degradation in polymers 11

2.1.2 Thermal degradation 12

2.1.3 Experimental methods for thermal degradation kinetic studies 14

2.2 Thermo-gravimetric analysis (TGA) 15

2.2.1 Overview of TGA 15

2.2.2 Determination of kinetic triplet 20

2.2.3 Experimental data of PC and PA6 30

2.3 Laser transmission welding 34

2.3.1 Laser light transmission 34

2.3.2 LTW process parameters 44

2.2.4 Modelling in contour LTW 46

2.2.5 Thermal degradation in LTW 54

Chapter 3 Thermo-Gravimetric Analysis (TGA) 57

3.1 Material 57

3.2 Experimental 58

3.3 Experimental results and discussion 60

Chapter 4 TGA Data Modelling 65

4.1 Determination of $\boldsymbol{E\alpha}$ 65

4.2 Selection of model 67

4.3 Non-linear model fitting 71

Chapter 5 Temperature-Time Profile 77

5.1 Overview of Chen's thermal model and LTW process conditions 77

5.1.1 Materials properties of PA6 and PC 78

5.1.3 LTW process conditions 83

5.2 Temperature-time profile obtained from FEM 84

Chapter 6 Thermal Degradation Simulation 89

6.1 Theory 89

6.2 Results and discussion 90

Chapter 7 Semi-Empirical Model for Maximum LTW Temperature-Time Data 103

7.1 Background 103

7.2 Creation of LTW temperature-time data master-curve 105

7.2.1 Heating phase 106

7.2.2 Cooling phase 108

7.3 Prediction of maximum temperature during LTW ($\boldsymbol{Tmax}$) 112

7.4 Validation of the semi-empirical model 120

Chapter 8 Conclusions and Recommendations 125

8.1 Conducted work 125

8.2 Conclusions 125

8.4 Recommendations 127

Appendix A 141

Appendix B 153

B.1 $\boldsymbol{E\alpha}$ of the materials 153

B.2 TGA curve-fitting 158

Appendix C 163

Appendix D 165

D.1 Thermal properties 165

D.2 Temperature profiles of pc along $\boldsymbol{y}$-axis 167

D.3 Temperature-time profile 168

Appendix E 171

E.1 Cooling phase temperature-time data for non-contact geometry 177

E.2 Conversion as funtion of time 178

Appendix F 185

List of Figures

Figure 1-1 Vehicle indicator light 1

Figure 1-2 Air intake manifold 1

Figure 1-3 Tea kettle 2

Figure 1-4 Lawnmower gas tank 2

Figure 1-5 schematic representation of laser transmission welding 4

Figure 1-6 Weld shear strength against laser power for different materials 7

Figure 2-1 LTW weld joint fractures after pull test of PC showing voids caused by thermal degradation (0.05 wt% CB, 25 mm/s) 14

Figure 2-2 Schematic of trends of temperature, mass lost and reaction rate during TGA for different heating methods 17

Figure 2-3 TG curves of isotactic polypropylene and 2.5wt% carbon nanotube blend at heat rates of 5°C/min, 10°C/min 15°C/min and 20°C/min respectively 19

Figure 2-4 Compensation effect for the degradation of different phases of HMX 21

Figure 2-5 $\mathrm{Y}(\alpha)$ master plots for different reaction models $f(\alpha)$ 27

Figure 2-6 $\mathrm{Z}(\alpha)$ master plots for different reaction models $f(\alpha)$[..... 28

Figure 2-7 Decision tree for model selection using $Z(\alpha)$ and $Y(\alpha)$ plots..... 29

Figure 2.8 Light beam interactions with polymer parts during LTW..... 35

Figure 2-9 Set up for measurement of laser light reflectance and transmittance through polymers..... 36

Figure 2-10. lnT_T vs. D and CB level for PA6..... 39

Figure 2-11 absorption coefficient vs CB level for PC,PA6 and PA6GF..... 41

Figure 2-12 T-NPFD profile after scattering by 3.2-mm PA6 GF30% plaque (line scan along X) compared with unscattered-beam profile (from pinhole-based measurements)..... 43

Figure 2-13 SDT (Line Energy) vs laser scan speed for PC..... 45

Figure 2-14 A Typical Contour LTW geometry..... 47

Figure 2-15 Experimental and predicted a melt width of PC (0.05 wt% CB, 25 mm/s speed) for non-contact model..... 51

Figure 2-16 Experimental and predicted a melt width of PA6 (0.2 wt% CB, 25 mm/s speed) for non-contact model..... 52

Figure 2-17 Experimental and predicted a weld width of PC (0.05 wt% CB, 25 mm/s speed) for contact mode..... 53

Figure 2-18 Experimental and predicted a weld width of PA6 (0.1 wt% CB, 25 mm/s speed) for contact model..... 53

FIGURE 2-19 Visual observation of laser-absorbent part of PC with 0.05wt% CB in a non-contact method at scan speed of 3000mm/min and different power level 56

Figure 3-1 Experiment 1, 2 and 3 TG curves of PC with 0.05wt%CB at heating rates of 5 and 20°C/min 59

Figure 3-2 Experiment 1, 2 and 3 TG curves of PC with 0.2wt%CB at heating rates of 5 and 20°C/min 59

Figure 3-3 Experiment 1 and 2 TG curves of PA6 with 0.05 and 0.2wt%CB at heating rates of 5 and 20°C/min. Each heating rate experiment was repeated two times for each CB level 60

Figure 3-4 TG curves of PC with 0.05wt% CB content at heating rates of 5, 10, 15 and 20°C 61

Figure 3-5 TG curves of PA6 with 0.05wt% CB content at heating rates of 5, 10, 15 and 20°C 61

Figure 3-6 TG curves of PC and PA6 with 0.05wt% CB content at different heating rate of 5°C 62

Figure 3-7 TG curves of PC with 0.05wt% and 0.2wt% CB content at a heating rate of 5°C..... 63

Figure 3-8 TG curves of PA6 with 0.05wt% and 0.2wt% CB content at heating rate of 5°C 64

Figure 4-1 E_α of PC, obtained with 0.05wtCB by Friedman, KAS and OFW methods 66

Figure 4-2 E_α of PC with 0.2wt% CB, obtained by Friedman, KAS and OFW methods 66

Figure 4-3 E_α of PA6 with 0.05 and 0.2wt%CB, obtained by Friedman, KAS and OFW methods 67

Figure 4-4 Experimental $Y(\alpha)$ plots of PC with 0.05wtCB at different heating rates 68

Figure 4-5 Experimental $Z(\alpha)$ plots of PC with 0.05wt% CB at different heating rates..... 68

Figure 4-6 Experimental $Y(\alpha)$ plots of PC with 0.2wt% CB at different heating rates..... 69

Figure 4-7 Experimental $Z(\alpha)$ plots of PC with 0.2wt% CB at different heating rates..... 69

Figure 4-8 Experimental $Y(\alpha)$ plots of PA6 at different heating rates..... 70

Figure 4.9 Experimental $Z(\alpha)$ plots of PA6 at different heating rates 70

Figure 4-10 Mass loss curves of PC (0.05wt% CB) samples at heating rates of 5 and 20°C and their fitting curves with Sestak-Beggren model 73

Figure 4-11 Mass loss curves of PC (0.2wt% CB) samples at heating rates of 5 and 20°C and their fitting curves with Sestak-Beggren model 73

Figure 4-12 Mass loss curves of PA6 samples at heating rates of 5 and 20°C and their fitting curves with *n*th-order model..... 74

Figure 5-1 Structure of the 3-D quasi-static model with its initial and boundary conditions..... 82

Figure 5.2 Schematic of experimental lap joint geometry and LTW setup used for the LTW 83

Figure 5-3 Typical comsol model output obtained by running Chen's model (PA6 0.1wt% CB, 20 W)..... 85

Figure 5-4 Typical temperature profile along the y direction for non-contact model (PA6 0.1wt% CB, 20 W)..... 85

Figure 5-5 Typical temperature profile along the y direction for contact model (PA6 0.1wt% CB, 20 W) 86

FIGURE 5-6 Temperature-time profile of PC (contact, 0.05wt%CB) at different laser power level 87

FIGURE 5-7 Temperature-time profile of PC (non-contact, 0.05wt%CB) at different laser power level..... 87

Figure 5-8 Temperature-time profile of PA6 (contact, 0.05CB) at different laser power level . 88

Figure 5-9 Temperature-time profile of PA6 (non-contact, 0.05wt%CB) at different laser power level..... 88

Figure 6-1 Predicted conversion vs time (PC 0.1wt% CB, 25mm/s, non-contact weld 91

Figure 6-2 Predicted conversion vs time (PA6 0.1wt% CB, 25mm/s, non-contact weld)..... 91

Figure 6-3 Predicted conversion vs time (PC 0.1wt% CB, 25mm/s, contact weld). 92

Figure 6-4 Predicted conversion vs time (PA6 0.1wt% CB, 25mm/s, contact weld) 92

Figure 6-5 Observed and predicted surface damage of laser-transparent for PC 94

Figure 6-6 Observed and predicted surface damage of laser-transparent for PA6 95

Figure 6-7 Weld strength (primary axis) and conversion vs laser power (secondary axis) of PC with 0.025wt% CB (contact weld)..... 97

Figure 6-8 Weld strength (primary axis) and conversion vs laser power (secondary axis) of PC with 0.05wt% CB (contact weld)..... 97

Figure 6-9 Weld strength (primary axis) and conversion vs laser power (secondary axis) of PC with 0.1wt% CB (contact weld)..... 98

Figure 6-10 Weld strength (primary axis) and conversion vs laser power (secondary axis) of PA6 with 0.025wt% CB (contact weld)..... 99

Figure 6-11 Weld strength (primary axis) and conversion vs laser power (secondary axis) of PA6 with 0.05wt% CB (contact weld). 99

Figure 6-12 Weld strength (primary axis) and conversion vs laser power (secondary axis) of PA6 with 0.1wt% CB (contact weld 100

Figure 6-13 Observed and predicted laser power causing onset of decline in weld strength and onset of thermal degradation respectively for PC..... 101

Figure 6-14 Observed and predicted laser power causing onset of decline in weld strength and onset of thermal degradation respectively for PA6 102

FIGURE 7-1 Temperature-time profile of PC at different laser power levels, CB levels and laser scan speeds 104

Figure 7-2 Dimension of the laser beam used for the LTW 106

Figure 7-3 Heating phase Master-curve of the materials at different laser scan speed and CB levels 107

Figure 7-4 $\ln(\Gamma)$ vs $\ln(t_c)$ for different CB levesl (0.050m) 109

Figure 7.5 $-[\text{slopes of } \ln(\Gamma) \text{ vs } \ln(t_c) \text{ plots}]$ vs CB wt % for different CB levesl (0.05m/s) ... 109

Figure 7.6 $\ln\Gamma/(-1.65CB^{0.304})$ vs $\ln(t_c)$ for different CB levesl and laser scan speeds (contact geometry)..... 110

Figure 7.7 $[\text{Slope of } \ln\Gamma/(-1.65CB^{0.304}) \text{ vs } \ln(t_c) \text{ plots}]$ vs v for different laser scan speeds (0.05 wt% CB)..... 111

Figure 7.8 Cooling phase Master-curve of the materials at different laser scan speed and CB levels 111

Figure 7.9 Predicted LTW maximum temperatures using FEM and analytical model (PC, 0.025wt%CB, 0.025m/s, FEM contact geometry**)**..... 114

Figure 7.10 Predicted LTW maximum temperatures using FEM and analytical model (PC, 0.05wt%CB, 0.025m/s, FEM contact geometry)..... 114

Figure 7.11 Predicted LTW maximum temperatures using FEM and analytical model (PC, 0.1wt%CB, 0.025m/s, FEM contact geometry)..... 115

Figure 7.12 plot of left side of the equation 7.8 (for different laser power and their corresponding T_{max}) vs – A (0.025, 0.05 and 0.1 wt %CB) (0.025m/s)..... 117

Figure 7.13 Predicted LTW maximum temperatures using FEM and analytical model (PC, 0.025wt%CB, 0.025m/s, at $y = y'$ for analytical model)..... 118

Figure 7.14 Predicted LTW maximum temperatures using FEM and analytical model (PC, 0.05wt%CB, 0.025m/s, at $y = y'$ for analytical model)..... 118

Figure 7.15 Predicted LTW maximum temperatures using FEM and analytical model (PC, 0.1wt%CB, 0.025m/s, at $y = y'$ for analytical model)..... 119

Figure 7.16 Predicted LTW maximum temperatures using FEM and analytical model (PC, 0.025 wt%CB, 20 W, at $y = y'$ for analytical model)..... 119

Figure 7.17 Figure 7-17 Predicted LTW maximum temperature-time profile using FEM and semi-empirical model (PC, 0.025m/s, Different CB levels)..... 121

Figure 7.18 Predicted LTW maximum temperature-time profile using FEM and semi-empirical model (PC, 0.05 wt% CB, different laser scan speeds) 121

Figure 7.19 FEM and Analytical model obtained material conversion vs laser power for PC with 0.025wt% CB (0.025m/s). 122

Figure 7.20 FEM and Analytical model obtained material conversion vs laser power for PC with 0.05wt% CB (0.025m/s) 123

Figure 7.21 FEM and Analytical model obtained material conversion vs laser power for PC with 0.1wt% CB (0.025m/s) 123

Figure A-1 Experiment 1, 2 and 3 TG curves of PC with 0.05wt%CB at heating rates of 10°C/min 141

Figure A-2 Experiment 1, 2 and 3 TG curves of PC with 0.05wt%CB at heating rates of 15°C/min 142

Figure A-3 Experiment 1, 2 and 3 TG curves of PC with 0.2wt%CB at heating rates of 10°C/min 142

Figure A-4 Experiment 1, 2 and 3 TG curves of PC with 0.2wt%CB at heating rates of 15°C/min 143

Figure A-5 Experiment 1and 2 TG curves of PA6 with 0.05 and 0.2wt%CB at heating rates of 10°C/min 143

Figure A-6 Experiment 1and 2 TG curves of PA6 with 0.05 and 0.2wt%CB at heating rates of 15°C/min 144

Figure A-7 TG curves of PC with 0.2wt% CB content at heating rates of 5, 10, 15 and 20°C..... 144

Figure A-8 TG curves of PA6 with 0.2wt% CB content at heating rates of 5, 10, 15 and 20°C... 145

Figure A-9 TG curves of PC and PA6 and with 0.05wt% CB content at different heating rate of 10 °C 145

Figure A-10 TG curves of PC and PA6 with 0.05wt% CB content at different heating rate of 15 °C 146

Figure A-11 TG curves of PC and PA6 with 0.05wt% CB content at different heating rate of 20 °C 146

Figure A-12 TG curves of PC and PA6 and with 0.2wt% CB content at different heating rate of 5 °C 147

Figure A-13 TG curves of PC and PA6 and with 0.2wt% CB content at different heating rate of 10 °C 147

Figure A-14 TG curves of PC and PA6 with 0.2wt% CB content at different heating rate of 15 °C 148

Figure A-15 TG curves of PC and PA6 with 0.05 wt% CB content at different heating rate of 20 °C 148

Figure A-16 TG curves of PC with 0.05wt% and 0.2wt% CB content at a heating rate of 10°C. 149

Figure A-17TG curves of PC with 0.05wt% and 0.2wt% CB content at a heating rate of 15°C. 149

Figure A-18 TG curves of PC with 0.05wt% and 0.2wt% CB content at a heating rate of 20°C 150

Figure A-19TG curves of PA6 with 0.05wt% and 0.2wt% CB content at a heating rate of 10°C. 150

Figure A-21 TG curves of PA6 with 0.05wt% and 0.2wt% CB content at a heating rate of 15°C 151

Figure A-22 TG curves of PA6 with 0.05wt% and 0.2wt% CB content at a heating rate of 20°C 151

Figure B-1 E_α of PC with 0.05 wt%CB, obtained by KAS, Friedman and OFW methods using TGA data from experiment 1. 153

Figure B-2 E_α of PC with 0.05 wt%CB, obtained by KAS, Friedman and OFW methods using TGA data from experiment 2 154

Figure B-3 E_α of PC with 0.05 wt%CB, obtained by KAS, Friedman and OFW methods using TGA data from experiment 3. 154

Figure B-4 α E_α of PC with 0.2 wt%CB, obtained by KAS, Friedman and OFW methods using TGA data from experiment 1. 155

Figure B-5 E_α of PC with 0.2 wt%CB, obtained by KAS, Friedman and OFW methods using TGA data from experiment 2. 155

Figure B-6 E_α of PC with 0.2 wt%CB, obtained by KAS, Friedman and OFW methods using TGA data from experiment 3. 156

Figure B-7 E_α of PA6 with 0.2 wt%CB, obtained by KAS, Friedman and OFW methods using TGA data from experiment 1. 156

Figure B-8 E_α of PA6 with 0.2 wt%CB, obtained by KAS, Friedman and OFW methods using TGA data from experiment 2 157

Figure B-9 E_α of PA6 with 0.05 wt%CB, obtained by KAS, Friedman and OFW methods using TGA data from experiment 1. 157

Figure B-10 E_α of PA6 with 0.05 wt%CB, obtained by KAS, Friedman and OFW methods using TGA data from experiment 2. 158

Figure B-11 Mass loss curves of PC (0.05wt% CB) samples at heating rates 10°C and their fitting curves with SB model. 159

Figure B-12 Mass loss curves of PC (0.05wt% CB) samples at heating rates 15°C and their fitting curves with SB model 159

Figure B-13 Mass loss curves of PC (0.2wt% CB) samples at heating rates 10°C and their fitting curves with SB model 160

Figure B-14 Mass loss curves of PC (0.2wt% CB) samples at heating rates 15°C and their fitting curves with *SB*-order model. 160

Figure B-15 Mass loss curves of PA6 samples at heating rate of 10°C and their fitting curves with *n*th-order model 161

Figure B-16 Mass loss curves of PA6 samples at heating rate of 15°C and their fitting curves with *n*th-order model 161

Figure D-1 Heat capacity of PC and PA6 as function of temperature 165

Figure D-2 Thermal Conductivity of PC and PA6 as function of temperature 166

Figure D-3 Density of PC, PA6 and PA6GF as function of temperature 166

Figure D-4 Typical temperature profile along the y direction for non-contact model (PC 0.1wt% CB, 20 W, 25mm/s). 167

Figure D-5 D-5 Typical temperature profile along the y direction for contact model (PC 0.1wt% CB, 20 W, 25mm/s) 167

Figure D-6 Temperature-time profile of PC (contact, 0.1wt%CB) at different laser power level 168

Figure D-7 Temperature-time profile of PC (contact, 0.05wt%CB) at different laser power level 168

Figure D-8 Temperature-time profile of PC (contact, 0.025wt%CB) at different laser power level 169

Figure D-9 Temperature-time profile of PA6 (contact, 0.1wt%CB) at different laser power level 169

Figure D-10 Temperature-time profile of PA6 (contact, 0.05wt%CB) at different laser power level 170

Figure D-11 Temperature-time profile of PA6 (contact, 0.025wt%CB) at different laser power level. 170

Figure E-1 ln$T$ vs time of the FEM temperature-time data (PA6, 0.05, 25mm/s, non-contact geometry) 178

Figure E-2 Predicted conversion vs time (PC 0.05wt% CB, 25mm/s, contact weld) 178

Figure E-3 Predicted conversion vs time (PC 0.025wt% CB, 25mm/s, contact weld) 179

Figure E.4 Predicted conversion vs time (PA6 0.05wt% CB, 25mm/s, contact weld)..... 179

Figure E.5 Predicted conversion vs time (PA6 0.025wt% CB, 25mm/s, contact weld weld)..... 180

Figure E.6 Predicted conversion vs time (PC 0.05wt% CB, 25mm/s, non-contact weld) 180

Figure E.7 Predicted conversion vs time (PC 0.025wt% CB, 25mm/s, non-contact weld). 181

Figure E.8 Predicted conversion vs time (PC 0.0125wt% CB, 25mm/s, non-contact 181

Figure E.9 Predicted conversion vs time (PA6 0.2wt% CB, 25mm/s, non-contact weld)..... 182

Figure E.10 Predicted conversion vs time (PA6 0.05wt% CB, 25mm/s, non-contact weld) 182

Figure E.11 Predicted conversion vs time (PA6 0.0167wt% CB, 25mm/s, non-contact weld) . 183

Figure E.12 Predicted conversion vs time (PA6 0.0125wt% CB, 25mm/s, non-contact weld) . 183

List of Tables

Table 2-1 Some kinetic models and their conversion function $f(\alpha)$ 16

Table 2-2 Typical α_m and α_P^{∞} of different $f(\alpha)$ 27

Table 2-3 Experimental data from previous studies of degradation of PC, PA6 and PA6GF 31

Table 4-1 kinetic parameters from references and from experiment..... 74

Table 4-2 R-square of the non-linear model-fitting of the materials 74

Table 5-1 Thermal and optical properties of the materials used in the FEM..... 78

Table 6-1 % Simulation error (non-contact geometry)..... 95

Table 6-2 % Simulation error (contact geometry) 100

Table 7.1 PC properties used for the analytical model..... 113

Table 7-2 Approximte y' values obtained from the FEM for different CB levels and laser scan speeds 116

Table 8-1 Obtained kinetic parameters 126

Table E-1 $f(t)$ for PC (0.1 wt% CB, 25mm/s, contact model) 171

Table E-2 $f(t)$ for PC (0.05 wt% CB, 25mm/s, contact mode) 172

Table E-3 $f(t)$ for PC (0.025 wt% CB, 25mm/s, contact model) 172

Table E-4 $f(t)$ for PA6 (0.1 wt% CB, 25mm/s, contact model) 173

Table E-5 $f(t)$ for PA6 (0.05 wt% CB, 25mm/s, contact model) 173

Table E-6 $f(t)$ for PA6 (0.025 wt% CB, 25mm/s, contact model) 174

Table E-7 $f(t)$ for PC (25mm/s, non-contact model)..... 175

Table E-8 $f(t)$ for PA6 (25mm/s, non-contact model) 176

Abbreviations

α	Degree of conversion
A	Absorption coefficient, 1/m
A_1	Apparent absorption coefficient, 1/m
A_T	Total reflectance
β	Heating rate, °C/min
c	Accommodation constant
C_p	Heat capacity, J/(kg K)
CB	Carbon black
C_{CB}	Carbon black content, wt.%
CNTs	Carbon nanotubes
CRTA	constant rate thermal analysis
DSC	Differential scanning calorimetry
ρ	Density, kg/m^3
E	Activation energy, kJ/mol
Ɛ	Simulation error, %
E_α	Activation energy at a given extent of conversion, kJ/mol
$f(\alpha)$	Reaction model
$f(t)$	Time function for temperature, °C
FDM	Finite difference method
FEM	Finite element method
$g(\alpha)$	Integral function of conversion

GF	Glass fibre
HAZ	Heat affected Zone
HMX	Cyclotetramethylenetetranitramine
ICTAC	International Confederation for Thermal Analysis and Calorimetry
K_1	Material-dependent proportionality constant, 1/(m.wt%)
K_2	A parameter which is a function of *CB* and v, 1/s
κ	Thermal conductivity, W/(m K)
K_E	Extinction coefficient, 1/m
k_0	Frequency factor, min^{-1}
$\mathrm{K}(T)$	Rate constant, s^{-1}
L_B	Length of laser beam (along the transverse direction), m
L_E	Line energy, J/m
LTW	Laser transmission welding
MLR	Multiple linear regression
MWNTs	Multi-walled carbon nanotubes
η	Surface reflectance
NMF	Non linear model-fitting
NPFD	Normalised power flux distribution, W/m^2
NIR	Near-Infrared
P	Power, W
P''	Laser light intensity, W/m^2
$P_L^{''}$	Laser source power intensity, W/m^2
P_L	Laser source power, W
PA6	Nylon 6

PA6GF	Nylon 6 containing 30wt% GF
PC	Polycarbonate
Q	Heat source or sink, W/m^3
δ	Power scattering ratio
σ	Shear strength
σ_s	Scattering standard deviation
$Q(x, y, z)$	Heat source or sink W/m
r	Coefficient of linear correlation
R	Gas constant, KJ /(K mol)
RSS	Residual sum of square
R_T	Total reflectance
SDT	Surface damage threshold, J/m
t	Time, s
TEDD	Transverse energy density distribution
Γ	Normalised temperature
t_c	Cooling time, s
τ_h	Normalised time for the heating phase
T_{max}	Maximum LTW temperature, °C
$T_{\max\_rate}$	Maximum degradation rate temperature, °C
T_0	Temperature for onset of thermal degradation, °C
T-NPFD	Transverse-normalised power flux distribution, W/m^2
TGA	Thermo-gravimetric analysis
T_T	Total transmittance
t_{start}	Time from the start of FEM simulation to the start of heating, s

UV	Ultra-violet
v	Laser scan speed, m/s
W	Width of laser beam (across the transverse direction), m
W_f	Final mass of the specimen, kg
W_0	Initial mass of the specimen, kg
W_t	Weight of specimen at a particular time, kg
y’	Depth for maximum LTW temperature, m
$\mathrm{Y}(\alpha)$	Function defined by equation 2-12
$\mathrm{Z}(\alpha)$	Function defined by equation 2-13

Chapter 1
Introduction

This chapter gives an overview of plastic joining techniques. Laser transmission welding (LTW) and its concepts are introduced. The objectives of this thesis are also elaborated in this chapter.

1.1 Plastic Joining

Plastics have continued to gain acceptance in materials engineering, replacing metals, ceramics, glass and other material in many applications. This is due their versatile properties, relatively low material and process costs. In industry, many plastic products are produced through moulding processes in which the plastic takes the shape of the mould cavity. However, due to complex geometries, large sizes and sometimes the need to have two different materials, some plastic products like vehicle indicator lamps, air intake manifolds, tea kettles and lawnmower shrouds/gas tanks cannot be moulded as one part [1, 2, 3]. This necessitates the joining of plastics.

Figure 1-1 Vehicle indicator light [1]

Figure 1-2 Air intake manifold [1]

Figure 1-3 Tea kettle [1]

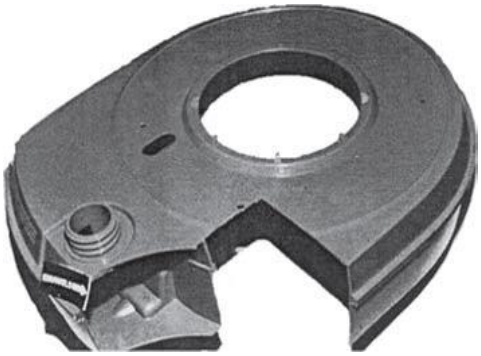

Figure 1-4 Lawnmower gas tank [1]

1.1.1 Plastic Joining Techniques

Plastic Joining techniques can be grouped into three major categories: chemical (adhesive) bonding, mechanical fastening and thermal (fusion) welding [2, 4, 5].

Mechanical fastening involves joining plastic together using fasteners that rely on mechanical principles [2, 4]. This technique is desirable because parts can be reopened and dissimilar materials can be used. However, mechanical fastening methods have disadvantages which may arise from extra costs of the fastener, thermal expansion coefficient mismatch and a non-hermetic interface between the connected parts [2]

Chemical bonding is a joining technique that applies an intermediate layer to join substrates of different materials [1, 4]. This plastic joining technique is advantageous because it produces hermetic seals and can be used to join dissimilar materials including thermosetting resins. The design of the moulded parts can also be simple for adhesive bonding. Chemical

bonding methods have a weakness due extra manufacturing cost, long curing time, difficulty of bonding to certain plastics and the possibility of chemical attack on the material [2, 5].

Welding is a technique that involves heating thermoplastics (to temperatures above their glass transition temperatures for amorphous plastics and above their melting point for semi-crystalline plastics), holding the parts together for inter-molecular diffusion at the interface and fusion upon cooling [1, 2, 4, 6, 7]. Welding is relatively fast compared to other joining techniques. They form hermetic seals, relatively strong joints and are generally recyclable [1, 4, 8, 9]. Generally, welding can be grouped into three categories: mechanical friction heating (like vibration and ultrasonic welding), thermal heating (like in hotplate and hot gas welding) and electromagnetic heating (like in radio frequency and laser welding) [7, 8]. Laser welding is the focus of this research.

1.2 Laser transmission welding (LTW)

1.2.1 Introduction and history

Laser transmission welding (LTW) is a welding technique that takes advantage of the transparency of plastics to near-infrared (NIR) wavelengths to join parts together [10]. In LTW, a laser beam passes through a transparent part and is absorbed by an absorbent part (as represented by Figure 1-5) while holding the components together under pressure. Upon absorption of the laser beam, the laser light energy is converted to heat which brings about a localized heating of the plastic substrate. The heat produced in the absorbent part is then

transferred by conduction to the transparent part, thereby bringing about a melting at the interface and fusion of the parts upon cooling [11, 12, 13, 14, 15]. A schematic representation of LTW is given in Figure 1-5. Since most thermoplastics are transparent to the laser light, an absorbent pigment (typically carbon black (CB)) is usually mixed with the laser-absorbent part which increases the absorptivity of the plastic substrate to laser light [11, 12].

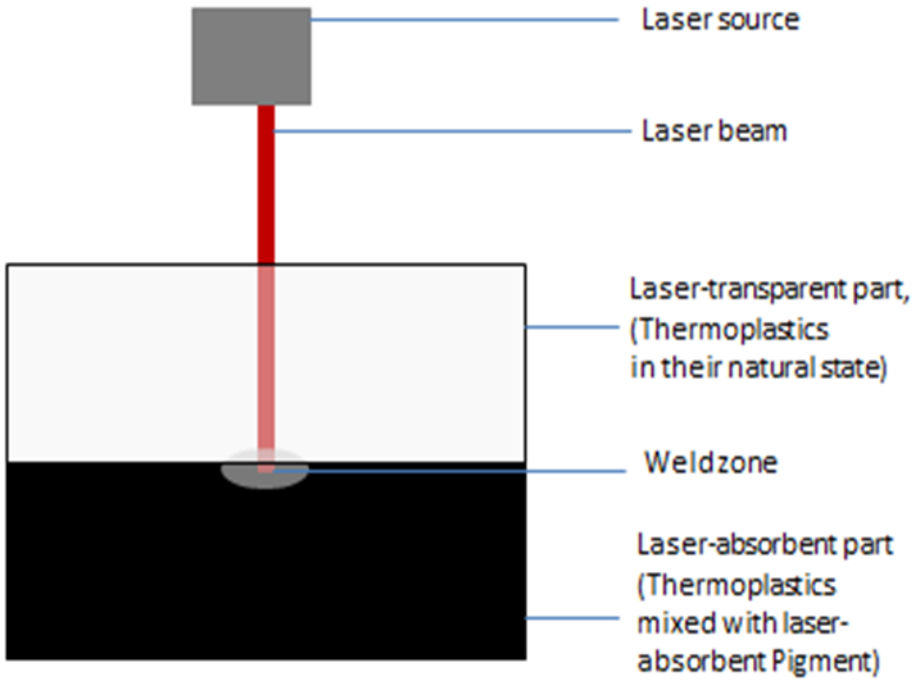

Figure 1-5 schematic representation of laser transmission welding

In 1970, the use of laser as a means of joining plastics was demonstrated [16]. In the mid-1980s, a laser was first used to join automotive components [7]. Although the use of laser joining technology is still at an early stage for wide range of industries [17], it is increasingly gaining acceptance as a means of joining plastics.

1.2.2 Advantages of LTW

Some advantages of LTW include:

- Relatively fast weld cycle time which is generally greater than 10 m/min of the weld seam. This makes LTW suitable for large scale productions of plastic components [17].
- No contact between the weld surface and foreign materials such as in hotplate welding [3].
- Small heat affected zone (HAZ). HAZ is the part of a material that melted or softened during welding. This makes LTW a preferred joining technique for microtechnology [3, 9].
- Relatively little flash (flash is material that melts and flows away from the interface during welding). This makes LTW a superior technology where aesthetics are an issue [3, 9].
- No relative movement of part. This makes it suitable for welding delicate electronics and materials with low elastic moduli [3, 18].
- Flexible and easy to automate [19].

1.2.3 Laser beam delivery techniques

Laser beam delivery techniques in LTW can be categorised into simultaneous, quasi-simultaneous and contour welding [3, 9, 10, 14, 15, 20]. Simultaneous welding is suitable for small parts in which the entire weld surface is irradiated at the same time with either one large or many small laser beams, making meltdown (which is a collapse at the joint interface due to outflow of molten polymer) possible [9, 10, 15]. Small gaps at the weld interface can be bridged by this method because of possible meltdown [10, 15]. Quasi-simultaneous welding involves the use of a galvo-mirror system to irradiate the weld joint surface repeatedly at very high speeds [10, 15]. Because of the low thermal conductivity of thermoplastics, the temperature increases almost uniformly along the weld seam making meltdown again possible [3, 10, 15]. This method is also able to bridge small gaps at weld interface but is limited to small part size and less complex part geometries. In contour welding, the laser beam is moved once along the weld surface [3, 10, 14, 15]. Meltdown is not possible with this method [3, 10]. It has therefore relatively limited gap bridging capabilities unlike its counterparts. However, this method can be used to weld plastic parts of large sizes and complex geometries [3]. It is therefore a popular laser delivery method.

This thesis will focus on contour LTW but the principles developed in the research can be applied to all LTW delivery techniques.

1.3 Objective

In LTW, the weld strength has been shown to increase with increases in laser power until a maximum weld strength is attained. This is followed by a decrease in the weld strength with increasing laser power as shown in Figure 1-6 below [6, 13, 15].

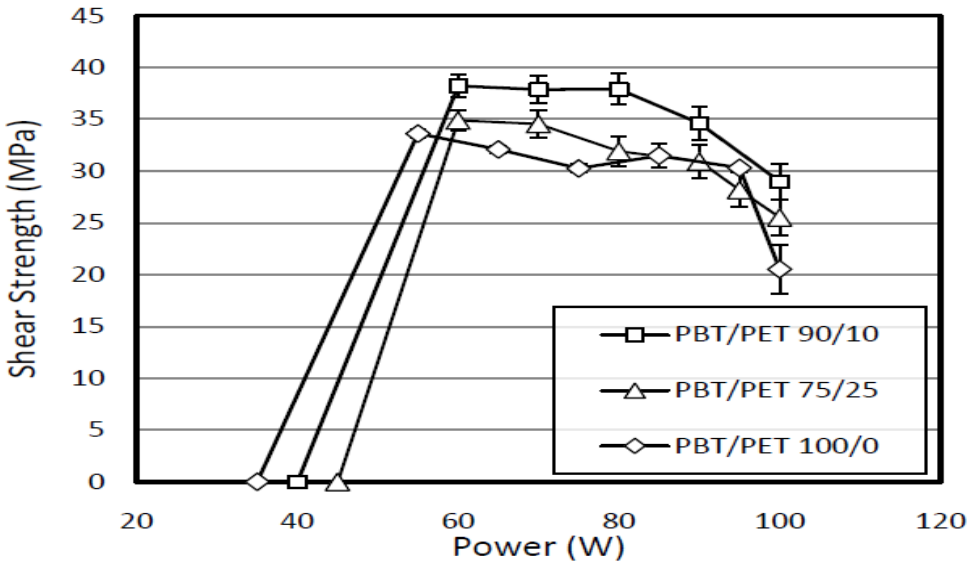

Figure 1-6 Weld shear strength against laser power for different materials [13]

The decrease in strength can be attributed to degradation of the polymer as a result of high welding temperatures caused by high laser power. Proper understanding of the influence of LTW power on material degradation is therefore very important. As part of his project on LTW of polybutylene terephthalate and polyethylene terephthalate blends, Khosravi [13] proposed a simple model for predicting material degradation during LTW. In order to validate and enhance Khosravi's approach, this project presents a more rigorous kinetic model for describing degradation during LTW and seeks to validate it using a wide range of material and

experimental techniques. In addition, a semi-empirical model for obtaining temperature-time profiles during LTW is provided in this thesis for amorphous polymers.

This research objective will be achieved by:

- Obtaining a kinetic model for the degradation of each material as a function of time and temperature. This requires an estimation of the kinetic triplet (frequency factor (k_0), activation energy (E), reaction model $f(\alpha)$ of each material using thermo-gravimetric analysis (TGA) [21]. It is acknowledged that molecular weight degradation may occur at lower temperature without mass loss. However, this project is limited to severe degradation that leads to mass loss during LTW. As most heating in LTW of polymers takes place in the bulk polymer, degradation is assumed in this work to be purely thermal.
- Estimating the maximum temperature as a function of time in each material during LTW. This will be done with a finite element model of the LTW process using Comsol® FEM software.
- Predicting the fraction of the material degraded at the location of maximum temperature (referred to here as the conversion) during LTW by combining the results in the kinetic and thermal models using a Matlab® code.
- Validating predicted conversion using a variety of experimental techniques.
- Development of a semi-empirical model as a simpler method for the prediction of temperature-time profile during LTW.

1.3.1 Thermo-gravimetric analysis (TGA)

TGA experiments were conducted for the selected materials (polycarbonate (PC) and nylon 6 (PA6)). A detailed description of the materials is found in Chapter 3. The TGA experiments make it possible to obtain weight loss with respect to temperature and time. TGA experiments and results are presented in Chapter 3 of this thesis.

1.3.2 Degradation kinetics model

Weight loss as a function of time and temperature can be related with the general equation for molecular degradation below [21]:

$$\frac{\mathrm{d}\alpha}{dt} = k_0 \exp\left(\frac{-E}{RT}\right) f(\alpha) \qquad 1\text{-}1$$

Where α is the degree of conversion, t is time, T is the reaction temperature, k_0 is the frequency factor, E is the activation energy, $f(\alpha)$ is the reaction model and R is the gas constant. Data from the TGA are used to obtain the kinetic triplets (k_0, E and $f(\alpha)$) of each material using a non-linear model-fitting method. The TGA degradation kinetic modelling is presented in Chapter 4.

1.3.3 Temperature-time profile

Mingliang Chen [6] a PhD graduate from the Department of Mechanical and Material Engineering, Queen's University, Canada, developed a 3-D quasi-static thermal (using finite element method (FEM) Comsol® software) model for the prediction of temperature as a

function of time and position during contour LTW. In this thesis, the maximum temperature-time profile of each material during LTW was obtained by running Chen's FEM model at different laser power levels. Chen's model and other contributions to this research from his thesis will be discussed in Chapter 5

1.3.4 Thermal degradation in LTW

Thermal degradation in LTW is predicted in this project by combining the degradation kinetic model (equation 1) with the maximum temperature-time data (obtained from Chen's FEM model) for each material.

Validation of the thermal degradation prediction is made by comparing the predicted maximum conversion of the different materials at different power levels with a number of experimental techniques from reference 6. Thermal degradation in LTW is presented in Chapter 6.

1.3.5 Semi-empirical model for temperature-time profiles

One of the difficulties in using this technique is estimating maximum temperature as a function of time. This is done here using FEM code. Alternatively, a simple semi-empirical, model which is based on Chen's FEM is developed for easier estimation of maximum temperature time profiles of amorphous polymers. This is presented in chapter 7.

Chapter 2
Literature Review

This chapter discusses thermal degradation of polymers in general. Section 2.1 reviews thermal degradation of polymers while section 2.2 discusses laser transmission welding (LTW).

2.1 Thermal degradation kinetics of polymers

2.1.1 Degradation in polymers

During processing or usage, polymers may be subjected to unfavourable conditions such as high temperature or UV radiation and therefore may degrade [22, 23]. Degradation can bring about changes in polymer properties [24, 25]. The type of degradation may depend on the environment the polymer is exposed to, the processing conditions and chemical structure of polymers [23, 25, 26]. Examples of polymer degradation types include:

Mechanical Degradation: This type of degradation occurs when the application of mechanical force brings about possible chain scission and reduction in molecular weight in a polymer or its solution [22, 24].

Ultrasonic Degradation: This type of degradation occurs by sound of a certain frequency that can induce polymer chain vibration, scission and decrease in molecular weight [26].

Chemical Degradation: This type of degradation occurs when corrosive chemicals attack the polymer structures causing chain scission, cross-linking and/or oxidation [25].

Biological degradation: This type of degradation occurs only in polymers that contain certain functional groups that can be attacked by micro-organisms [27, 28].

Photo-oxidative degradation: This is a type of degradation that occurs by ultraviolet (UV) radiation in combination with oxidative effects of atmospheric oxygen and/or hydrolytic effects of water [23].

Thermal degradation: This type of degradation occurs when elevated temperature brings about changes in the chemical structure of polymers and physical properties [29, 30]. This degradation mechanism is the major focus of this thesis.

2.1.2 Thermal degradation

At elevated temperatures, polymers experience the effects of thermal energy. Reaction to the thermal effects may be physical or chemical [30]. Overall, these thermal effects can bring about changes in the properties of the material [29, 31]. It is therefore necessary to understand the thermal degradation of polymers.

Chemical changes due to elevated temperature in polymers may proceed by the action of heat only (thermal degradation) or by the action of heat and oxidant (specifically called thermal oxidative degradation) [22, 32]. The mechanisms in the degradation of polymers include chain-scission in which bonds in the main polymer chain are broken at random locations

or at the chain ends, cross-linking in which bonds are created between polymer chains, side chain-stripping in which atoms or group of atoms, not part of the polymer chains, are removed causing chain unsaturation and further reactions which may include scission, char formation and aromatization [25, 30]. Generally, the thermal degradation of polymers is complex, involving more than one chemical mechanism [30].

Various polymer production and part forming processes subject polymers to high temperatures. For instance in moulding, it is required that a material be heated to enable it to flow and to be formed into the required shapes [22]. In the recycling of polymers, they are also subjected to high temperatures in order to remelt the material [31]. In welding, polymeric materials are also subjected to high temperatures in order to create a molten interface which is a necessary condition for the joining of plastic materials [1, 13]. It has been shown that, in LTW, if too much energy is delivered to the weld (either by increases in power, decreases in scan speed or increasing the CB level as will be elaborated later in section 2.2), excessive temperatures and consequently thermal degradation may occur [6, 13]. This is shown in Figure 2-1 which portrays voids in the weld fracture of PC after a pull test. The smaller void at laser power of 14W was caused by thermal expansion which squeezed molten polymers out of the weld interface [6]. The bigger void at 17W was a result of thermal degradation [6]. This may affect the weld strength of LTW joints. It is therefore essential to understand the effect of LTW parameters on material degradation and weld strength in order to better define the LTW process window.

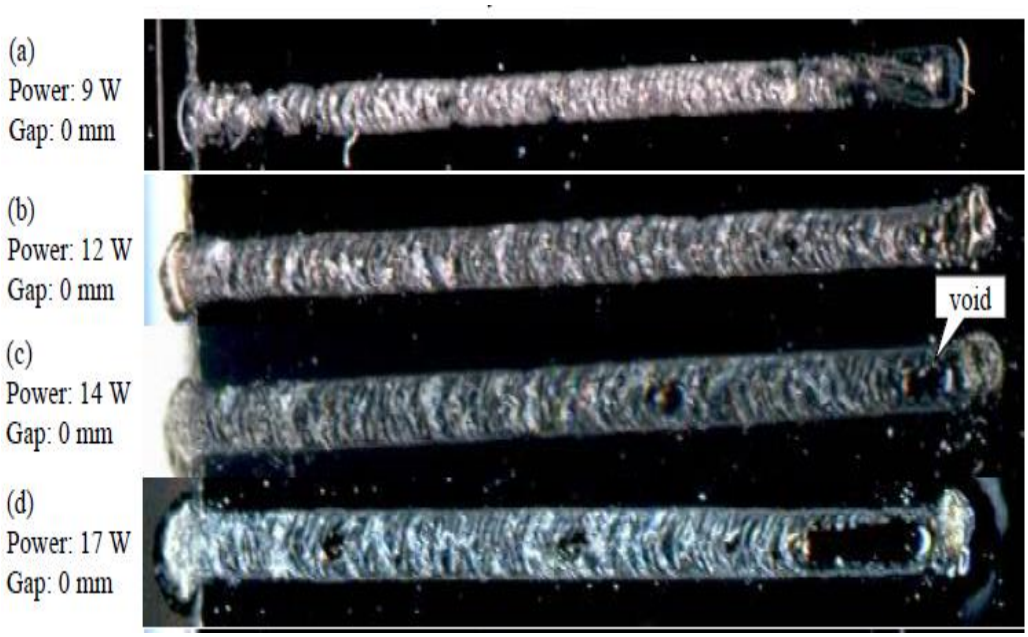

Figure 2-1 LTW weld joint fractures after pull test of PC showing voids caused by thermal degradation (0.05 wt% CB, 25 mm/s) [6].

2.1.3 Experimental methods for thermal degradation kinetic studies

The kinetics of thermoplastic degradation can be studied by several methods which include thermo-gravimetric analysis (TGA), differential scanning calorimetry (DSC) and transient flow experiments [33, 34, 35]. DSC experiments involve monitoring heat flow during polymer heating to track their degradation. Since this technique is normally carried out in sealed sample holders, it is therefore not suitable for quantifying the decomposition of materials that involves gaseous emissions [30]. Transient flow experiments involve monitoring the molecular weight via torque measurements as a function of time at varying processing temperatures [34]. TGA is a technique that measures the change of mass of a polymer sample while it is heated [34]. It is therefore ideally suited for degradation processes that lead to mass loss at high temperatures [36, 37] like the degradation of polymers at the weld-line during LTW.

2.2 Thermo-gravimetric analysis (TGA)

2.2.1 Overview of TGA

Thermo-gravimetric analysis (TGA) is a common means of studying the kinetics of thermoplastic degradation [31, 36, 38, 39, 40, 41]. It is a preferred method because the relevant mass changes are often easier to measure than the associated heat effects [36, 37]. Generally, the rate of a solid state reaction is assumed to be described by [21, 33, 38, 42]:

$$\frac{\mathrm{d}\alpha}{dt} = \mathrm{K}(T) f(\alpha) \qquad 2\text{-}1$$

Where α is the extent of conversion or the fractional conversion (ie degradation) which can be represented mathematically by equation 2-2 [38, 40, 43], $\mathrm{K}(T)$ is the rate constant and $f(\alpha)$ is the reaction model which is an algebraic expression of the kinetic model as function of α [44]. It is usually associated with a physical model that describes the kinetics of the solid state reaction [45]. Some of the forms of $f(\alpha)$ are presented in Table 2.1.

$$\alpha = \frac{W_0 - W_t}{W_0 - W_f} \qquad 2\text{-}2$$

In equation 2-2, W_0 is the initial mass of the specimen, W_t is the weight of the sample at a particular time or temperature while W_f is the final mass of the specimen [40, 43]. This form of the conversion is used in this work to predict material thermal degradation during LTW.

Table 2-1 Some kinetic models and their conversion function $f(\alpha)$ [21, 42].

REACTION MODEL	Abbreviation	$f(\alpha)$
n^{th} order reaction	*Fn (or RO)*	$(1-\alpha)^n$
Prout- Tompkins	*B1*	$\alpha(1-\alpha)$
Sestak-Beggren	*SB*	$(1-\alpha)^n\alpha^m$
n^{th} Order with autocatalysis	*Cn*	$(1-\alpha)^{n(1+\mathrm{Kcat}\,x)}$
Avrami-Erofeev	*An*	$n(1-\alpha)[-\ln(1-\alpha)]^{(n-1)/n}$
Power Law	*P3*	$3\,\alpha^{3/4}$
Contracting sphere	*R2*	$3\,(1-\alpha)^{2/3}$
Contracting Cylinder	*R3*	$2\,(1-\alpha)^{1/2}$
Two-Dimensional Diffusion	*D2*	$[-\ln(1-\alpha)]^{-1}$

By substituting $\mathrm{K}(T)$ in equation 2-1 with an Arrhenius expression, the following equation can be obtained [37, 40, 44, 46, 47]:

$$\frac{d\alpha}{dt} = k_0 \exp\left(\frac{-E}{RT}\right) f(\alpha) \qquad 2\text{-}3$$

Where k_0 is the frequency factor, E is the activation energy, T is the reaction temperature and R is the gas constant. In this thesis, k_0, E and $f(\alpha)$ found in equation 2-3 are defined as the kinetic triplet [21, 47]. The components of the kinetic triplet represent important physical concepts [48]. Transition-state theory links E to the energy barrier and k_0 to the vibrational frequency of the activated complex while $f(\alpha)$ is linked to the reaction mechanism by numerous solid state reaction models [48].

TGA experiments can be performed using a number of different heating rate programs (or heating pathways) [36, 45]. Equation 2-3 is valid for all TGA heating rate programs [49]. The heating rate programs that can be used in TGA experiments include isothermal heating, sample-controlled thermal analysis (an example is a constant rate thermal analysis (CRTA)) and non-isothermal heating (an example is a linear heating rate) [36, 45]. Figure 2-2 shows the time-trends of temperature, mass loss and reaction rate during thermal degradation for the different heating rate programs. In isothermal experiments, samples are heated rapidly to the final temperature and maintained at this temperature [45]. In sample-controlled experiment, the reaction rate is defined by the user [36]. While in linear heating rate, the temperature varies linearly with time [36]. The non-isothermal heating is the most common heating rate programs used in TGA [36, 45].

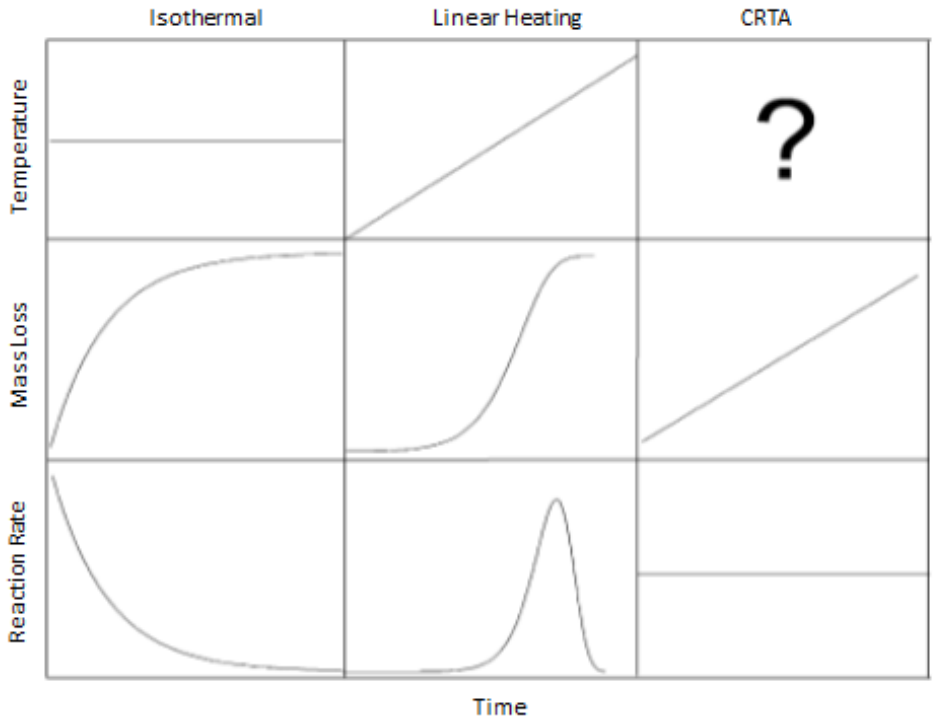

Figure 2-2 Schematic of trends of temperature, mass lost and reaction rate during TGA for different heating methods.[36, 50]

For non-isothermal experiments with a linear heating rate (β), β can be expressed as [38, 45, 47]:

$$\beta = \frac{dT}{dt} \qquad 2\text{-}4$$

Substituting dt with an expression from equation 2-4 into equation 2-3 produces the following equation:

$$\frac{\mathrm{d}\alpha}{dT} = \frac{k_0}{\beta}\exp\left(\frac{-E}{RT}\right) f(\alpha) \qquad 2\text{-}5$$

Equation 2-5 is applicable to non-isothermal TGA experiments with a linear heating rate [41].

For linear heating rate programs, as the heating rate of a process increases, the TG (thermo-gravimetry) mass loss vs temperature curves have been observed to shift to higher temperatures as shown by Figure 2-3. This is because, at higher rates, materials spend less time at each temperature and therefore require a higher temperature for a given amount of degradation. This shift to higher temperature with increases in heating rate shows that thermal degradation of polymers is a kinetic phenomenon which depends on both temperature and time.

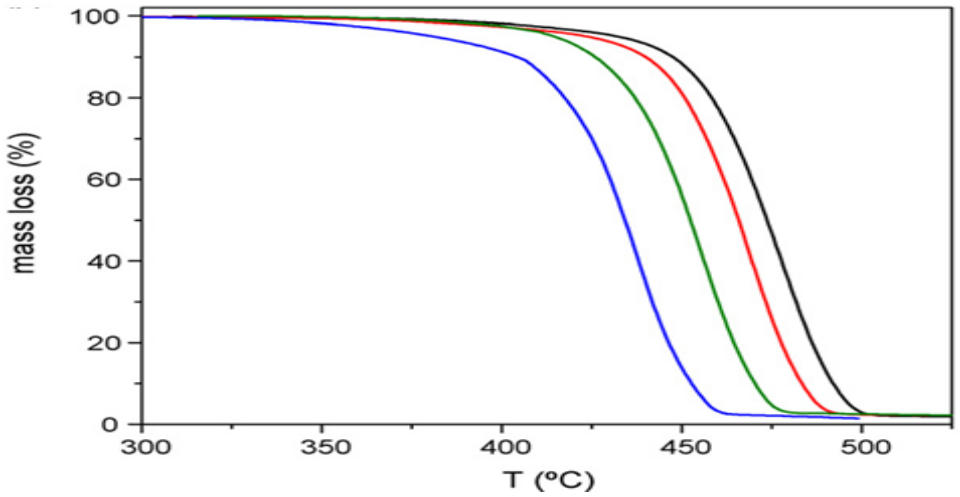

Figure 2-3 TG curves of isotactic polypropylene and 2.5wt% carbon nanotube blend at heat rates of 5°C min^{-1} , 10°C min^{-1} 15°C min^{-1} and 20°C min^{-1} respectively. [41]

TGA data of materials from different heating rates are often reproduced with a unique kinetic triplet [21, 41, 42] as changes in basic kinetic parameters k_0 and E with changes in heating rate have not been substantiated by any theoretical explanation [41]. Prediction of TGA data from different heating rates with a unique kinetic triplet is therefore reasonable and is the approach used to model degradation during LTW in this work. LTW's heating rate varies with time, is very fast and can be as high as 350°C /s [13]. Moreover, heating rates observed in LTW are not normally used in TGA experiments. For one family of materials (polyesters), Khosravi showed that the degradation kinetics of thermoplastics in an LTW process can be reasonably predicted with kinetic triplet obtained from single heating rate TGA experiment with heating rate of 10°C/min, which obviously differs significantly from the heating rate of a real LTW process [6, 13]. However, data from single heating rate TGA is not trusted for reliable kinetic evaluations [21, 40, 42, 57].

2.2.2 Determination of kinetic triplet

By kinetic modelling, this thesis refers to predicting α, $\frac{\mathrm{d}\alpha}{dT}$, or $\frac{\mathrm{d}\alpha}{dt}$ as a function of the kinetic triplet. Estimating the kinetic triplet is performed using TGA data. It is possible to reproduce a TG curve with polynomial functions that have meaningless kinetic parameters. Different researchers have also obtained different kinetic triplets for the same material [21, 41, 42]. Discrepancies in the estimated kinetic triplet can be due to several reasons. For instance, the purge gas used has been shown to influence the values of the kinetic triplet. Experiments have shown variation in the kinetic triplet obtained from so called thermal degradation (which uses an inert gas such as nitrogen as the purge gas) and thermal oxidative degradation (which uses air as the purge gas) [37, 39]. This is because of different chemical reaction pathways in different chemical atmospheres. Sample size also influences the value of the kinetic parameters [41]. Heat transfer affects the value of E in different sample sizes [51].

Other studies have shown that there is a strong dependence of k_0 and E on the adopted $f(\alpha)$ [42, 47]. Studies have also shown that E can have a linear relationship with k_0 as shown by Figure 2-4 and therefore one can compensate for the other in TGA experimental data [48, 52, 53]. This correlation is known as the compensation effect [48, 53]. As a result, when different values of E and k_0 are used with their corresponding compensating counterparts, TGA experimental data may thereby be reproduced with almost the same precision.

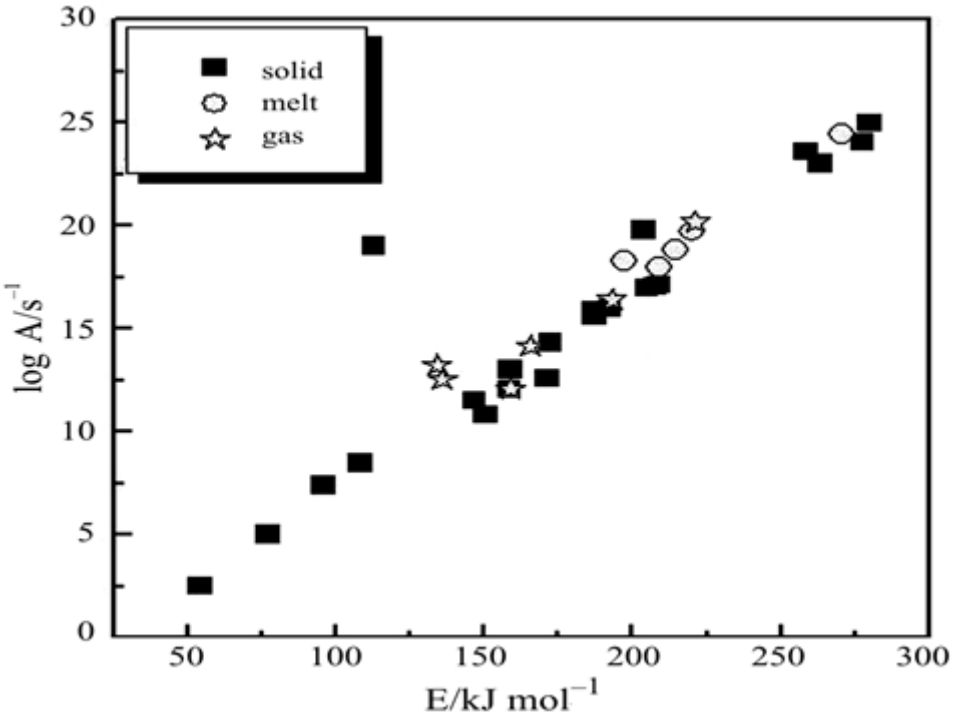

Figure 2-4 Compensation effect for the degradation of different phases of HMX [48]

If determined correctly, the kinetic triplets can be used to reproduce the original kinetic data and for predicting process kinetics outside the experimental temperature region [48]. The International Confederation for Thermal Analysis and Calorimetry (ICTAC) kinetic committee recommended the use of TGA kinetic curves obtained from multiple heating rates or at multiple heating programs for reliable kinetic evaluations [48].

Two major methods used in determination of kinetic triplets are the model free and model fitting methods [21, 32, 42].

Model free methods

Model free methods are mostly the isoconversional methods. Isoconversional methods are based on the principle that the reaction rate is only a function of temperature at a constant extent of reaction [21, 48]. These methods can be used to obtain conversion-dependent activation energy (E_α) without any previous knowledge of the $f(\alpha)$ [38]. Because of their ability to obtain the activation energy without the knowledge of the reaction model, they are known to give reliable values of activation energy [39, 42, 47, 48]. The isoconversional methods can be further grouped into two sub-divisions, the differential isoconversional and the integral isoconversional methods [21]. An example of the differential method is the Friedman method [52]. The integral methods include the Ozawa, Flynn and Wall method (OFW) and Kissinger-Akahira-Sunose (KAS) method [21]. Both the integral and differential methods have errors that are specific to each of them and have been shown to give activation energy values in a similar range with variations at the initial and final stages [21, 42, 47].

Friedman Method

The Friedman method is obtained by taking the logarithm of equation 2-5 and solving for $ln\left[\beta \frac{d\alpha}{dT_\alpha}\right]$. It can be expressed by the following equation [21]:

$$ln\left[\beta \frac{d\alpha}{dT_\alpha}\right] = lnk_0 + lnf(\alpha) - \frac{E_\alpha}{RT_\alpha} \qquad 2\text{-}6$$

Where T_α is the temperature to reach a given value of α.

It is obvious from equation 2-6 that a plot of $ln\left[\beta\left(\frac{d\alpha}{dT_\alpha}\right)\right]$ vs. $\frac{1}{T_\alpha}$ will give the E_α without the use of the reaction model $f(\alpha)$. The plot of $ln\left[\beta\left(\frac{d\alpha}{d}\right)\right]$ vs. $\frac{1}{T_\alpha}$ is made at constant values of α obtained at a series different heating rates.

Ozawa, Flynn and Wall method

By rearranging equation 2-5 the integral function of conversion ($g(\alpha)$) can be obtained as the following [21, 48]:

$$g(\alpha) = \int_0^\alpha \frac{d\alpha}{f(\alpha)} = \frac{k_0}{\beta}\int_0^{T_\alpha} exp\left(\frac{-E}{RT_\alpha}\right) dT_\alpha \qquad 2\text{-}7$$

Approximating the integral in equation 2.7 using the Doyle method [21] (since the temperature integral cannot be integrated analytically [54]), the OFW equation can be obtained as the following [23]:

$$ln(\beta) = constant - 1.052\left(\frac{E_\alpha}{RT_\alpha}\right) \qquad 2\text{-}8$$

A plot of the left side of equation 2.8 vs. $\frac{1}{T_\alpha}$ produces E_α from the slope of the equation.

Kissinger, Akahira and Sunose (KAS) method

KAS equation is obtained by approximating the integral in equation 2.7 using a method developed by Murray and White [21]. It can be represented as the following [21]:

$$ln\left(\frac{\beta}{T_\alpha{}^2}\right) = constant - \left(\frac{E_\alpha}{RT_\alpha}\right) \quad \text{2-9}$$

A plot of the left side of equation 2.9 vs. $\frac{1}{T_\alpha}$ produces E_α from the slope of the equation. With this method, an improved value of E_α can be obtained compared to that obtained by the OFW method [21].

Differential methods are potentially more accurate than the integral methods since they are not obtained by approximation [21]. However, differential methods are more sensitive to experimental noise in TGA experiments [21].

Model-fitting methods

These methods involve fitting different models to the α-Tcurve and simultaneously determining the values of E and k_0 [42]. Model-fitting methods can be divided into two major groups. These two groups are the linear and non-linear model fitting methods [21, 42].

Linear model-fitting methods

Linear model-fitting involves the use of linear regression to obtain the kinetic parameters [21]. This can be achieved by taking the logarithm of the rate equation in order to transform it to a linear regression problem [42]. An example of linear model fitting is the "combined kinetic analysis" developed by Perez-Maqueda et al [45]. This method uses only the modified form of the truncated Sestak-Beggren model ($c(1-\alpha)^n\alpha^m$), as an umbrella function

that fits several reaction models listed in Table 1. This is achieved by transformation of the kinetic equation into the following:

$$ln\left[\frac{d\alpha}{dt}\frac{1}{\alpha^m(1-\alpha)^n}\right] = ln(ck_0) - \frac{E}{RT} \quad \text{2-10}$$

Perez-Maqueda et al [45] described c as an "accommodation constant" for determining the value of k_0. By varying the values of parameters m and n in equation 2-10, a linear relationship can be created between the left hand side of equation 2-10 and the inverse of temperature ($\frac{1}{T}$). The linearity is evaluated by the coefficient of linear correlation, (*r*) whose maximum is found through numerical optimization of the parameters n and m between the left hand side of equation 2-10 and the inverse of temperature ($\frac{1}{T}$) [21, 45]. This allows E and $ln(ck_0)$ to be obtained respectively from the slope and the intercept of the plot. The accommodation constant c can then be obtained by fitting the modified form of the truncated Sestak-Beggren model ($c(1-\alpha)^n\alpha^m$) to an appropriate reaction model $f(\alpha)$ for a thermal degradation process.

Non-Linear Model-Fitting

This method involves minimising the difference between experimentally-generated and calculated data [21, 40, 42]. It can be represented by the following equation [21]:

$$RSS = \sum_1^N (\mathrm{Yexp} - \mathrm{Ycalc})^2 = Minimum \quad \text{2-11}$$

RSS is the residual sum of squares, N is the number of data points. Yexp is the experimentally-generated data while Ycalc is calculated data [21, 43]. Examples of Ycalc and Yexp that can be used are experimentally-generated and model-calculated values of α or $\frac{d\alpha}{dt}$. By manipulation of the rate equation to solve for Ycalc and by varying the values of k_0, E and the kinetic exponents (example, n and m) contained in a reaction model $f(\alpha)$, the kinetic parameters can be determined as the set of parameters that gives a minimum difference between calculated-data and experimentally-generated data (Ycalc and Yexp) [21, 42, 43].

A fit of the model to experimental data can be achieved by transforming the rate equation to a linear regression problem as discussed earlier, however this will distort the error structure of the rate equation [42]. This makes non-linear model fitting, which allows a direct fit of the model to experimental data without any transformation, better than the analysis of the rate equation with linear model fitting [21, 42].

Model selection

The appropriateness of a reaction model $f(\alpha)$ must be based on its ability to reproduce experimental data and on the variations of the kinetic parameters obtained using the reaction model from their trues values [42]. The greater the difference between the E obtained from a model and isoconversional techniques, the less likely is the reaction model $f(\alpha)$ to be a true one [42]. Different methods have been developed to select an appropriate reaction model of a thermal degradation process.

Malek [44, 52] developed a method of determining the reaction model of a thermal degradation process by creating so-called $Z(\alpha)$ and $Y(\alpha)$ master plots. The shapes of the $Y(\alpha)$ master plots as shown by Figure 2-6 are specific to certain kinetic models. Furthermore, $Z(\alpha)$ and $Y(\alpha)$ have respective maximums values at α_P^{∞} and α_m (presented in Table 2-2) which are also specific to certain forms of $f(\alpha)$ and hence certain degradation processes. For SB and JMA ($n > 1$) models, α_m has a value between 0 and α_p. α_p is the value of α corresponding to maximum rate ($\frac{d\alpha}{dt}$). By plotting the experimental $Z(\alpha)$ and $Y(\alpha)$ master plots and comparing them with typical $Z(\alpha)$and $Y(\alpha)$ information available in the literature, an appropriate reaction model can be selected. These comparisons are presented as a decision tree in Figure 2-7.

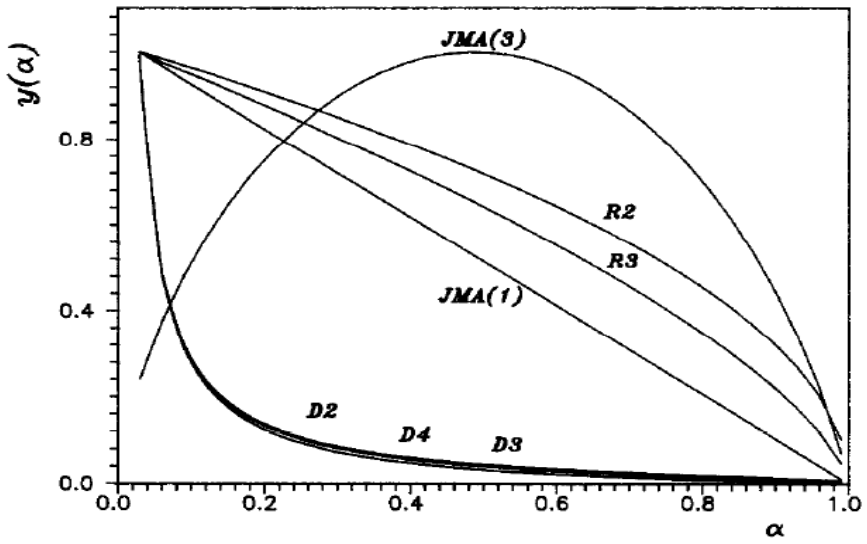

Figure 2-5 $Y(\alpha)$ master plots for different reaction models $f(\alpha)$[52]

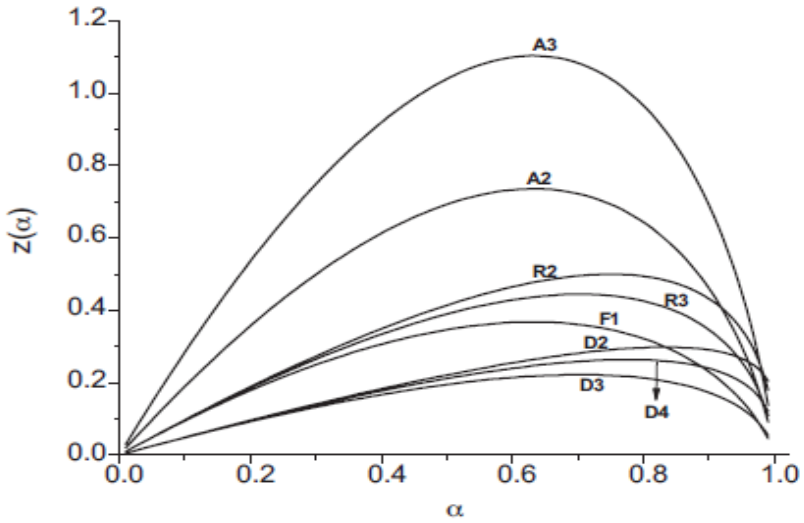

Figure 2-6 $\mathbf{Z(\alpha)}$ master plots for different reaction models $\boldsymbol{f(\alpha)}$[21]

Table 2-2 Typical α_m and α_P^∞ of different $\boldsymbol{f(\alpha)}$ [21, 52]

Model	α_m	α_P^∞
$R2$	0	0.750
$R3$	0	0.704
$D2$	0	0.834
$D3$	0	0.704
$D4$	0	0.776
FI	0	0.632
SB	$m/(n+m)$	-
$A2$ (JMA (2))	0.393	0.632
$A3$ (JMA (3))	0.283	0.632

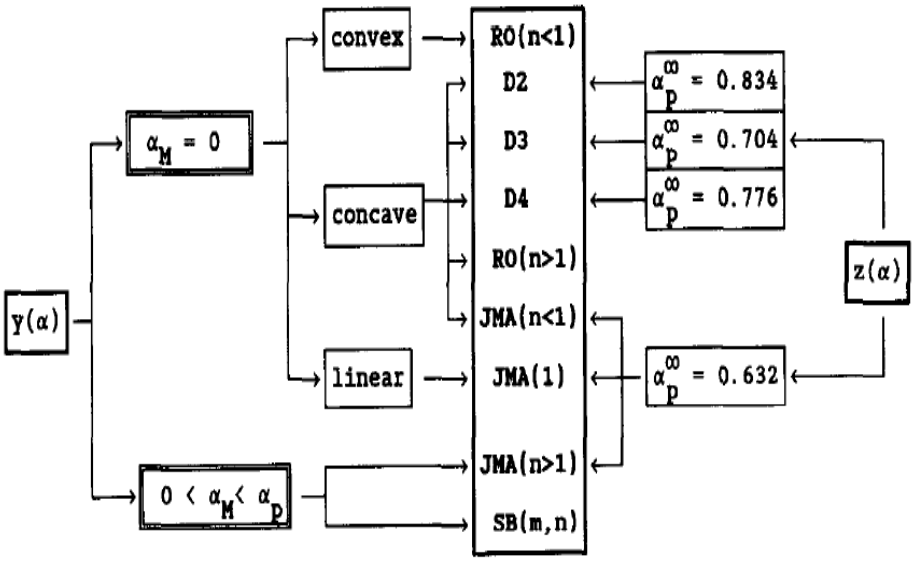

Figure 2-7 Decision tree for model selection using $\mathrm{Z}(\alpha)$ and $\mathrm{Y}(\alpha)$ plots [52]

The experimental $\mathrm{Z}(\alpha)$ and $\mathrm{Y}(\alpha)$ can be calculated by equations 2-12 and 2-13 [22, 43, 52].

$$\mathrm{Y}(\alpha)_\beta = \left(\frac{d\alpha}{dt}\right)_\alpha \exp(x_\alpha) \qquad 2\text{-}12$$

$$\mathrm{Z}(\alpha)_\beta = \pi(x_\alpha)\left(\frac{d\alpha}{dt}\right)_\alpha \frac{T_\alpha}{\beta} \qquad 2\text{-}13$$

Where:

$$x_\alpha = \frac{E_o}{RT_\alpha} \qquad 2\text{-}14$$

$$\pi(x_\alpha) = \frac{x^3+18x^2+88x+96}{x^4+20x^3+120x^2+240x+120} \qquad 2\text{-}15$$

The subscripts β and α denote values at given heating rate and conversion respectively while E_o is the average of approximately constant E_α estimated from an isoconversional method.

Another method of determining an appropriate reaction model is linear model-fitting proposed by Perez-Maqueda et al [46]. This method is based on the fact that the simplified

Sestak-Beggren model matches several $f(\alpha)$ as demonstrated by the authors in their work [45]. By plotting a graph of the normalised reaction model $f(\alpha)$ ((α) / $f(0.5)$) versus α, the reaction model can be picked as that reaction model which best matches with the truncated Sestak-Beggren equation [45].

2.2.3 Experimental data of PC and PA6

This review will only focus on previous degradation studies of polycarbonate (PC) and nylon 6 (PA6) polymers involved in this project. Various studies have been conducted on the degradation kinetics of PC and PA6. Some of these works are summarized below in Table 2-3. It shows the influence of heating rate, and various multi-walled carbon nanotubes (MWNTs) on the onset degradation temperature (T_0), maximum degradation rate temperature ($T_{\max\_rate}$) and kinetic triplets of PC and PA6.

For all the materials presented in Table 2-3, the values of T_0 and $T_{\max\_rate}$ increased with increases in the heating rate [31, 37, 39]. The values of T_0 and $T_{\max\_rate}$ are less when air is used as a purge gas than when nitrogen is used for PC and PA6. This shows that, for these materials, thermal stability is reduced by oxidation.

The work of Wang et al [55] shows that addition of carboxyl MWNTs (MWNTs-COOH) and diaminopropyl terminated dimethylpolysiloxane (DPD) modified MWNTs-COOH (MWNTs-DPD) improved the thermal stability of PC. The authors attributed this to numerous interconnected carbon nanotubes (CNTs) that promoted the formation of stable char layers, which protects the underlying polymeric matrix from thermal degradation. Furthermore, PC/

MWNTs-DPD ,as can be seen in Table 2-3, is more thermally stable than PC/ MWNTs-COOH because it is better dispersed in the polymer matrix [55]. Wu et al [56] also observed improvement in the thermal stability of PC with the addition of MWNTs.

Li et al [57] observed no significant change in the thermal stability of PA6 with the addition of purified MWNTs (p-MWNT). However, they showed that under air, the degradation process of PA6 is double step (which is evident by their double $T_{\max\_rate}$ values) as opposed to a single step observed under a nitrogen purge gas. Their work also shows that, under air as the purge gas, the thermal stability of PA6 improved with the addition of p-MWNT. They explained that the presence of MWNTs may hinder thermo-oxidation of PA6 and thus improve the thermal stability of the composites.

Table 2-3 Experimental data from studies of degradation of PC and PA6

Ref/(Material)	β (°C/min)	T_0 (°C)	T_{max_rate} (°C)	Technique	Method	E (kJ/mol)	$\frac{E}{RT_0}$	Log k_0 (min^{-1})	n	$f(\alpha)$
Al-Mulla et al [37]/(PC)	5	449	492	TGA(N_2)	Kissinger Ozawa	165.2 160-221	27.5	12.25	1.6	*Fn*
	10	469	512	TGA(N_2)			26.8			
	15	477	519	TGA(N_2)			26.5			
	20	489	527	TGA(N_2)			26			
	5	405	441	TGA(Air)	Kissinger Ozawa	188.5 98-106	33.4	14.36	1.1	*Fn*
	10	430	480	TGA(Air)			32.2			
	15	444	497	TGA(Air)			31.6			
	20	460	515	TGA(Air)			30.9			
Polli [35]/(LPC)	5	380		TGA(N_2)	Vyazovkin	177 ± 10	32.6			
Polli [35]/(BPC)	5	430		TGA(N_2)	Vyazovkin	193 ± 7	33			
Wang et al [55]/(PC)	10	423	520	TGA(N_2)						
Wang et al [55]/(PC/0.1wt %MWNTs-COOH)	10	440	522							
Wang et al [55]/(PC/0.1wt %MWNTs-COOH-DPD)	10	446	533							
Wang et al [55]/(PC/1wt% MWNTs-COOH)	10	448	526							
Wang et al [55]/(PC/1wt% MWNTs-COOH-DPD)	10	452	538							
Wu et al [56]/ PC	10	488		TGA						
Wu et al [56]/ PC/2wt% MWNTs	10	495		TGA						
Holland [29]/(PA6)	Isotherm al			TGA(Ar)		190 ± 10				
LEE [58]/ PA6				TGA(N_2)	Friedman	184 ± 5.2		12.88	0.6	*Fn*
					Kissinger	178				
Li [57]/ (PA6)	10		451, 536	TGA(Air)	Kissinger	153	25.4, 22.7			
Li [57]/ (PA6)	10		457	TGA(N_2)						
Li [57]/ (PA6/0.1wt%P-MWTs)	10		446, 548	TGA(Air)						
Li [57]/ (PA6/0.1wt%P-MWTs)	10		456, 559	TGA(N_2)						
Li [57]/ (PA6/0.5wt%P-MWTs)	10		454, 539	TGA(Air)						
Zong [39]/(PA6)	10	363.5		TGA(N_2)	Kissinger	217	41			
					MLR	216.7	39	13.5	1	*Fn*
PASHAEI [31]/(PA6)	20	391	492	TGA(N_2)						

Table 2-3 contd											
Ref/(Material)	β **(°C/min)**	T_0 **(°C)**	T_{max_rate} **(°C)**	**Technique**	**Method**	E **(kJ/mol)**	$\frac{E}{RT_0}$	**Log** k_0 **min^{-1}**	n	m	$f(\alpha)$
Author, PC 0.05 wt% CB	5	456	502	TGA(N_2)	NMF	225	37.1	14.8	1.3	0.4	*SB*
	10	470	516				36.4				
	15	482	526				35.8				
	20	488	533				35.6				
Author, PC 0.2 wt% CB	5	470	507			253	41	16.7	1.5	0.6	*SB*
	10	480	518				40.4				
	15	488	527				40				
	20	493	533				39.7				
Author, PA6 0.05 wt% CB	5	342	419			177	34.6	12.6	0.8		*Fn*
	10	365	435				33.4				
	15	376	445				32.8				
	20	383	451				32.5				
Author, PA6 0.2 wt% CB	5	340	419				34.7				
	10	364	434				33.4				
	15	375	445				32.9				
	20	383	452				32.5				

2.3 Laser transmission welding

2.3.1 Laser light transmission

As mentioned in chapter 1, LTW involves the transmission of laser power through a laser-transparent part. In their natural state, most thermoplastics are relatively transparent to laser light at wavelengths (around 1 µm) used in LTW [59]. As laser light travels through thermoplastics during LTW, some of the power is reflected by the thermoplastic while some is absorbed [60]. Therefore, laser transmission in LTW is often described by three parameters which include total reflectance, total absorbance and total transmittance [13]. Total reflectance can be defined as the ratio of total reflected power to total incident laser power. Total absorbance is the ratio of total absorbed power to the total incident light while total transmittance, can be defined as the ratio of total transmitted light to the total incident laser power [12]. Mathematically, these ratios can be related with the following equation [13]:

$$1 = T_T + R_T + A_T \qquad \text{2-16}$$

Where R_T is the reflectance A_T is the total absorbance while T_T is the total transmittance.

Laser light interaction during transmssion in a polymer part is shown by Figure 2-8. The term “light scattering” in the figure is dicussed later in this chapter.

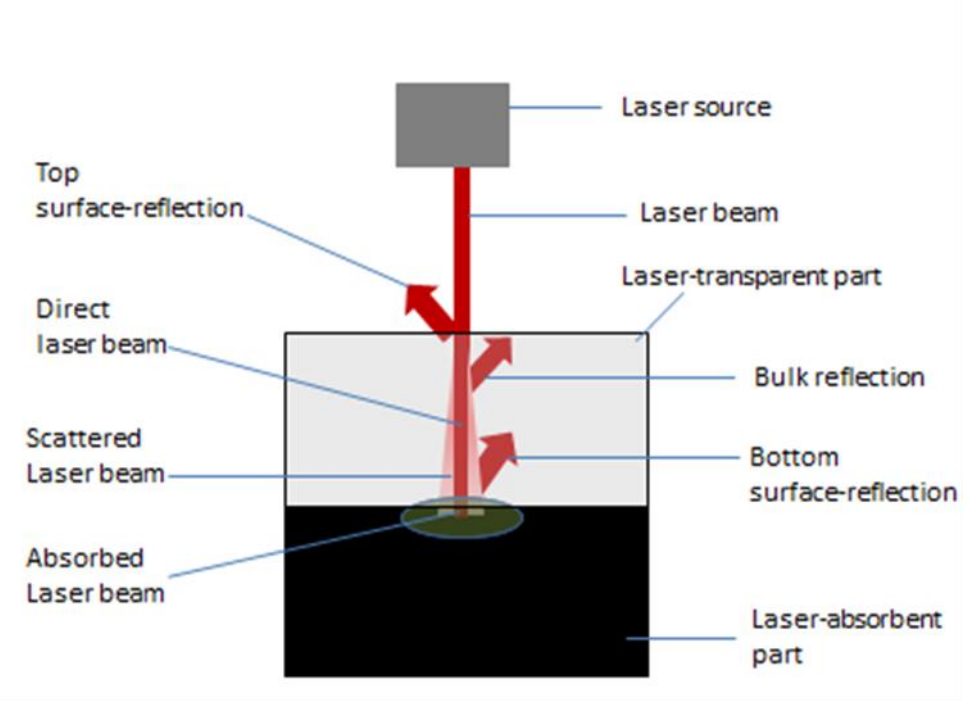

Figure 2.8 Laser beam interactions with polymer parts during LTW

Total reflectance

In LTW, incident light on the laser-transparent part may be reflected at the top or bottom surfaces of the part or between phases inside the polymer bulk [6]. Therefore, total reflectance is a summation of surface (top and bottom) and back reflection from the bulk. Total reflection reduces the magnitude of transmitted laser light. Reflected light may also cause unintentional overheating of weld features surrounding a part especially when the laser incidence angle is non-zero [61]. The angle of incidence, material optical properties, thickness of the transparent path, surface quality and magnitude of the incident laser light are factors that can affect the magnitude and distribution of reflected light during LTW [61].

The Fresnel relation can be used to determine the specular reflection of light on smooth surfaces [62]. Several works have been conducted by researchers to assess light reflection in LTW [6, 60, 61, 63].

Azhikannickal et al [61] characterized laser light reflection from thermoplastics as a function of part thickness using thermal imaging. Wang et al [64] measured laser light reflectance of PP, PC, PA6 and PAmXD6 using a spectrophotometer with an integrating sphere. Geiger et al [60] measured the transmittance and reflectance of POM, PP, PA6, SAN, PMMA and PC using two coupled integrating spheres equipped with a photodiode as shown by Figure 2-9.

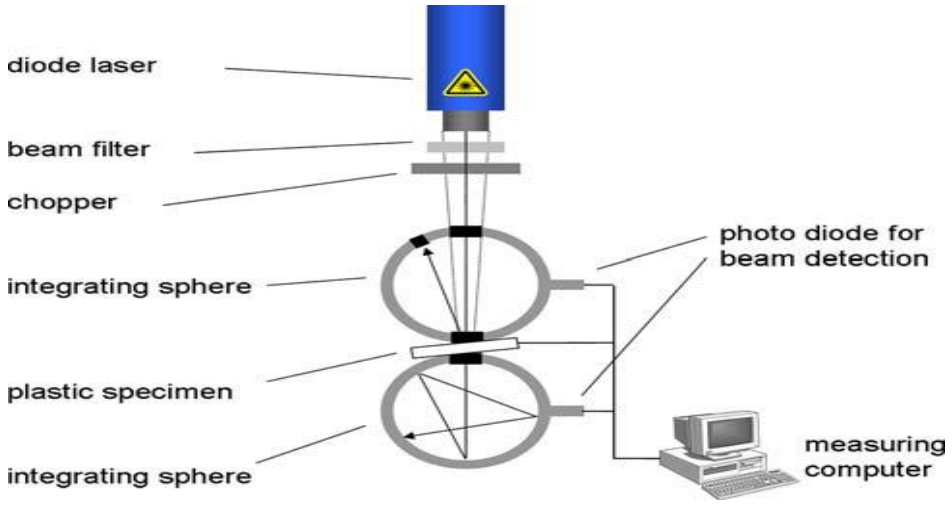

Figure 2-9 Set up for measurement of laser light reflectance and transmittance through polymers [60]

It has been shown that laser reflectance varies with materials. Wang et al [64] observed that for a 3.2 mm thick sample at wavelengths between 500 and 1000 nm, polyamide (PA6) exhibited a higher reflectance compared with the polycarbonate.

The influence of glass fibre content on laser light reflectance has also been studied. The work of Wang et al [64] showed that unreinforced PAmXD6 had the lowest reflectance which increased to its highest value at a GF content of 30wt% and then decreased slightly as GF content increased further. They hypothesized that below a certain critical value, glass fibre promotes back scattering.

Laser light reflectance as a function of path thickness has also been studied by researchers. Wang et al [64] observed that the reflectance of PAmXD6 containing 50% GF increased with increase in sample thickness due to back scattering caused by GF. Azhikannickal et al [61] observed that, for thicknesses of 1 to 3.1 mm, the apparent total reflectance at the top of the transparent part was greater than Fresnel reflectance due to laser light reflection from the bulk and bottom surface of the specimen.

Transmittance

As mentioned earlier, equation 2-16 shows that increases in the total absorbance and reflectance will decrease the total transmittance. Different methods have been employed by researchers in order to measure laser transmittance. Wang et al [65] measured laser light reflectance of PP, PC, PA6 and PAmXD6 using spectrophotometer with an integrating sphere. Chen et al [12] measured the transmittance of laser diode beam through PC, PA6 and PA6GF as a function of part thickness and CB level using an air-cooled thermopile sensor and power meter.

Laser transmittance has been shown to vary with materials. Crystalline materials are generally more laser light scattering than amorphous materials due to the co-existence of crystalline and amorphous phases [12, 62]. Wang et al [64] showed that PAmXD6 produced at a low injection mould temperature of 60 ℃ had higher transmittance than that of parts made using the normal mould temperature of 120°C due to its lower crystallinity in the cold-moulded specimen. Rhew et al [63] showed that, at an incident angle of 0°, the transmittance of PC is approximately 90% regardless of the thickness of 0.37 to 12.2mm. The transmittance of HDPE decreased with increases in thickness and was much lower than PC due to scattering effects from the spherulitic structure. Wang et al [64] showed that for a sample thickness of 3.2mm, PC exhibited the highest transmittance compared with PA6 and PP.

Glass fibre content has also been shown to affect the total transmittance in LTW. Kagan et al [66] showed that laser transmittance in PA6 decreased monotonically with increases in glass fibre content from 0 to 63wt%. They attributed this to the increased path length of the laser light caused by more scattering introduced by glass fibre [66].

Studies have also been conducted by researchers on the influence of part thickness on material transmittance to laser light. Wang et al [64] showed that the transmittance of PAmXD6 containing 50% GF decreased with increase in the sample thickness due to scattering which caused an increased effective path length of the laser light. Chen et el [12] observed a linear relationship between the measured natural log of the polymer transmittance and the part thickness (D) as shown by Figure 2-10. This was in agreement with a modified Bouguer–Lambert relationship they developed. The linear relationship also showed that the

transmittance in the materials decreased with part thickness and CB content. However, they observed that transmittance of PC was almost independent of part thickness at 0wt% CB level.

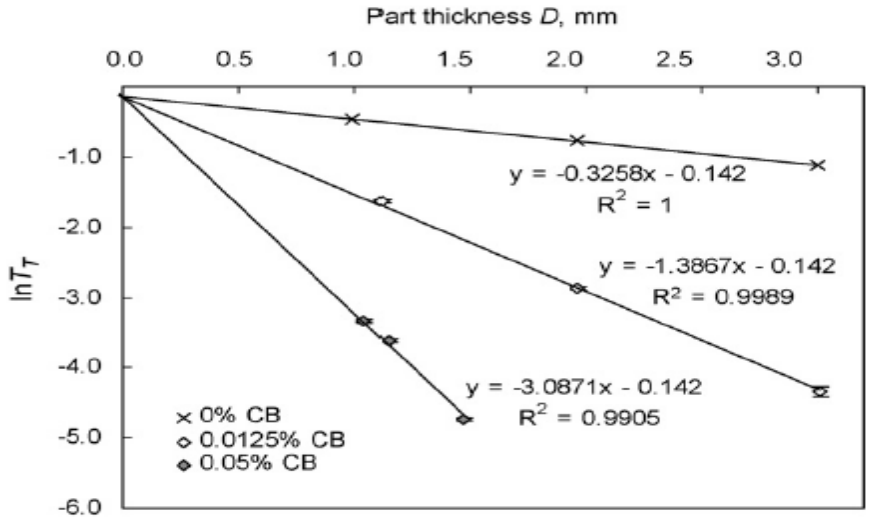

Fig. 2-10. lnT_T vs.D and CB level for PA6 [12].

Laser light absorption

During the transmission of the laser beam through thermoplastics, the laser power can be reduced by material absorption [12]. Beer's law, given by equation 2-17, can be used to calculate laser light absorption in thermoplastics if multi-scattering (in which light is scattered more than once along its path) and bulk reflection are negligible [13].

$$P''_y = (1-\eta)P''_L e^{-(A+S)y} \qquad 2\text{-}17$$

Where A is the absorption coefficient, η is the surface reflectance of the thermoplastic, S is the laser light scattering coefficient, P''_L is the incident laser light intensity (at y = 0) and, P''_y is the laser light intensity at depth y in the thermoplastic.

Chen et al [6, 12] developed a modified Beer's Law (given by equation 2-18) that can be used to calculate the "apparent absorption (A_1)" coefficient for non-scattering, single scattering and multi-scattering material for a laser incident power (P_L) that passed through a material of given thickness (D) and with power output (P_{out}). A_1 accounts for laser light absorption along the incident direction and along the increased path length caused by scattering.

$$P_{out} = (1 - R_T)(1 - \eta)P_L e^{-A_1 D} \qquad 2\text{-}18$$

Since plastics are relatively transparent to a laser beam, the absorbance of thermoplastics laser beam is normally increased by additives that absorb laser energy [18]. Pigments, typically carbon black are used to increase the absorbance of thermoplastics to laser light while changing the colour of the plastic substrate [12, 16]. Figure 2-11 is a plot of laser absorption coefficient vs carbon black content showing an increase in the absorption coefficient of PC, PA6 and PA6GF with an increase in carbon black content. Nevertheless, it has been shown with technologies like Clearweld™ and Lumogen™ that it is possible to increase the absorbance of thermoplastics to laser light without changing the colour of the plastic substrate by using additives that are very absorbent to laser light but transparent in the visible spectrum [16, 67].

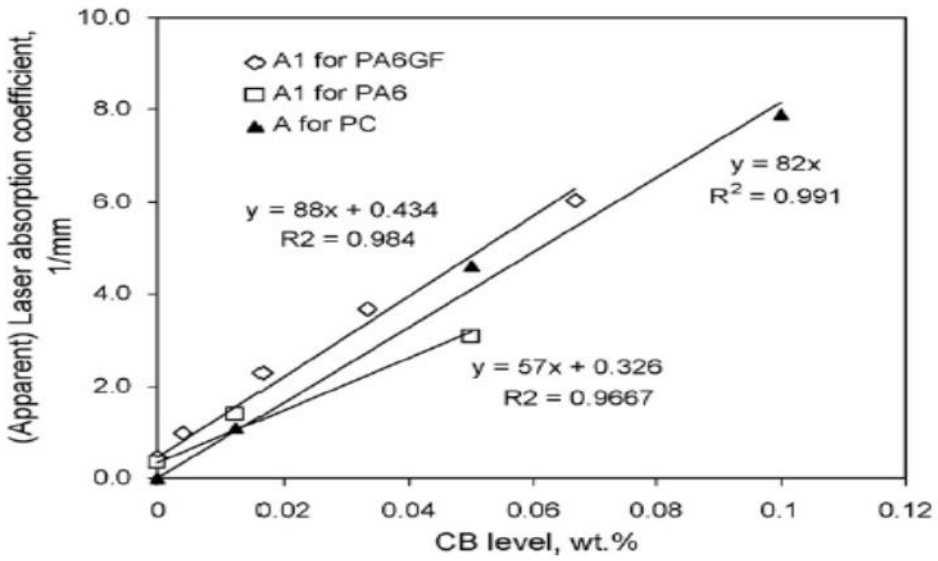

Figure 2-11 absorption coefficient vs CB level for PC, PA6 and PA6GF [12].

Higher concentration of laser light absorbance additives like carbon black have been shown to decrease the depth [6] of the HAZ, thereby reducing laser power requirements for welding. This is consistent with Beer's law. Higher concentration of absorbance additives also increases the molten depth ratio (transparent/absorbing) and increase weld width [18]. This is because higher concentrations of laser light absorbance additives increase the amount of laser-energy absorption near the surface of the laser-absorbent part.

Laser light absorption has been shown to be material-dependent as evident in works of different researchers [12, 60]. Chen et al [12] observed that, for the same CB concentration, PA6GF had higher value of A_1 than PA6 due to an increased path length as a result of light scattering caused by GF which ultimately increase the chances of energy absorption. They also observed that the measured value of A is higher than the A_1 for PA6 due to smaller dispersed CB aggregate in PC and higher density of PC. Gieger et al [60] observed that for semi-crystalline materials (POM, PA6 and PP), the absorption coefficient showed distinctly different

progressions with temperature while for amorphous materials (PMMA, SAN and PC) the absorption coefficient of the materials showed no significant change with temperature.

Light scattering

Light scattering in LTW can be defined as the deviation of laser light as it passes through different optical phases (example, crystalline, amorphous and reinforcements) with different refractive indices [12]. Light scattering increases the path length of light and thereby increasing both the total reflectance and absorbance. It is obvious from equation 2-16, that an increase in light scattering will reduce the total transmittance of a polymer material during LTW (since it increases both the total reflectance and absorbance). Light scattering is therefore an important factor in light transmission through materials during LTW [59]. Zak et al [59] developed a method for characterization of laser scattering using the so called transverse energy density distribution. Figure 2-12 is the normalised power flux distribution perpendicular to weld-line direction (T-NPFD) of PA6GF before and after transmission through a laser-transparent part.

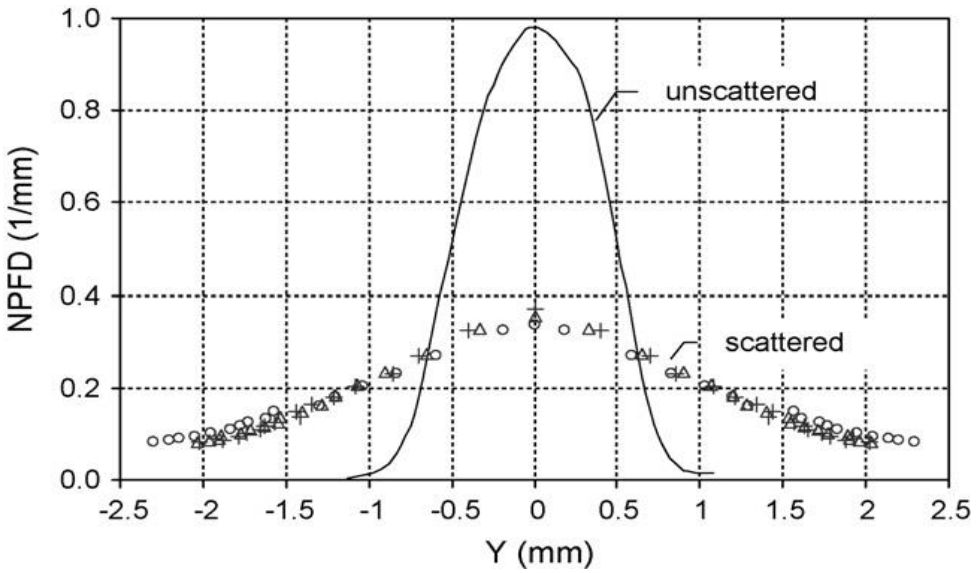

Figure 2-12 T-NPFD profile after scattering by 3.2-mm PA6 GF30% plaque (line scan along X) compared with unscattered-beam profile (from pinhole-based measurements) [59].

Generally, amorphous materials like PC and PS are significantly less laser light scattering than their semi-crytalline counter-parts [6]. Semi-crystalline materials like PA6 and PP scatter laser light passing through them due the presence of both crystalline and amorphous phases [12, 59, 62]. Al-Wohoush et al [68] showed that the weld width of PC, PA6 and PA6GF increased linearly with the laser power over the range of power studied. The observed increase of width with power was less pronounced in polycarbonate. The difference in the weld width of the materials with power is due to different degrees of light scattering of the materials.

Researchers have also shown that increasing the GF content also increases light scattering. Bates et al [10] observed that a grade containing 0wt% GF reaches a force of rupture at approximately 500 N while reinforced grades, regardless of GF content, attained a force at rupture of approximately 1000 N due wider weld-seam widths caused by GF-induced scattering. Wang et al [65] showed that light scattering in PAmXD6 increased with increasing GF content

from 0 to 50 wt% due to more scattering introduced by GF. Kagan et al [17] showed that at optimized process conditions, the weld strength of PA6 decreased with increase in fibre glass content due to laser light scattering. They also observed that the maximum width of the HAZ increased with increase in fibre glass content due increased laser light scattering.

Other works have also shown that light scattering increases with part thickness. Bates et al [10] studied force at break as a function of laser power for different part thicknesses of PAmXD6 containing 50 wt%GF. They observed that the maximum force at break for the 2 mm thick part was significantly higher than that of 0.5 and 1 mm thick specimens due wider weld seam caused by scattering.

2.3.2 LTW process parameters

Laser power (P), laser scan speed (v), laser line energy (L_E), size of the laser beam spot on the work-piece and clamping pressure are process parameters that can affect weld quality in LTW [13, 14]. Laser line energy can be related to the laser scan speed and laser power with the following equation [59]:

$$L_E = \frac{P}{v} \qquad \text{2-19}$$

Studies by different researchers have shown that line energy has a strong influence on the weld quality.

Bates et al [10] showed that at 3000 and 6000 mm/min scan speeds, lap-shear strength of PA mXD6 plotted as a function of *LE* are superimposable for the different scan speeds with

part thickness of 1 and 2mm. However, studies by Chen et al [20] showed that higher SDT (Surface damage threshold) can be tolerated at lower scan speed due to greater conductive heat losses into the polymer bulk over the longer irradiation time of lower scan speed of 1500mm/min (25mm/s). SDT is the critical line energy above which laser energy causes damage on the surface of the laser-transparent part. They observed that heat loss is insignificant for scan speed above 3000mm/min (50mm/s) which portrays steady SDT with laser scan speed above 3000mm/min as shown by Figure 2-13, because of negligible heat loss for shorter irradiation times. This suggests that results obtained at equal line energies may not be comparable if the speeds (and corresponding power) are low resulting in heat loss into the polymer bulk by conduction. Furthermore, Chen [6] showed that the weld strength of PC, PA6 and PA6GF increases with line energy and then begin to decline due to material degradation caused by high welding temperatures. This is consistent with other studies [6, 10, 69].

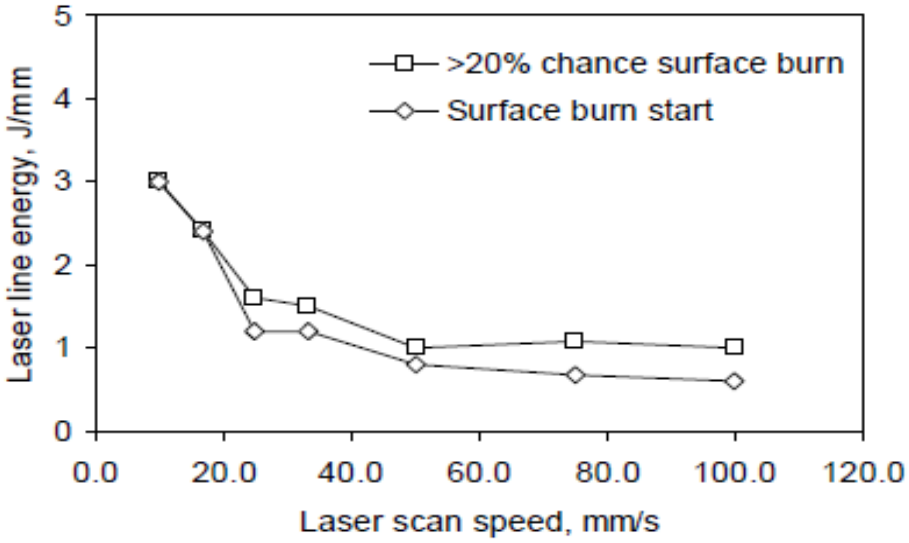

Figure 2-13 SDT (Line Energy) vs laser scan speed for PC [20]

The influence of laser power and scan speed on the weld strength are evident in several other research works. Wang et al [70] used response model methodology to study the quasi-simultaneous welding of PC. It showed that at lower scan speeds, the joint strength of PC increased with increase in laser power and then start decline at higher laser power due to thermal degradation. At higher scan speeds and powers, they observed that joint strength decreased with increases in power and decrease in scan speed due to thermal degradation. This phenomenon is also observed in other works [6, 13, 15].

Weld width has been shown to increase with increase in laser power and decrease in laser scan speed [10, 15, 70]. This is because of increased energy deposited at the weld-line as can be deduced from equation 2-19 which ultimately increases the HAZ of the parts.

Weld pressure has been shown to be a useful parameter that ensures contact between the laser-absorbent and transparent parts which is necessary for heat conduction [70]. Further increases in weld pressure have been shown to cause no significant change on the weld quality. Wang et al [70] work showed that clamp pressure had an insignificant effect on the weld strength.

2.2.4 Modelling in contour LTW

LTW, as represented by Figure 2-14, is a 3-D heat transfer problem. However, some authors, as will be presented later in this chapter, have shown that 1-D and 2-D thermal models can be used to obtain solutions of the temperature distributions in LTW as a function of time.

Challenges to accurately modelling LTW include temperature-dependent thermal properties and interactions of the laser beam with materials such as light scattering and reflection [5]. Some authors have made efforts to measure these variable properties. Assumptions are sometimes made to simplify the LTW thermal problem.

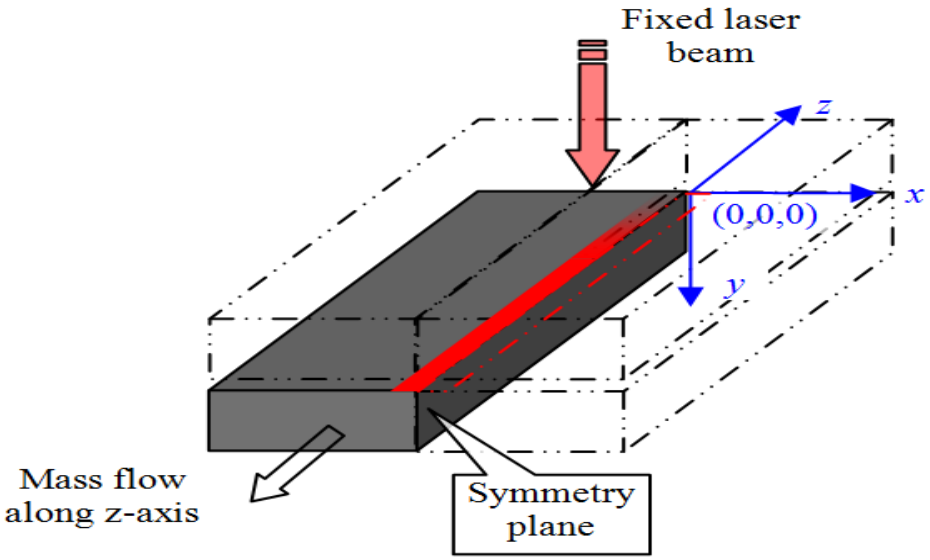

Figure 2-14 A Typical Contour LTW geometry [6]

Laser beam profile

The laser beam profile is the spatial distribution of the power flux (power per unit area) over the beam cross-section [13]. Accurate determination of the laser beam profile as it travels through material is vital for precise simulation of outputs in LTW.

Zak et al [59] developed the so called transverse energy density distribution (TEDD) for measuring laser light scattering caused by the laser-transparent part in laser LTW. This technique takes advantage of relatively low thermal conductivity of thermoplastics and fast

heating rate caused by a rapidly moving laser beam to measure energy distribution at the weld-line.

Azhikannickal et al [62] developed a technique for characterizing laser light reflection from thermoplastics using thermal imaging. In their technique, time-varying temperature distribution caused by laser energy absorption by a black plastic plate containing 0.2wt% CB was measured by an IR camera. They assumed a semi-infinite body since most of the laser energy was absorbed at the surface of a high CB content plate and obtained the laser power and the distribution of the power flux from the temperatures using a simple heat transfer model. The laser power and NFPD they obtained with this method were in good agreement with actual laser power and NFPD. This method is also able to obtain the power distribution of non-zero incident laser beam as demonstrated by the authors in their work.

Modelling work by different authors

Different authors have simulated the temperature rise at the weld interface during LTW using different thermal models. Temperature rise at the weld interface is difficult to measure during LTW [71]. Researchers therefore often validate their results by comparison of simulated and experimentally measured weld zone dimensions.

Potente et al [18] predicted the melt layer thickness of PA6 with a 1-D analytical thermal, constant heat flow model. They assumed negligible convective heat loss, negligible outflow of melt from the joining zone, semi-infinite body, symmetrical thermal conductivity for both parts joined, ideal material behaviour and negligible heat conduction along the weld seam

and the seam width. The measured laser light intensity was approximated with a 4^{th} order polynomial. The measured melt layer thickness was in good agreement with the predicted melt layer thickness.

Chen [6] developed a 2-D thermal-mechanical coupled FE model to examine the effect of material (light scattering, CB level) and process parameters (laser power, scan speed) on the thermal expansion of the weld region. He showed that 2-D coupled model can be used to adequately describe the temperature rise and thermal expansion of PC and PA6 for laser scan speeds above 25 mm/s.

Khosravi [13] simulated the temperature distribution during LTW of PBT, PET and PBT/PET blend using a 2-D FEM Comsol software model. Light scattering was measured using the technique developed by Zak [59]. The extinction coefficients (K_E) of the materials were obtained using a sensitivity study that compared predicted weld widths with simulated values.

Hadriche et al [71] simulated the temperature rise at th weld interface during LTW using a 2-D finite difference model (FDM). The thermo-physical parameters were either measured or obtained from the literature. Heat generation at the weld interface was modelled as a uniform heat flow. The temperature-time profile they calculated and the temperature-time profile obtained by FEM in the literature were in good agreement.

Mayboudi et al [5, 72] simulated the heating and cooling stage of unreinforced nylon 6 during LTW using a transient 3-D thermal model ANSYS software. The predicted weld dimension in reference 5 and experimental weld dimension were in good agreement but with some discrepancy due the assumption of uniform laser beam profile for laser scattering nylon 6. In

reference 72, the authors obtained better results by accounting for light scattering during laser beam transmission using the technique developed by Zak et al [59].

Acherjee etal [73] et al predicted weld width and molten depth of polycarbonate with a transient 3-D heat transfer finite element ANSYS code. The predicted and published experimental data were in good agreement.

Chen [6] developed a 3-D quasi-static finite element model (FEM) using Comsol software and predicted temperature as a function of position during LTW of PC, PA6 and PA6GF using this model. This was achieved by changing the time-dependent problem of contour LTW to a time-independent problem by introducing of mass flow under a static laser beam and thereby reducing computation memory and time. He obtained temperature-dependent thermal properties of the material such as densities, heat capacities, thermal conductivities by measurement using the appropriate instruments and from the literature. This is the model implemented by the author to obtain the temperature-time profiles of the studied materials. For this reason, the validation of this model will be thoroughly discussed here. More details of this model will also be presented in chapter 5.

Chen [6] validated his simulation results by comparing the predicted maximum soften/melt widths with the experimentally measured values. Figures 2-15 and 2-16 are plots of measured and predicted soften/melt widths of PC and PA6 for a non-contact geometry at different laser powers. Figures 2-17 and 2-18 are plots of measured and predicted weld width of PC and PA6 for a contact geometry at different laser powers. In a contact geometry, the laser-absorbent and laser-transparent parts are kept in contact. In a non-contact geometry

there exists a gap between the laser-absorbent and laser-transparent which is sufficient to hinder heat and mass transfer between the parts. LTW is ideally carried out in a contact geometry. Non-contact geometry is used as an aid to analyse LTW heat transfer.

Figure 2-15 shows that the predicted melt width of PC at a temperature of 145°C is in agreement with the measured weld width of PC (softening temperature of PC is 145°C). Figure 2-16 shows that the predicted weld width of PA6 at a temperature of 220°C is in agreement with the measured weld width of PA6 (melt temperatures of PA6 is 220°C).

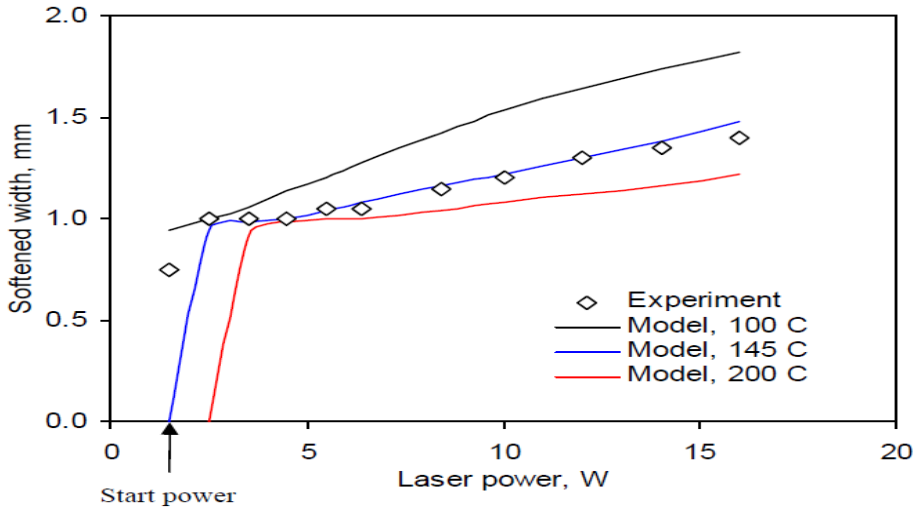

Figure 2-15 Experimental and predicted a melt width of PC (0.05 wt% CB, 25 mm/s speed) for non-contact model [6]

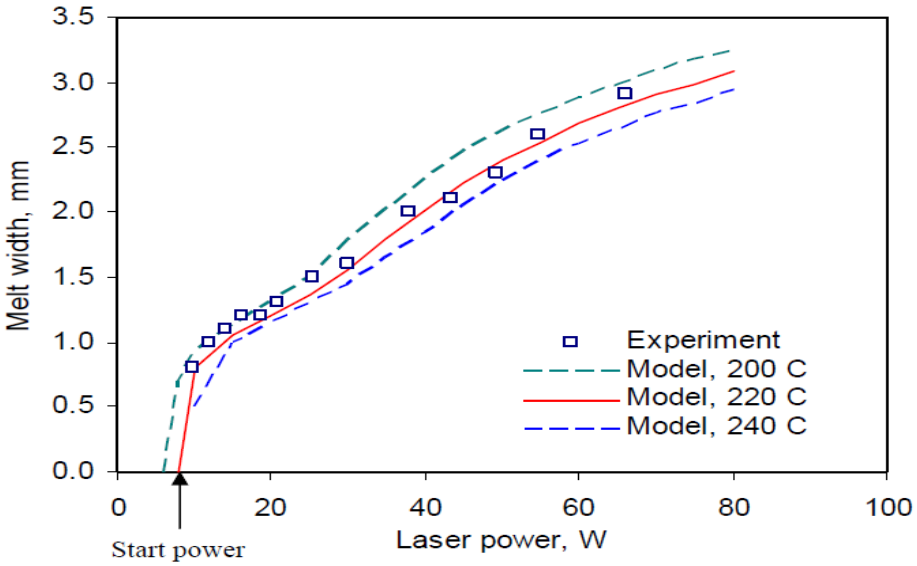

Figure 2-16 Experimental and predicted a melt width of PA6 (0.2 wt% CB, 25 mm/s speed) for non-contact model [6]

Figure 2-17 shows that the predicted weld width of PC based on the laser power that causes a weld-interface temperature of 200°C is in agreement with the measured weld width of PC (the softening temperature of PC is 145°C). Chen explained that although the softening of PC will take place at 145°C, diffusion and welding may only occur if the maximum interface temperature reaches 200°C.

Figure 2-18 shows that the predicted weld width of PA6 based on the laser power that causes a temperature rise at the weld in interface to a range of 180-200°C is in agreement with the measured weld width of PA6 (the melt temperatures of PA6 is 220°C). This means that higher laser power will be needed to meet the slightly higher measured melting point of PA6.

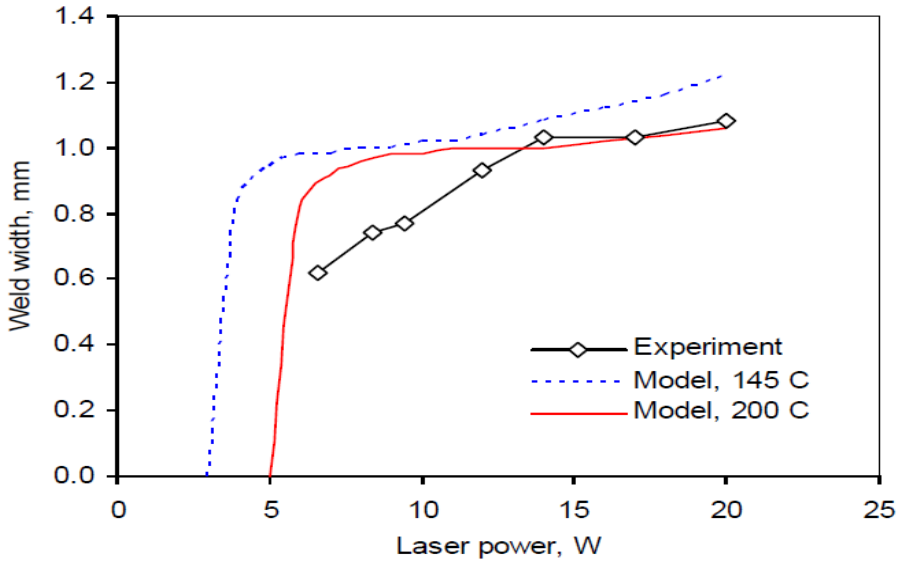

Figure 2-17 Experimental and predicted a weld width of PC (0.05 wt% CB, 25 mm/s speed) for contact model [6]

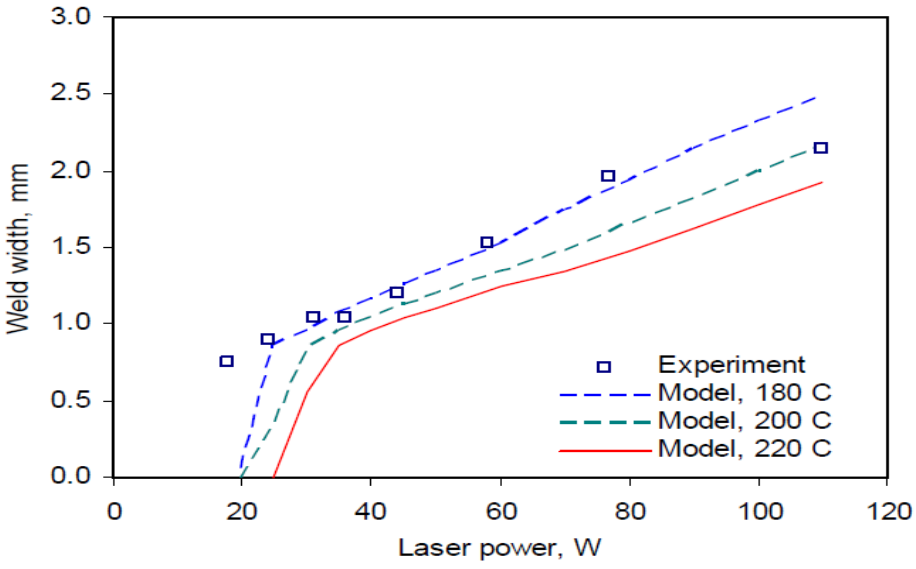

Figure 2-18 Experimental and predicted a weld width of PA6 (0.1 wt% CB, 25 mm/s speed) for contact model [6]

2.2.5 Thermal degradation in LTW

Variations in the process and material parameters such as laser power, CB level and scan speed can affect the welding temperature of a material during LTW [6]. Increases in temperature will improve the gap bridging ability and weld strength but too high a temperature can bring about material thermal degradation which can create voids at the weld interface and lower the LTW weld strength [6]. The decline in LTW weld strength caused by thermal degradation due to too high welding temperatures is evident in several studies [6, 11, 13, 15, 74]. High welding temperatures can also cause surface damage of the transparent part during LTW [20]. It is obvious that degradation places a limit on the laser power and scan speed that may be used during LTW. Therefore thermal degradation is a very important phenomenon in LTW. However, only a few studies of thermal degradation during LTW have been performed.

Khosravi [13] developed a method for simulating thermal degradation during LTW. He predicted thermal degradation of polybutylene terephthalate and polyethylene terephthalate blends using a kinetic triplet obtained from a single heating rate TGA and temperature-time profile obtained from a 2-D FEM thermal model. The kinetic triplets were obtained using the Freeman-Carroll method. A comparison of predicted degradation data with a lap-shear strength tests showed that the weld strength of the materials starts to decline at powers where significant degradation was predicted by his degradation model.

Chen et al [20] studied the so-called surface damage threshold (SDT, which is defined as the line energy at which visible degradation takes place on the surface of the laser-transparent part) of PC during contour LTW. Higher SDT was observed at lower scan speeds due to

increased time of heat conduction. At scan speeds above 3000mm/min, laser speed was observed to have no influence on the SDT. They also studied the effects of surface contamination and defects on the damage of the laser-transparent part by laser light. Their studies indicated that surface burning was aggravated by marks on either side of the transparent part, by pencil mark or by ejector pins.

Chen et al [15] also developed a non-contact method in which laser-transparent and absorbent parts are separated with spacers in order to estimate the power and speed required for optimal contour laser transmission welding as a function of material. In this method, they conducted series of line scans (at different powers and speeds) across the plates of PP, PC, PA6 and PA6GF in a non-contact method. The same welding conditions used in the non-contact method were also used to weld the parts together. The laser-absorbent part of the non-contact method was then examined after scans as shown by Figure 2-19 while lap-shears strength of the weld parts was also measured. They showed that the laser power at given scan speed required to initiate visual degradation on the laser-absorbent part in a non-contact geometry was closely related to the conditions required for maximum shear strength in a contact geometry.

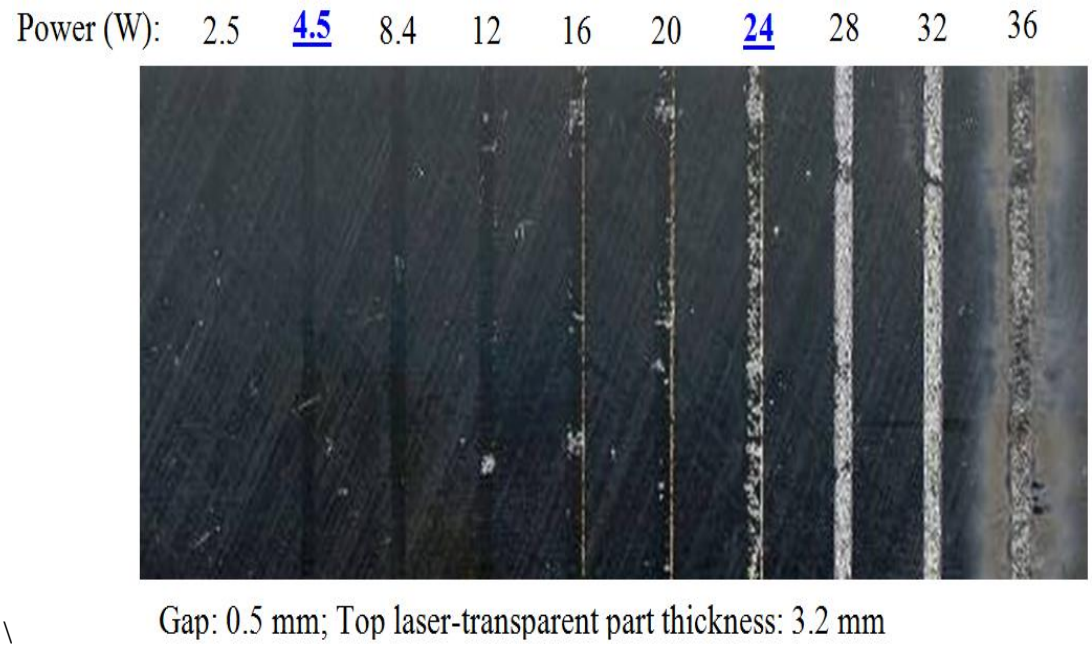

FIGURE 2-19 Visual observation of laser-absorbent part of PC with 0.05wt% CB in a non-contact method at scan speed of 3000mm/min and different power level [15]

Chapter 3
Thermo-Gravimetric Analysis (TGA)

This chapter presents the thermo-gravimetric analysis (TGA), carried out in this research. Section 3.1 presents the materials used. The experimental procedure for the TGA is presented in section3.2. Section 3.3 presents and discusses the results of the TGA.

3.1 Material

The materials used for the TGA were prepared from mixtures of natural (that does not contain carbon black (CB)) and CB containing materials:

- Unreinforced Nylon 6 (PA6) (0.05wt% CB and 0.2wt % CB) prepared from mixtures of:
    - AKULON F223-DH NATL (natural, unreinforced).
    - AKULON F223-D BK223 (0.2 wt.% carbon black, unreinforced).
- Polycarbonate (PC) (0.05wt% CB and 0.2wt % CB) prepared from mixtures of:
    - Makrolon AL2647-551070 (natural)
    - Makrolon 2605-901510(0.2 wt.% carbon black))

PC materials were produced by Bayer Inc while PA6 materials were produced by DSM. All materials were dry blended to achieve the desired final CB level and then injection moulded into 100 mm x 100 mm x 3.2 mm plaques using an Engel 55 ton injection moulding machine [6]. Nylon plaques were sealed in aluminium lined bags to minimize moisture pick-up [6].

3.2 Experimental

Small specimens of the materials (about 7mg) were cut out from the plaques and used for the TGA analysis. In order to remove/reduce moisture from the materials, PA6 was dried at about 104 °C for 5 hours while PC was dried at about 120 °C for about 5 hours. The drying conditions were recommended in references 75 and 76.

A TGA Q500 located at Queen's University was used to conduct the heating at rates of 5, 10, 15 and 20 °C/min for all the materials. Nitrogen, at a flow rate of 40ml/min, was used as the purge gas. The specimen were heated from 30 °C to 750 °C for nylon 6 (PA6) and from 30 °C to 900 °C for the polycarbonates (PC).

The experiments were checked for reproducibility. Figures 3-1 to 3-3 are plots of repeated experiments for PC and PA6. The PC experiment was repeated three times for each CB level while PA6 experiments were repeated two times for each CB level. It can be observed from Figures 3-1 to 3-3 that the experiments are reproducible. TGA curves for heating rates of 10 and 15°C/min not presented here can be found in appendix A.

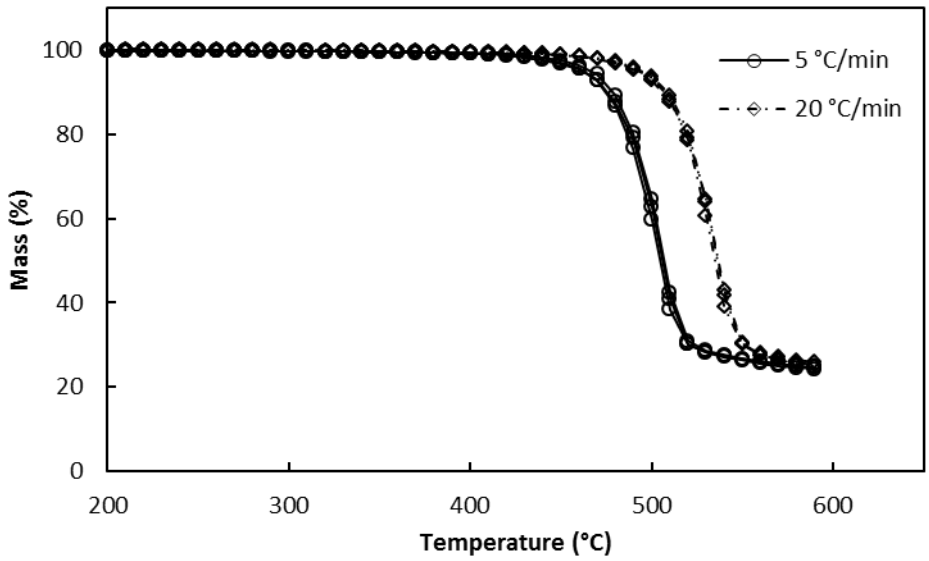

Figure 3-1 TG curves of PC with 0.05wt%CB at heating rates of 5 and 20°C/min. Each heating rate experiment was repeated three times.

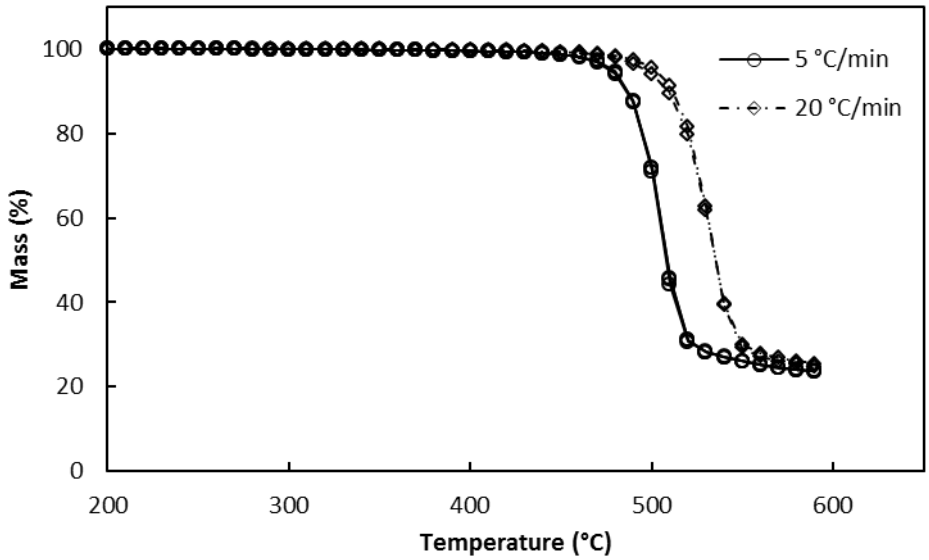

Figure 3-2 Experiment 1, 2 and 3 TG curves of PC with 0.2wt%CB at heating rates of 5 and 20°C/min. Each heating rate experiment was repeated three times.

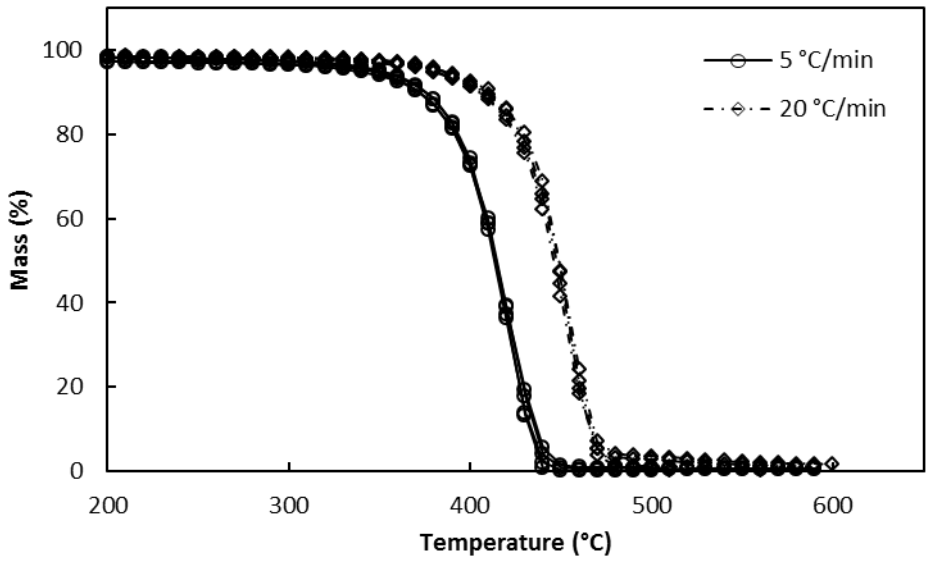

Figure 3-3 Experiment 1 and 2 TG curves of PA6 with 0.05 and 0.2wt%CB at heating rates of 5 and 20°C/min. Each heating rate experiment was repeated two times for each CB level.

3.3 Experimental results and discussion

Figures 3-4 and 3-5 show the average TG curves (remaining mass fraction) as a function of temperature for PC and PA6 respectively at different heating rates and a CB content of 0.05wt%. It can be seen from Figures 3-4 and 3-5 that the TG curves shifted to higher temperatures with increased heating rates. These same phenomena were also observed for the materials at 0.2wt% CB content as reported in the Appendix A. This shift to higher temperatures with increased heating rate is also evident in the works of Al-Mulla et al [37] and Zong [39] for PC and PA6 respectively.

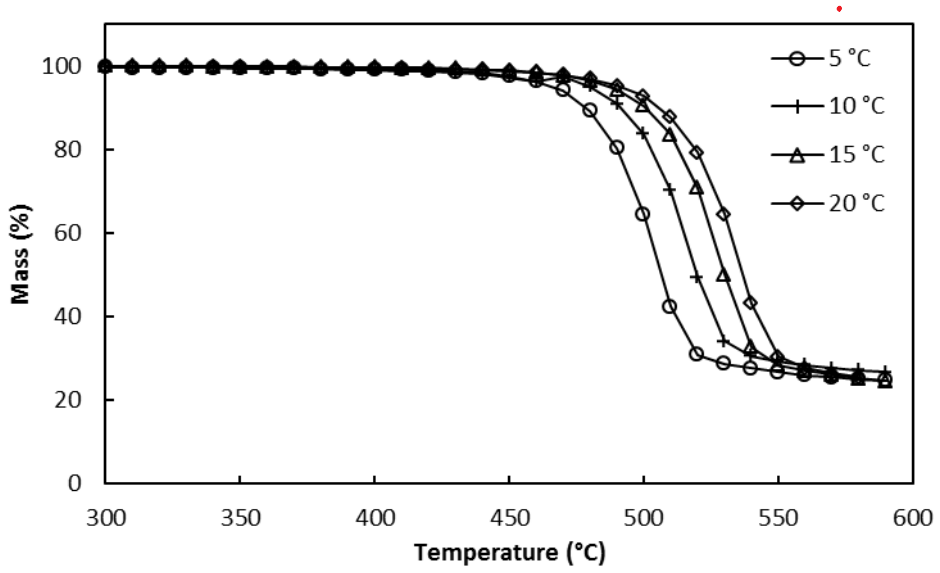

Figure 3-4 TG curves of PC with 0.05wt% CB content at heating rates of 5, 10, 15 and 20°C.

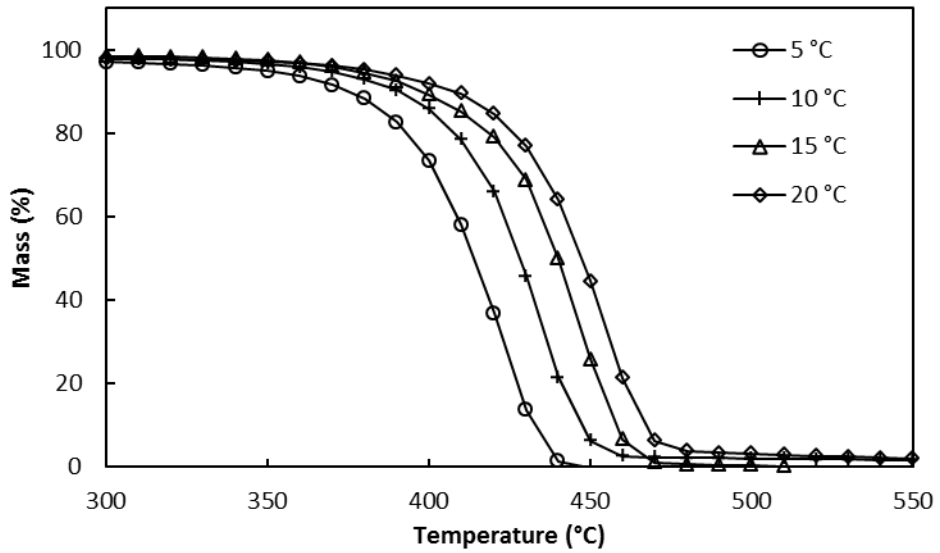

Figure 3-5 TG curves of PA6 with 0.05wt% CB content at heating rates of 5, 10, 15 and 20°C.

Figure 3-6 shows the average TG curves from replicate TGA experiments of PC and PA6 respectively at a heating rate of 5°C/min and a 0.05wt% CB content. It can be seen from Figure 3-6 that the PC TG curve is shifted to higher temperatures compared to that of PA6. The same phenomenon was observed at the other heating rates which are presented in Appendix A. This is consistent with previous works on PC and PA6 shown in Table 2-2.

More residues can be observed in the TG curve of PC than that of PA6 (which leaves no residue).

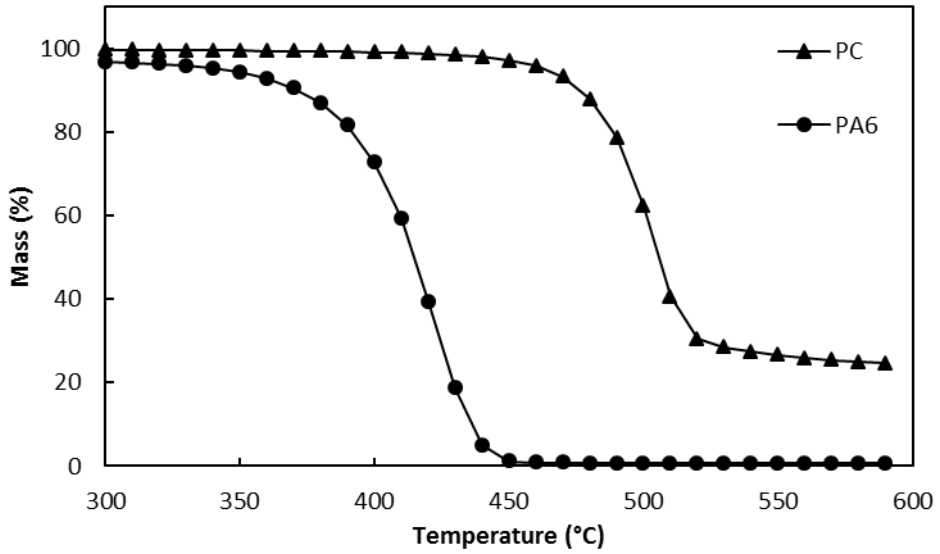

Figure 3-6 TG curves of PC and PA6 with 0.05wt% CB content at different heating rate of 5 °C

Figure 3-7 shows the average TG curves from replicate experiments of PC containing 0.05wt% and 0.2wt% CB at a heating rate of 5°C/min. It can be seen that increasing the CB level shifts the curves towards higher temperatures. Similar phenomena at the other heating rates are reported in Appendix A. This shows that increasing the CB content of PC from 0.05wt% to 0.2wt% CB improved its thermal stability. A similar observation was made by Wang et al [55] when MWNTs-COOH and MWNTs-DPD were added to neat PC. They attributed this to

numerous interconnected CNTs that promoted the formation of a stable char layer and thereby efficiently protected the underlying polymeric materials from thermal degradation as mentioned in section 2.2.3.

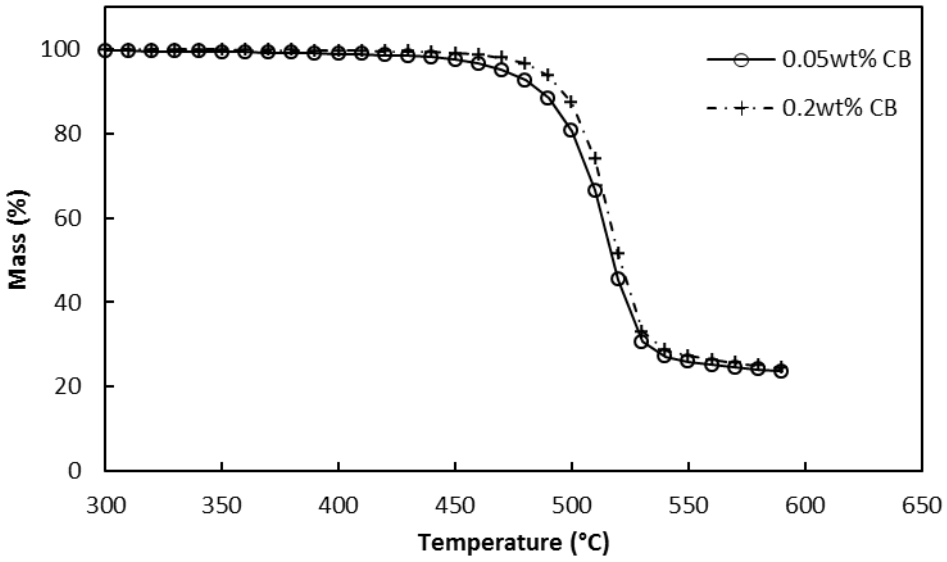

Figure 3-7 TG curves of PC with 0.05wt% and 0.2wt% CB content at a heating rate of 5°C

Figures 3-8 shows the TG curves of PA6 containing 0.05wt% and 0.2wt% CB at a heating rate of 5°C/min. It can be seen from Figures 3-8 that there is no significant shift of the TG curves to higher temperatures with increases in CB content for nylon. Similar observations at the other heating rates are reported in the Appendix A. This indicates that increasing the CB content of PA6 from 0.05wt% to 0.2wt% has no significant effect on the thermal stability of PA6. Li et al [57] observed that addition of up to 2wt% p-MWNT and f-MWNT to neat PA6 had no significant effect on its thermal stability.

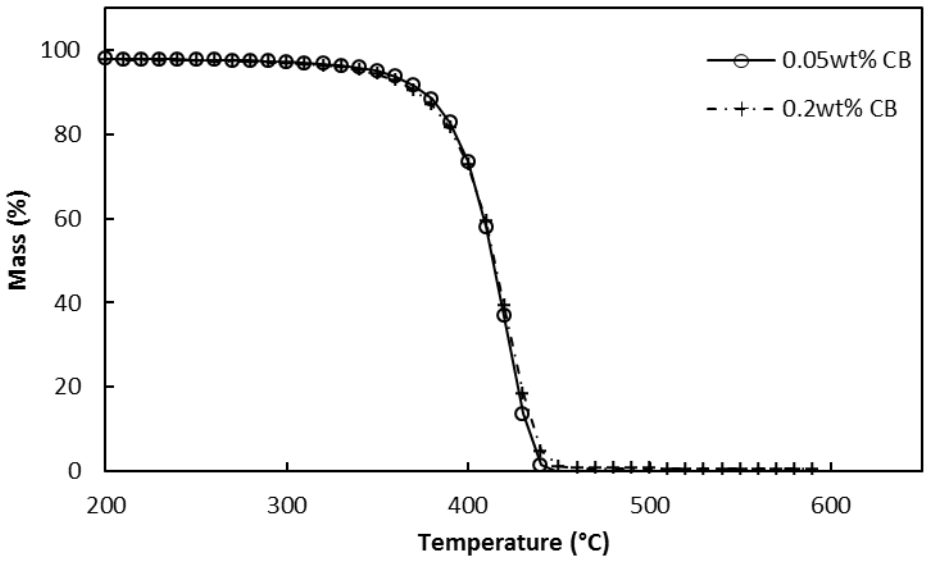

Figure 3-8 TG curves of PA6 with 0.05wt% and 0.2wt% CB content at heating rate of 5°C.

Chapter 4
TGA Data Modelling

This chapter presents the method used to obtain the kinetic triplets. Section 4.1 presents the determination of conversion dependent activation energy (E_α). Section 4.2 presents the determination of $f(\alpha)$. Furthermore, determination of the kinetic triplet using non-linear model-fitting is presented in section 4.3.

4.1 Determination of E_α

The E_α values, as discussed in section 2.2.2, are necessary for model selection and thus TGA data modelling. These values were obtained by Friedman, KAS and OFW methods as given by Equations 2-6, 2-7 and 2-8. The results from these methods for PC at CB contents of 0.05wt% and 0.2wt% are presented in Figures 4-1 to 4-2 respectively. For PA6, the results for each CB contents were pooled for each material given that CB-level had no significant effect on degradation rate. The results are presented in Figure 4-3 for PA6. The error bars in the plots represents minimum and maximum values obtained from pooled replicate data. The separate results for the materials are presented in Appendix B.

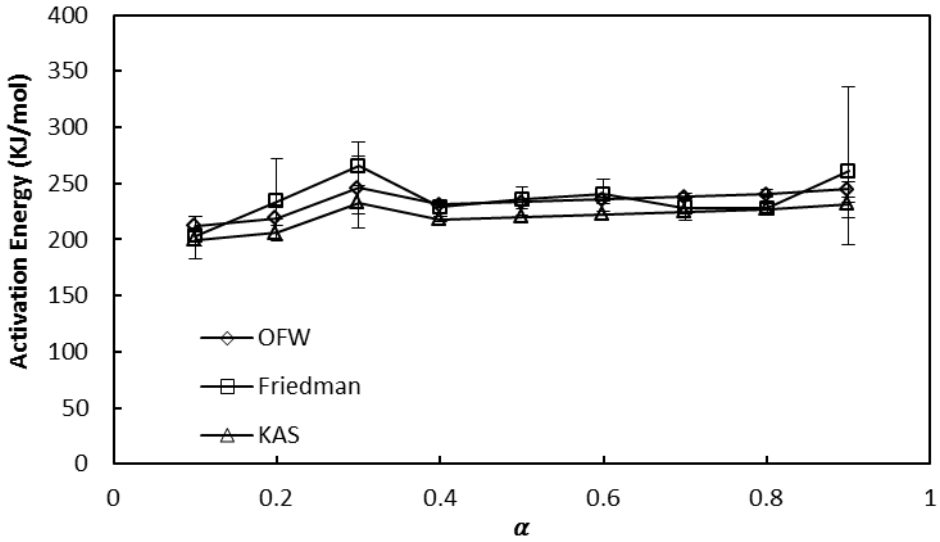

Figure 4-1 E_α of PC, obtained with 0.05wtCB by Friedman, KAS and OFW methods.

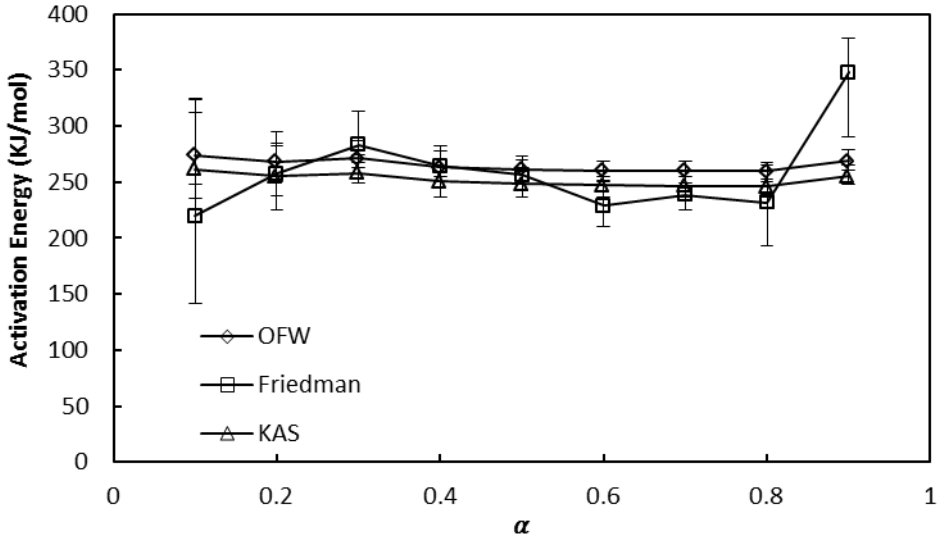

Figure 4-2 E_α of PC with 0.2wt% CB, obtained by Friedman, KAS and OFW methods.

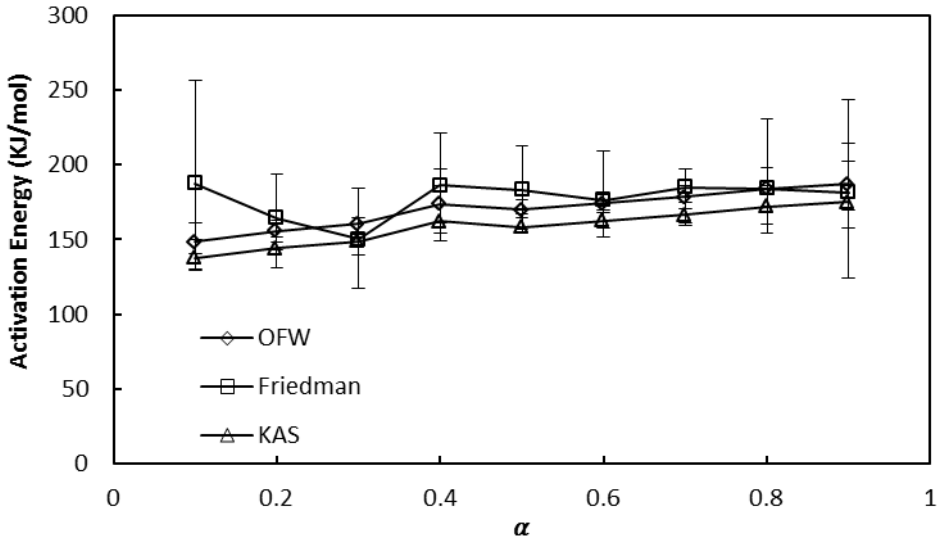

Figure 4-3 E_α of PA6 with 0.05 and 0.2wt%CB, obtained by Friedman, KAS and OFW methods.

It can be seen from Figures 4-1 to 4-3 that all model-free methods implemented in this work produced activation energies in a similar range. The Friedman method is considered mathematically to produce more accurate values of E_α than OFW and KAS methods [21]. However it is more sensitive to experimental noise as mentioned in section 2.2.2 and as can be observed in Figures 4-1 to 4-3. Therefore, E_α of the materials obtained by KAS method (which is more accurate than the OFW method as mentioned in section 2.2.2) is adopted for model selection in section 4.2.

4.2 Selection of model

Malek's method, which has been described in section 2.2.2, is used to determine an appropriate $f(\alpha)$ for the degradation processes.

The average experimental values of $Y(\alpha)$ and $Z(\alpha)$ of the materials were computed from the replicate experiments and plotted against their corresponding α values as presented in Figures 4-4 to 4-10 for PC and PA6. The computation is as given by equations 2-15 and 2-16 .

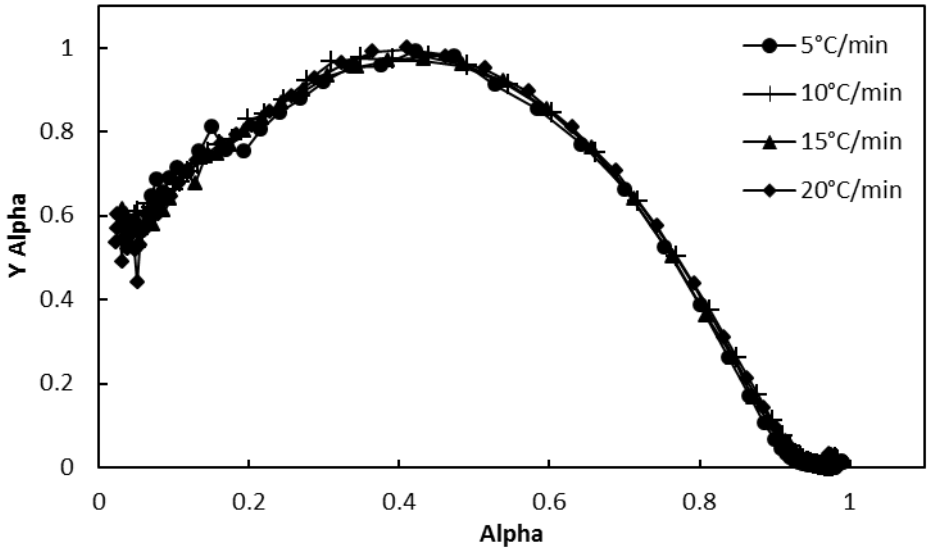

Figure 4-4 Experimental $Y(\alpha)$ plots of PC with 0.05wtCB at different heating rates.

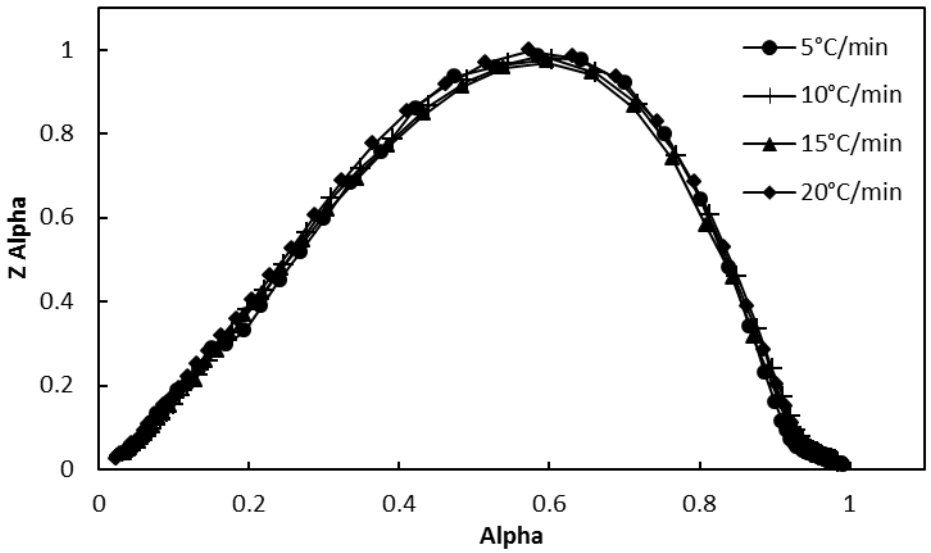

Figure 4-5 Experimental $Z(\alpha)$ plots of PC with 0.05wt% CB at different heating rates.

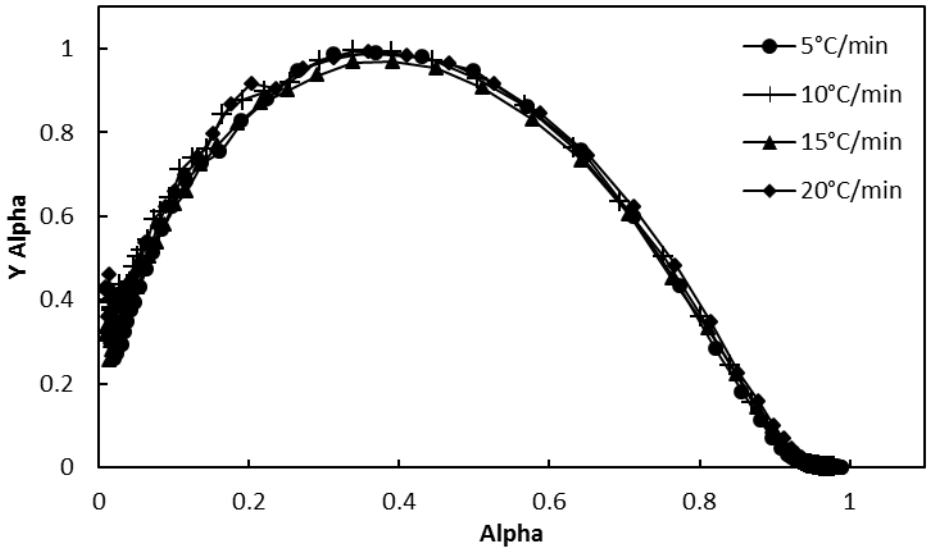

Figure 4-6 Experimental $Y(\alpha)$ plots of PC with 0.2wt% CB at different heating rates.

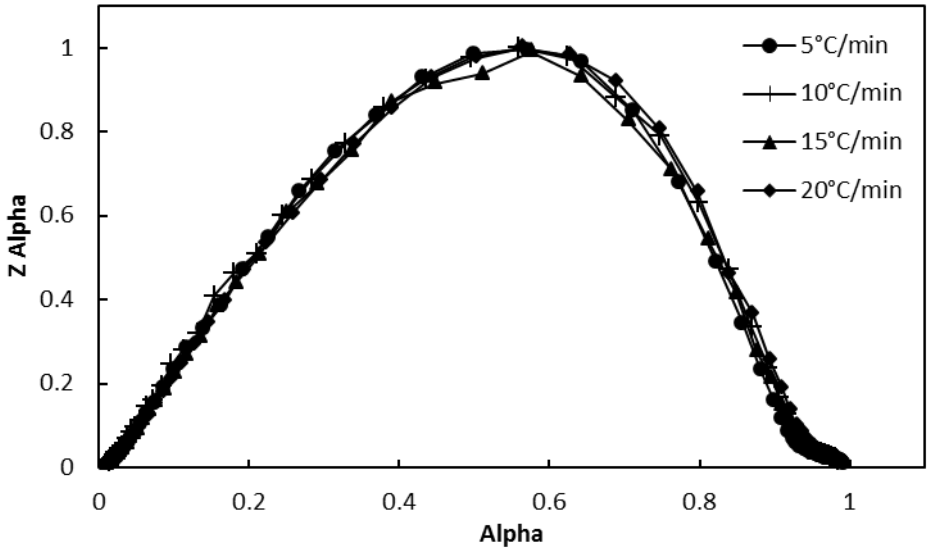

Figure 4-7 Experimental $Z(\alpha)$ plots of PC with 0.2wt% CB at different heating rates.

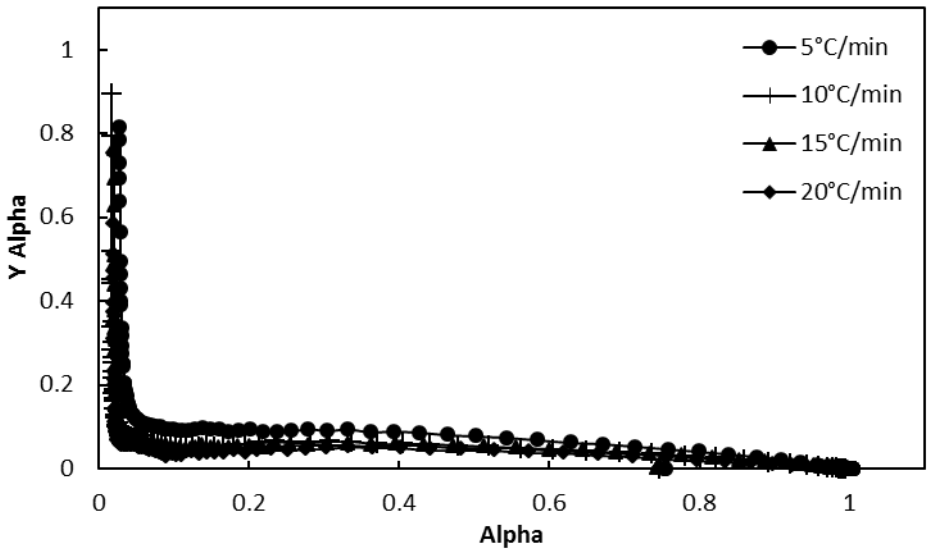

Figure 4-8 Experimental $Y(\alpha)$ plots of PA6 at different heating rates.

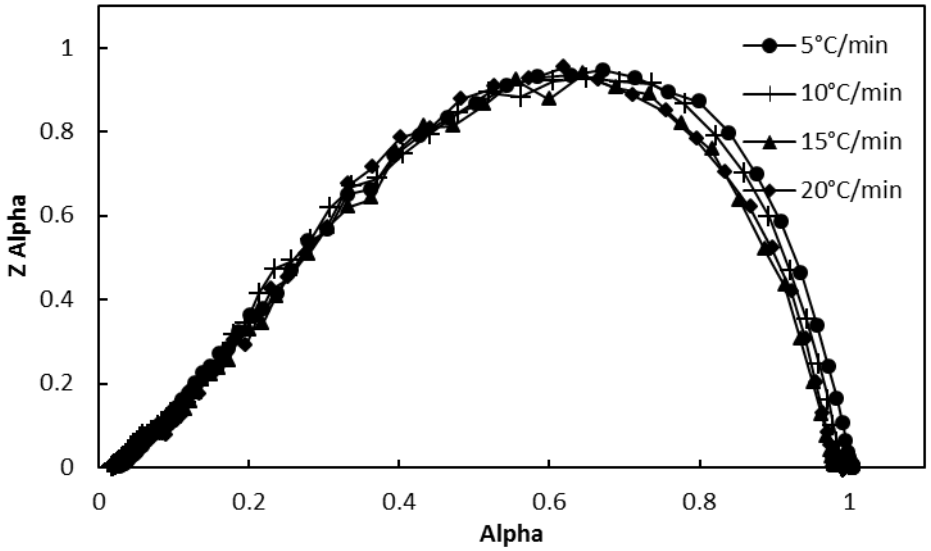

Figure 4.9 Experimental $Z(\alpha)$ plots of PA6 at different heating rates.

Figures 4-4 and 4-6 show that the $Y(\alpha)$ plots of PC are convex with α_m values of 0.43 and 0.37 for PC containing 0.05 and 0.2wt% CB respectively. PC containing 0.05 and 0.2wt% CB has α_p values of about 0.61 and 0.55 respectively. According to Figure 2-3 and Figure 2-4, the reaction model of the PC materials corresponds to either the SB or An reaction models. The

$Z(\alpha)$ plots of PC with 0.05 and 0.2wt% CB (Figures 4-5 and 4-7) exhibit α_p values of 0.59 and 0.57 respectively which, in combination with the value of α_m and typical values of α_p and α_m presented in Section 2.2.2, confirms that the SB model is an appropriate $f(\alpha)$ for the thermal degradation of the PC materials. This is consistent with the work of Al-Mulla et al [37] who obtained the kinetic parameters of PC using Fn model which has a form of the SB model.

The $Y(\alpha)$ plot of PA6 (Figures 4-8) is concave. The $Y(\alpha)$ plot has an α_m value of 0 (zero) which corresponds to either the $D2$, An and Fn models. The values of α_p for PA6 (from Figures 4-9) is 0.62, which, in combination with the value of α_m and values available in literatures, shows that an Fn model is an appropriate $f(\alpha)$ for the thermal degradation of PA6. Zong et al [39] modelled the TGA data of PA6 in a N_2 atmosphere with an *Fn* model. Lee et al [58] also modelled the TGA data of PA6 in a N_2 atmosphere with an *Fn* model.

4.3 Non-linear model fitting

By substituting the appropriate reaction models $f(\alpha)$ for PC and PA6 into equation 2-3 in order to obtain $\left(\frac{d\alpha}{dt}\right)_{calc}$ and then taking the difference between $\left(\frac{d\alpha}{dt}\right)_{expt}$ and $\left(\frac{d\alpha}{dt}\right)_{calc}$ as given by equation 2-11 ($\left(\frac{d\alpha}{dt}\right)_{expt}$ and $\left(\frac{d\alpha}{dt}\right)_{calc}$ are experimentally obtained and calculated values of $\frac{d\alpha}{dt}$ respectively), the parameters k_0, E, m and n are determined as those values which minimise the objective function (equation 2-11). The optimization of the objective function was constrained within the range of E values obtained from the isoconversional method. Average values of the TGA data from the replicate TGA experiments were used for these computations.

Lsqnonlin, a Matlab curve fitting toolbox was used to perform this minimization of the objective function.

By substituting the values of k_0, E, m and n obtained from the optimization into equation 2-3, and integrating, the calculated mass conversion (α) for the materials were obtained. This integration was performed using Matlab ode45. The Matlab code used for this optimization and integration is presented in Appendix C.

Figures 4-10 to 4-12 are the plots of experimental and model predicted mass conversion by thermal degradation as a function of temperature during TGA experiments at heating rates of 5 and 20°C. These plots for heating rates of 10 and 15°C not presented here can be found in Appendix B. Table 4-1 displays the kinetic parameters generated by the non-linear model-fitting for the materials. Table 4-2 displays the R squared values of the fit of the model to experimentally obtained mass conversion as a function of temperature for a conversion range of 0.01 to 0.7.

Figures 4-10 to 4-12 and Table 4-2, show that the *SB* model is able to reproduce the TGA data of PC materials (containing 0.05wt%CB and 0.02wt%CB) while *Fn* model is able to reproduce the TGA data of PA6. For PA6, the TGA data of the materials from different CB contents were pooled together as it has been shown earlier in section 3.3 that CB has no noticeable effect on the thermal stability of the nylon materials.

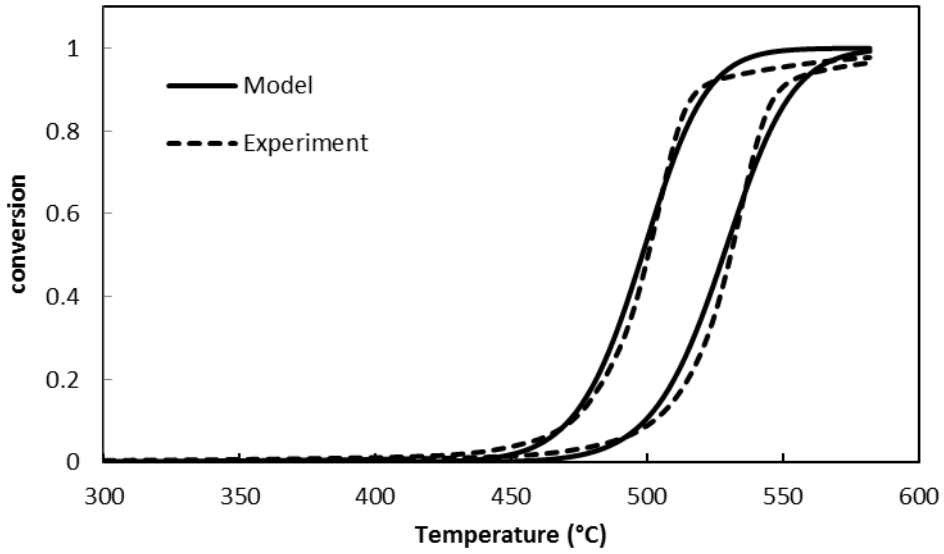

Figure 4-10 Mass loss curves of PC (0.05wt% CB) samples at heating rates of 5 and 20°C and their fitting curves with Sestak-Beggren model.

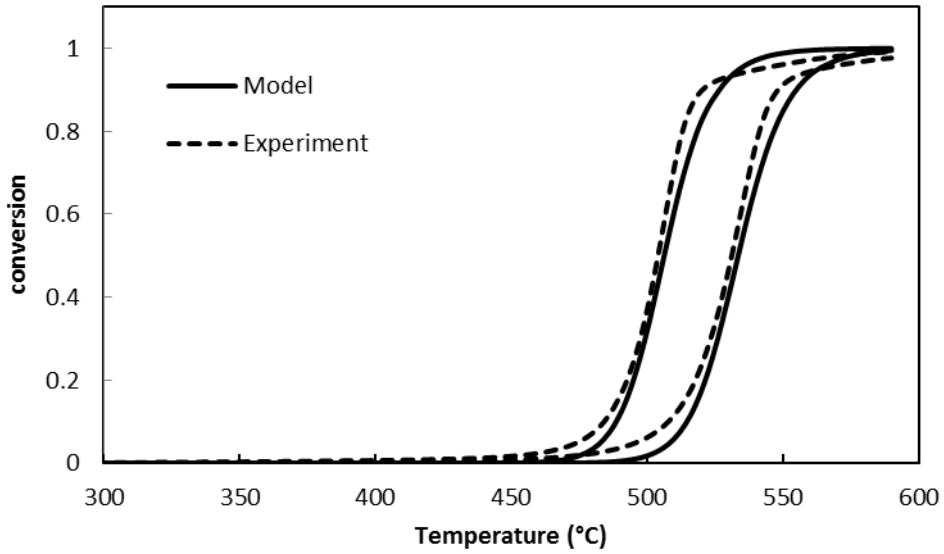

Figure 4-11 Mass loss curves of PC (0.2wt% CB) samples at heating rates of 5 and 20°C and their fitting curves with Sestak-Beggren model

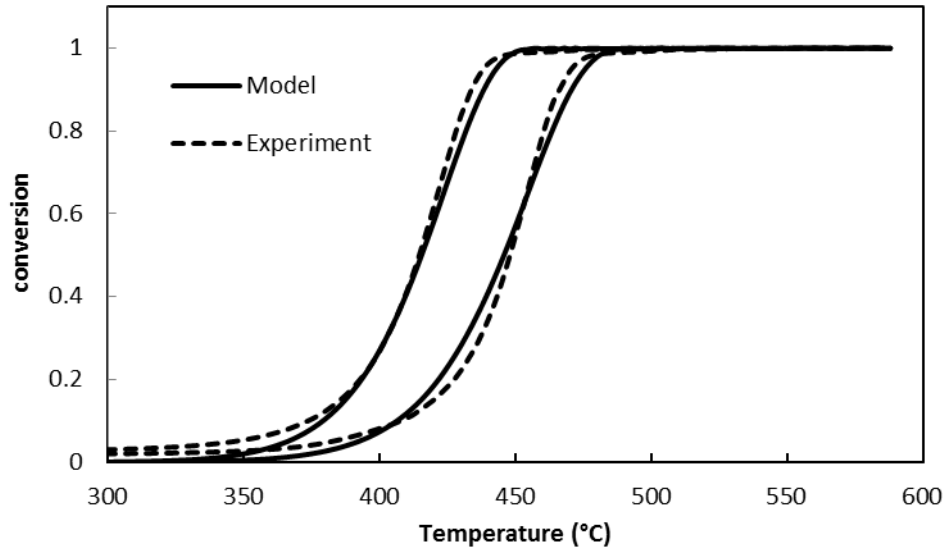

Figure 4-12 Mass loss curves of PA6 samples at heating rates of 5 and 20°C and their fitting curves with *n*th-order model.

Table 4-1 kinetic parameters from references and from the experiments

MATERIAL	PC [40]	PC (0.05)	PC (0.2)	PA6[27]	PA6
Log k_0 (min^{-1})	8.3-16.1	14.8	16.7	12.87	12.6
E (kJ/mol)	160-221	225	253	184 ± 5.2	177
n	-	1.3	1.5	0.6	0.8
m	-	0.3	0.6	-	-
$f(\alpha)$	-	*SB*		*Fn*	*Fn*

Table 4-2 R-squared values of the non-linear model-fitting of the materials

Material	PC (0.05)	PC (0.2)	PA6
R squared	0.973	0.936	0.992

For PC containing 0.05% CB, the Log k_0 value obtained from this work is within the range of log k_0 obtained by Al-Mulla et al [37] while the E value obtained from this work shown in Table 4-1 is about 1.8% higher than the range of E obtained by Al-Mulla et al [40]. For PC containing

0.2wt% CB, the E and k_0 values obtained from this work are about 14.5% and 3.7% higher than the range of E and k_0 values respectively obtained by Al-Mulla et al [37]. Al-Mulla et al used neat PC in their work while PC and CB mixtures were used here. The higher values of E obtained in this work are likely due to the increased thermal stability associated with higher CB levels (section 3.3). For PA6, the log $k_0$and E values obtained from this work are both within 3% of the values obtained by Lee et al [58]. Also for PA6 the value of n obtained from this work shown in Table 4-1 is about 25% higher than the n value obtained by Lee et al [45] which is 0.6. These comparisons show that the kinetic parameters obtained from this work are consistent with values found in the literature. The R-squared values as seen in table 4-2 show that the model exhibits a reasonable fit to experimental data.

Chapter 5
Temperature-Time Profile

This chapter presents the method used to obtain the temperature-time profiles of the materials during LTW. In section 5.1 an overview of Chen's thermal finite element method (FEM) model is elaborated. The temperature-time profile for the materials during LTW obtained by running Chen's FEM thermal model is then presented in section 5.2.

5.1 Overview of Chen's thermal model and LTW process conditions

Mingliang Chen [6] developed a quasi-static 3-D FEM model for the prediction of temperature-time as a function of position during LTW using Comsol® software. The temperature-time profile used in this work was generated by modifying and running Chen's FEM thermal models for the materials at different laser power levels. An overview of Chen's FEM model and LTW process conditions presented in this chapter includes:

- Material properties of PA6 and PC
- 3-D quasi static FEM thermal model for PA6 and PC
- Material geometry and LTW working distance

5.1.1 Materials properties of PA6 and PC

Table 5.1 summarizes the thermal and optimal properties used in the FEM simulation. For more information, the reader is referred to reference 6

Table 5-1 Thermal and optical properties of the materials used in the FEM

Property	PC	PA	Notes
Heat capacity (C_p), J/(kgk)	Temperature dependent function found on page 80 and 82 of reference 6 for PC and PA6 respectively		Determined by DSC
Thermal conductivity (κ), W/(m K)	Temperature dependent function found on page 79 and 80 of reference 6 for PC and PA6 respectively		Determined by UNITHERM™ and from values in the literature
Density (ρ), kg/m^3	Temperature dependent function found on page 85 of reference 6 for PC and PA6		Obtained from PVT curves available in the literature
Absorption coefficient (A), 1/mm	$A = 82C_{CB}$ C_{CB} is CB level in wt%.	-	Determined by so-called reduced transmission method for PC for the laser-transparent part and laser-absorbent part. Irrelevant for PA6 FEM model.
Apparent absorbance of the laser-transparent part (A_{1t}), 1/mm	$A_{1t} = A$	0.24 1/mm	Computed from the value of A for PC. Determined by spectrophotometer method for PA6
Apparent absorption coefficient of the laser-absorbent part (A_{1a}), 1/mm	$A_{1a} = A$	$A_{1a} = 52C_{CB} + 0.24$	For non-scattering materials like PC, $A_{1a} = A$. Determined by the so-called direct scan method for PA6
Surface reflectance of the laser-transparent part (η_t)	0.08	0.04	Determined by the so-called reduced transmission method for PC and based on Fresnel equation for PA6

Table 5-1 Contd			
Surface reflectance of the laser-absorbent part (η_a)	$\eta_a = \eta_t$	$\eta_a = \eta_t$	Determined by the so-called reduced transmission method for PC and based on Fresnel equation for PA6
Total reflectance of the laser-transparent part (R_{Tt})	$R_{Tt} = 1 - (1 - \eta_t)^2$	0.14	Computed from the value of η_t for PC. Determined by spectrophotometer method for PA6.
Total reflectance R_{Ta} of the laser-absorbent part	$R_{Ta} \approx \eta_a$	$R_{Ta} \approx \eta_a$	Computed from their values of η_a
Scattering ratio ($\delta\ (0)$)	0	0.64	PC is assumed to be completely non-laser scattering. Computed from the values of scattered laser power P_{si} and total laser power P_i of laser beam beam of power intensity ($P_L^{"}$) discretized into i^{th} point beams of power intensity ($P_{Li}^{"}$)
scattering standard deviation ($\sigma\ (0)$), mm	-	0.9	Irrelevant for PC. Fitted to Gaussian function used to describe the experimental laser beam distribution at $y = 0$
Laser extinction coefficient K_t	$\mathrm{K}_t = A$	0.551	Computed from Beer's law for PA6
Laser extinction coefficient K_a	$\mathrm{K}_a = A$	0.551	Computed from Beer's law for PA6
Scattering coefficient (S_t), 1/mm	0	$\mathrm{K}_t = \mathrm{A}_t + \mathrm{S}_t$ For $\mathrm{S}_t >> \mathrm{A}_t$, $\mathrm{S}_t = 0.551$	PC assumed to be completely non-scattering. Based on assumption that $\mathrm{S}_t >> \mathrm{A}_t$ for natural polymers

Table 5-1 Contd			
Scattering coefficient (S_a), 1/mm	0	$S_a \approx S_t$	PC assumed to be completely non-scattering Computed from S_t for PA6
Generated heat energy Q, W/m^3	$Q\ (x,y,z) = A_1 P^{"}(x,y,z)$		Computed based on loss of laser energy with depth into polymer according to Beer's law

5.1.2 3-D quasi-static FEM thermal model

Introduction

The 3-D quasi static model developed by Chen, shown schematically in Figure 5-1, changes the time-dependent problem of contour LTW to time-independent problem by the introduction of mass flow under a static laser beam. This approach reduces the simulation time of the contour LTW problem. A typical computation time of 2.8 and 15 minutes was achieved for a set of parameters for PC and PA6 respectively.The heating-cooling time simulated by 3-D quasi-static model is limited by the length of model.

In Chen's 3-D quasi static model, the general heat transfer equation (in a Cartesian coordinate system), which is used for the FEM heat transfer modelling and given by equation 5-1 [6], is simplified as a time independent function (with mass velocity along z axis), as given by equation 5-2, by removing time-dependency in equation 5-1.

$$C_p \rho \left(\frac{\partial T}{\partial t} + v_x \frac{\partial T}{\partial x} + v_y \frac{\partial T}{\partial y} + v_z \frac{\partial T}{\partial z}\right) = \kappa \left(\frac{\partial^2 T}{\partial x^2} + \frac{\partial^2 T}{\partial y^2} + \frac{\partial^2 T}{\partial z^2}\right) + Q \qquad 5\text{-}1$$

$$\kappa \nabla^2 T + C_p \rho v \frac{\partial T}{\partial z} + Q = 0 \qquad 5\text{-}2$$

In the above equations, C_p is heat capacity, ρ is density, v is velocity, the subscripts x, y and z denote different axes in a Cartesian coordinate system, κ is thermal conductivity and Q is the heat source.

Simulated heat transfer conditions and boundary conditions

The two heat transfer conditions simulated by Chen were the contact and non-contact models for contact and non-contact geometry respectively.

The contact model was used for thermal analysis in contour LTW with no gap at the interface between the laser-transparent and absorbent parts. Surface reflection from the top and bottom surface of the transparent part, bulk reflection, absorption, scattering of the laser beam by the transparent part as well as radiative heat transfer at the top of the laser-transparent and at the bottom of laser-absorbent parts were all accounted for in the contact model. In addition, conductive heat transfer was permitted at the interface of the laser-absorbent and transparent parts in the contact model as shown in Figure 5-1.

The non-contact model was used for thermal analysis in contour LTW with gaps at the interface between the laser-transparent and absorbent parts. In this model, no conductive heat transfer was permitted at the interface of the laser-absorbent and transparent parts. However, surface reflection from the top and bottom surface of the transparent part, bulk reflection, absorption, scattering of the laser beam by the transparent part were considered in the FEM

model. Radiative heat transfer at the top and bottom of the laser-absorbent part, conduction into polymer bulk and convection at the boundary as given by Figure 5-4 were also accounted for in the FEM model. The thickness of the gap at the interface was assumed to be too small to affect the laser beam transmission.

In Chen's thermal model, at a set speed, the polymer parts initially at 23°C moved through a static laser beam. For PA6, Chen used Lagrange-linear elements (tetrahedral, first order/linear shape function) (with 431,604 tetrahedral elements and 75,356 degrees of freedom for a 15 mm-long model under the contact condition) for the thermal modelling. This had a controlled maximum mesh size of $\leq$ 0.05 mm with a growth rate of 1.1 for the weld interface. The details of the mesh size can be found in reference 6.

The author used the FEM code written by Chen in order to generate the specific maximum temperature-time profiles corresponding to the LTW process conditions described in Section 5.1.3.

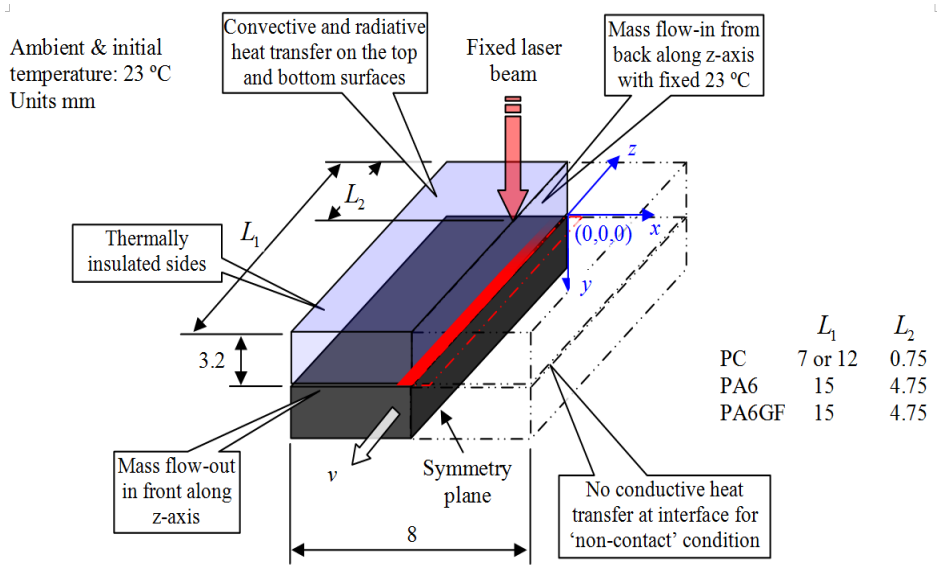

Figure 5-1 Structure of the 3-D quasi-static model with its initial and boundary conditions [6]

5.1.3 LTW process conditions

The experimental LTW of the materials was conducted using a Rofin-Sinar DLx16 HP diode laser at a working distance of 82.5mm and scan speed of 1500mm/min. The power used varied with the material being tested. Plaques of 3.2 mm part thicknesses were used in the experiments for all the materials. The force at break of the lap-joint of the welds was obtained using INSTRON Model 4206 Universal Testing machine at a cross-head speed of 5 mm/min. The experimental lap joint geometry and LTW setup for the LTW is shown by Figure 5.2.

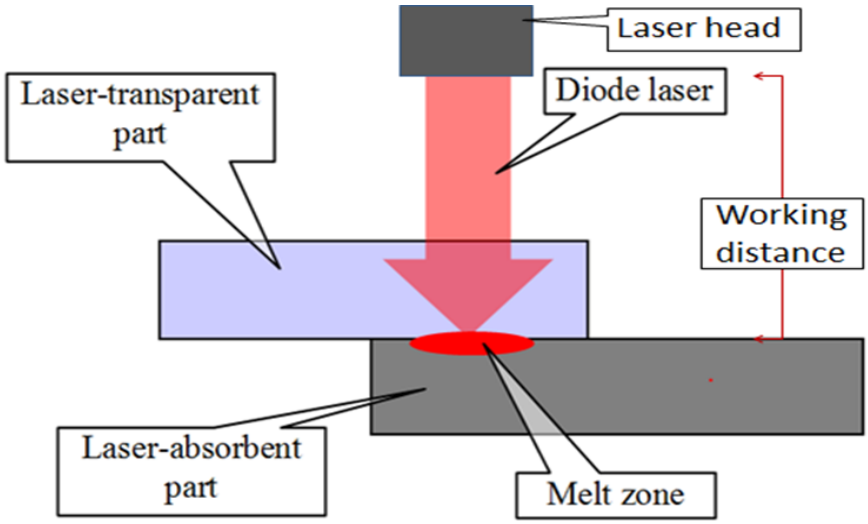

Figure 5.2 Schematic of experimental lap joint geometry and LTW setup used for the LTW [6]

5.2 Temperature-time profile obtained from FEM

The temperature-time profiles used for modelling thermal degradation during LTW of PC and PA6 were obtained by running Chen's thermal FEM model for the materials at a scan speed of 1500mm/min and different power levels. The temperature varies throughout the part particularly throughout the depth. A typical FEM output obtained is presented in Figure 5-3 for the contact geometry.

The result of the FEM shows that maximum temperature for the non-contact geometry along the y-axis was at the top surface ($y = 0$) of the absorbent part as presented by Figure 5-4. However, for a contact geometry, the point of maximum temperature was at a certain depth (y) below the top surface of the absorbent part as presented by Figure 5-5. The depth at which the maximum temperature occurs is dependent on the material properties and the CB content of the polymer.

The trends of Figures 5-4 and 5-5 are also the same for PC. These data for PC can be found in Appendix D. In this work, the temperature-time profile at the hottest spot of the assembly is used to predict the onset of thermal degradation and then compared with experimental data as discussed further in Chapter 6.

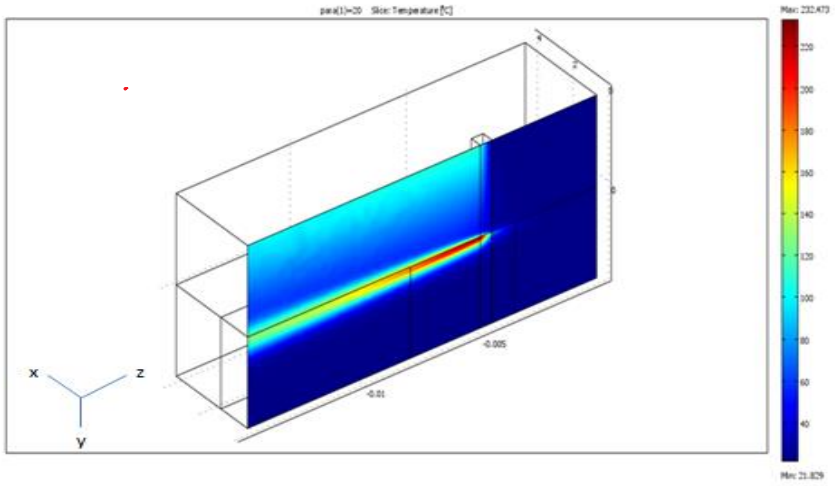

Figure 5-3 Typical FEM output obtained by running Chen's model (PA6 0.1wt% CB, 20 W, 25mm/s contact model) [6]

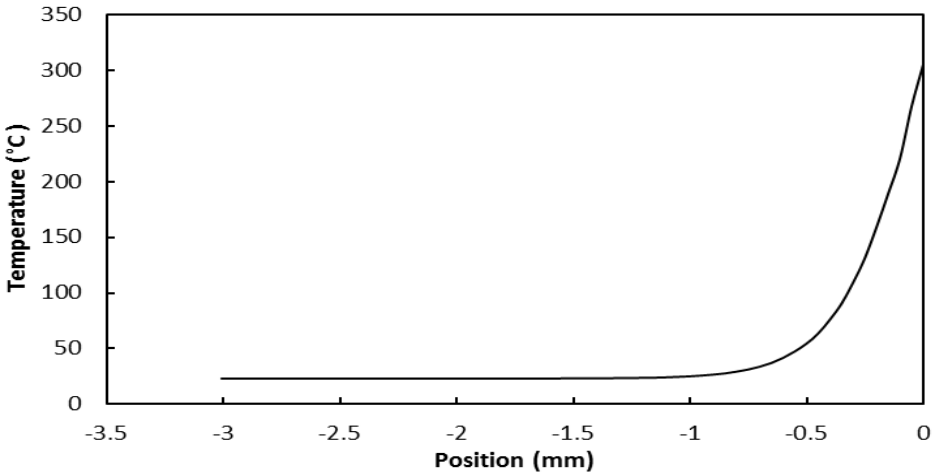

Figure 5-4 Typical temperature profile along the y direction in the laser-absorbent part for non-contact model (PA6 0.1wt% CB, 20 W, 25mm/s)

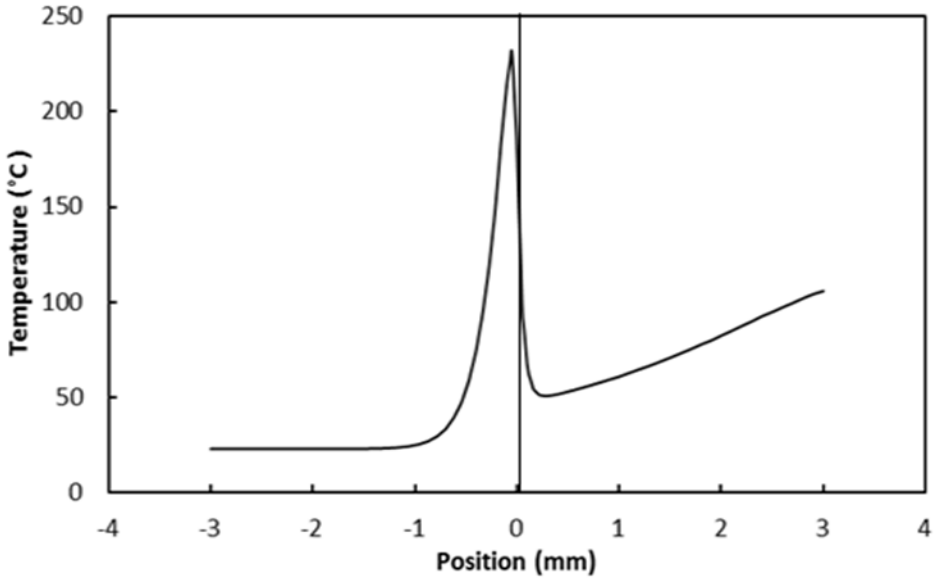

Figure 5-5 Typical temperature profile along the y direction for contact model (PA6 0.1wt% CB, 20 W, 25mm/s)

Figures 5-6 to 5-9 are temperature-time profiles obtained from running the FEM model. The regions of rise and decline in temperature with time for the materials shown by Figures 5-6 to 5-9 corresponds to heating and cooling respectively during LTW. These figures show that welding temperatures increase with increase in laser power in both contact and non-contact weld conditions. It can also be seen that, for the same material and laser power, non-contact weld condition yields higher temperatures than its counterpart contact weld condition. This is due to heat loss by conduction to the cold laser-transparent part in the contact method which is much greater than heat loss by natural convection in the non-contact method. The difference in the heating times between the materials is due to a difference in the light scattering abilities of the materials. PA6 is more laser-light scattering than PC. This causes the dimensions of the transmitted beam to increase and results in a longer heating time albeit at a lower power flux. It can also be observed from Figures 5-6 to 5-9 that PC requires lower power to reach higher

temperatures than PA6. This is because more laser energy is lost in the transparent part for PA6 than in PC due to light scattering and also the resultant longer heating time in PA6 means there is more time for heat loss in PA6 than in PC.

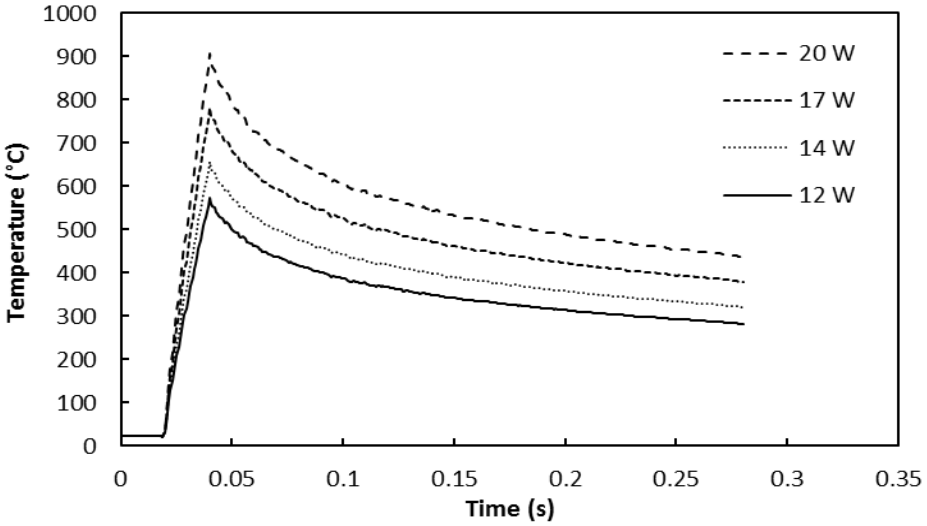

FIGURE 5-6 Temperature-time profile of PC (contact, 0.05wt%CB, 25mm/s) at different laser power level.

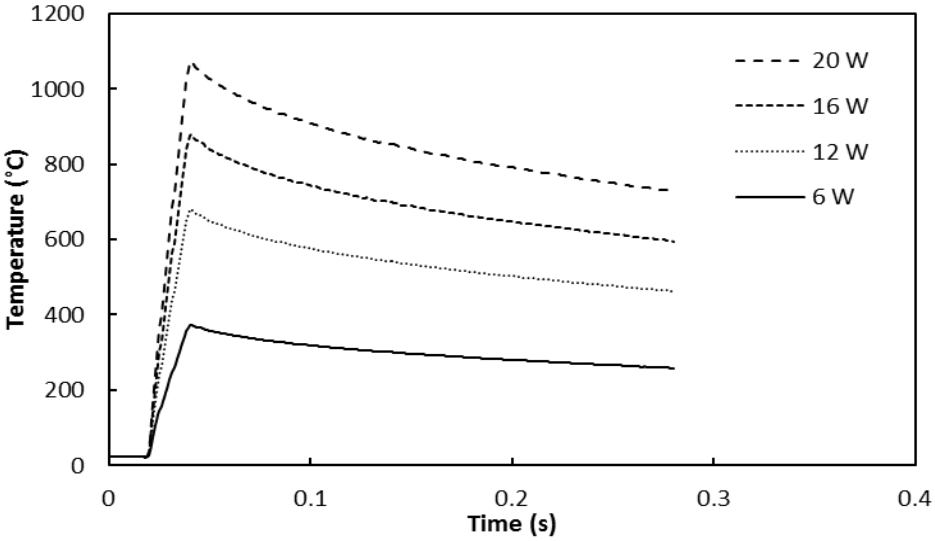

FIGURE 5-7 Temperature-time profile of PC (non-contact, 0.05wt%CB, 25mm/s) at different laser power level

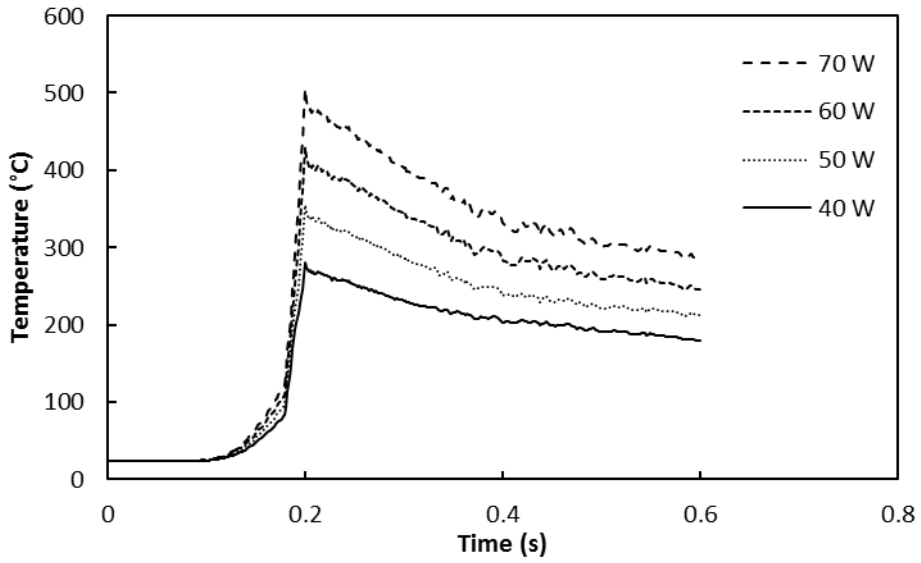

Figure 5-8 Temperature-time profile of PA6 (contact, 0.05CB, 25mm/s) at different laser power level

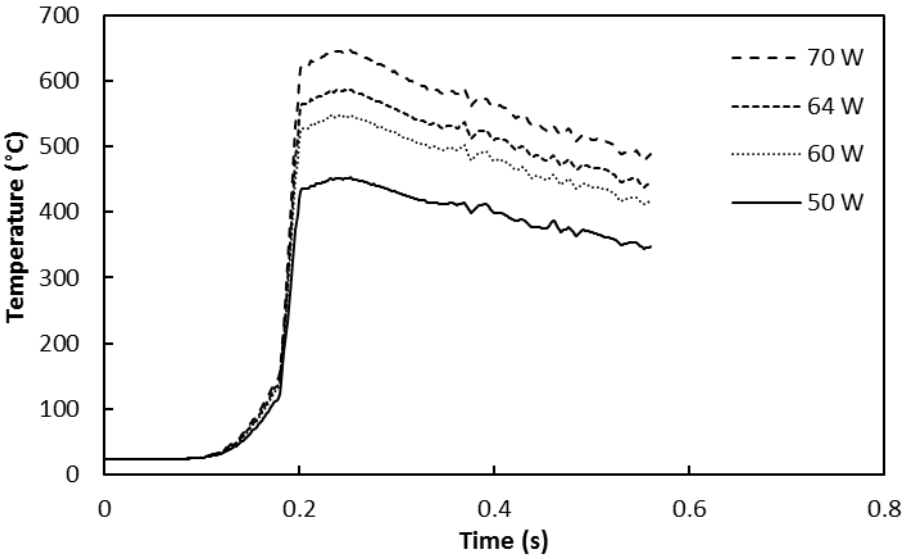

Figure 5-9 Temperature-time profile of PA6 (non-contact, 0.05wt%CB, 25mm/s) at different laser power level

Chapter 6
Thermal Degradation Simulation

In this chapter, the temperature time profile obtained from the FEM model and the kinetic parameters are used to predict thermal degradation during LTW. In section 6.1 the theory of this prediction is presented. The results obtained by this method are presented and discussed in section 6.2.

6.1 Theory

The thermal degradation simulation conducted in this work is based on estimating the material conversion caused by thermal degradation during LTW. This is achieved by solving the kinetic degradation model (complete with fitted kinetic triplets) of each material using its temperature-time profile obtained from the FEM. The FEM did not provide a direct equation to relate the temperature and time. Therefore, Matlab was used to generate polynomials for T in terms of t as shown by equation 6-1. The equations used for $T = f(t)$ are found in Appendix E. The generated temperature-time relationship ($f(t)$) was substituted into equation 2-3 as given by equation 6-2. The integration of Equation 6-2 was then performed numerically using Matlab ODE 45 in order to predict the material conversion at different laser powers and CB -levels. This Matlab code is presented in Appendix F.

$$T = f(t) \qquad 6\text{-}1$$

$$\frac{\mathrm{d}\alpha}{dt} = k_0 \exp\left(\frac{-E}{Rf(t)}\right) f(\alpha) \qquad 6\text{-}2$$

6.2 Results and discussion

Figures 6-1 and 6-2 are the predicted degradation conversion (α) vs time obtained by the model for PA6 and PC in a non-contact geometry. The temperature-time data used for the prediction of conversion (α) in a non-contact geometry are the maximum temperature time data which is at the top surface of the laser absorbent part ($y = 0$). This is reasonable because the degradation in the non-contact geometry was observed at the top surface of the laser absorbent part ($y = 0$). Figures 6-3 and 6-4 are the predicted degradation conversion (α) vs time obtained by the model for PA6 and PC in a contact geometry. The temperature-time data used for the prediction of conversion (α) for contact geometries are the maximum temperature time data which is at depth y (depending on the CB content) in the laser absorbent. The maximum temperature data is used to predict upper bound of LTW parameters because decline in weld strength starts before degradation that result to mass loss as suggested by Chen weld strength and weld microstructure studies. The remaining plots of predicted degradation conversion (α) vs time of the materials not presented here are shown in Appendix E.

These plots show that degradation reactions have essentially stopped after approximately 0.05 s and 0.15 s for PC and PA respectively. From Figures 5-6 to 5-9, one can see that these times correspond to the heating times during which the laser irradiates a given point along the weld seam. The longer heating time for PA6 is related to its scattered beam.

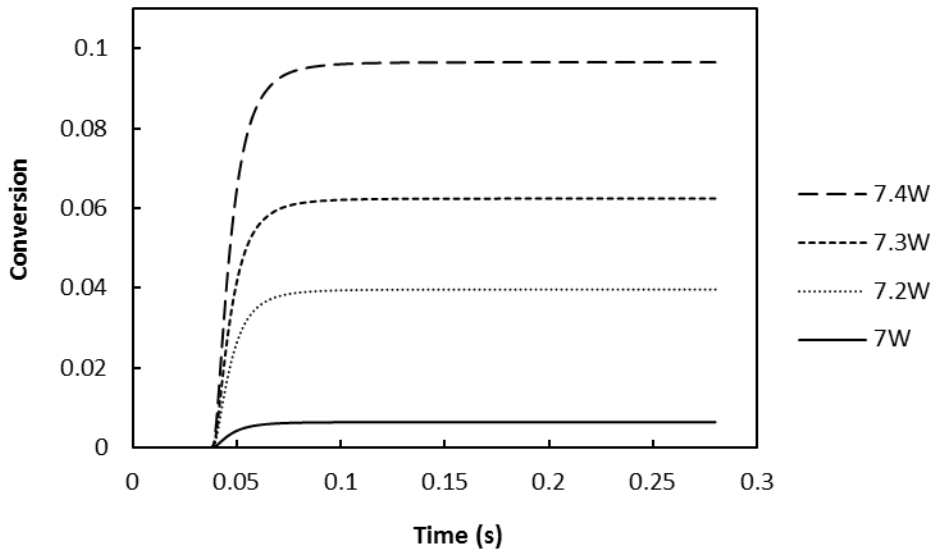

Figure 6-1 Predicted conversion vs time (PC 0.1wt% CB, 25mm/s, non-contact weld).

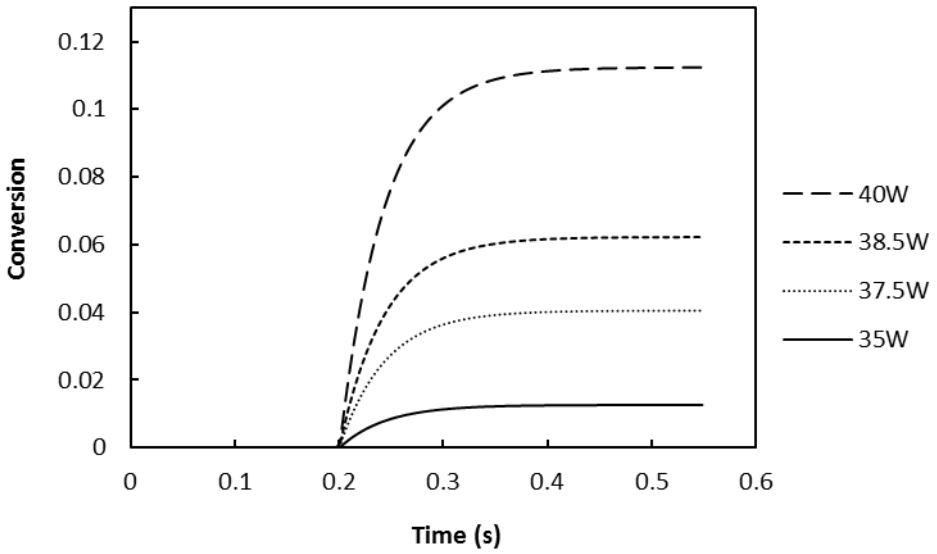

Figure 6-2 Predicted conversion vs time (PA6 0.1wt% CB, 25mm/s, non-contact weld).

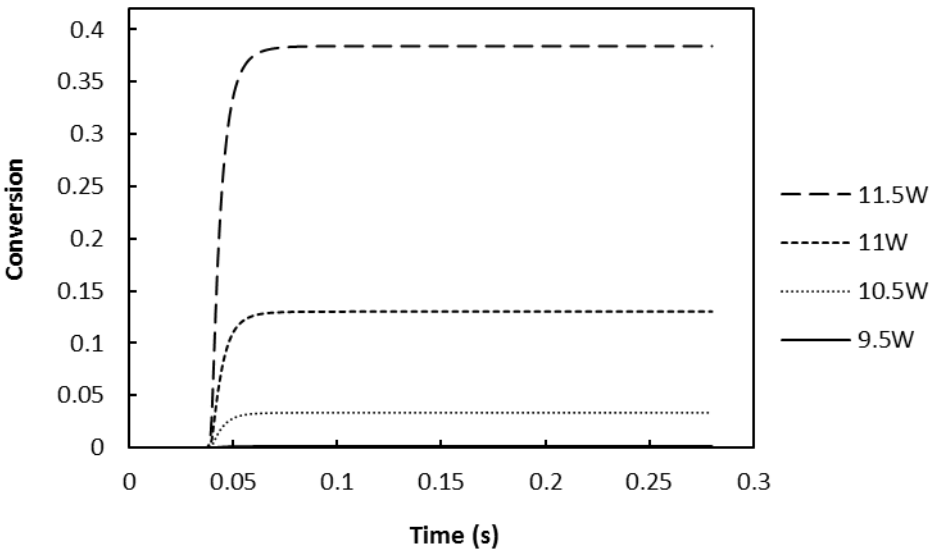

Figure 6-3 Predicted conversion vs time (PC 0.1wt% CB, 25mm/s, contact weld).

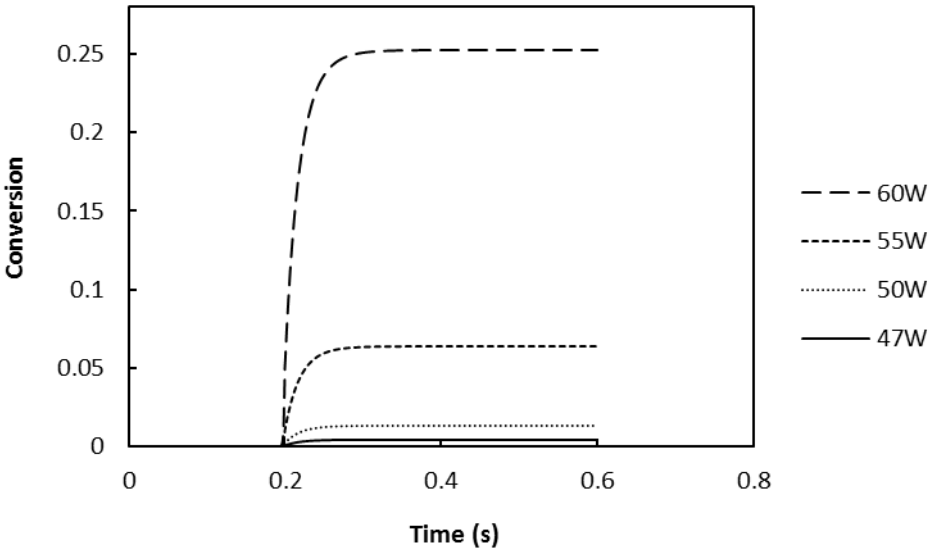

Figure 6-4 Predicted conversion vs time (PA6 0.1wt% CB, 25mm/s, contact weld)

Figures 6-5 and 6-6 are plots of power causing the onset of thermal degradation in a non-contact geometry as a function of CB-level for each of the two materials. Due to the small shift in the TGA curve of PC to higher temperature (shown in Figure 3-7) with changes of the CB content from 0.05wt% to 0.2wt%, the kinetic parameters obtained from PC (0.2wt% CB) were used for 0.1wt% CB. The kinetic parameters obtained from PC (0.05wt%) were also used for the prediction of degradation during LTW for other PC CB levels. For PA6, all prediction of degradation during LTW is done using the kinetic parameters obtained from the pooled TGA data. Figures 6-5 and 6-6 show the experimental results of Chen and the degradation model. Experimentally, the power causing degradation was characterised by burn marks, bubbles or vapour condensation on the bottom surface of the laser-transparent part [6]. From the simulation, the power level causing 1, 5 and 10% degradation conversion (α) were noted for each different material and CB level. Table 6-1 shows the difference between simulation and experimental data expressed as a percentage. Positive value in the Table 6-1 signifies that the model predicted 1, 5 or 10% conversion at power higher than the power observed to experimentally cause thermal degradation during LTW. The % simulation errors (Ɛ**)** in this work are computed based on the equation 6-3.

$$\text{Ɛ} = \frac{P_{Predicted} - P_{Observed}}{P_{Observed}} * 100 \qquad \text{6-3}$$

Where $P_{Observed}$ is power experimentally observed by Chen to cause degradation on the surface of the laser-absorbent part in a non-contact geometry or onset of a decline in weld strength in a contact geometry. $P_{Predicted}$ is power predicted by the degradation model to cause a given thermal degradation conversion.

Figures 6-5 and 6-6 show a good agreement between power predicted to cause 1, 5 and 10% degradation conversion (α) and the power experimentally observed to cause onset of degradation in a non-contact method for PC and PA6 respectively. The results at different conversions are close because for the welding conditions used, not much laser power is need to complete degradation to 100% once degradation starts in the materials.

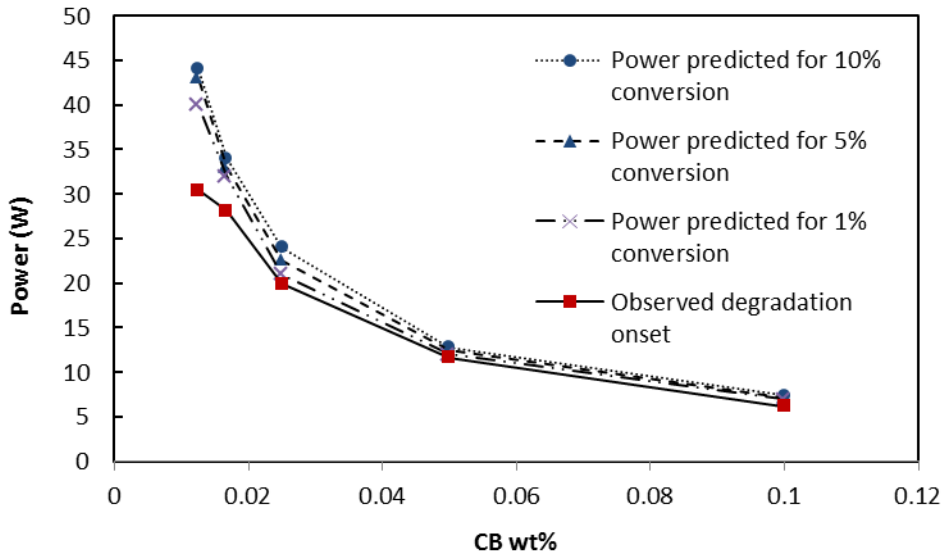

Figure 6-5 Observed power for degradation of the surface of the absorbent part and predicted power for 1, 5 and 10% material conversion (PC, 25mm/s, non-contact)

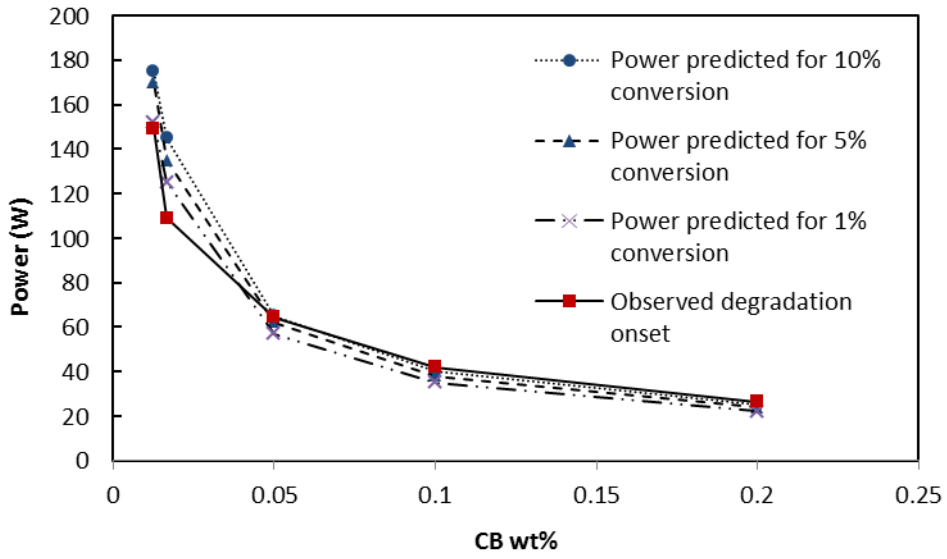

Figure 6-6 Observed power for degradation of the surface of the absorbent part and predicted power for 1, 5 and 10% material conversion (PA6, 25mm/s, non-contact)

Table 6-1 % Simulation error (non-contact geometry)

% Simulation error (Ɛ) of different predicted % material conversion (α) for PC				
CB wt%	10% α	5% α	1% α	Absolute Average
0.1	19	16	12	16
0.05	10	7	3	7
0.025	21	14	6	14
0.0165	21	17	14	17
0.0125	45	41	31	39
Absolute Average	23	19	13	
% Simulation error (Ɛ) of different predicted % material conversion for PA6				
0.2	-5	-9	-16	10
0.1	-5	-10	-17	11
0.05	1	-4	-11	5
0.0167	33	23	15	24
0.0125	17	13	2	11
Absolute Average	12	12	12	

Figures 6-7 to 6-9 show the experimental progression of shear strength of the materials with laser power for different CB levels for the contact geometry for PC. Figures 6-10 to 6-12 show the results for PA6. As discussed in section 2.3.2, experimentally, these results show that the weld strength reaches a maximum with laser power and then begins to decline due to thermal degradation. These figures also show maximum degradation on the secondary axes of these plots as a function of laser power. The vertical lines in these figures correspond to the laser power predicted by the thermal degradation model to cause 1% thermal material conversion during LTW. 1% conversion is used here to predict the upper bound of laser parameters for weld strength decline because decline in weld strength starts before mass loss by degradation in LTW as suggested by weld strength and weld microstructure studies conducted by Chen [6]. This loss in weld strength before mass loss by degradation can be attributed to thermal expansion which squeezes out molten polymer from the weld interface and to molecular degradation that did not lead to mass loss. Table 6-2 shows percentage simulation errors for the materials. Positive values of the % simulation error in the Table 6-2 signify that the model predicted 1% conversion at a power higher than the power that was experimentally observed to cause the onset of decline in weld strength.

Figures 6-7 to 6-9 shows a reasonable agreement between the measured onset of a decline in the weld-shear strength and predicted onset of material degradation for PC. The calculated difference between simulation and experimental results shown in Table 6-2 is about 25% with all positive values across all CB levels. This indicates that the laser power predicted by the model to cause onset of thermal degradation was higher than the experimentally measured laser power causing the onset of a decline in weld strength for all CB levels in PC.

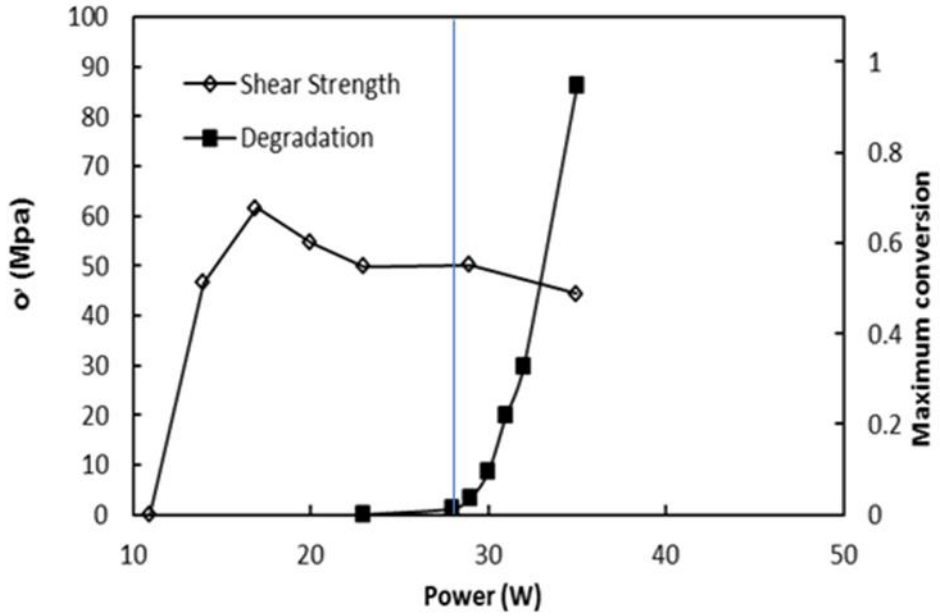

Figure 6-7 Weld strength (primary axis) and maximum conversion vs laser power (secondary axis) of PC with 0.025wt% CB (contact weld).

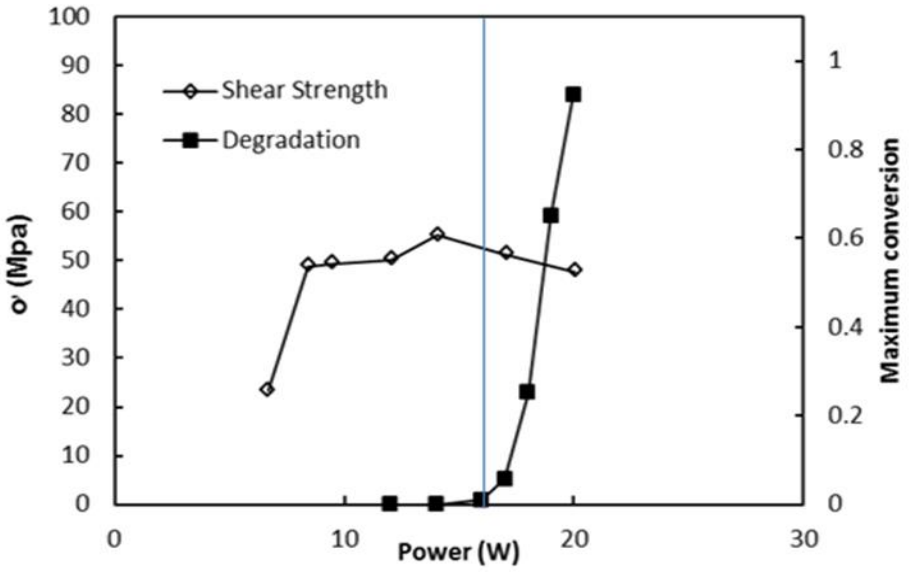

Figure 6-8 Weld strength (primary axis) and maximum conversion vs laser power (secondary axis) of PC with 0.05wt% CB (contact weld).

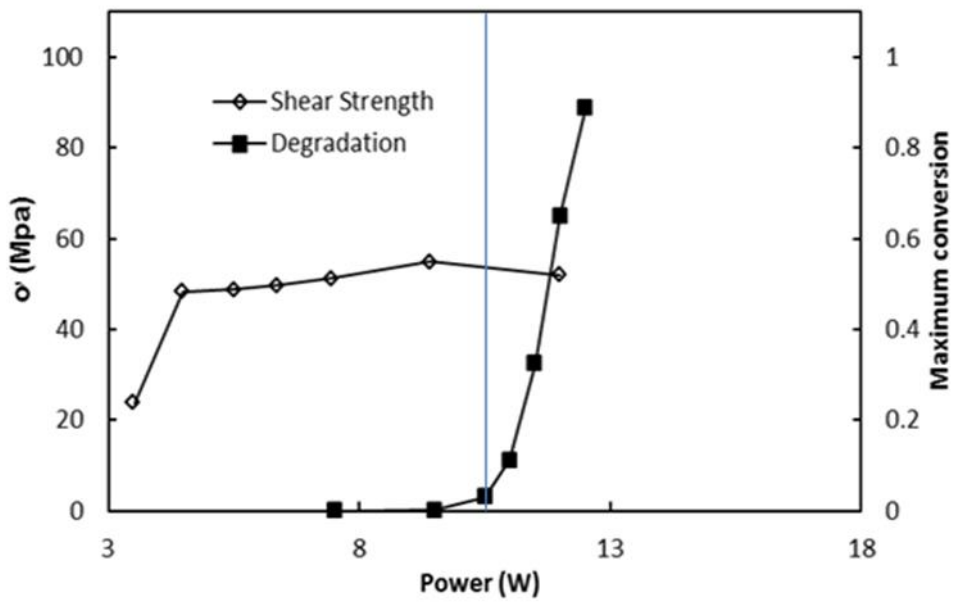

Figure 6-9 Weld strength (primary axis) and maximum conversion vs laser power (secondary axis) of PC with 0.1wt% CB (contact weld).

Similarly, Figures 6-10 to 6-12 also show a reasonable agreement between the measured onset of weld strength decline and the predicted onset of material degradation for PA6. The calculated % simulation as shown in Table 6-2 is about 30% with all positive values for all CB levels (which shows that the model predicted thermal degradation onset was higher than experimentally measure laser power causing a decline in the onset of weld strength for all CB levels in PA6).

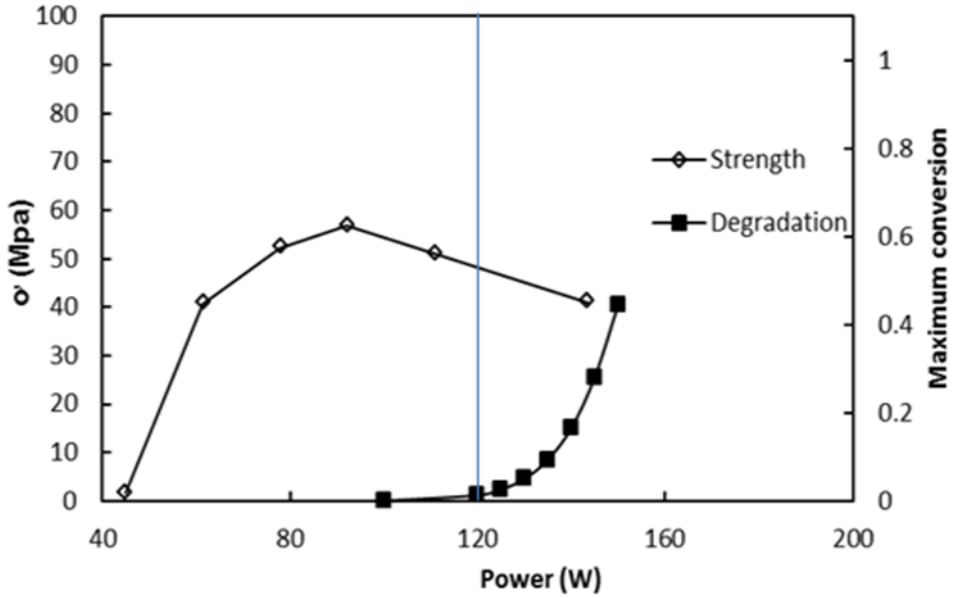

Figure 6-10 Weld strength (primary axis) and maximum conversion vs laser power (secondary axis) of PA6 with 0.025wt% CB (contact weld).

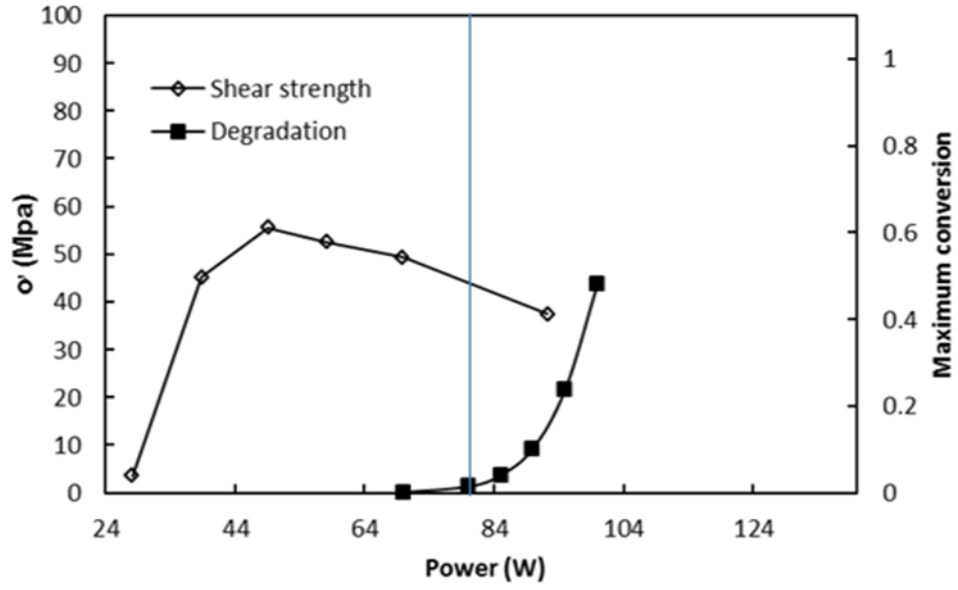

Figure 6-11 Weld strength (primary axis) and maximum conversion vs laser power (secondary axis) of PA6 with 0.05wt% CB (contact weld).

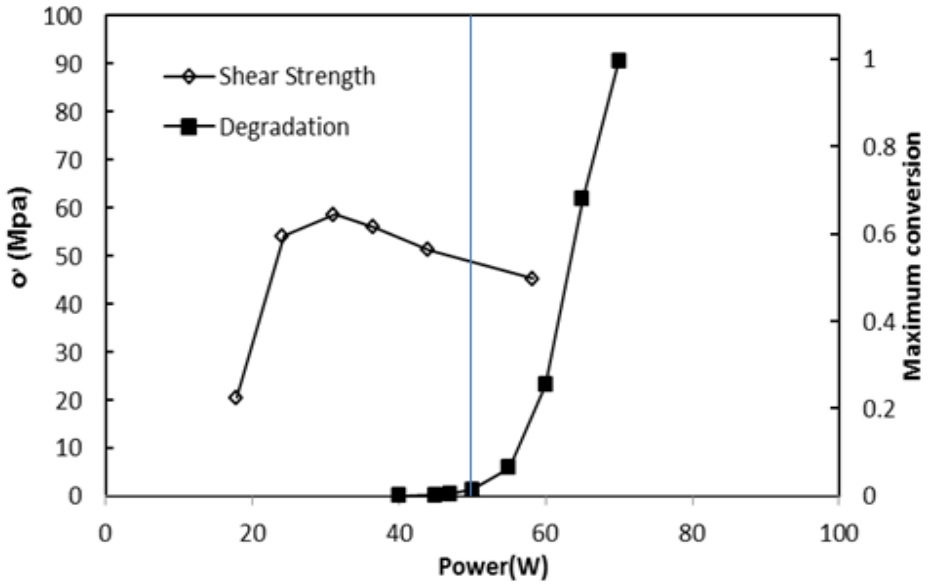

Figure 6-12 Weld strength (primary axis) and maximum conversion vs laser power (secondary axis) of PA6 with 0.1wt% CB (contact weld).

Table 6-2 % Simulation error (contact geometry)

Material	% Simulation error (Ɛ)			
	0.025 wt% CB	0.05 wt% CB	0.1 wt% CB	Absolute average
PC	39	12	10	20
PA6	23	38	37	33

Figures 6-13 and 6-14 show that the simulated power which causes degradation is systematically higher than the observed drop in mechanical properties for the contact geometry. This is likely due to molecular weight modifications that occur at powers lower than those causing mass loss and due to thermal expansion which created voids by squeezing out molten polymer from the weld interface. Drops in molecular weight are not accounted for in this model and may influence the mechanical properties of the materials. The model used in this work (since it is based of kinetic parameters obtained by TGA) predicts only thermal degradation that leads to mass loss. Therefore, the visual experimental test (used in the non-

contact geometry) which is related to mass loss is expected to be closer to the simulation result than the weld strength evaluation.

The results from the contact geometry in this work show some difference with the results obtained by Khosravi [13] which predicted the onset of weld strength decline at powers where significant degradation was predicted by his degradation model. This may be because of differences in the methods used to obtain the kinetic parameters. Khosravi obtained kinetic parameters using single heating rate TGA. More accurate values of the kinetic parameters are expected from this work because they were obtained from multiple heating rates TGA data which is recommended (ICTAC) kinetic committee for reliable kinetic evaluations as mentioned in section 2-2. Weld strength and weld microstructure studies conducted by Chen [6] also suggest that decline in weld strength starts before mass loss by thermal degradation.

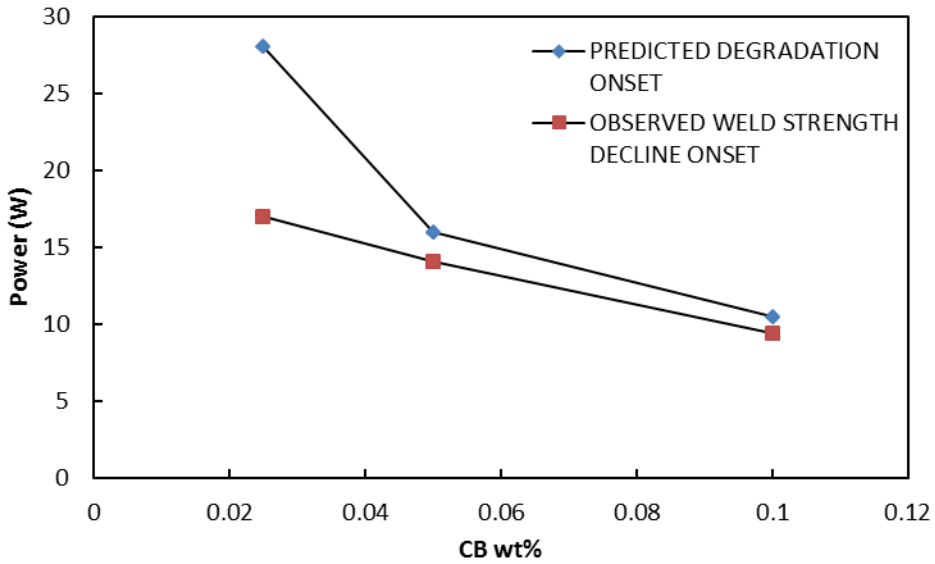

Figure 6-13 Observed and predicted laser power causing onset of decline in weld strength and onset of thermal degradation respectively for PC

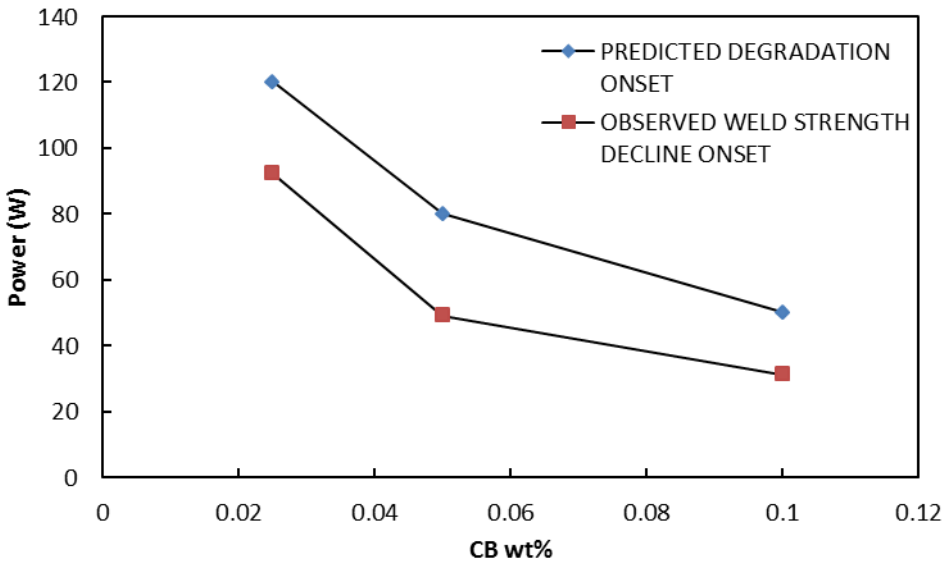

Figure 6-14 Observed and predicted laser power causing onset of decline in weld strength and onset of thermal degradation respectively for PA6

Chapter 7
Semi-Empirical Model for Maximum LTW Temperature-Time Data

In this chapter, a semi-empirical model based on the FEM model is developed for obtaining the maximum temperature-time data during LTW. This is carried out in order to provide a simpler alternative to FEM simulation to obtain the maximum LTW temperature-time data for predicting thermal degradation during LTW.

7.1 Background

In chapter 6, it was shown that maximum temperature-time data obtained from the FEM model in the laser absorbent part can be used to predict thermal degradation. In this chapter, analysis is conducted on this FEM maximum LTW temperature-time data in order to develop a simpler alternate method for obtaining LTW maximum temperature profiles for amorphous materials. In all cases, the contact geometry is used in order to simulate LTW.

A closer look at maximum temperature-time data obtained by the FEM model (Figure 7-1) shows the existence of similar temperature-time trends for different laser powers, laser scan speeds and CB levels. Distinct heating and cooling phases can also be observed for the different welding parameters.

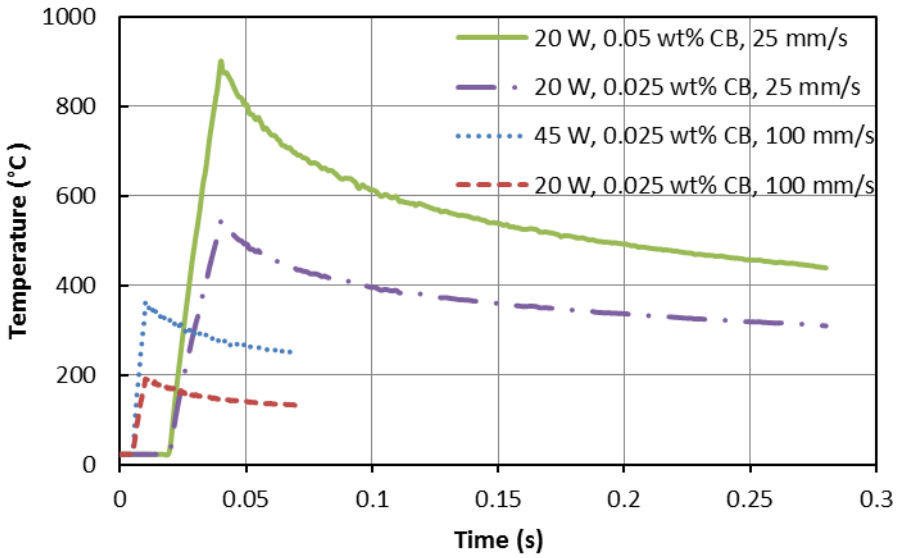

FIGURE 7-1 Temperature-time data of PC at different laser power levels, CB levels and laser scan speeds

Since the FEM temperature-time data of different welding parameters have similar trends, it suggests that different temperature-time data can perhaps be combined into a single master-curve. The approach used here will be to develop a simpler semi-empirical model based on the FEM results that can be used to predict maximum LTW temperature-time data. In this work, only PC (an amorphous polymer) is considered because of complications associated with the widening of the laser beam in semi-crystalline materials. This semi-empirical model assumes that FEM model developed in reference 6 is sufficient for the prediction of the temperature-time profile during LTW.

The approach used for the development of this model is:

- Creation of a LTW maximum temperature-time data master-curve as a function of T_{max} which is the maximum temperature experienced by a material during LTW. Accurate prediction of T_{max}, as will be elaborated in section 7-3, is a requirement of this semi-empirical model.
- Prediction of the T_{max} during LTW using an analytical model developed by Chen [6].
- Validation of the semi-empirical model by comparing predicted material conversion during LTW by the semi-empirical model and the FEM model

7.2 Creation of LTW temperature-time data master-curve

In order to combine the temperature-time data, temperature-time data obtained from the FEM is separated into heating and cooling phases. The heating phase is the region of a steady rise in temperature with time while cooling phase is the region of a steady decline in temperature.

7.2.1 Heating phase

Temperature is normalised (Γ in equation 7-1) to make it scale from 0 to 1 for different laser powers, CB levels and laser scan speeds. 0 corresponds to the initial temperature and 1 corresponds to the maximum temperature. Similarly, the heating time (τ_h in equation 7-2) is also scaled from 0 and 1. 0 and 1 correspond to the start and end of laser heating respectively.

$$\Gamma = \frac{T - T_i}{T_{max} - T_i} \quad 7\text{-}1$$

$$\tau_h = (t - t_{start}) / \left(\frac{L_B}{v}\right) \quad 7\text{-}2$$

Where T_{max} is maximum temperature, T_i is initial temperature of material, T is temperature at any given time, t is time from the FEM simulation, t_{start} is the time from the start of the FEM simulation to the start of heating, v is the laser speed and L_B is the length of the laser beam in along the z axis. The dimension of the laser beam used for the LTW is presented in Figure 7.2

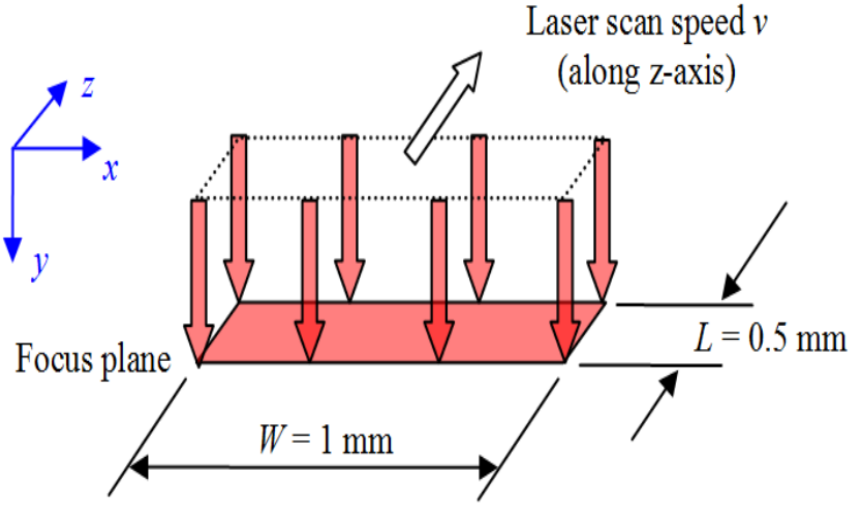

Figure 7.2 Dimension of laser beam used for the LTW [6]

Application of Equations 7-1 and 7-2 to the temperature-time data allows one to combine the FEM temperature-time data of different speeds, laser powers and CB levels (for the heating phase) into a single master-curve shown by Figure 7-3. Figure 7-3 shows that the heating phase model cannot be accurately applied to the cooling phase for different CB levels and laser scan speeds.

By definition, the normalised temperature and time for the heating phase both start from 0 and end at 1. If the heating phase plot of Figure 7-3 which spans from $\tau_h = 0$ to 1 is assumed to be a straight line, a relationship between the normalised heating time (τ_h) and the normalised temperature (Γ) can be approximated by equation 7-3 for the heating phase.

$$\Gamma = \tau_h \qquad 7\text{-}3$$

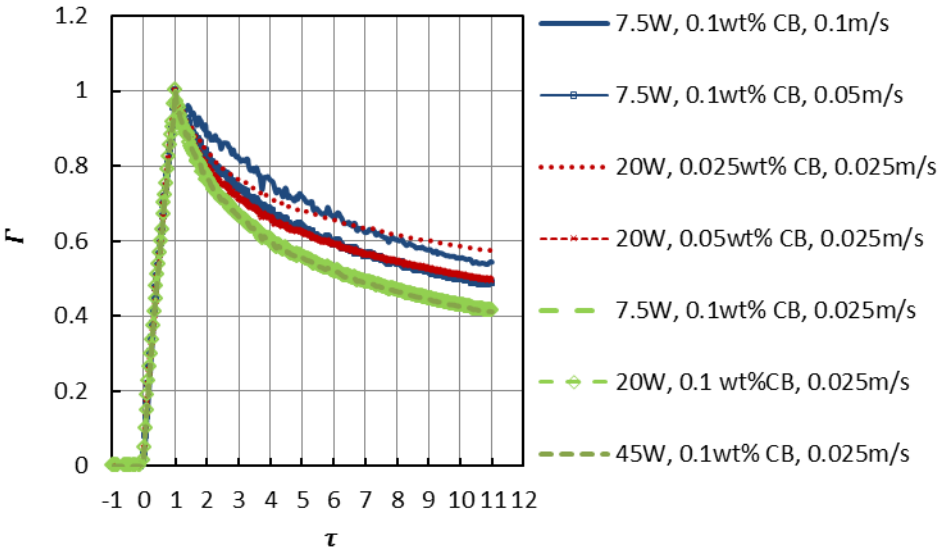

Figure 7-3 Heating phase Master-curve of the materials at different laser scan speed and CB levels

7.2.2 Cooling phase

For the cooling phase, the application of equations 7-1 and 7-2 does not yield a master curve. This suggests that there is significant influence of different laser scan speeds and CB levels on thermal gradient of the HAZ during LTW. Different laser powers would largely affect the maximum temperature. This effect is captured in the T_{max} parameter which is part of the semi-empirical model and will be discussed later in this chapter.

In order to combine the temperature data for the cooling phase, the same definition of normalized temperature (Γ in equation 7-1) is used. The FEM cooling time (t) is set to start at zero for all the laser scan speeds using the definition for the actual cooling time (t_c) given by equation 7-4.

$$t_c = t - t_{start} - \left(\frac{L_B}{v}\right) \qquad 7\text{-}4$$

Plots of $\ln(\Gamma)$ vs $\ln(t_c)$ for different CB levels and at a constant laser scan speed of 0.05m/s shows an obvious trend between the CB level and the slopes of $\ln(\Gamma)$ vs $\ln(t_c)$ as shown by Figure 7-4. These plots of $\ln(\Gamma)$ vs $\ln(t_c)$ can be approximated as a straight line for each CB level. For this scan speed, a plot of the negative slope as a function of CB level yields a curve shown in Figure 7.5. This relationship can be used to generate an equation linking $\ln(t_c)$ and $\ln(\Gamma)$ (equation 7-5) as a function of CB and for the constant scan speed of 0.05m/s.

$$t_c = \frac{ln\Gamma}{-1.65{C_{CB}}^{0.304}} \qquad 7\text{-}5$$

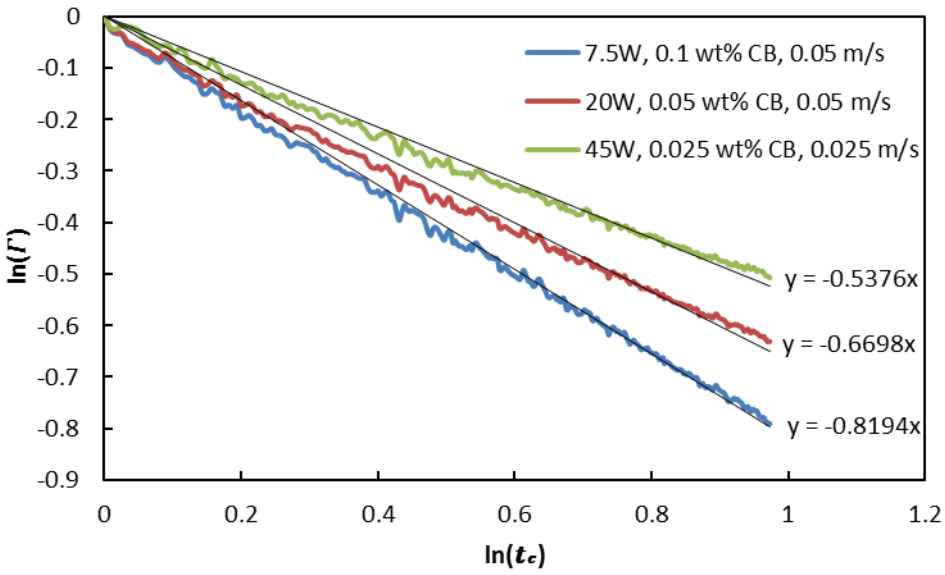

FIGURE 7-4 $\ln(\Gamma)$ vs $\ln(t_c)$ for different CB level (0.05m/s)

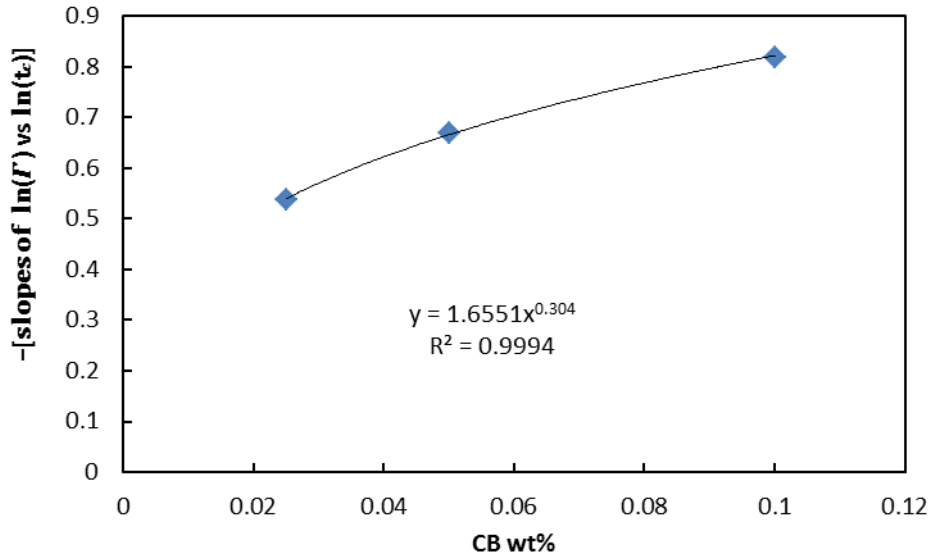

FIGURE 7-5 $-[\text{slopes of } \ln(\Gamma) \text{vs } \ln(t_c) \text{ plots}]$ vs CB wt % for different CB levesl (0.05m/s)

Figure 7-6 shows the results for plot of left and right side of equation 7-5 for a range of powers, CB levels and laser scan speeds. It is also reasonable from Figure 7.6 that equation 7.5 is also able to model the effect of CB-level on normalized temperature-time for each of the three scan speeds. However, Equation 7-5 does not capture the individual effects of scan speed.

Similar to the approach used to isolate the CB-effect, a plot of $(\ln(\Gamma)\ /-1.65{C_{CB}}^{0.304})$ vs $\ln(t_c)$ shows a trend between the speed and the slopes. Figure 7-7 shows a plot of the slopes as a function of scan speed yields a single curve. This relationship can be used to generate an equation linking $\ln(t_c)$ and $\ln(\Gamma)$ (equation 7-5) as a function of both CB and scan speed (equations 7.6 and 7-7).

$$lnt_c = \frac{ln\Gamma}{-K_1 v^{-0.322} * {C_{CB}}^{0.304}} \qquad 7\text{-}6$$

$$lnt_c = \frac{ln\Gamma}{K_2} \qquad 7\text{-}7$$

Where, C_{CB} is the carbon black level in wt%, K_1 is a material-dependent proportionality constant that, in this case, has a value of 0.62 1/(m wt %) and K_2 is a parameter that is a function of *CB,* K_1 and v. It has a unit of 1/s. Equation 7-7 can be used to reasonably collapse all cooling phase data as shown in Figure 7-8.

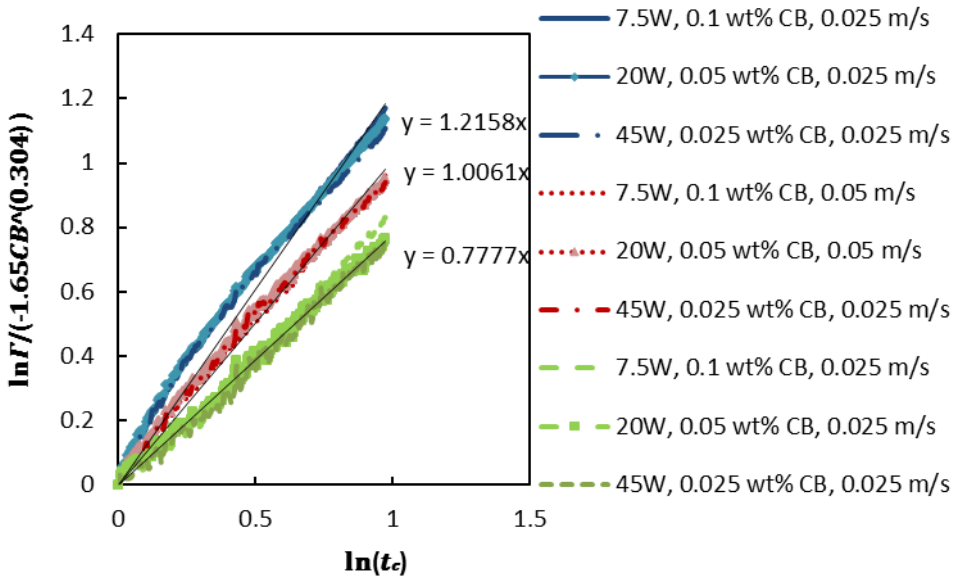

FIGURE 7-6 $\ln\Gamma/\left(-1.65{C_{CB}}^{0.304}\right)$ vs $\ln(t_c)$ for different CB levels and laser scan speeds

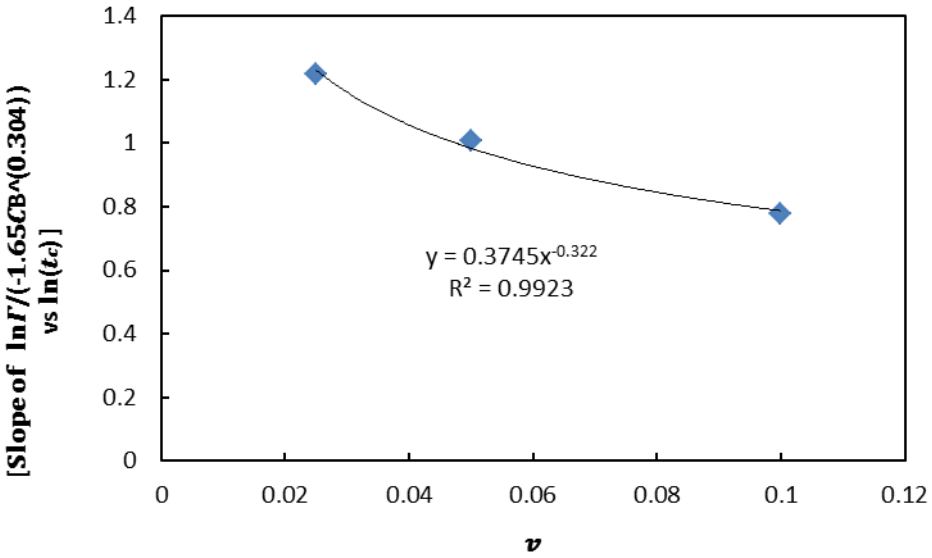

FIGURE 7-7 [Slope of $\ln\Gamma/\left(-1.65{C_{CB}}^{0.304}\right)$ vs $\ln(t_c)$ plots] vs v for different laser scan speeds (0.05 wt% CB)

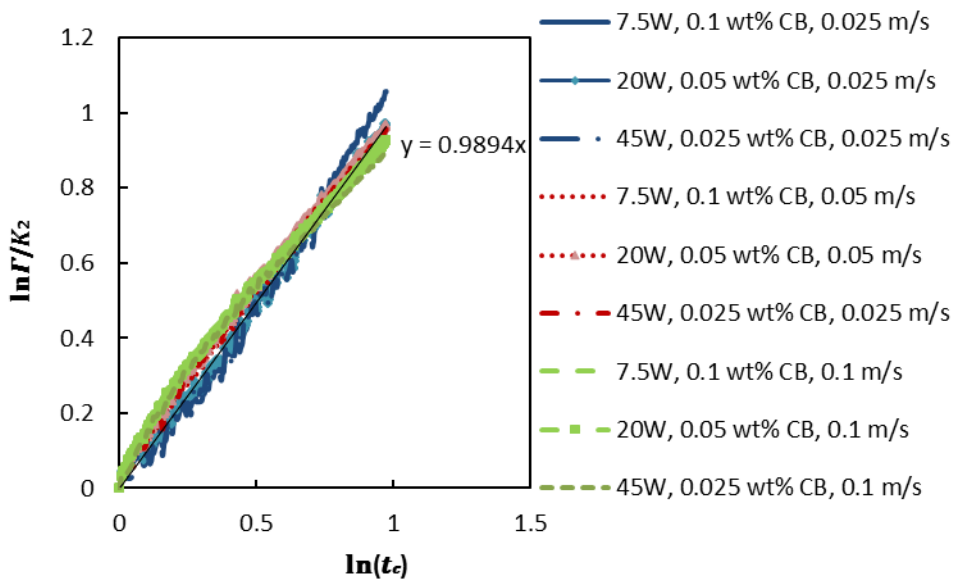

Figure 7-8 Cooling phase Master-curve of the materials at different laser scan speed and CB levels

7.3 Prediction of maximum temperature during LTW (T_{max})

It becomes obvious from equations 7-3 and 7-7 that the maximum temperature-time data for a given laser power, scan speed and CB level becomes a function of maximum LTW temperature (T_{max}). The effect of laser power is captured in the T_{max} parameter.

The maximum temperature at any given depth y in a material can be obtained from the analytical model developed by Chen [6] for amorphous polymers which is given by equation 7-6. Chen's analytical model was developed using the Beer's law with an assumption that no conductive heat loss occurs during the laser-heating period due to the small heating time scale for a fast moving laser [6]. Based on this assumption of no heat loss, Chen's analytical model maximum temperature is at the top surface of the laser-absorbent part ($y = 0$). At $y = 0$, equation 7.6 reduces to equation 7-7.

$$T_y = \frac{(1-R_s)P_L A}{C_p \rho W v} \exp(-Ay) + T_i \qquad 7\text{-}6$$

$$T_{max} = \frac{(1-R_s)P_L A}{C_p \rho W v} + T_i \qquad 7\text{-}7$$

Where, T_y is maximum temperature at a given depth y immediately after laser irradiation, R_s is the total reflectance of the input laser beam by the top and bottom surfaces of the laser-transparent part, and the top surface of the laser-absorbent part under the laser-transparent part [6]. C_p is heat capacity, ρ is density, W is the width of the laser beam in the x-direction, v is velocity, and T_i is initial temperature. The properties of PC (at 400 °C for the thermal

properties) used for the analytical model are listed in the Table 7.1. The thermal properties were estimated from temperature dependent function found in reference 6. R_s of PC is estimated from the surface reflectance of the transparent part (η_t). Surface reflectance of the laser-transparent part (η_t) is equal to surface reflectance of the laser-absorbent part (η_a) [6]. The A values for each CB level of PC are computed based on equation found on table 5.1.

The use of equation 7-7 to predict T_{max} as shown by Figures 7-9 to 7-11 results in prediction of T_{max} that is higher than that of the FEM model. This is because equation 7-7 is based on the assumption that heat loss during the LTW heating phase is negligible. As the CB level goes up, the temperature gradient goes up. Hence the heat loss by conduction (into the transparent and absorbent parts) during the heating period increases. This creates a bigger gap between analytical and FEM models as CB levels gets larger as can be observed from Figures 7-9 to 7-11.

Table 7.1 PC properties used for the analytical model

Parameter	Values for each CB level		
	0.1 wt% CB	0.05 wt% CB	0.025 wt% CB
A (1/m)	8200	4100	2050
R_s	$1-(1-\eta_t)^3=0.22$		
C_p (J/(kgk))	2246		
ρ (kg/m^3)	974		

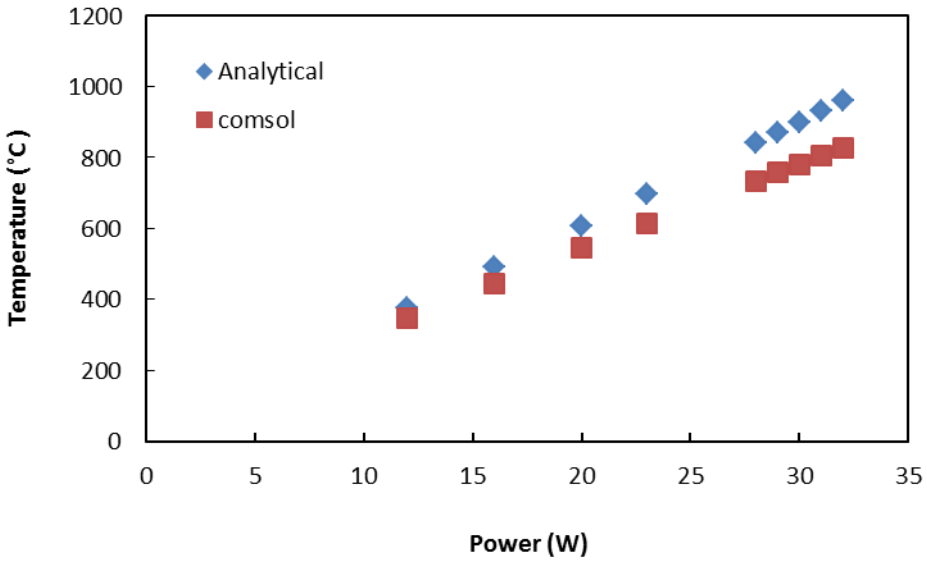

Figure 7.9 Predicted LTW maximum temperatures using FEM and analytical model (PC, 0.025wt%CB, 0.025m/s, FEM contact geometry, at $y = 0$ for analytical model)

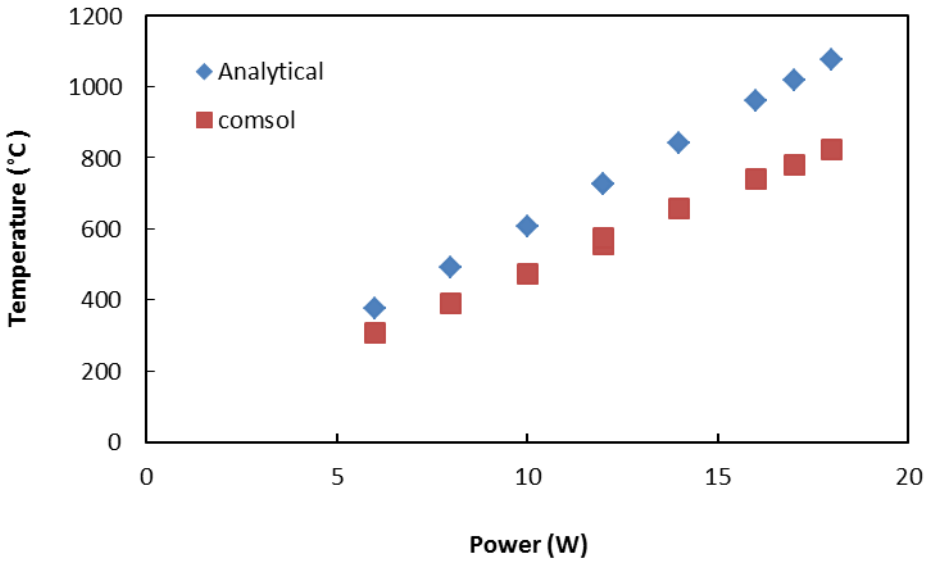

Figure 7.10 Predicted LTW maximum temperatures using FEM and analytical model (PC, 0.05wt%CB, 0.025m/s, FEM contact geometry, at $y = 0$ for analytical model)

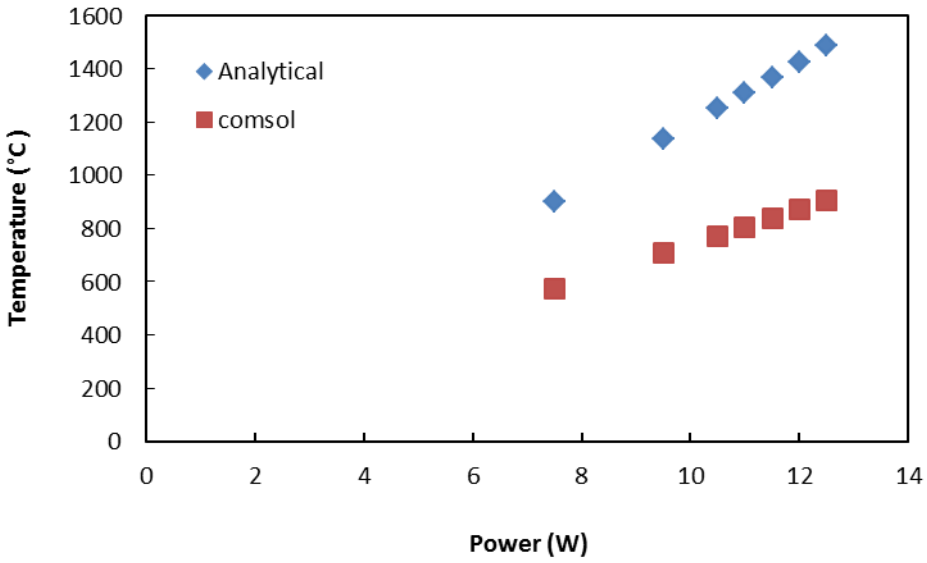

Figure 7.11 Predicted LTW maximum temperatures using FEM and analytical model (PC, 0.1wt%CB, 0.025m/s, FEM contact geometry, at $y = 0$ for analytical model)

The T_{max} of the analytical model occurs at $y = 0$ [6]. Based on the FEM simulation, this is not happening because during the period of heating, some heat is continually lost by conduction from the region where the laser energy was absorbed. This shifts the position of maximum temperature to a certain depth below the weld interface along the y-axis. Assuming most of the heat lost during the heating period comes from the hottest region very close to the interface ($y = 0$) and that the heat is lost into the transparent part (due to the highest thermal gradient), it is not unreasonable to assume that the temperature further inside the absorbent part would be relatively unaffected by this heat loss and that its temperature could be reasonably estimated by the analytical model. Therefore one could use the maximum temperature estimated by the FEM model (called $T_{max'}$) to estimate its location (y') with the analytical model. By rearranging equation 7-6 to obtain equation 7-8 and plotting the left side

of the equation 7-8 against $-A$ (while forcing the intercept to be zero in order to conform to equation 7-8) for different CB levels, average y' value for different CB levels can be estimated from the slope of the plot shown in Figure 7-12.

$$\ln\left[\frac{(T_{max'}-T_i)C_p\rho Wv}{(1-R_s)AP_L}\right] = y'(-A) \qquad 7\text{-}8$$

This method assumes that the value of y' does not vary strongly with CB level and laser scan speed. Based on the y' values from the FEM simulation for PC at different CB levels and laser scan speeds presented in Table 7.2, this assumption appears reasonable. Table 7.2 shows a slight variation in the FEM y' values (for different CB levels and laser scan speeds) due to differences in their thermal gradient. It can also be seen from Table 7.2 and Figure 7-12 that the y' values from the FEM and Figure 7.12 are comparable.

Table 7.2 Approximte y' values obtained from the FEM for different CB levels and laser scan speeds

CB wt%	y' value (m) for different laser scan speeds		
	0.025 m/s	0.05 m/s	0.1m/s
0.025	0.000060	0.000055	0.000055
0.05	0.000055	0.000054	0.000054
0.1	0.000055	0.000026	0.000026

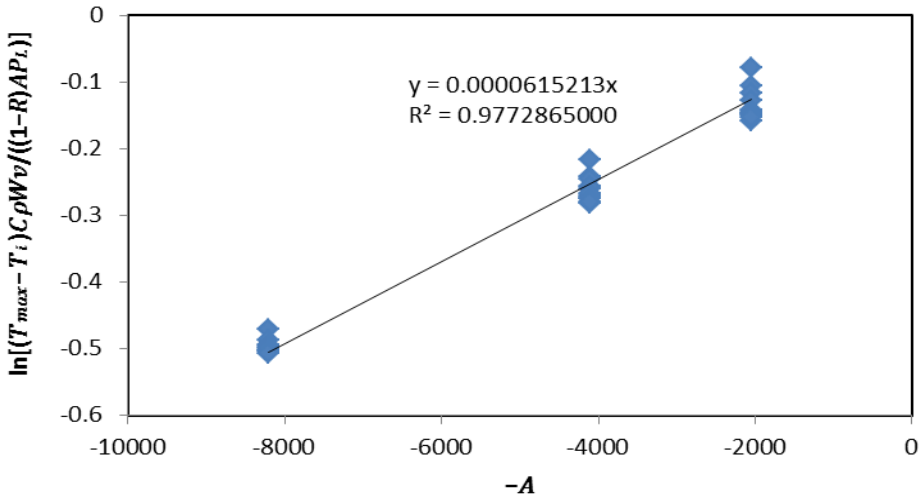

Figure 7.12 Plot of left side of the equation 7.8 (for different laser power, CB levels and their corresponding T_{max}) vs $-A$ (of 0.025, 0.05 and 0.1 wt %CB) (0.025m/s)

The obtained value of y' is then substituted for y in equation 7-6 to form equation 7-9 in order to approximate T_{max}. Figures 7-13 to 7-16 show good agreement between the $T_{max'}$ predicted by the FEM and T_{max} predicted by equation 7-9.

$$T_{max} = \frac{(1-R_s)P_L A}{C_p \rho W v}\exp(-Ay') + T_i \qquad 7\text{-}9$$

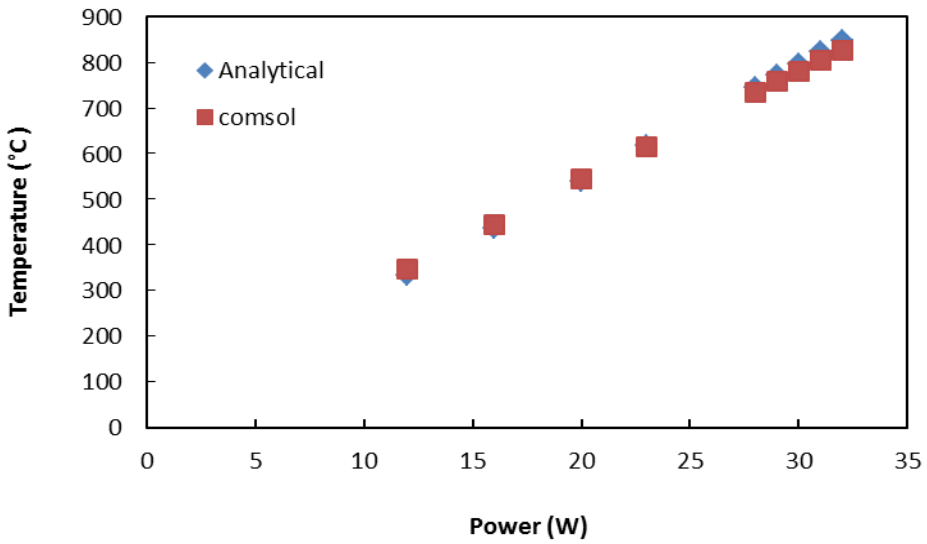

Figure 7.13 Predicted LTW maximum temperatures using FEM and analytical model (PC, 0.025wt%CB, 0.025m/s, at $y = y'$ for analytical model)

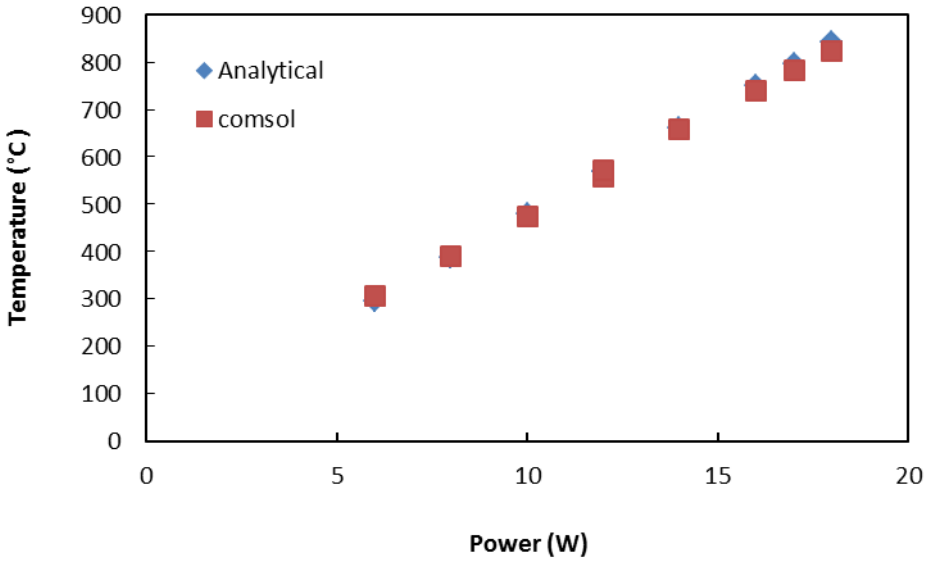

Figure 7.14 Predicted LTW maximum temperatures using FEM and analytical model (PC, 0.05wt%CB, 0.025m/s, at $y = y'$ for analytical model)

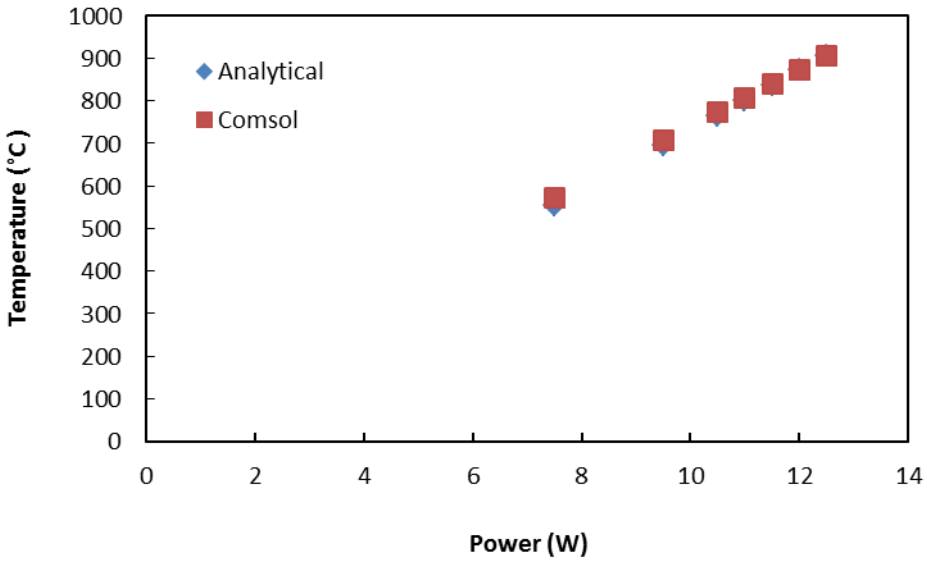

Figure 7.15 Predicted LTW maximum temperatures using FEM and analytical model (PC, 0.1wt%CB, 0.025m/s, at $y = y'$ for analytical model)

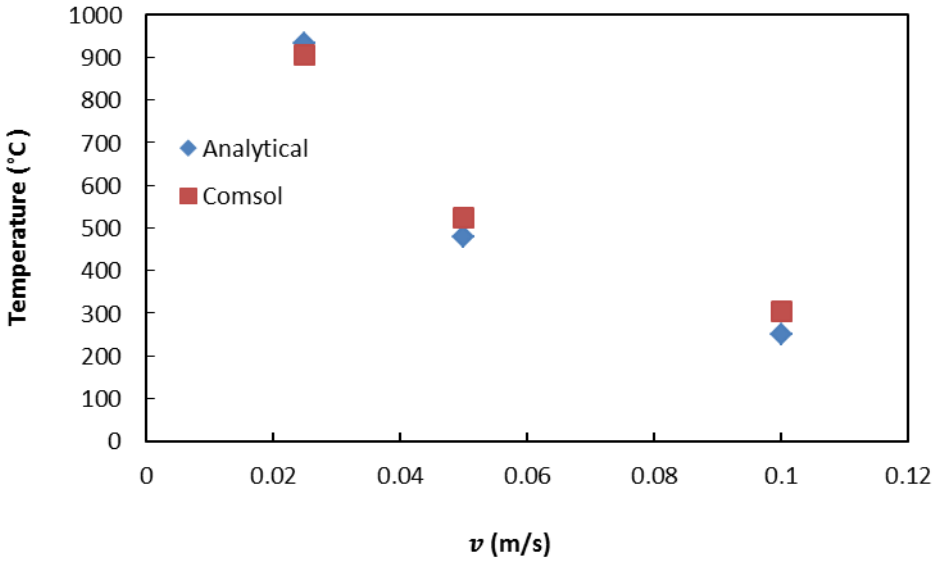

Figure 7.16 Predicted LTW maximum temperatures using FEM and analytical model (PC, 0.05 wt%CB, 20 W, at $y = y'$ for analytical model)

7.4 Validation of the semi-empirical model

The developed semi-empirical model is validated by comparing the maximum temperature-time profile obtained by the semi-empirical model with maximum temperature-time profile obtained by the FEM model. Comparison is also made between maximum conversion predicted using maximum temperature-time profile obtained by the FEM and semi-empirical model.

By substituting an expression for Γ from equations 7.1 into equations 7.3 and 7.7, the following equations can be obtained:

$$T_h = (T_{max} - T_i)\tau_h + T_i \quad \text{7-10}$$

$$T_c = (T_{max} - T_i)exp(K_2 lnt_c) + T_i \quad \text{7-11}$$

Where, T_h is temperature for heating phase and T_c is temperature for cooling phase Equations 7-10 and 7-11 are the equations developed in this work for predicting temperature as function of time during LTW using the semi-empirical models.

Figure 7-17 shows the maximum temperature-time profiles obtained using FEM and semi-empirical models for different laser powers, CB levels and a laser scan speed of 0.025m/s. Figure 7-18 show maximum temperature-time profiles obtained using FEM and semi-empirical models for different laser powers, laser scan speeds and CB level of 0.05wt%. It can be seen from these two figures that that there is good agreement between the maximum temperature-time profiles obtained using the semi-empirical model and FEM model.

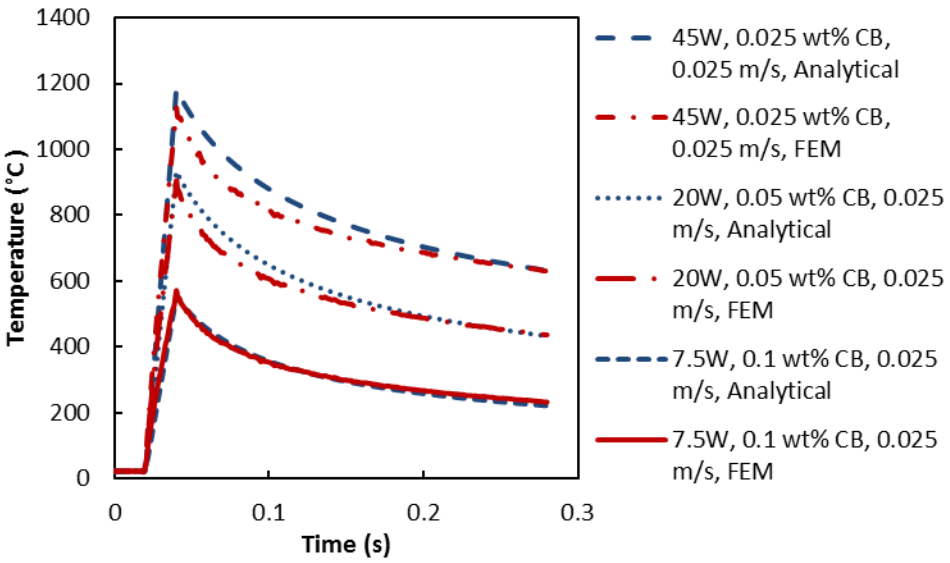

Figure 7-17 Predicted LTW maximum temperature-time profile using FEM and semi-empirical model (PC, 0.025m/s, Different CB levels)

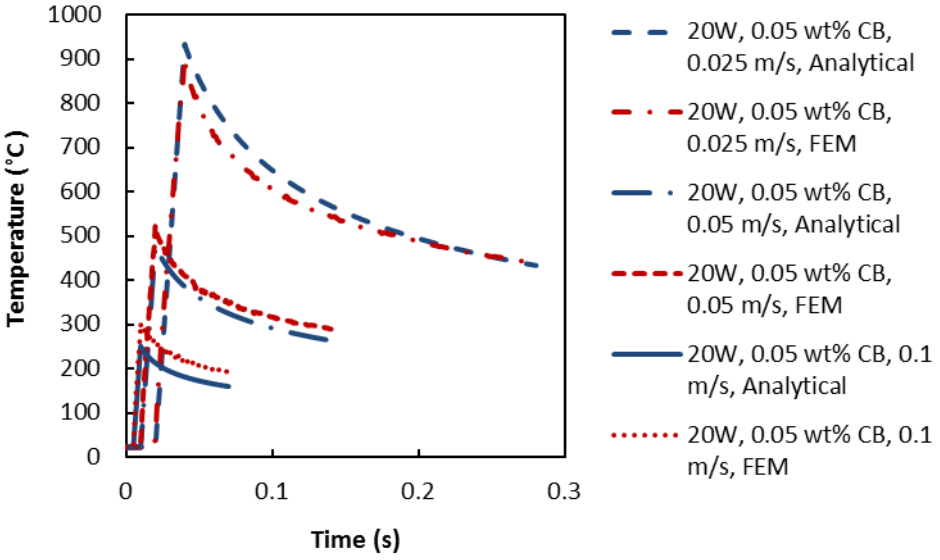

Figure 7.18 Predicted LTW maximum temperature-time profile using FEM and semi-empirical model (PC, 0.05 wt% CB, different laser scan speeds)

Figures 7-19 to 7-21 show the maximum material conversion obtained using FEM and the semi-empirical temperature-time profile for PC with different CB levels. It can be seen from Figures 7-19 to 7-21 that there is good agreement between the maximum material conversion obtained using maximum temperature-time data from FEM and the semi-empirical model

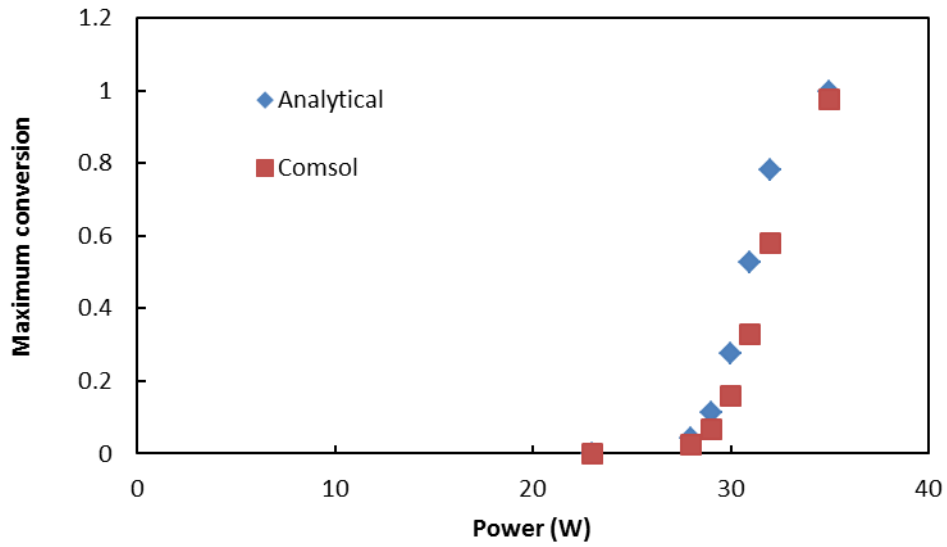

Figure 7-19 FEM and Analytical model obtained material conversion vs laser power for PC with 0.025wt% CB (0.025m/s)

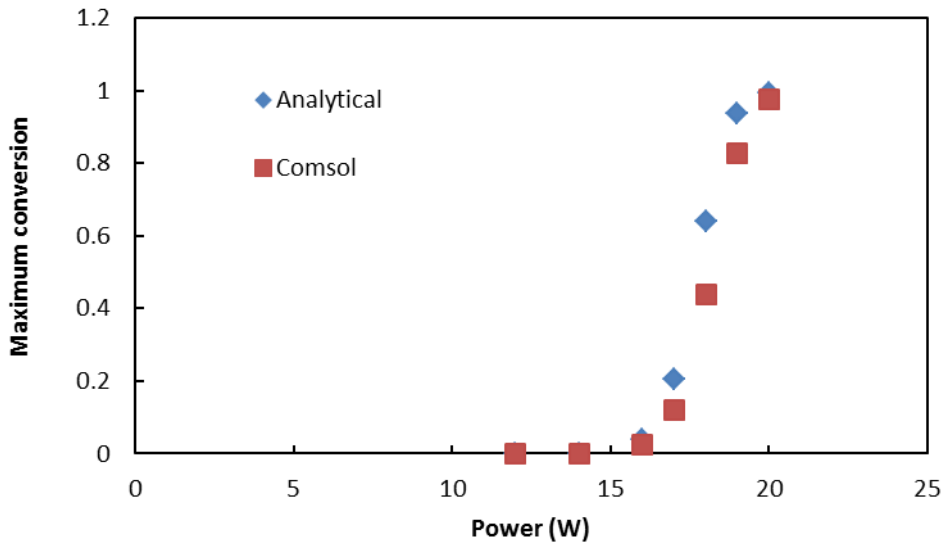

Figure 7-20 FEM and Analytical model obtained material conversion vs laser power for PC with 0.05wt% CB (0.025m/s)

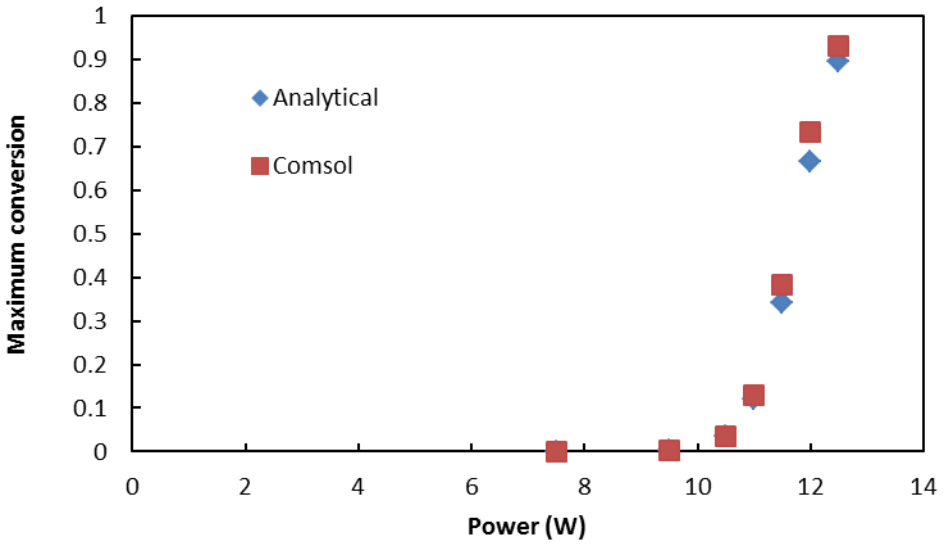

Figure 7-21 FEM and Analytical model obtained material conversion vs laser power for PC with 0.1wt% CB (0.025m/s).

Chapter 8
Conclusions and Recommendations

8.1 Conducted work

PC and PA6 were studied in this work. TGA was used to assess the experimental degradation kinetics of the two polymers as a function the CB content. Friedmann, KAS and OFW methods were used to determine the conversion-dependent activation energy (E_α). The kinetic parameters of the materials were then determined using non-linear model-fitting. The kinetic parameters and the temperature-time profile were inserted into a chemical kinetic rate equation to predict thermal degradation of the materials during LTW. A semi-empirical model based on Chen's FEM model was developed to provide a simpler alternative to FEM for estimation of maximum temperature-time data during LTW.

8.2 Conclusions

a. TGA experiments of PA6 showed that increasing the CB content from 0.05 to 0.2wt% had no significant influence on the thermal degradation kinetics.

b. On the other hand the TGA experiments on PC showed that increased CB content in the range 0.05 to 0.2wt% improved the thermal degradation resistance.

c. Analysis of the kinetic degradation data shows that an *SB* model can be used to model the degradation kinetics of PC and an *Fn* model is suitable for PA6.

d. The frequency factors, activation energies and reaction orders are summarized in Table 8.1

Table 8-1 Obtained kinetic parameters

MATERIAL	PC (0.05)	PC (0.2)	PA6
Log k_0 (min^{-1})	14.8	16.7	12.6
E (KJ/mol)	225	253	177
n	1.3	1.5	0.8
m	0.3	0.6	
$f(\alpha)$	*SB*		*Fn*

e. There is a good agreement between the experimentally observed degradation of the laser absorbing specimen and that predicted for 1% material conversion of PC and PA6 in a non-contact geometry. This suggests that kinetic triplets from TGA experiments and temperature-time data from FEM inserted into kinetic equation analysis can be used to predict material thermal degradation during LTW.

f. Greater differences between experimental observations and simulation results were observed in the contact geometry. This is attributed to molecular weight degradation that is not captured in the simulation.

g. The modelling of thermal degradation using TGA combined with temperature-time data from FEM or other sources can be used to estimate major degradation during LTW.

Therefore, it can be used by those modeling LTW to estimate an upper bound on the power and speed conditions.

h. A semi-empirical technique was developed to estimate temperature-time data without using FEM simulation. The agreement between the semi-empirical and FEM temperature estimations was acceptable.

i. Temperature profile obtained using the semi-empirical model can be used as an alternative to that of FEM for prediction of maximum conversion during LTW.

8.4 Recommendations

The following are recommended for future research:

- Further research is recommended to be carried on the influence of carbon black on the thermal stability of the studied materials (PC and PA6) by examination of their natural polymers (which contain no carbon black).
- Methods that are able to measure molecular weight thermal degradation (without mass loss) like DSC and transient flow experiments should be used to study the decline in weld strength of LTW in order to better understand thermal degradation during LTW.
- The degradation products from the weld interface should be analysed with methods like Fourier transform infrared spectroscopy (FTIR) in order to ascertain the possibility of occurrence of thermal-oxidative degradation.

References

[1] Troughton, M. J. (2008). Handbook of plastics joining: A practical guide.

[2] Balkan, O., Demirer, H., Ezdeşir, A., & Yıldırım, H. (2008). Effects of welding procedures on mechanical and morphological properties of hot gas butt welded PE, PP, and PVC sheets. *Polymer Engineering & Science, 48*(4), 732-746.

[3] Chen, M., Zak, G., Bates, P. J., Baylis, B., & McLeod, M. (2011). Experimental study on gap bridging in contour laser transmission welding of polycarbonate and polyamide. *Polymer Engineering & Science, 51*(8), 1626-1635.

[4] Staff, P. (1997). Handbook of plastics joining.

[5] Mayboudi, L., Birk, A., Zak, G., & Bates, P. (2007). A 3-D thermal model of laser transmission contour welding for a lap joint. *Antec-Conference Proceedings, 5* 2796

[6] Chen, M. (2009). Gap bridging in laser transmission welding of thermoplastics. Queen's University Kingston, Department of Mechanical Engineering.

[7] Hartley, S., & Sallavanti, R. A. (2003). Clearweld laser transmission welding of thermoplastic polymers: Light transmission and color considerations. *LAMP 2002: International Congress on Laser Advanced Materials Processing,* 63-68.

[8] Marczis, B., & Czigany, T. (2006). Interrelationships between welding parameters of hot-gas welded polypropylene. *Polymer Engineering & Science, 46*(9), 1173-1181.

[9] Haberstroh, E., & Hoffmann, W. (2008). Laser transmission welding of complex micro plastic parts. *Proceedings of the Institution of Mechanical Engineers, Part B: Journal of Engineering Manufacture, 222*(1), 47-54.

[10] Bates, P., Druart, M., Chen, M., Zak, G., & Billiet, J. (2007). Influence of part thickness, glass fibre content and line energy on laser transmission welding of polyamide mXD6. *Antec-Conference Proceedings, 5* 2766.

[11] Taha, Z., Roy, G., Hajim, K., & Manna, I. (2009). Mathematical modeling of laser-assisted transmission lap welding of polymers. *Scripta Materialia, 60*(8), 663-666.

[12] Chen, M., Zak, G., & Bates, P. J. (2011). Effect of carbon black on light transmission in laser welding of thermoplastics. *Journal of Materials Processing Technology, 211*(1), 43-47.

[13] KHOSRAVI, S. (2010). Laser transmission welding of polybutylene terephthalate and polyethylene terephthalate blends. Queen's University Kingston, Department of Chemical Engineering.

[14] P. J. Bates, G. Zak, M. Chen. Contour laser transmission welding. (2013). How fast is fast enough. *Antec-Conference Proceedings*

[15] Chen, M., Zak, G., & Bates, P. (2008). Estimating contour laser transmission welding start-up conditions using a novel non-contact method. *Welding in the World, 52*(11-12), 71-76.

[16] Hilton, P. A., Jones, I., & Kennish, Y. (2003). Transmission laser welding of plastics. *LAMP 2002: International Congress on Laser Advanced Materials Processing,* 44-52.

[17] Kagan, V., & Pinho, G. (2004). Laser transmission welding of semicrystalline thermoplastics-part II: Analysis of mechanical performance of welded nylon. *Journal of Reinforced Plastics and Composites, 23*(1), 95-107.

[18] Potente, H., Korte, J., & Becker, F. (1999). Laser transmission welding of thermoplastics: Analysis of the heating phase. *Ronald M.Harris, Editor,* , 283.

[19]. Acherjee, B., Kuar, A. S., Mitra, S., & Misra, D. (2012). Modeling of laser transmission contour welding process using FEA and DoE. *Optics & Laser Technology, 44*(5), 1281-1289.

[20] Chen, M., Zak, G., Bates, P., McLeod, M., & Rouison, D. (2007). Surface damage threshold in laser transmission welding of polycarbonate. *Antec-Conference Proceedings-, , 5* 2781.

[21] Vyazovkin, S., Burnham, A. K., Criado, J. M., Pérez-Maqueda, L. A., Popescu, C., & Sbirrazzuoli, N. (2011). ICTAC kinetics committee recommendations for performing kinetic computations on thermal analysis data. *Thermochimica Acta, 520*(1), 1-19

[22] Capone, C., Di Landro, L., Inzoli, F., Penco, M., & Sartore, L. (2007). Thermal and mechanical degradation during polymer extrusion processing. *Polymer Engineering & Science, 47*(11), 1813-1819.

[23] Feldman, D. (2002). Polymer weathering: Photo-oxidation. *Journal of Polymers and the Environment, 10*(4), 163-173

[24] Booth, C. (1963). The mechanical degradation of polymers. *Polymer, 4*, 471-478.

[25] Moiseev, Y. V., Markin, V., & Zaikov, G. E. (1976). Chemical degradation of polymers in corrosive liquid media. *Russian Chemical Reviews, 45*(3), 246.

[26] Xiaodong, Z., Qunfang, L., Gance, D., & Faxiang, J. (1998). Ultrasonic degradation of polysilane polymers. *Polymer Degradation and Stability, 60*(2), 409-413.

[27] Chandra, R., & Rustgi, R. (1998). Biodegradable polymers. *Progress in Polymer Science, 23*(7), 1273-1335.

[28] Partini, M., Argenio, O., Coccorullo, I., & Pantani, R. (2009). Degradation kinetics and rheology of biodegradable polymers. *Journal of Thermal Analysis and Calorimetry, 98*(3), 645-653.

[29] Holland, B. J., & Hay, J. N. (2000). Thermal degradation of nylon polymers. *Polymer International, 49*(9), 943-948.

[30] Beyler, C. L., & Hirschler, M. M. (2002). Thermal decomposition of polymers. *SFPE Handbook of Fire Protection Engineering, 2*.

[31] Pashaei, S., Avval, M. M., & Syed, A. A. (2011). Thermal degradation kinetics of nylon6/GF/crysnano nanoclay nanocomposites by TGA. *Chemical Industry and Chemical Engineering Quarterly/CICEQ, 17*(2), 141-151.

[32] Dong, Q., Gao, C., Ding, Y., Wang, F., Wen, B., Zhang, S., Yang, M. (2012). A polycarbonate/magnesium oxide nanocomposite with high flame retardancy. *Journal of Applied Polymer Science, 123*(2), 1085-1093.

[33] Papageorgiou, D. G., Bikiaris, D. N., & Chrissafis, K. (2012). Effect of crystalline structure of polypropylene random copolymers on mechanical properties and thermal degradation kinetics. *Thermochimica Acta, 543*, 288-294.

[34] Daly, P. A., Bruce, D. A., Melik, D. H., & Harrison, G. M. (2005). Thermal degradation kinetics of poly (3-hydroxybutyrate-co-3-hydroxyhexanoate). *Journal of Applied Polymer Science, 98*(1), 66-74.

[35] Polli, H., Pontes, L., & Araujo, A. (2005). Application of model-free kinetics to the study of thermal degradation of polycarbonate. *Journal of Thermal Analysis and Calorimetry, 79*(2), 383-387.

[36] Sánchez-Jiménez, P. E., Pérez-Maqueda, L. A., Perejón, A., & Criado, J. M. (2011). Constant rate thermal analysis for thermal stability studies of polymers. *Polymer Degradation and Stability, 96*(5), 974-981.

[37] Al-Mulla, A., Mathew, J., Al-Omairi, L., & Bhattacharya, S. (2011). Thermal decomposition kinetics of tricomponent polyester/polycarbonate systems. *Polymer Engineering & Science, 51*(11), 2335-2344.

[38] Sengupta, R., Sabharwal, S., Bhowmick, A. K., & Chaki, T. K. (2006). Thermogravimetric studies on polyamide-6, 6 modified by electron beam irradiation and by nanofillers. *Polymer Degradation and Stability, 91*(6), 1311-1318.

[39] Zong, R., Hu, Y., Liu, N., Li, S., & Liao, G. (2007). Investigation of thermal degradation and flammability of polyamide-6 and polyamide-6 nanocomposites. *Journal of Applied Polymer Science, 104*(4), 2297-2303.

[40] Saha, B., & Ghoshal, A. K. (2006). Model-fitting methods for evaluation of the kinetics triplet during thermal decomposition of poly (ethylene terephthalate)(PET) soft drink bottles. *Industrial & Engineering Chemistry Research, 45*(23), 7752-7759.

[41] Chrissafis, K., Paraskevopoulos, K., Stavrev, S., Docoslis, A., Vassiliou, A., & Bikiaris, D. (2007). Characterization and thermal degradation mechanism of isotactic polypropylene/carbon black nanocomposites. *Thermochimica Acta, 465*(1), 6-17.

[42] Chrissafis, K. (2009). Kinetics of thermal degradation of polymers. *Journal of Thermal Analysis and Calorimetry, 95*(1), 273-283.

[43] Yao, F., Wu, Q., & Zhou, D. (2009). Thermal decomposition of natural fibers: Global kinetic modeling with nonisothermal thermogravimetric analysis. *Journal of Applied Polymer Science, 114*(2), 834-842.

[44] Málek, J., Mitsuhashi, T., & Criado, J. M. (2001). Kinetic analysis of solid-state processes. *Journal of Materials Research, 16*(6), 1862-1871.

[45] Perez-Maqueda, L., Criado, J., & Sanchez-Jimenez, P. (2006). Combined kinetic analysis of solid-state reactions: A powerful tool for the simultaneous determination of kinetic parameters and the kinetic model without previous assumptions on the reaction mechanism. *The Journal of Physical Chemistry A, 110*(45), 12456-12462.

[46] Onbattuvelli, V. P., Rochefort, W. E., Simonsen, J., Park, S., German, R. M., & Atre, S. V. (2010). Studies on the thermal stability and degradation kinetics of Pd/PC nanocomposites. *Journal of Applied Polymer Science, 118*(6), 3602-3611.

[47] Vyazovkin, S. (2000). Computational aspects of kinetic analysis.: Part C. the ICTAC kinetics Project—the light at the end of the tunnel? *Thermochimica Acta, 355*(1), 155-163.

[48] Vyazovkin, S. (2006). Model-free kinetics. *Journal of Thermal Analysis and Calorimetry, 83*(1), 45-51.

[49] Sánchez-Jiménez, P. E., Pérez-Maqueda, L. A., Perejón, A., & Criado, J. M. (2010). A new model for the kinetic analysis of thermal degradation of polymers driven by random scission. *Polymer Degradation and Stability, 95*(5), 733-739.

[50] Reading, M. (1988). The kinetics of heterogeneous solid state decomposition reactions: A new way forward? *Thermochimica Acta, 135*, 37-57.

[51] Reich, L., Stivala, S. (1970). Heat transfer effects during teflon degradation by TGA. *Thermochimica Acta, 1*(1), 65-70.

[52] Málek, J. (1992). The kinetic analysis of non-isothermal data. *Thermochimica Acta, 200*, 257-269.

[53] Brill, T., Gongwer, P., & Williams, G. (1994). Thermal decomposition of energetic materials. 66. kinetic compensation effects in HMX, RDX, and NTO. *The Journal of Physical Chemistry, 98*(47), 12242-12247.

[54] Agrawal, R., & Sivasubramanian, M. (1987). Integral approximations for nonisothermal kinetics. *AIChE Journal, 33*(7), 1212-1214.

[55] Wang, M., Li, B., Wang, J., & Bai, P. (2011). Preparation and properties of polysiloxane grafting multi-walled carbon nanotubes/polycarbonate nanocomposites. *Polymers for Advanced Technologies, 22*(12), 1738-1746.

[56] Wu, T., Chen, E., Lin, Y., Chiang, M., & Chang, G. (2008). Preparation and characterization of melt-processed polycarbonate/multiwalled carbon nanotube composites. *Polymer Engineering & Science, 48*(7), 1369-1375.

[57] Li, J., Tong, L., Fang, Z., Gu, A., & Xu, Z. (2006). Thermal degradation behavior of multi-walled carbon nanotubes/polyamide 6 composites. *Polymer Degradation and Stability, 91*(9), 2046-2052.

[58] Lee, J., Liao, Y., Nagahata, R., & Horiuchi, S. (2006). Effect of metal nanoparticles on thermal stabilization of polymer/metal nanocomposites prepared by a one-step dry process. *Polymer, 47*(23), 7970-7979.

[59] Zak, G., Mayboudi, L., Chen, M., Bates, P., & Birk, M. (2010). Weld line transverse energy density distribution measurement in laser transmission welding of thermoplastics. *Journal of Materials Processing Technology, 210*(1), 24-31.

[60] Geiger, M., Frick, T., & Schmidt, M. (2009). Optical properties of plastics and their role for the modelling of the laser transmission welding process. *Production Engineering, 3*(1), 49-55.

[61] Azhikannickal, E., Bates, P. J., & Zak, G. (2012). Use of thermal imaging to characterize laser light reflection from thermoplastics as a function of thickness, laser incidence angle and surface roughness. *Optics & Laser Technology, 44*(5), 1491-1496.

[62] Azhikannickal, E., Bates, P. J., & Zak, G. (2012). Thermal imaging technique to characterize laser light reflection from thermoplastics. *Optics & Laser Technology, 44*(5), 1456-1462.

[63] Rhew, M., Mokhtarzadeh, A., & Benatar, A. (2003). Diode laser characterization and measurement of optical properties of polycarbonate and high-density polyethylene. *ANTEC 2003 Conference Proceedings,* 1056-1060.

[64] Wang, C., Bates, P., & Zak, G. (2009). Optical properties characterization of thermoplastics used in laser transmission welding: Transmittance and reflectance. *ANTEC2009, Society of Plastics Engineers,* 1278-1282.

[65] Zak, G., Wang, C., & Bates, P. (2010). Optical properties characterization of thermoplastics used in laser transmission welding: Scattering and absorbance. *Advanced Materials Research, 97*, 3836-3841.

[66] Kagan, V., Bray, R., & Kuhn, W. (2002). Laser transmission welding of semi-crystalline thermoplastics—Part I: Optical characterization of nylon based plastics. *Journal of Reinforced Plastics and Composites, 21*(12), 1101-1122.

[67] Sari, F., Hoffmann, W., Haberstroh, E., & Poprawe, R. (2008). Applications of laser transmission processes for the joining of plastics, silicon and glass micro parts. *Microsystem Technologies, 14*(12), 1879-1886.

[68] Al-Wohoush, M., Sanchez Garcia, S., & Kamal, M. (2007). Microstructure of thermoplastic laser welded joints. *Antec-Conference Proceedings, 5* 2786.

[69] Coelho, J. M., Abreu, M. A., & Carvalho Rodrigues, F. (2004). Methodologies for determining thermoplastic films optical parameters at 10.6 μm laser wavelength. *Polymer Testing, 23*(3), 307-312.

[70] Wang, X., Zhang, C., Wang, K., Li, P., Hu, Y., & Liu, H. (2012). Multi-objective optimization of laser transmission joining of thermoplastics. *Optics & Laser Technology, 44*(8), 2393-2402.

[71] Hadriche, I., Ghorbel, E., Masmoudi, N., & Casalino, G. (2010). Investigation on the effects of laser power and scanning speed on polypropylene diode transmission welds. *The International Journal of Advanced Manufacturing Technology, 50*(1-4), 217-226.

[72] Mayboudi, L., Birk, A., Zak, G., & Bates, P. (2009). A three-dimensional thermal finite element model of laser transmission welding for lap-joint. *International Journal of Modeling and Simulation, 29*(2)

[73] Acherjee, B., Kuar, A. S., Mitra, S., & Misra, D. (2012). Modeling and analysis of simultaneous laser transmission welding of polycarbonates using an FEM and RSM combined approach. *Optics & Laser Technology, 44*(3), 995–1006.

[74] Jaeschke, P., Herzog, D., Haferkamp, H., Peters, C., & Herrmann, A. S. (2010). Laser transmission welding of high-performance polymers and reinforced composites-a fundamental study. *Journal of Reinforced Plastics and Composites, 29*(20), 3083-3094.

[75] http://www.plasticsgroup.com/pdfs/guides/Processing_Guide_Nylon.pdf

[76]http://plastics.bayer.com/. Makrolon® 2605, 2607, 2805 and 2807

Appendix A

TGA is used in this work to study the effect of changing the CB levels of PC and PA6 from 0.05wt% to 0.2wt% on the thermal stability of the materials. These studies and their reproducibility were presented earlier in chapter 3 of this work. The remaining TGA plots used in these studies not found in the chapter 3 are presented in this appendix.

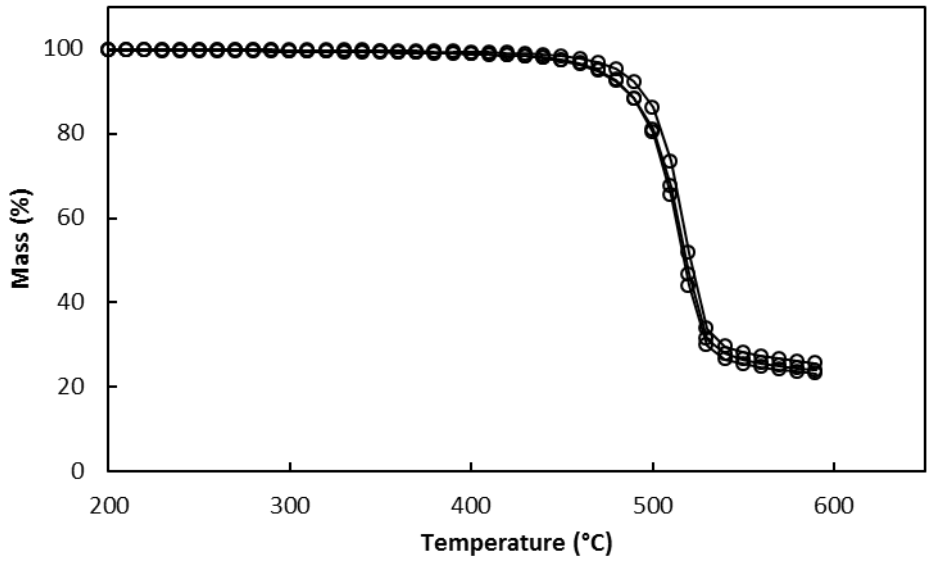

Figure A-1 Experiment 1, 2 and 3 TG curves of PC with 0.05wt%CB at heating rates of 10°C/min

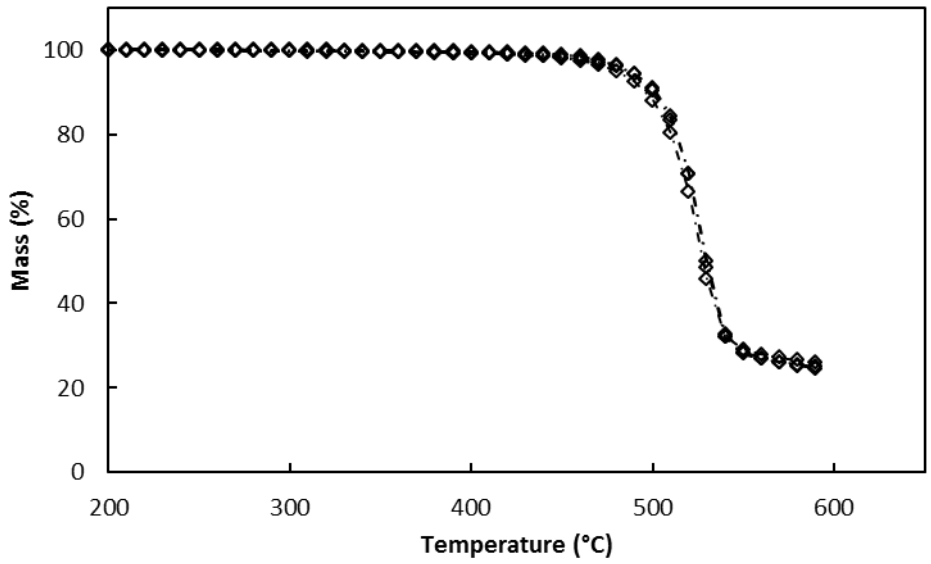

Figure A-2 Experiment 1, 2 and 3 TG curves of PC with 0.05wt%CB at heating rates of 15°C/min

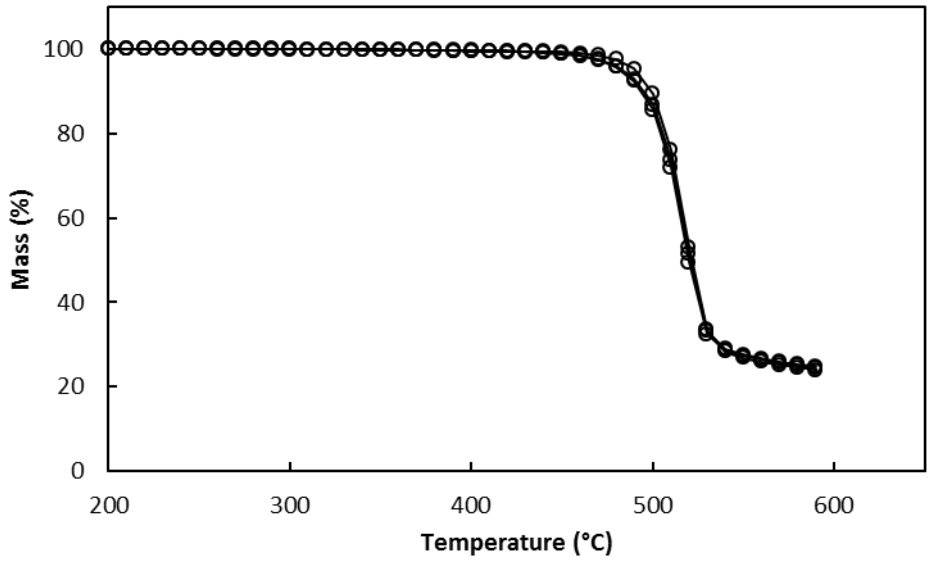

Figure A-3 Experiment 1, 2 and 3 TG curves of PC with 0.2wt%CB at heating rates of 10°C/min

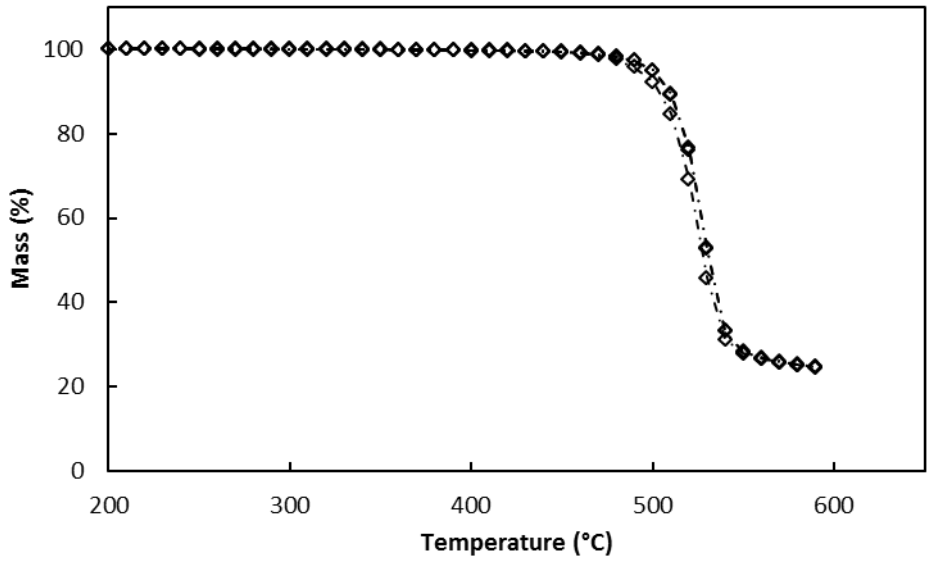

Figure A-4 Experiment 1, 2 and 3 TG curves of PC with 0.2wt%CB at heating rates of 15°C/min

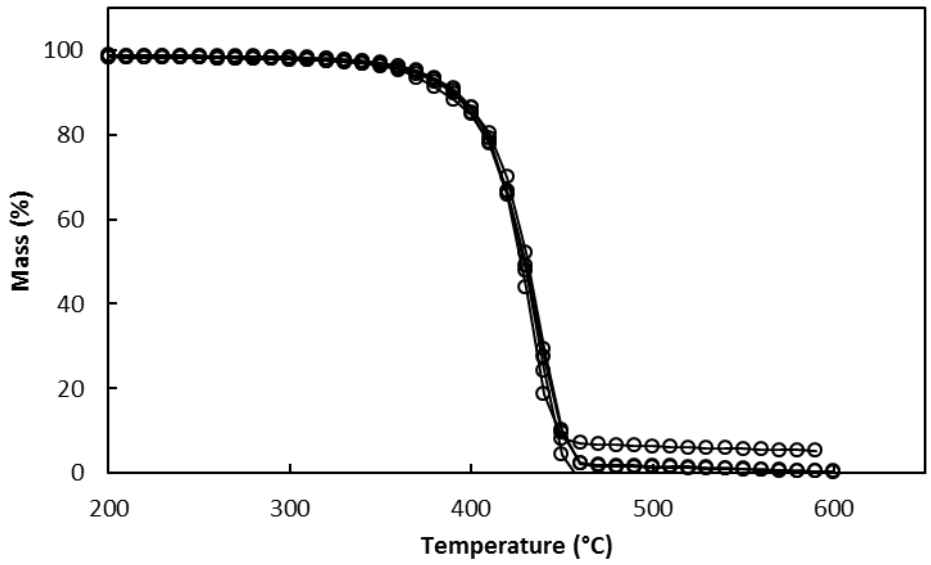

Figure A-5 Experiment 1 and 2 TG curves of PA6 with 0.05 and 0.2wt%CB at heating rates of 10°C/min

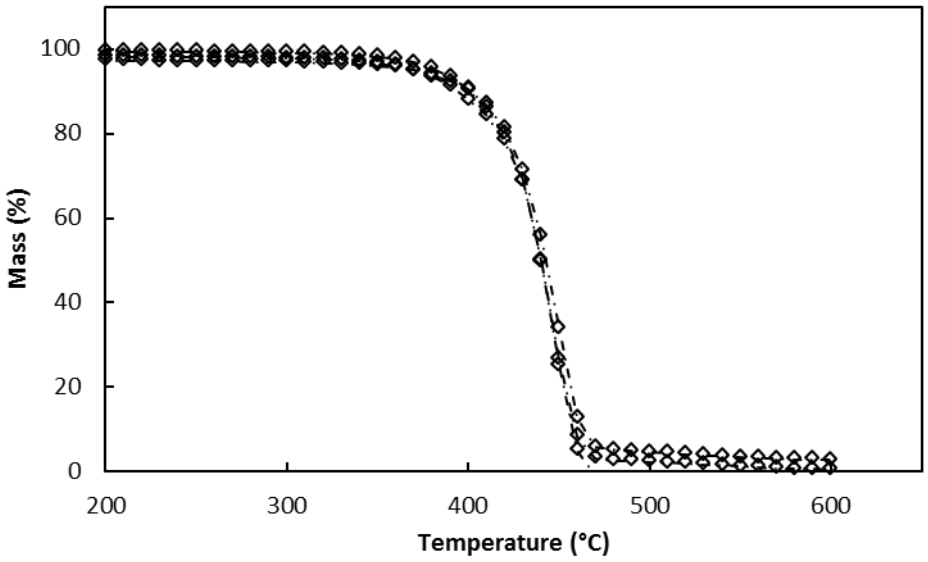

Figure A-6 Experiment 1 and 2 TG curves of PA6 with 0.05 and 0.2wt%CB at heating rates of 15°C/min

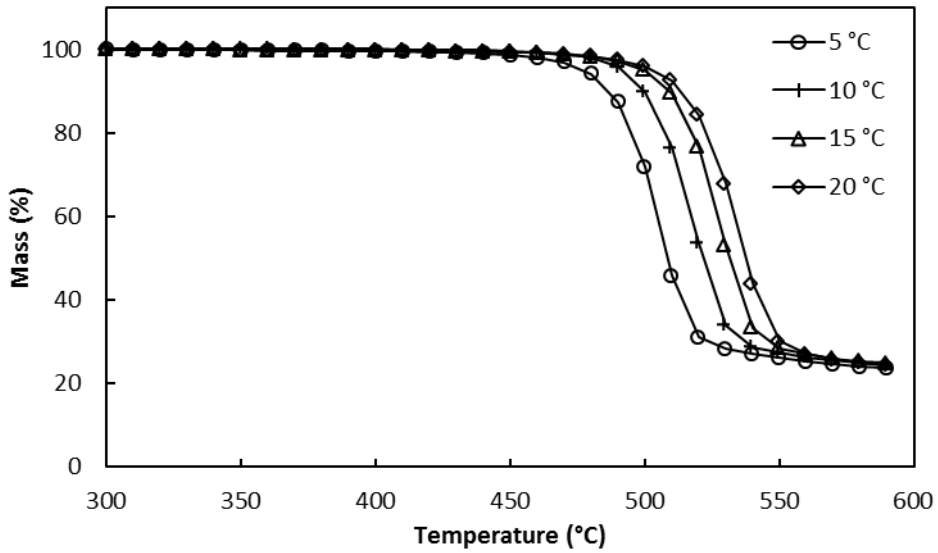

Figure A-7 TG curves of PC with 0.2wt% CB content at heating rates of 5, 10, 15 and 20°C.

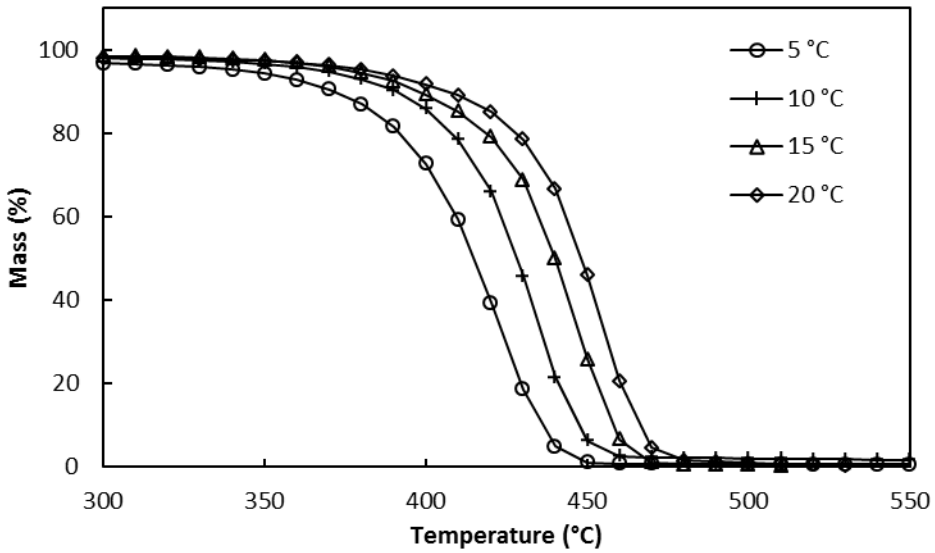

Figure A-8 TG curves of PA6 with 0.2wt% CB content at heating rates of 5, 10, 15 and 20°C.

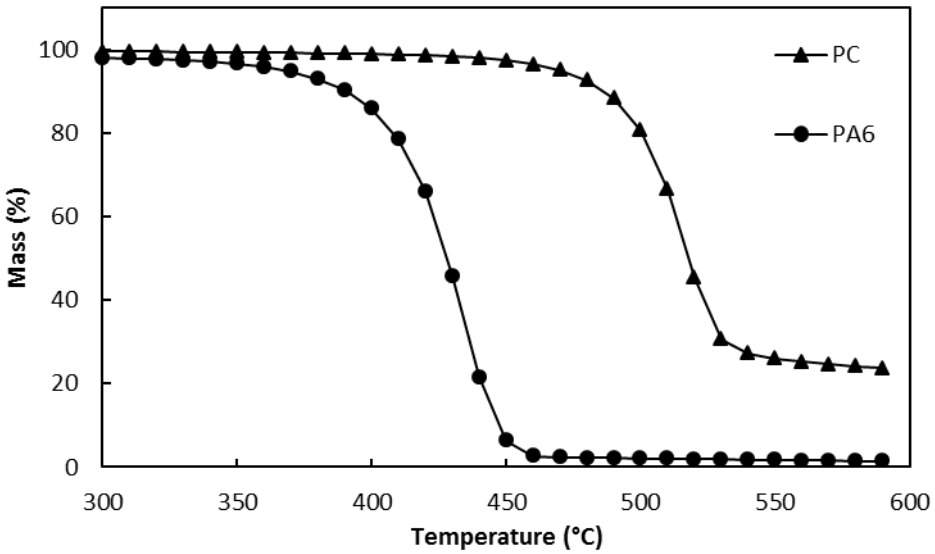

Figure A-9 TG curves of PC and PA6 and with 0.05wt% CB content at different heating rate of 10 °C

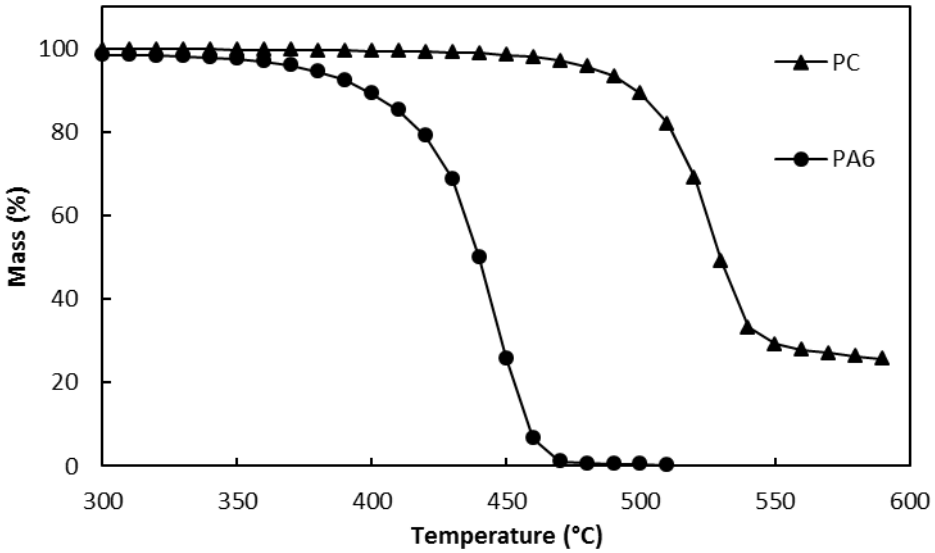

Figure A-10 TG curves of PC and PA6 with 0.05wt% CB content at different heating rate of 15 °C

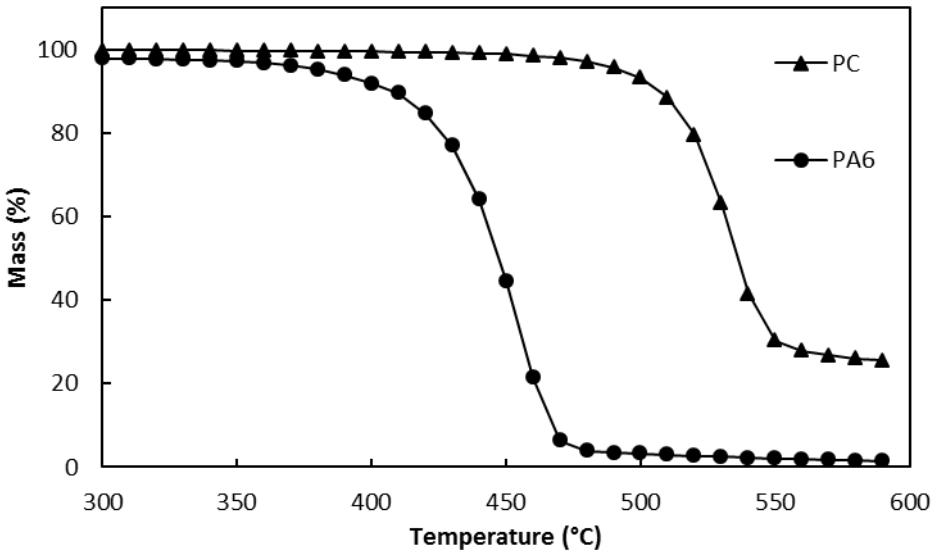

Figure A-11 TG curves of PC and PA6 with 0.05wt% CB content at different heating rate of 20 °C

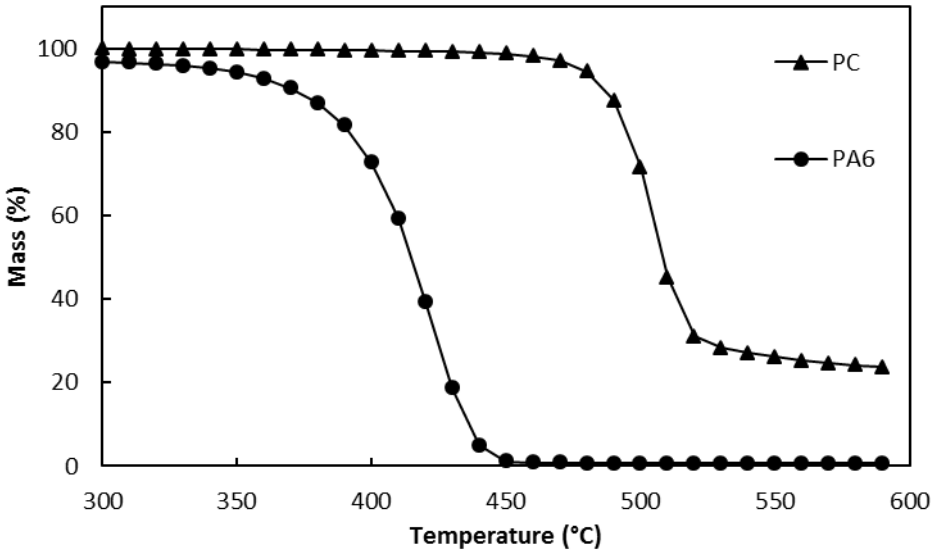

Figure A-12 TG curves of PC and PA6 and with 0.2wt% CB content at different heating rate of 5 °C

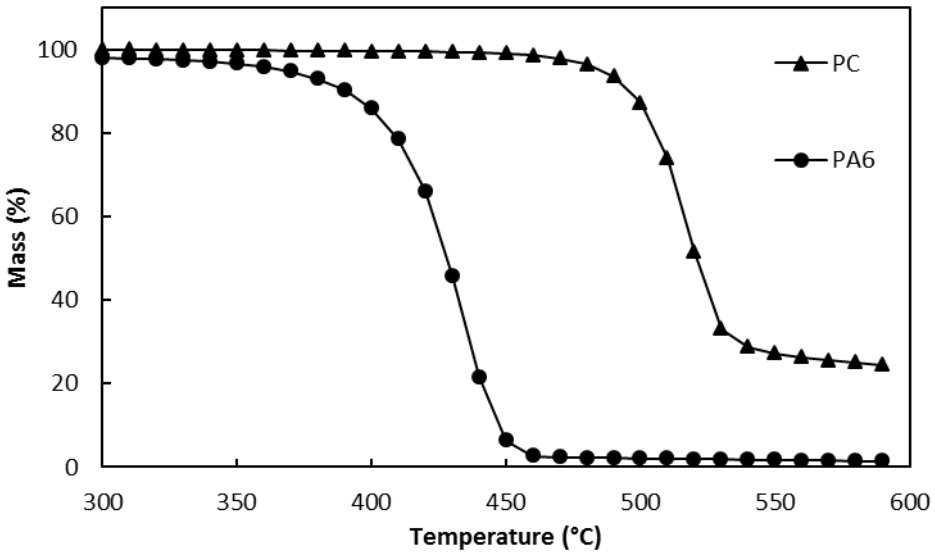

Figure A-13 TG curves of PC and PA6 and with 0.2wt% CB content at different heating rate of 10 °C

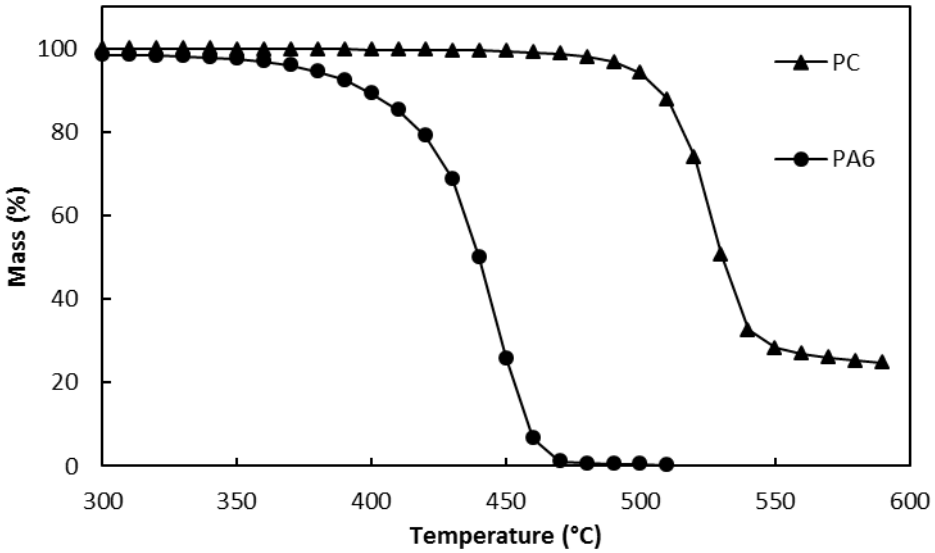

Figure A-14 TG curves of PC and PA6 with 0.2wt% CB content at different heating rate of 15 °C

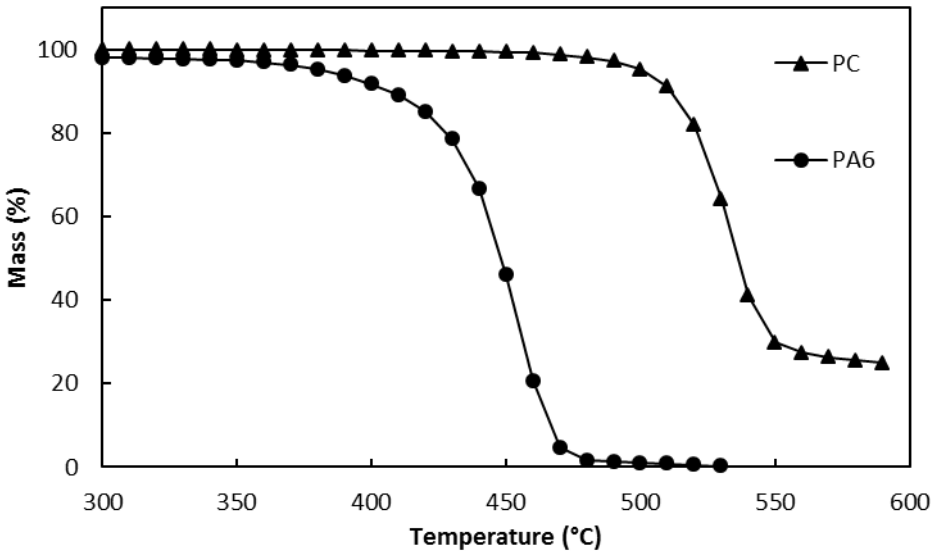

Figure A-15 TG curves of PC and PA6 with 0.05wt% CB content at different heating rate of 20 °C

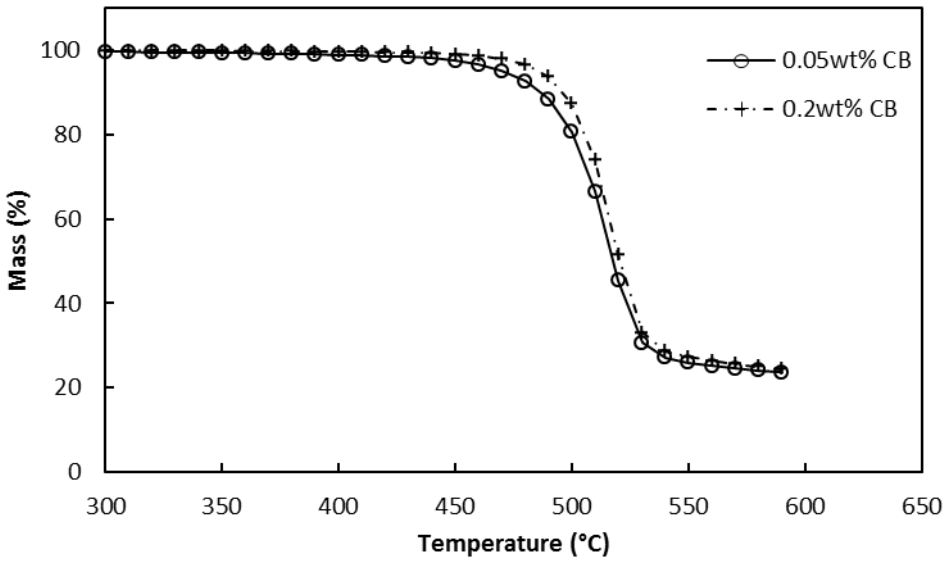

Figure A-16 TG curves of PC with 0.05wt% and 0.2wt% CB content at a heating rate of 10°C.

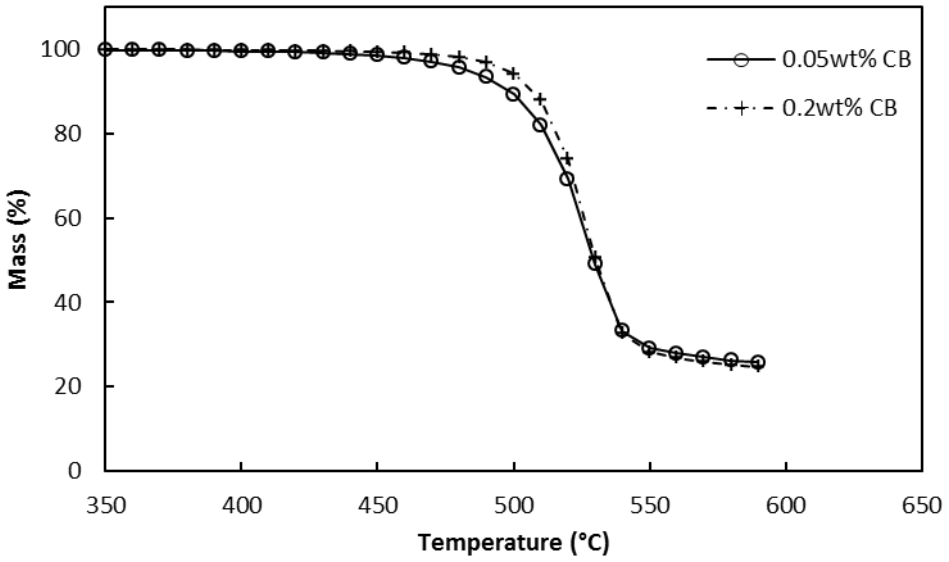

Figure A-17 TG curves of PC with 0.05wt% and 0.2wt% CB content at a heating rate of 15°C.

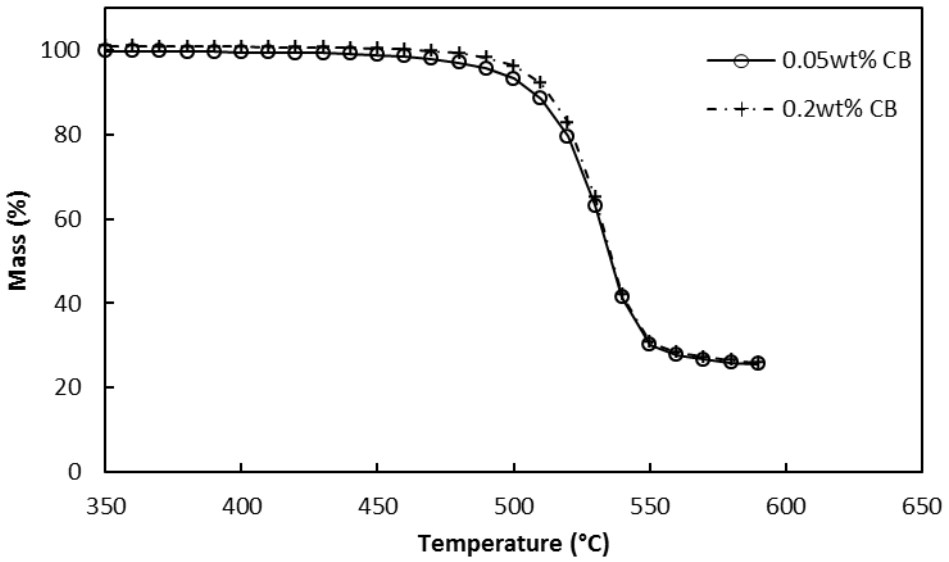

Figure A-18 TG curves of PC with 0.05wt% and 0.2wt% CB content at a heating rate of 20°C.

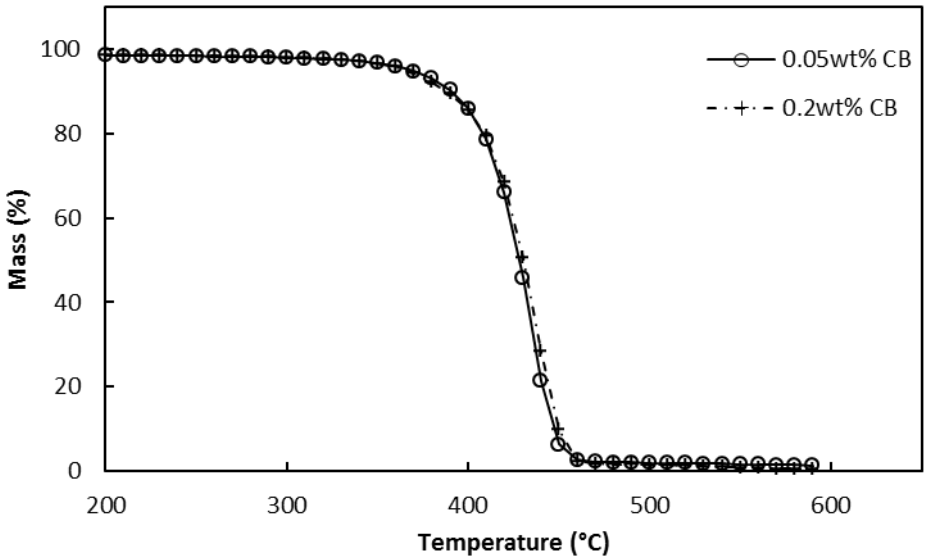

Figure A-19 TG curves of PA6 with 0.05wt% and 0.2wt% CB content at a heating rate of 10°C.

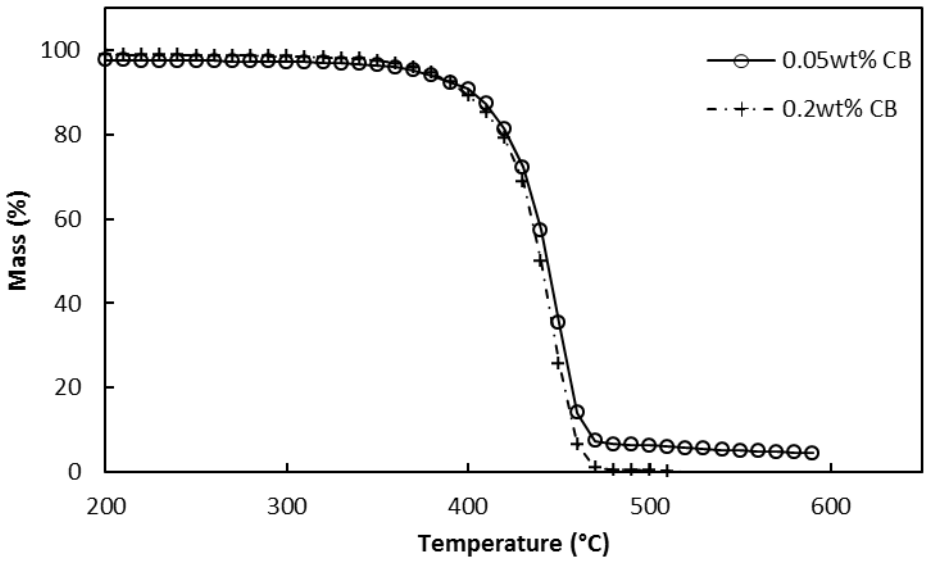

Figure A-20 TG curves of PA6 with 0.05wt% and 0.2wt% CB content at a heating rate of 15°C.

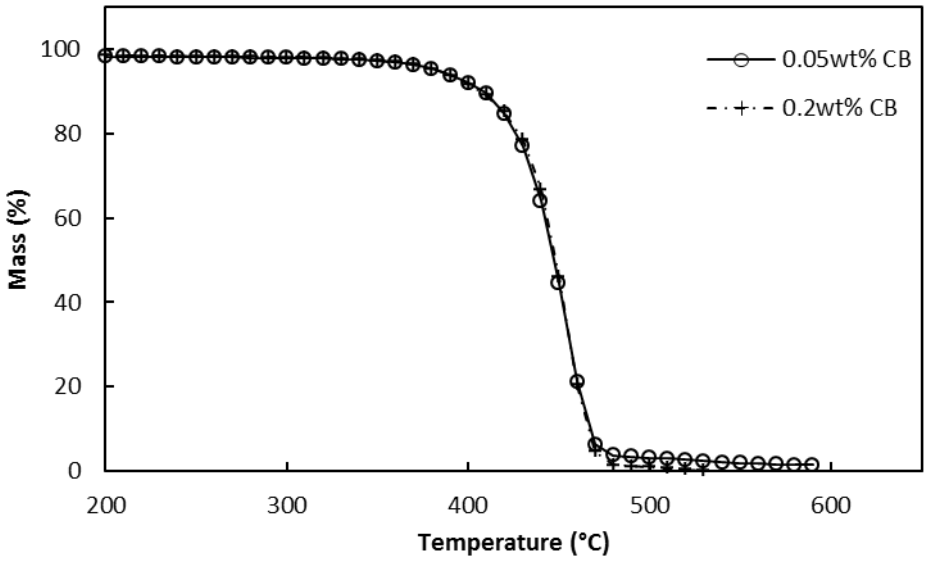

Figure A-21 TG curves of PA6 with 0.05wt% and 0.2wt% CB content at a heating rate of 20°C.

Appendix B

B.1 E_α of the materials

In chapter 4 of this work the average E_α of the materials PC and PA6 from the repeated experiments were presented. Figures B-1 to B-14 show the separate results from the repeated TGA experiments of the materials.

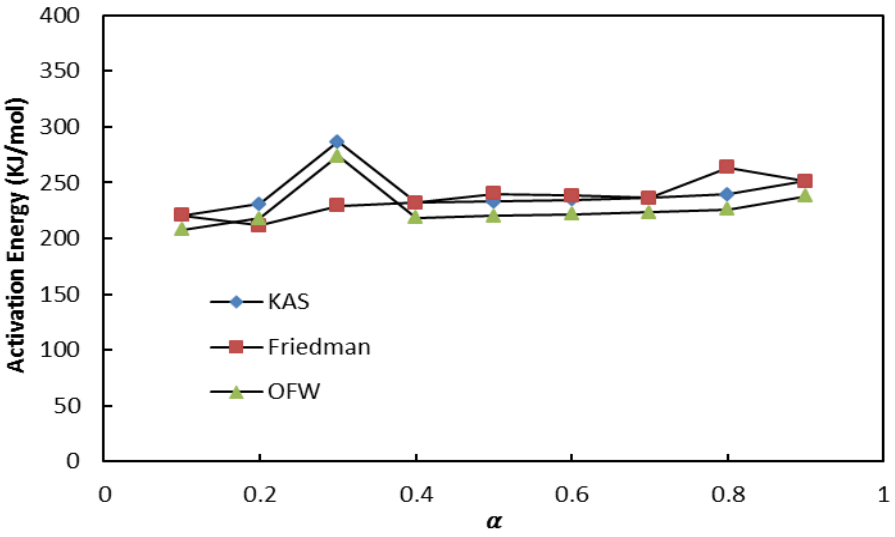

Figure B-1 α dependent *E* of PC with 0.05wt% CB, obtained by KAS, Friedman and OFW methods using TGA data from experiment 1.

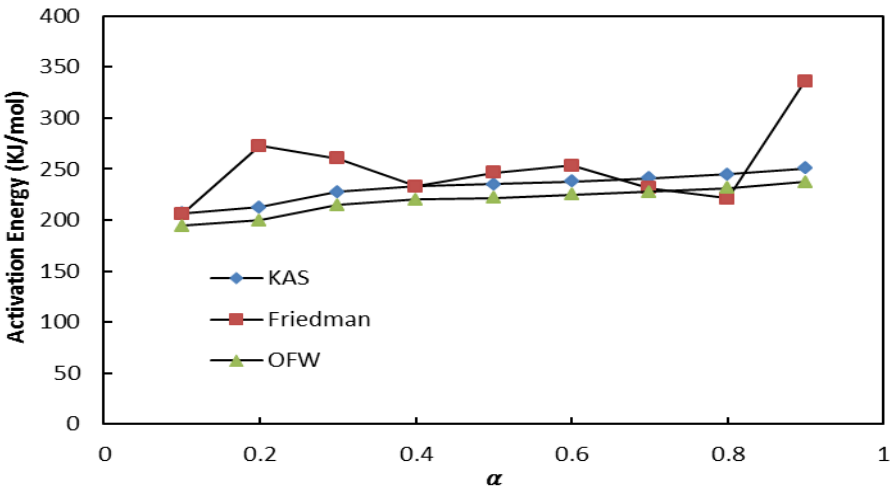

Figure B-2 α dependent *E* of PC with 0.05wt% CB, obtained by KAS, Friedman and OFW methods using TGA data from experiment 2.

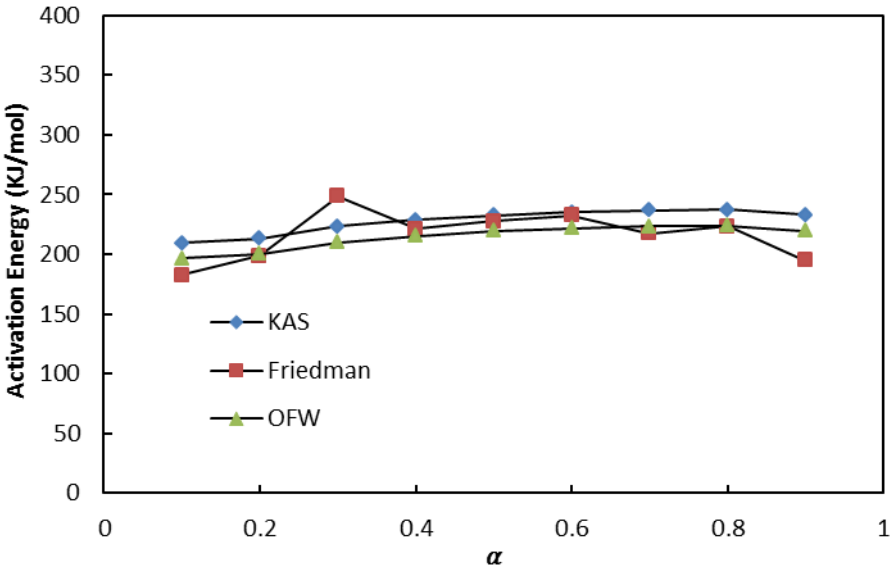

Figure B-3 α dependent *E* of PC with 0.05wt% CB, obtained by KAS, Friedman and OFW methods using TGA data from experiment 3.

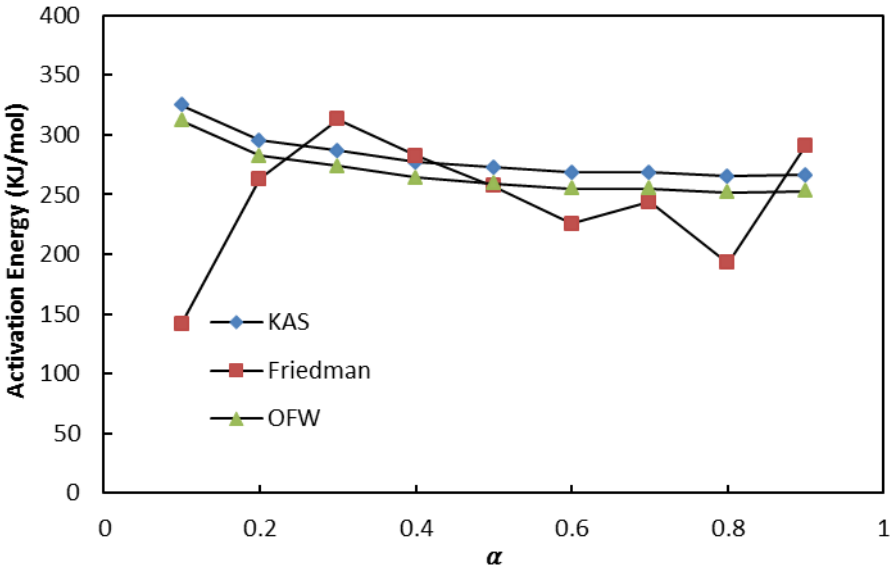

Figure B-4 α dependent *E* of PC with 0.2wt% CB, obtained by KAS, Friedman and OFW methods using TGA data from experiment 1.

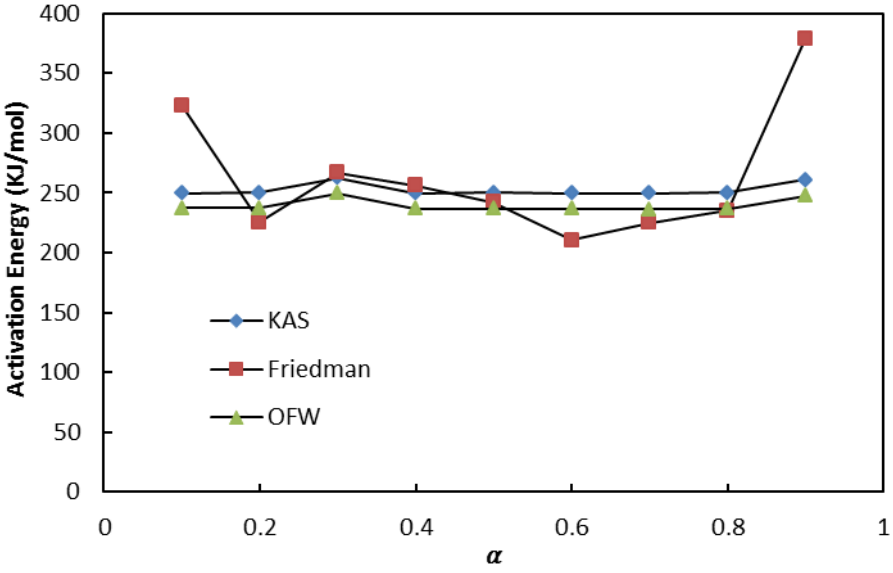

Figure B-5 α dependent *E* of PC with 0.2wt% CB, obtained by KAS, Friedman and OFW methods using TGA data from experiment 2.

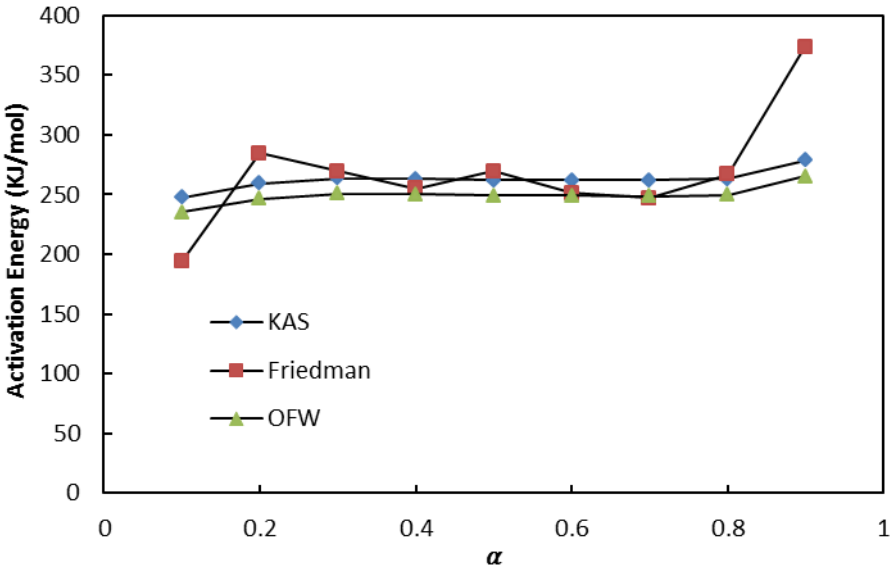

Figure B-6 α dependent *E* of PC with 0.2wt% CB, obtained by KAS, Friedman and OFW methods using TGA data from experiment 3.

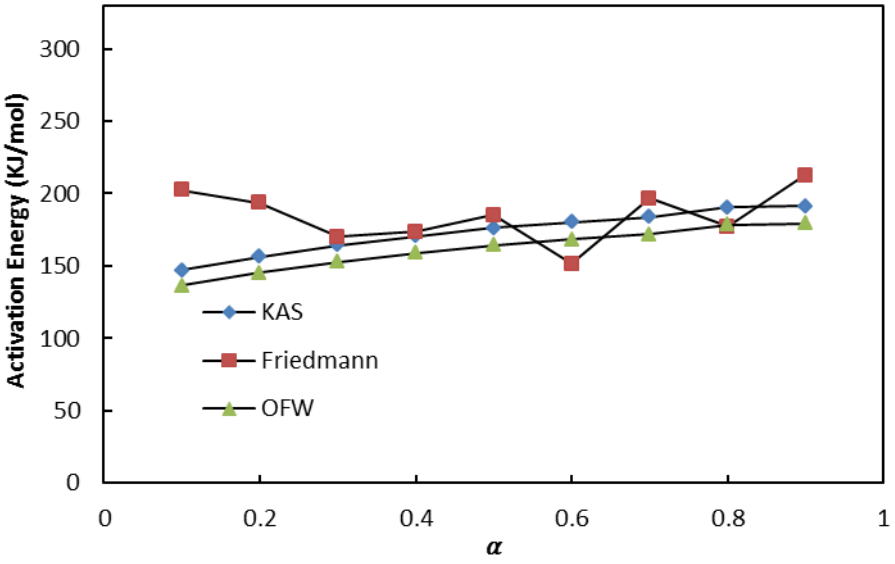

Figure B-7 α dependent *E* of PA6 with 0.2wt% CB, obtained by KAS, Friedman and OFW methods using TGA data from experiment 1.

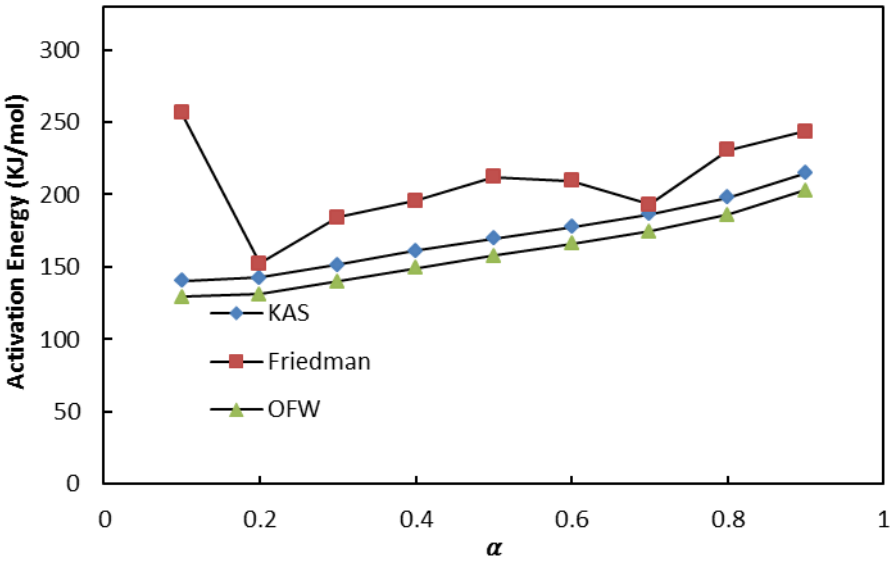

Figure B-8 α dependent *E* of PA6 with 0.2wt% CB, obtained by KAS, Friedman and OFW methods using TGA data from experiment 2.

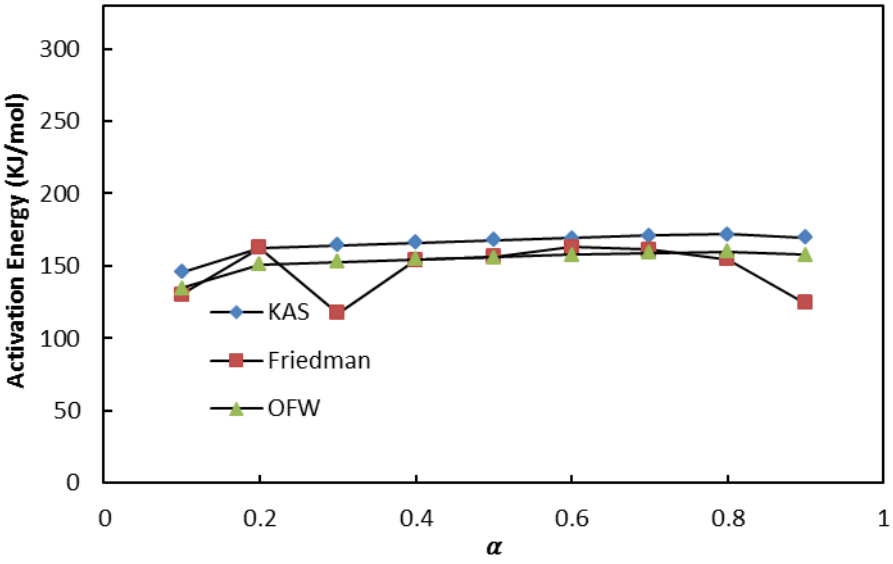

Figure B-9 α dependent *E* of PA6 with 0.05wt% CB, obtained by KAS, Friedman and OFW methods using TGA data from experiment 1.

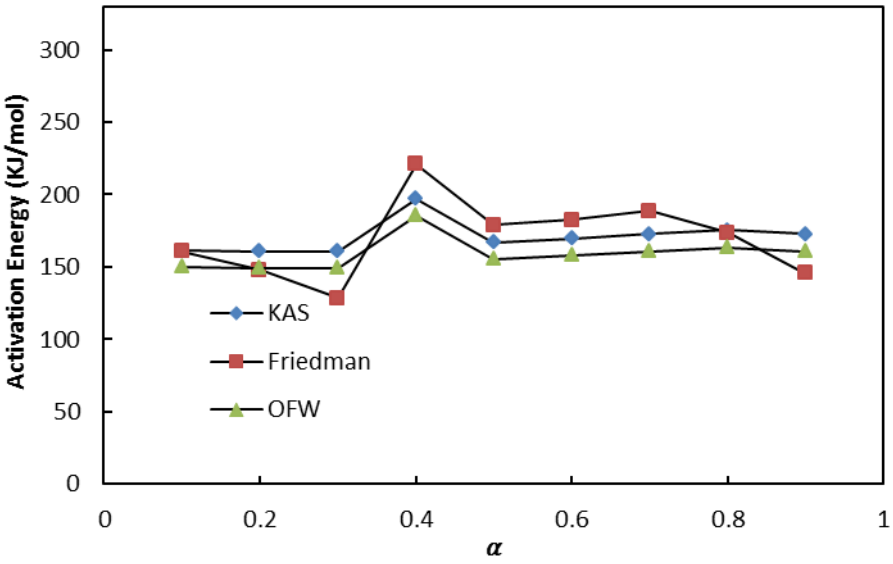

Figure B-10 α dependent *E* of PA6 with 0.05wt% CB, obtained by KAS, Friedman and OFW methods using TGA data from experiment 2.

B.2 TGA curve-fitting

The curve fitting results for average TGA curves of the materials from the repeated experiments at heating rates of 10 and 15°C are presented in Figures B-11 to B-16. It can be seen from Figures B-14 to B-21 the TGA data are reasonably reproduced by the models at these heating rates. The average R-square of the curve-fitting for all heating rates was presented in chapter 4.

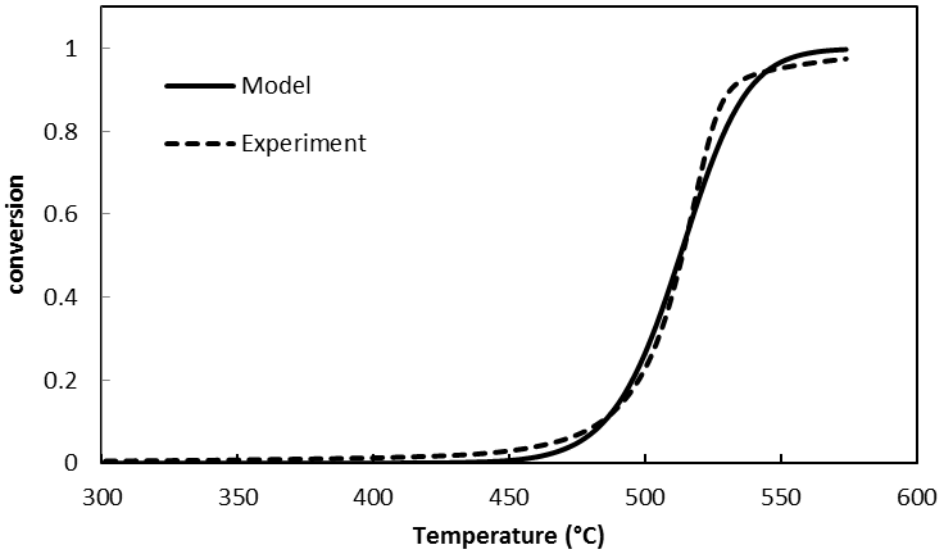

Figure B-11 Mass loss curves of PC (0.05wt% CB) samples at heating rates 10°C and their fitting curves with SB model.

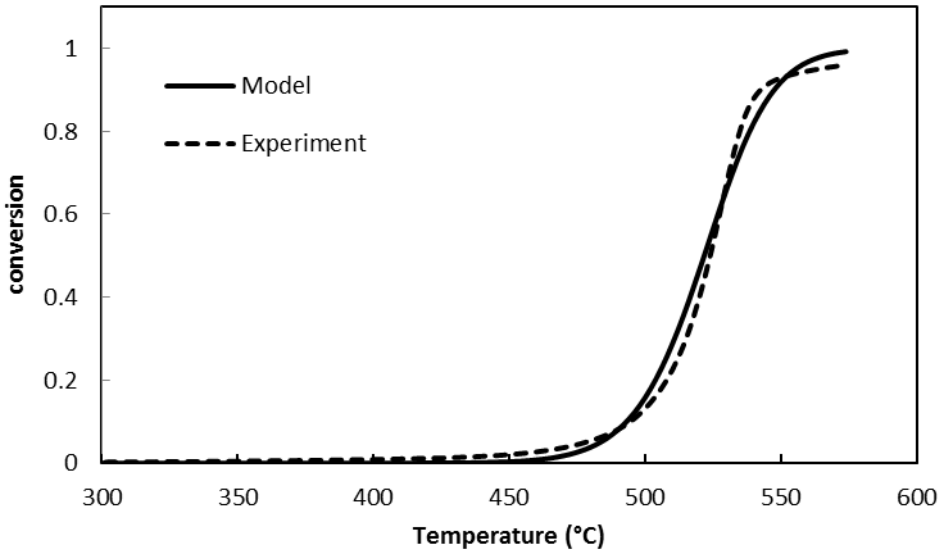

Figure B-12 Mass loss curves of PC (0.05wt% CB) samples at heating rates 15°C and their fitting curves with SB model.

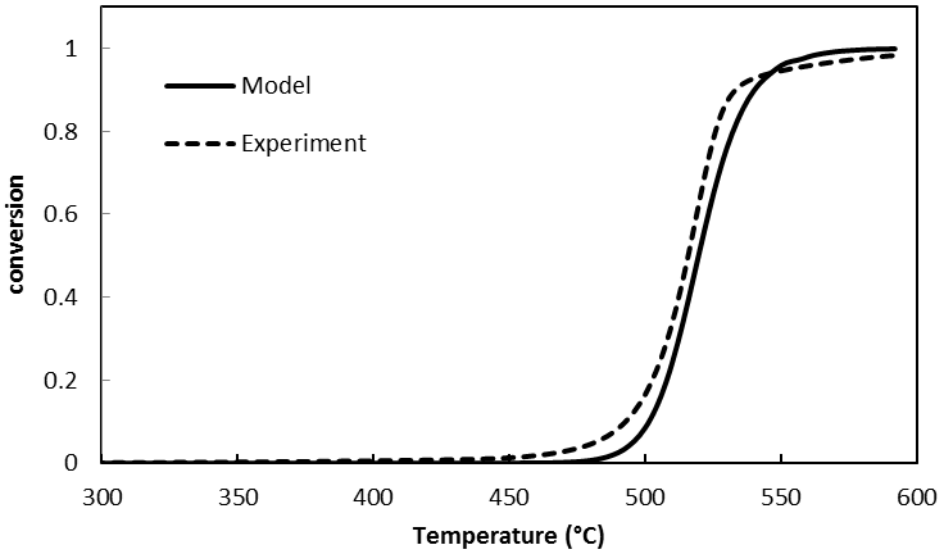

Figure B-13 Mass loss curves of PC (0.2wt% CB) samples at heating rates 10°C and their fitting curves with SB model.

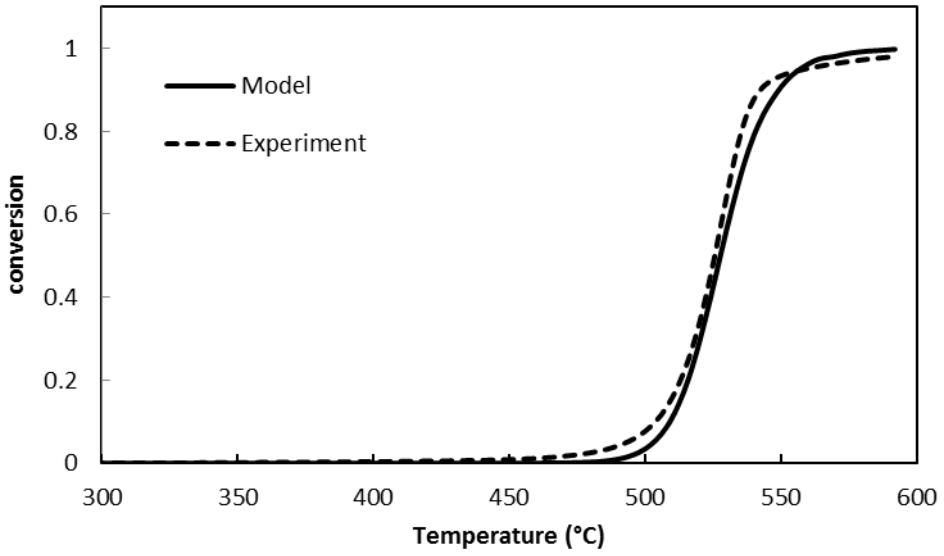

Figure B-14 Mass loss curves of PC (0.2wt% CB) samples at heating rates 15°C and their fitting curves with *SB*-order model.

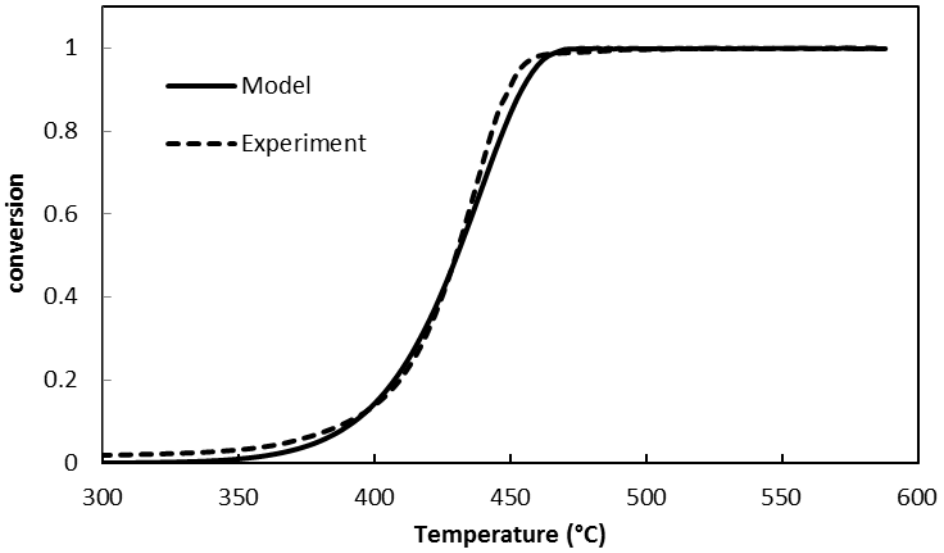

Figure B-15 Mass loss curves of PA6 samples at heating rate of 10°C and their fitting curves with *n*th-order model

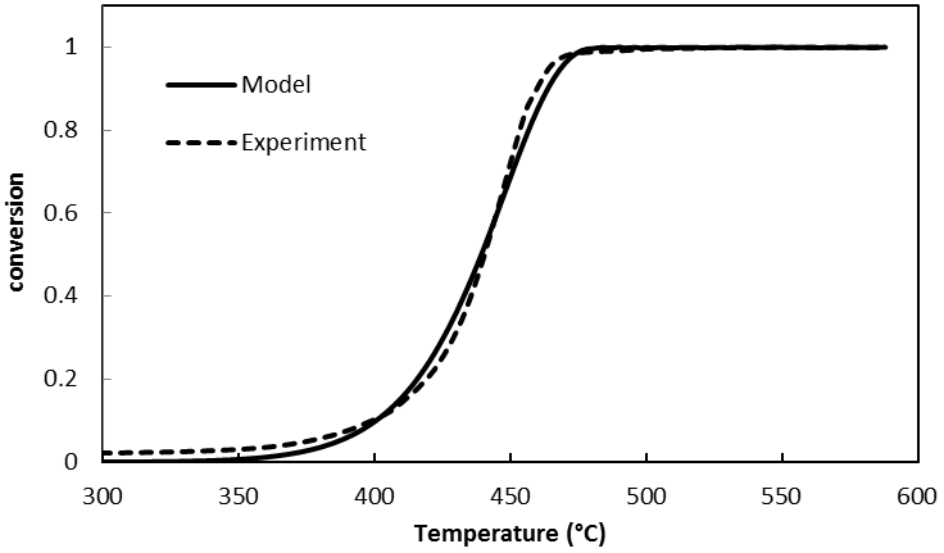

Figure B-16 Mass loss curves of PA6 samples at heating rate of 15°C and their fitting curves with *n*th-order model

Appendix C

Matlab file used to perform curve-fitting in order to obtain the kinetic parameters

```
%xslread, reads the TGA experimental data from excel file
%Alpha is experimental α
%da_dt is experimental dα/dt
%Temp is temperature during TGA



Temp        =   xlsread('pco_2cb.xls',1, 'A4:A404')';
alpha_5     =   xlsread('pco_2cb.xls',1, 'B4:B404')';
alpha_10    =   xlsread('pco_2cb.xls',1, 'C4:C404')';
alpha_15    =   xlsread('pco_2cb.xls',1, 'D4:D404')';
alpha_20    =   xlsread('pco_2cb.xls',1, 'E4:E404')';
da_dt_5     =   xlsread('pco_2cb.xls',1, 'F4:F404')';
da_dt_10    =   xlsread('pco_2cb.xls',1, 'G4:G404')';
da_dt_15    =   xlsread('pco_2cb.xls',1, 'H4:H404')';
da_dt_20    =   xlsread('pco_2cb.xls',1, 'I4:I404')';



%calculation of time from experimental temperature

t_5 = (Temp-(24+273.15))/5;
t_10 = (Temp-(24+273.15))/10;
t_15 = (Temp-(24+273.15))/15;
t_20 = (Temp-(24+273.15))/20;

% Gas constant
R = 0.0083144621;


% Matlab curve fitting toolbox

% F is used to compute the objective function
F = @(x)((da_dt_20-((x(1)*exp(-(x(2)./(R*Temp))).*((1-alpha_20).^x(3))))) +
(da_dt_15-((x(1)*exp(-(x(2)./(R*Temp))).*((1-alpha_15).^x(3))))) +
(da_dt_10-((x(1)*exp(-(x(2)./(R*Temp))).*((1-alpha_10).^x(3))))) +
(da_dt_5-((x(1)*exp(-(x(2)./(R*Temp))).*((1-alpha_5).^x(3)))))
)


% Initial values assigned to the parameters
x0= [2.54174E+13, 160, 1.1];
```

```
% Upper and lower boundary used to constrain the parameters
ub = [2.04174E+17, 215,   1.3 ];

lb = [2.54174E+10, 130,  0.6 ] ;


problem =
createOptimProblem('lsqnonlin','objective',F,'x0',x0,'lb',lb,'ub',ub);
ms = MultiStart;
[x,f] = run(ms,problem,100); %x is optimised parameters



t = t_5;

%Intergration using Matlab Ode 45

dy = @(t,y5)(x(1).*exp(-(x(2)./(R*(t*5+(24+273.15))))).*((1-y5).^x(3)));

y0 =0.00000000001;

[t,y5]= ode45(dy,t,y0);

Temp5 = t*5+(24+273.15);




t = t_20;

dy = @(t,y20)(x(1).*exp(-(x(2)./(R*(t*20+(24+273.15))))).*((1-y20).^x(3)));

y0 =0.00000000000000000000000000000000000000000000001;

[t,y20]= ode45(dy,t,y0);

Temp20 = t*20+(24+273.15)



%Ploting the results and the experimental

     figure (1)

   plot (Temp5,y5,Temp5,alpha_5,   Temp20,y20,Temp20,alpha_20)


   ylabel('Conversion')
xlabel ('Temp (k)')

legend('MODEL5','EXPT5', 'MODEL20','EXPT20')
```

Appendix D

D.1 Thermal properties

The thermal properties (density, heat capacity and thermal conductivity) of the materials used in reference 7 as inputs in the FEM are presented graphically in Figures D-1 to D-3.

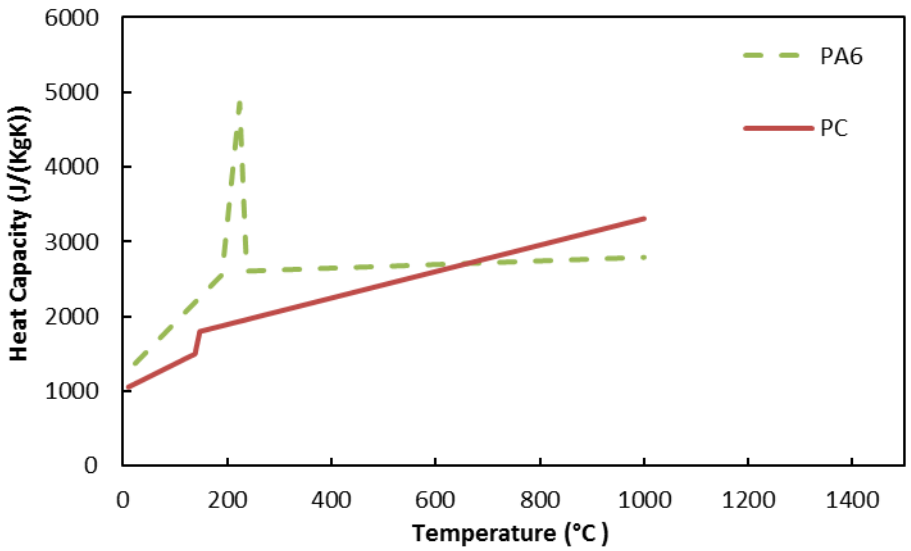

Figure D-1 Heat capacity of PC and PA6 as function of temperature

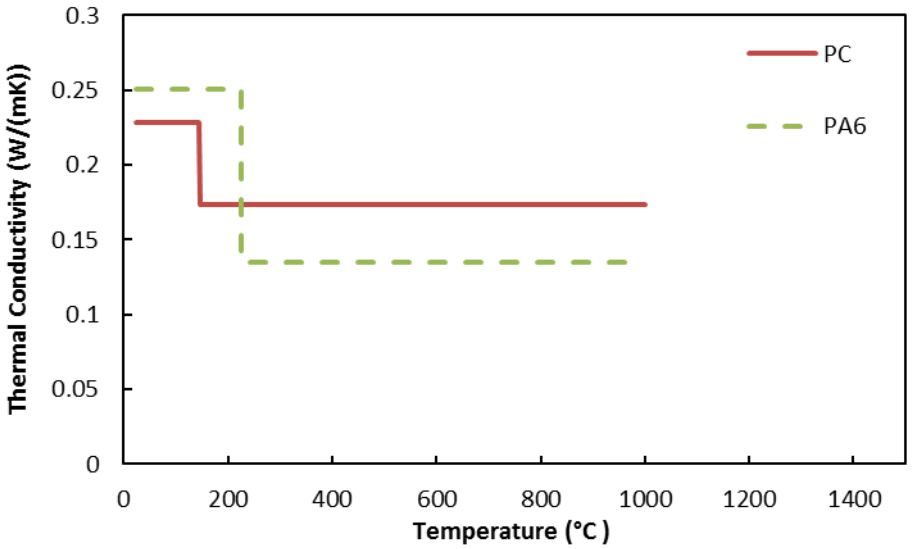

Figure D-2 Thermal Conductivity of PC and PA6 as function of temperature

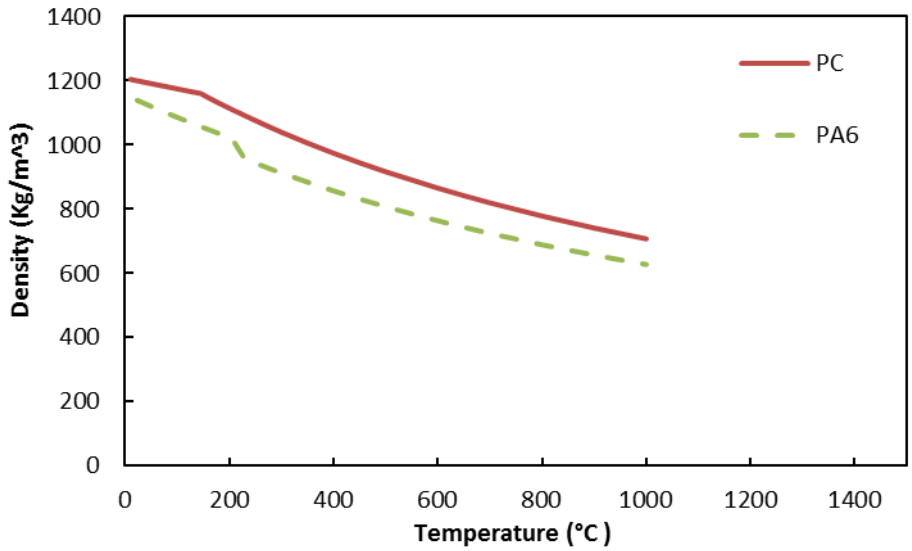

Figure D-3 Density of PC, PA6 and PA6GF as function of temperature

D.2 Temperature profiles of PC along y-axis

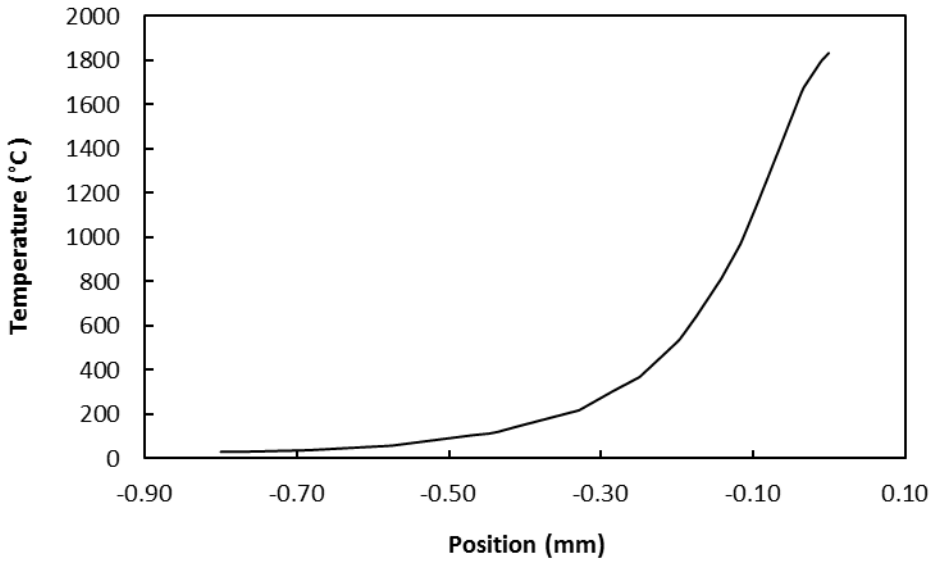

D-4 Typical temperature profile along the y direction for non-contact model (PC 0.1wt% CB, 20 W, 25mm/s)

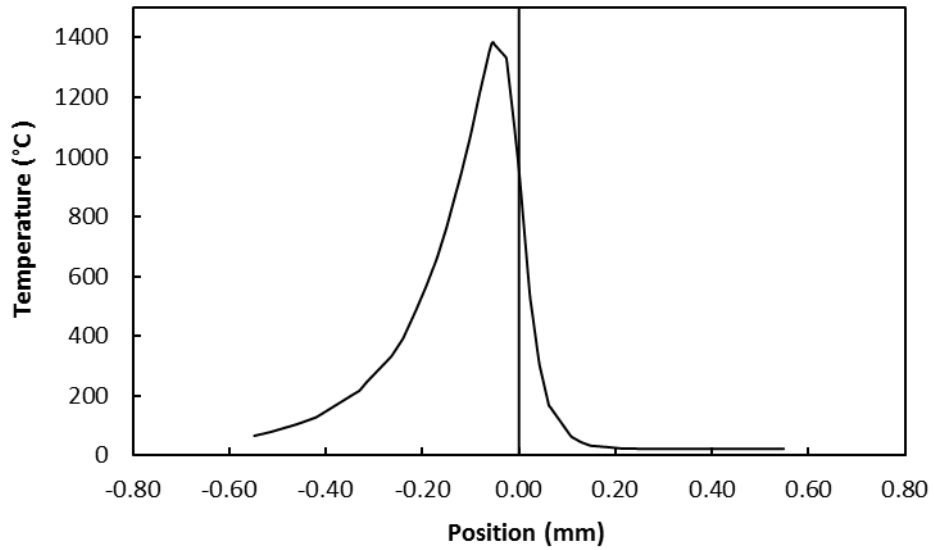

D-5 Typical temperature profile along the y direction for contact model (PC 0.1wt% CB, 20 W, 25mm/s)

D.3 Temperature-time profile

The temperature-time profile generated from running the Comsol model for the materials at diferent CB, power levels and laser scan speed of 25mm/s are presented here in Figures D-4 to D-9.

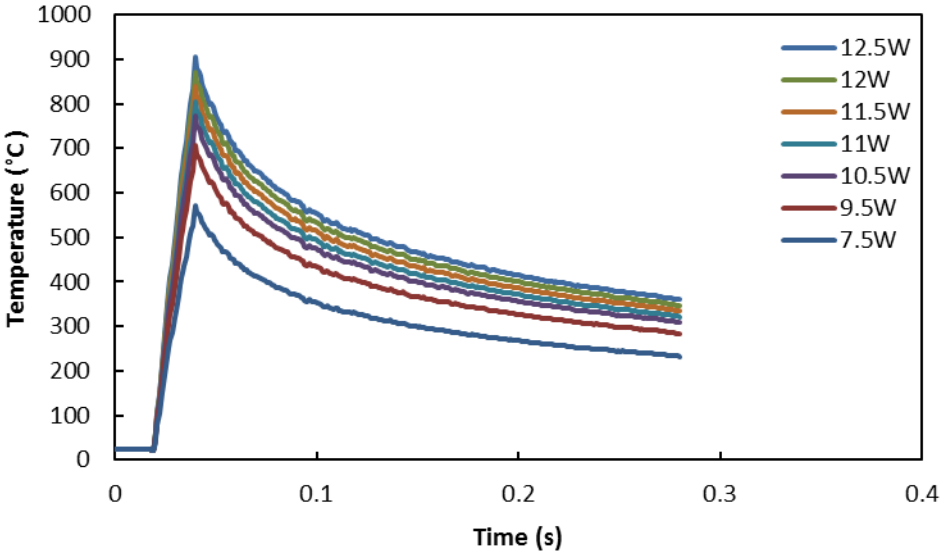

Figure D-6 Temperature-time profile of PC (contact, 0.1wt% CB) at different laser power level.

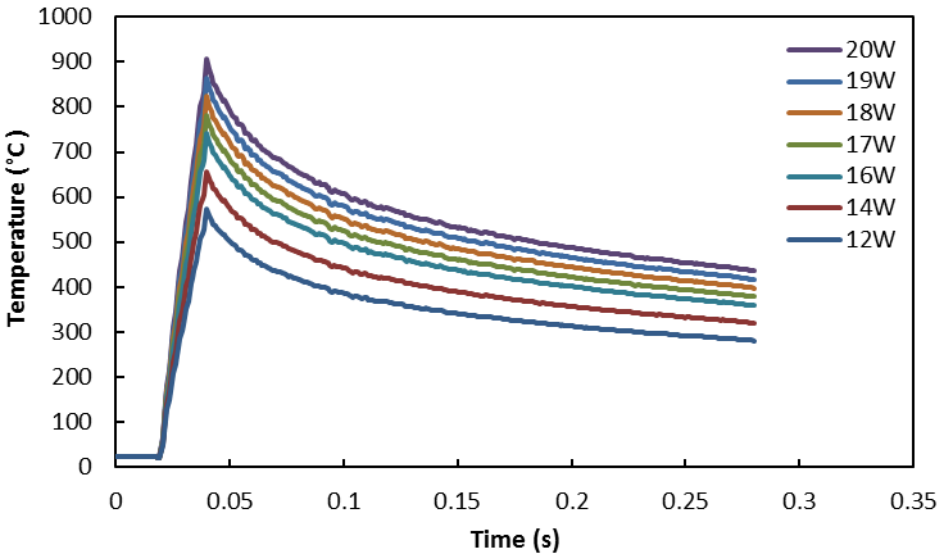

Figure D-7 Temperature-time profile of PC (contact, 0.05wt% CB) at different laser power level.

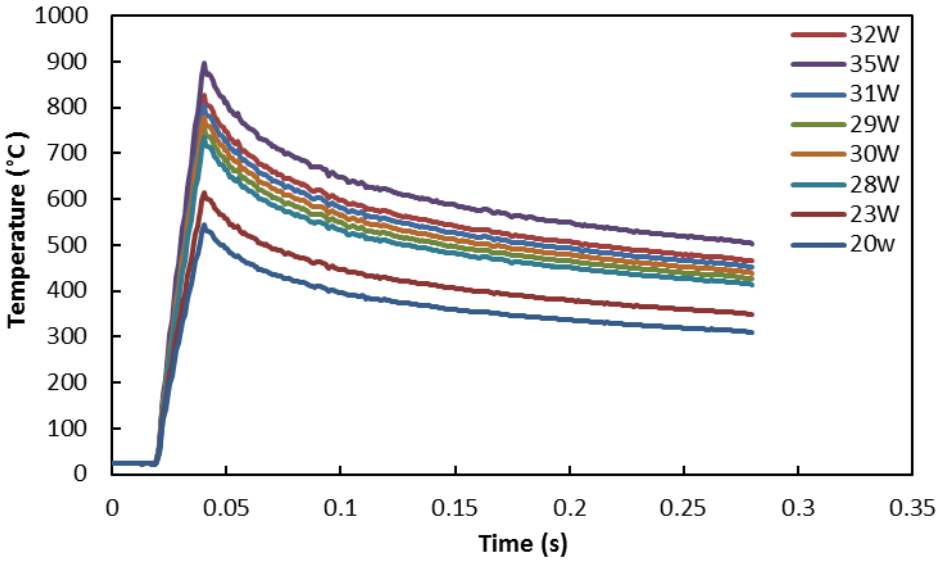

Figure D-8 Temperature-time profile of PC (contact, 0.025wt% CB) at different laser power level.

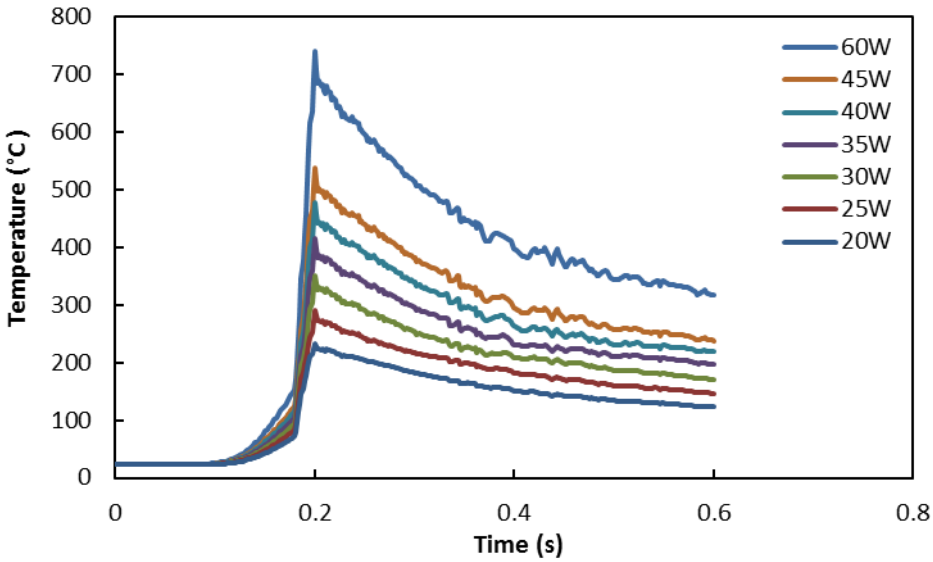

Figure D-9 Temperature-time profile of PA6 (contact, 0.1wt% CB) at different laser power level.

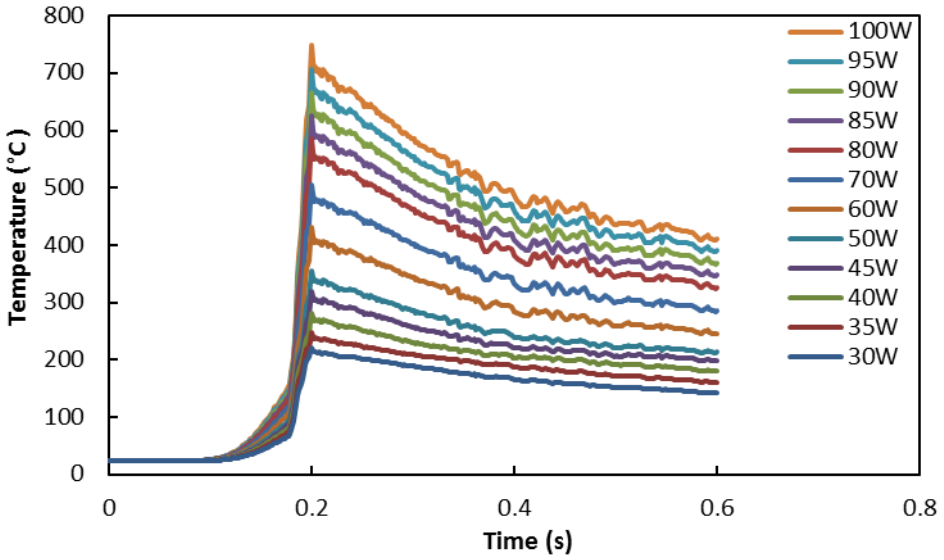

Figure D-10 Temperature-time profile of PA6 (contact, 0.05wt% CB) at different laser power level.

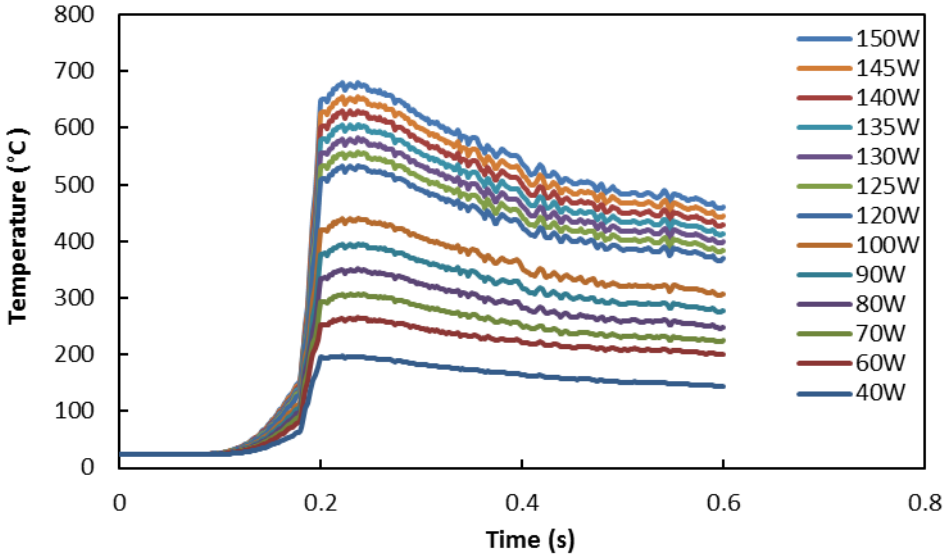

Figure D-11 Temperature-time profile of PA6 (contact, 0.025wt% CB) at different laser power level.

Appendix E

The $f(t)$ for the applicable conditions generated by Matlab for computing temperature as a function of time, which was applied to equation 6.2 in order to estimate material conversion as a result of thermal degradation during LTW, are presented in this appendix. In Tables E-1 to E-8 t_1 represents heating time while t_2 represents cooling time

Table E-1 $f(t)$ for PC (0.1 wt% CB, 25mm/s, contact model)

Power (W), Heating	$f(t)$ (°K), Applied for $t = 0.02s$ to $0.04s$
7.5	-9.275e+04*t_1^2+3.077e+04*t_1-2.375e+02
9.5	-8.875e+04*t_1^2+3.681e+04*t_1-3.5e+02
10.5	-8.636e+04*t_1.^2+3.97e+04*t_1-4.063e+02
11	-8.524e+04*t_1^2+4.127e+04*t_1-4.341e+02
11.5	-8.448e+04*t_1^2+4.277e+04*t_1-4.621e+02
12	-8.454e+04*t_1^2+4.432e+04*t_1-4.906e+02
Power (W), Cooling	$f(t)$ (°K), Applied for $t = 0.04s$ to $0.28s$
7.5	2.6025e+07*t_2^6-2.814e+07*t_2^5+1.237e+07*t_2^4-2.842e+06*t_2^3+3.642e+05*t_2^2-2.594e+04*t_2+1.438e+03
9.5	-3.59e+08*t_2^7+4.348e+08*t_2^6-2.196e+08*t_2^5+6e+07*t_2^4-9.657e+06*t_2^3+9.239e+05*t_2^2-5.0968e+04*t_2+2.01e+03
10.5	-3.926e+08*t_2^7+4.74659e+08*t_2^6-2.397e+08*t_2^5+6.56e+07*t_2^4-1.054e+07*t_2^3+1e+06*t_2^2-5.57e+04*t_2+2.17e+03
11	-4.0857e+08*t_2^7+4.94e+08*t_2^6-2.49e+08*t_2^5+6.82e+07*t_2^4-1.097e+07*t_2^3+1.05e+06*t_2^2-5.8e+04*t_2^1+2.25e+03
11.5	-4.24e+08*t_2^7+5.13e+08*t_2^6-2.59e+08*t_2^5+7e+07*t_2^4-1.14e+07*t_2^3+1.1e+06*t_2^2-6.034e+04*t_2^1+2.335e+03
12	-4.409e+08*t_2^7+5.34e+08*t_2^6-2.69e+08*t_2^5+7.364e+07*t_2^4-1.2e+07*t_2^3+1.1340e+06*t_2^2-6.269e+04*t_2^1+2.415e+03

Table E-2 $f(t)$ for PC (0.05wt% CB, 25mm/s, contact mode)

Power (W), Heating	$f(t)$ (°K), Applied for t = 0.02s to 0.04s
12	-7.57e+04*t_1^2+2.98e+04*t_1^1-2.26e+02
14	-7.065e+04*t_1^2+3.35e+04*t_1^1-2.945e+02
16	-6.566e+04*t_1^2+3.71e+04*t_1.^1-3.6e+02
18	-6e+04*t_1^2+4e+04*t_1.^1-4.3e+02
19	-5.78e+04*t_1^2+4.245e+04*t_1.^1-4.65e+02
20	-5.6e+04*t_1^2+4.4e+04*t_1.^1-5e+02
Power (W), Cooling	$f(t)$ (°K), Applied for t = 0.04s to 0.28s
12	-2.68e+08*t_2^7+3.243e+08*t_2^6-1.63e+08*t_2^5+4.44e+07*t_2^4-7.1e+06*t_2^3+6.7e+05*t_2^2-3.6e+04*t_2^1+1.58e+03
14	-3e+08*t_2^7+3.7e+08*t_2^6-1.9e+08*t_2^5+5e+07*t_2^4-8.1e+06*t_2^3+7.7e+05*t_2^2-4.2e+04*t_2^1+1.8e+03
16	-3.46e+08*t_2^7+4.18e+08*t_2^6-2.1e+08*t_2^5+5.73e+07*t_2^4-9.17e+06*t_2^3+8.7e+05*t_2^2-4.74e+04*t_2^1+1.96e+03
17	-4.2e+08*t_2^7+5e+08*t_2^6-2.6e+08*t_2^5+7e+07*t_2^4-1.1e+07*t_2^3+1e+06*t_2^2-5.8e+04*t_2^1+2.33e+03
18	-3.8e+08*t_2^7+4.6e+08*t_2^6-2.3e+08*t_2^5+6.36e+07*t_2^4-1e+07*t_2^3+9.7e+05*t_2^2-5.26e+04*t_2^1+2.15e+03
19	-4e+08*t_2^7+4.9e+08*t_2^6-2.4e+08*t_2^5+6.7e+07*t_2^4-1e+07*t_2^3+1e+06*t_2^2-5.5e+04*t_2^1+2.2e+03
20	-4.2e+08*t_2^7+5e+08*t_2^6-2.56e+08*t_2^5+6.98e+07*t_2^4-1.12e+07*t_2^3+1.06e+06*t_2^2-5.8e+04*t_2^1+2.3e+03

Table E-3 $f(t)$ for PC (0.025wt% CB, 25mm/s, contact model)

Power (W), Heating	$f(t)$ (°K), Applied for t = 0.02s to 0.04s
23	-3.6e+04*t_1^2+3e+04*t_1^1-2.3e+02
28	-2e+04*t_1^2+3.4e+04*t_1^1-3.3e+02
29	-1.8e+04*t_1^2+3.5e+04*t_1^1-3.4e+02
30	-1.46e+04*t_1^2+3.6e+04*t_1^1-3.6e+02
31	-1.12e+04*t_1^2+3.7e+04*t_1^1-3.8e+02
35	-2.21e+02*t_1^2+4e+04*t_1^1-4.5e+02
Power (W), Cooling	$f(t)$ (°K), Applied for t = 0.04s to 0.28s
23	-2.3e+08*t_2^7+2.8e+08*t_2^6-1.4e+08*t_2^5+3.8e+07*t_2^4-6e+06*t_2^3+5.9e+05*t_2^2-3.2e+04*t_2^1+1.5e+03
28	-2.7e+08*t_2^7+3.3e+08*t_2^6-1.7e+08*t_2^5+4.5e+07*t_2^4-7.3e+06*t_2^3+7e+05*t_2^2-3.9e+04*t_2^1+1.8e+03
29	-2.8e+08*t_2^7+3.4e+08*t_2^6-1.7e+08*t_2^5+4.7e+07*t_2^4-7.5e+06*t_2^3+7.2e+05*t_2^2-4e+04*t_2^1+1.8e+03
30	-2.9e+08*t_2^7+3.5e+08*t_2^6-1.8e+08*t_2^5+4.8e+07*t_2^4-7.8e+06*t_2^3+7.4e+05*t_2^2-4.1e+04*t_2^1+1.9e+03
31	-3e+08*t_2^7+3.6e+08*t_2^6-1.8e+08*t_2^5+5e+07*t_2^4-8e+06*t_2^3+7.7e+05*t_2^2-4.e+04*t_2^1+2e+03
32	-3e+08*t_2.^7+3.7e+08*t_2^6-1.9e+08*t_2^5+5e+07*t_2^4-8e+06*t_2^3+7.9e+05*t_2^2-4e+04*t_2^1+2e+03
35	-3.3e+08*t_2^7+4e+08*t_2^6-2e+08*t_2^5+5.55e+07*t_2^4-8.9e+06*t_2^3+8.5e+05*t_2^2-4.7e+04*t_2^1+2.1e+03

Table E-4 $f(t)$ for PA6 (0.1wt% CB, 25mm/s, contact model)

Power (W), heating	$f(t)$ (°K), Applied for t = 0.1s to 0.2s
40	4.127e+06 *t_1^3-1.899e+06 *t_1^2+3e+05*t_1^1-1.461286828112854e+04
45	4.9e+06*t_1^3-2.2e+06 *t_1^2+3.46e+05*t_1^1-1.74e+04
47	-2.3e+08*t_1^4+1.67e+08*t_1.^3-4.48e+07*t_1^2+5.3e+06*t_1^1-2.3e+05
50	-2.7e+08*t_1^4+2e+08*t_1^3-5.3e+07*t_1^2+6.2e+06*t_1^1-2.72e+05
55	-3.05+08*t_1^4+2.21e+08*t_1^3-6e+07*t_1^2+7e+06*t_1^1-3e+05
60	7.14e+06 *t_1^3-3.3e+06 *t_1^2+5e+05*t_1^1-2.6e+04
65	-3.8e+08*t_1^4+2.7e+08*t_1^3-7.32e+07*t_1^2+8.66e+06*t_1^1-3.8e+05
Power (W), Cooling	$f(t)$ (°K), Applied for t = 0.2s to 0.6s
40	-9e+03*t_2^4+1.22e+04*t_2^3-3.93e+03*t_2^2-8.93e+02*t_2^1+9.78e+02
45	-2.88e+03*t_2^3+5.32e+03*t_2^2-3.44e+03*t_2^1+1.28e+03
47	-3.14e+03*t_2^3+5.73e+03*t_2.^2-3.67e+03*t_2^1+1.34e+03
50	-3.48e+03*t_2^3+6.32e+03*t_2.^2-4.02e+03*t_2^1+1.43e+03
55	-4.33e+03*t_2^3+7.56e+03*t_2^2-4.66e+03*t_2^1+1.58e+03
60	-5.22e+03*t_2^3+8.9e+03*t_2^2-5.36e+03 *t_2^1+1.73e+03
65	-5.9e+03*t_2^3+1e+04*t_2^2-6e+03*t_2^1+1.89e+03

Table E-5 $f(t)$ for PA6 (0.05wt% CB, 25mm/s, contact model)

Power (W), Heating	$f(t)$ (°K), Applied for t = 0.1s to 0.2s
70	4.43e+06*t_1^3-2.04e+06*t_1^2+3.14e+05*t_1^1-1.58e+04
80	5.34e+06*t_1.3-2.47e+06*t_1^2+3.8e+05*t_1^1-1.92e+04
85	4.59e+07*t_1^4-2.54e+07*t_1^3+5.25e+06*t_1^2-4.77e+05*t_1^1+1.64e+04
90	6.27e+06*t_1^3-2.9e+06*t_1^2+4.47e+05*t_1^1-2.26e+04*t_1
95	5.39e+07*t_1^4-2.99e+07*t_1^3+6.18e+06*t_1^2-5.62e+05*t_1^1+1.93e+04
100	5.7e+07*t_1^4-3.2e+07*t_1^3+6.6e+06*t_1.^2-6e+05*t_1^1+2e+04
Power (W), Cooling	$f(t)$ (°K), Applied for t = 0.2s to 0.6s
70	-7.82e+02*t_2^3+2.24e+03*t_2^2-1.88e+03*t_2^1+1e+03
80	-1.36e+03*t_2^3+3.14e+03*t_2^2-2.39e+03*t_2^1+1.2e+03
85	-1.56e+03*t_2^3+3.49e+03*t_2^2-2.6e+03*t_2^1+1.28e+03
90	-1.75e+03*t_2^3+3.856e+03*t_2^2-2.84e+03*t_2^1+1.35e+03*
95	-2.02e+03*t_2^3+4.29e+03*t_2^2-3.1e+03*t_2^1+1.42e+03
100	-2.27e+03*t_2^3+4.7e+03*t_2.^2-3.35e+03*t_2^1+1.5e+03

Table E-6 $f(t)$ for PA6 (0.025wt% CB, 25mm/s, contact model)

Power (W), Heating	$f(t)$ (°K), Applied for t = $0.1s$ to $0.23s$
100	-1e+05*t_1^2+4.64e+04*t_1^1-4.63e+03*t_1^0
120	-1.23e+05*t_1^2+5.69e+04*t_1^1-5.7e+03
125	4e+06*t_1^3-2.8e+06*t_1^2+6.42e+05*t_1^1-4.8e+04
130	4.32e+06*t_1^3-2.97e+06*t_1^2+6.79e+05*t_1^1-5.08e+04
135	4.54e+06*t_1^3-3.12e+06*t_1^2+7.13e+05*t_1^1-5.34e+04
140	-1.48e+05*t_1^2+6.8e+04*t_1^1-6.97e+03
145	5e+06*t_1^3-3.43e+06*t_1^2+7.84e+05*t_1^1-5.87e+04
Power (W), Cooling	$f(t)$ (°K), Applied for t = $0.23s$ to $0.6s$
100	9.58e+02*t_2^2-1.177e+03*t_2^1+9.46e+02
120	1.2e+03*t_2^2-1.46e+03*t_2^1+1.09e+03
125	1.25e+03*t_2^2-1.53e+03*t_2^1+1.13e+03
130	1.32e+03*t_2^2-1.61e+03*t_2^1+1.17e+03
135	1.37e+03*t_2^2-1.68e+03*t_2^1+1.2e+03
140	1.43e+03*t_2^2-1.75e+03*t_2^1+1.25e+03
145	1.49e+03*t_2^2-1.82e+03*t_2^1+1.285e+03

Table E-7 $f(t)$ for PC (25mm/s, non-contact model)

Power (W), Heating	$f(t)$ (°K), Applied for t = $0.02s$ to $0.04s$
0.1wt% CB, 7W	-3.443e+05*t_1^2+5.333e+04*t_1^1-5.995e+02
0.1wt% CB, 7.2W	-3.385e+05*t_1^2+5.390e+04*t_1.^1-6.129e+02
0.1wt% CB, 7.3W	-3.415e+05*t_1^2+5.451e+04*t_1^1-6.236e+02
0.1wt% CB, 7.4W	-3.445e+05*t_1^2+5.51e+04*t_1^1-6.344e+02
0.05wt% CB, 12W	-1.04e+05*t_1^2+2.24e+04*t_1^1-81.08*t_1^0
0.05wt% CB, 12.4W	-2.426e+05*t_1^2+4.702e+04*t_1^1-5.171e+02
0.05wt% CB, 12.6W	-2.446e+05*t_1^2+4.763e+04*t_1^1-5.28e+02
0.05wt% CB, 12.8W	-2.464e+05*t_1^2+4.823e+04*t_1^1-5.38e+02
0.025wt% CB, 21W	-1.243e+10*t_1^4+1644e+09*t_1^3-8.130e+07*t_1^2+1.80e+06*t_1^1-1.47e+04
0.025wt% CB, 22.4W	-1.31e+10*t_1^4+1.74e+09*t_1^3-8.62e+07*t_1^2+1.91e+06*t_1^1-1.56e+04
0.025wt% CB, 22.6W	-1.329e+10*t_1^4+1.758e+09*t_1^3-8.695e+07*t_1^2+1.934e+06*t_1^1-1.582e+04
0.025wt% CB, 24W	-1.405e+10*t_1^4+1.858e+09*t_1^3-9.191e+07*t_1^2+2.044e+06*t_1^1-1.675e+04
0.0125wt% CB, 40W	-2.737e+05*t_1^2+4.578e+04*t_1^1-5e+02
0.0125wt% CB, 42W	-2.082e+05*t_1^2+4.244e+04*t_1^1-4.43e+02
0.0125wt% CB, 44W	-2.131e+05*t_1^2+4.405e+04*t_1^1-4.724e+02
0.0125wt% CB, 46W	-2.179e+05*t_1^2+4.565e+04*t_1^1-5.0164e+02
Power (W), Cooling	$f(t)$ (°K), Applied for t = $0.04s$ to $0.28s$
0.1wt% CB, 7W	-2.191e+06*t_2^5+2e+06*t_2^4-7.19e+05*t_2^3+1.294e+05*t_2^2-1.275e+04*t_2^1+1.317e+03
0.1wt% CB, 7.2W	-2.241e+06*t_2^5+2.0487e+06*t_2^4-7.359e+05*t_2^3+1.324e+05*t_2^2-1.307e+04*t_2^1+1.343e+03
0.1wt% CB, 7.3W	-2.269e+06*t_2^5+2.073e+06*t_2^4-7.449e+05*t_2^3+1.341e+05*t_2^2-1.323e+04*t_2^1+1.357e+03
0.1wt% CB, 7.4W	-2.296e+06*t_2^5+2.098e+06*t_2^4-7.539e+05*t_2^3+1.357e+05*t_2^2-1.339e+04*t_2^1+1.37e+03
0.05wt% CB, 12W	6.138e+04*t_2^4-4.837e+04*t_2^3+1.442e+04*t_2^2-2.24e+03*t_2^1+7.134e+02
0.05wt% CB, 12.4W	1.172e+05*t_2^4-9.25e+04*t_2^3+2.77e+04*t_2^2-4.35e+03*t_2^1+1.102e+03
0.05wt% CB, 12.6W	1.188e+05*t_2^4-9.382e+04*t_2^3+2.815e+04*t_2^2-4.412e+03*t_2^1+1.114e+03
0.05wt% CB, 12.8W	1.205e+05*t_2.^4-9.512e+04*t_2.^3+2.855e+04*t_2.^2-4.475e+03*t_2.^1+1.126e+03
	$f(t)$ (°K), Applied for t = $0.04s$ to $15s$
0.025wt% CB, 21W	exp(-0.1101*log(t_2) + 6.1122)+273
0.025wt% CB, 22.4W	exp(-0.1104*log(t_2) + 6.1683)+273
0.025wt% CB, 22.6W	exp(-0.1104*log(t_2) + 6.176)+273
0.025wt% CB, 24W	exp(-0.1106*log(t_2) + 6.2286)+273
0.0125wt% CB, 40W	exp(-0.4467*t_2 + 6.4399)+273
0.0125wt% CB, 42W	exp(-0.4471*t_2+ 6.4828)+273
0.0125wt% CB, 44W	exp(-0.4474*t_2+ 6.5237)+273
0.0125wt% CB, 46W	exp(-0.4477*t_2+ 6.5629)+273

Table E-8 $f(t)$ for PA6 (25mm/s, non-contact model)

Power (W), Heating	$f(t)$ (°K), Applied for t = $0.02s$ to $0.19s$
0.2wt% CB, 22W	6.129e+06*t_1^4-2.3517e+06*t_1^3+3.157e+05*t_1^2-1.7e+04*t_1^1+5.97e+02
0.2wt% CB, 24W	1.212e+07*t_1^4-4.7e+06*t_1.^3+6.537e+05*t_1^2-3.773e+04*t_1^1+1.05e+03
0.2wt% CB, 25W	1.278e+07*t_1^4-4.967e+06*t_1^3+6.899e+05*t_1^2-3.982e+04*t_1^1+1.092e+03
0.2wt% CB, 26W	7.611e+06*t_1^4-2.929e+06*t_1^3+3.939e+05*t_1^2-2.124e+04*t_1^1+6.726e+02
	$f(t)$ (°K), Applied for t = $0.02s$ to $0.2s$
0.1wt% CB, 35W	5.426e+06*t_1^4-2.075e+06*t_1^3+2.785e+05*t_1^2-1.501e+04*t_1^1+5.622e+02
0.1wt% CB, 37.5W	7.463e+06*t_1^4-3.052e+06*t_1^3+4.45e+05*t_1^2-2.69e+04*t_1^1+8.55e+02
0.1wt% CB, 38.5W	7.74e+06*t_1^4-3.16e+06*t_1^3+4.63e+05*t_1^2-2.79e+04*t_1^1+8.7708e+02
0.1wt% CB, 40W	6.474e+06*t_1^4-2.484e+06*t_1^3+3.339e+05*t_1^2-1.802e+04*t_1^1+6.158e+02
	$f(t)$ (°K), Applied for t = $0.02s$ to $0.24s$
0.05wt% CB, 57W	4.74e+06*t_1^3-3.21e+06*t_1^2+7.254e+05*t_1^1-5.37e+04
0.05wt% CB, 58W	4.862e+06*t_1^3-3.294e+06*t_1^2+7.432e+05*t_1^1-5.5e+04
0.05wt% CB, 62W	5.347e+06*t_1^3-3.621e+06*t_1^2+8.165e+05*t_1^1-6.0459e+04
0.05wt% CB, 64W	5.582e+06*t_1^3-3.780e+06*t_1^2+8.522e+05*t_1^1-6.31e+04
	$f(t)$ (°K), Applied for t = $0.02s$ to $0.26s$
0.0167wt% CB, 109W	2.714e+06*t_1^3-1.87e+06*t_1^2+4.293e+05*t_1^1-3.213e+04
0.0167wt% CB, 125W	3.258e+06*t_1^3-2.245e+06*t_1^2+5.152e+05*t_1^1-3.86e+04
0.0167wt% CB, 150W	4.199e+06*t_1^3-2.891e+06*t_1^2+6.6291e+05*t_1^1-4.976e+04
0.0167wt% CB, 153W	-4.36e+07*t_1^4+4.183e+07*t_1^3-1.503e+07*t_1^2+2.397e+06*t_1^1-1.423e+05
	$f(t)$ (°K), Applied for t = $0.02s$ to $0.25s$
0.0125wt% CB, 130W	2.568e+06*t_1^3-1.77e+06*t_1^2+4.0657e+05*t_1^1-3.0427e+04
0.0125wt% CB, 151W	3.013e+06*t_1^3-2.09e+06*t_1^2+4.83e+05*t_1^1-3.64e+04
0.0125wt% CB, 170W	3.7e+06*t_1^3-2.549e+06*t_1^2+5.85e+05*t_1^1-4.39e+04
0.0125wt% CB, 175W	-3.826e+07*t_1^4+3.676e+07*t_1^3-1.322e+07*t_1^2+2.113e+06*t_1^1-1.256e+05
Power (W), Cooling	
	$f(t)$ (°K), Applied for t = $0.19s$ to $0.6s$
0.2wt% CB, 22W	2.614e+04*t_2^4-4.48e+04*t_2^3+2.949e+04*t_2^2-9.447e+03*t_2^1+1.875e+03
0.2wt% CB, 24W	2.747e+04*t_2^4-4.646e+04*t_2^3+3.0377e+04*t_2^2-9.736e+03*t_2^1+1.933e+03
0.2wt% CB, 25W	2.9e+04*t_2^4-4.91e+04*t_2^3+3.204e+04*t_2^2-1.024e+04*t_2^1+2.014e+03
0.2wt% CB, 26W	3.233e+04*t_2.^4-5.553e+04*t_2.^3+3.665e+04*t_2.^2-1.174e+04*t_2.^1+2.239e+03
	$f(t)$ (°K), Applied for t = $0.2s$ to $0.6s$
0.1wt% CB, 35W	4.885e+02*t_2^2-9.59e+02*t_2^1+9.97e+02
0.1wt% CB, 37.5W	5.639e+02*t_2^2-1.0669e+03*t_2^1+1.0583e+03
0.1wt% CB, 38.5W	6.028e+02*t_2^2-1.117e+03*t_2^1+1.084e+03
0.1wt% CB, 40W	6.455e+02*t_2^2-1.18e+03*t_2^1+1.12e+03

Table E-8 contd	
	$\boldsymbol{f(t)}$ (°K), Applied for t = 0.024s to 15s
0.05wt% CB, 57W	exp(-0.8769*t_2 + 6.4687)+273
0.05wt% CB, 58W	exp(-0.8802*t_2 + 6.4878)+273
0.05wt% CB, 62W	exp(-0.8962*t_2 + 6.5595)+273
0.05wt% CB, 64W	exp(-0.9034*t_2 + 6.5955)+273
	$\boldsymbol{f(t)}$ (°K), Applied for t = 0.026s to 15s
0.0167wt% CB, 109W	exp(-0.4581*t_2 + 6.1871)+273
0.0167wt% CB, 125W	exp(-0.4763*t_2 + 6.3343)+273
0.0167wt% CB, 150W	exp(-0.5102*t_2 + 6.5387)+273
0.0167wt% CB, 153W	exp(-0.5138*t_2 + 6.5612)+273
	$\boldsymbol{f(t)}$ (°K), Applied for t = 0.025s to 15s
0.0125wt% CB, 130W	exp(-0.3973*t_2 + 6.1444)+273
0.0125wt% CB, 151W	exp(-0.4173*t_2 + 6.3054)+273
0.0125wt% CB, 170W	exp(-0.436*t_2 + 6.4364)+273
0.0125wt% CB, 175W	exp(-0.4408*t_2 + 6.4691)+273

E.1 Cooling phase temperature-time data for non-contact geometry

Temperature dropped rapidly with time in the contact geometry because of contact between the laser-heated absorbent part and the cold laser-transparent part. Therefore the cooling phase temperature-time data obtained from the FEM code was sufficient for conversion prediction given the length of time obtained from the FEM model. For the non-contact geometry, cooling time provided by the FEM model was not sufficient for the cooling of the material after heating (for PC 0.025, 0. 0167 and 0.0125wt% CB and for PA6 0.05, 0. 0167 and 0.0125wt% CB) because of slower cooling rate at this CB levels. Therefore the equations used to fit them described by Figure E.1 (for PA6 0.05) were used to extrapolate their cooling temperatures to time not provided by the FEM model.

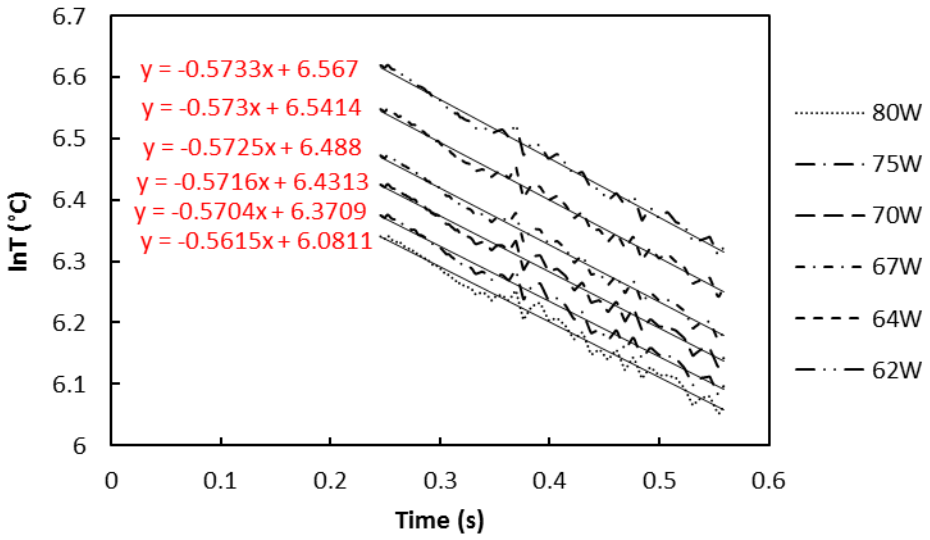

E.1 ln*T* vs time of the FEM temperature-time data (PA6, 0.05, 25mm/s, non-contact geometry)

E.2 Conversion as funtion of time

The plots of conversion as a function of time not presented in section 6.2 are presented here.

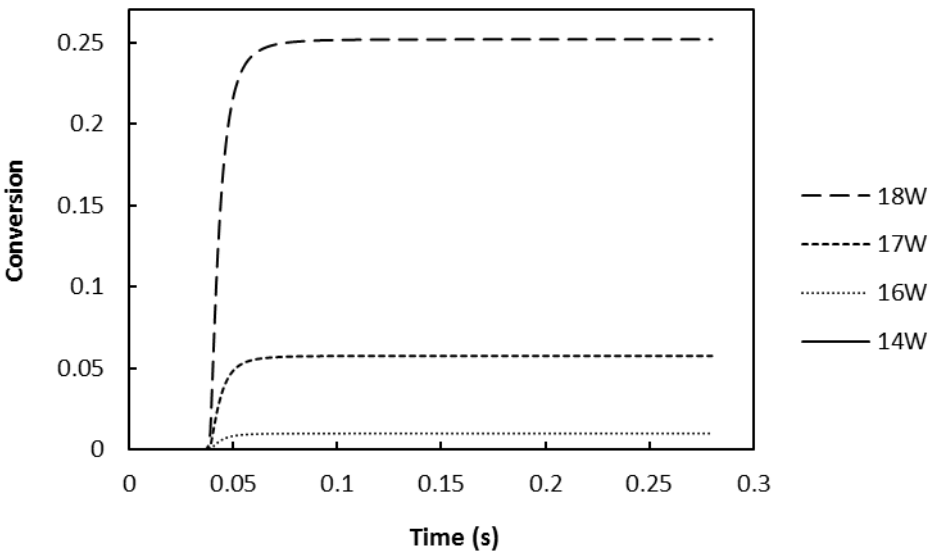

Figure E.2 Predicted conversion vs time (PC 0.05wt% CB, 25mm/s, contact weld)

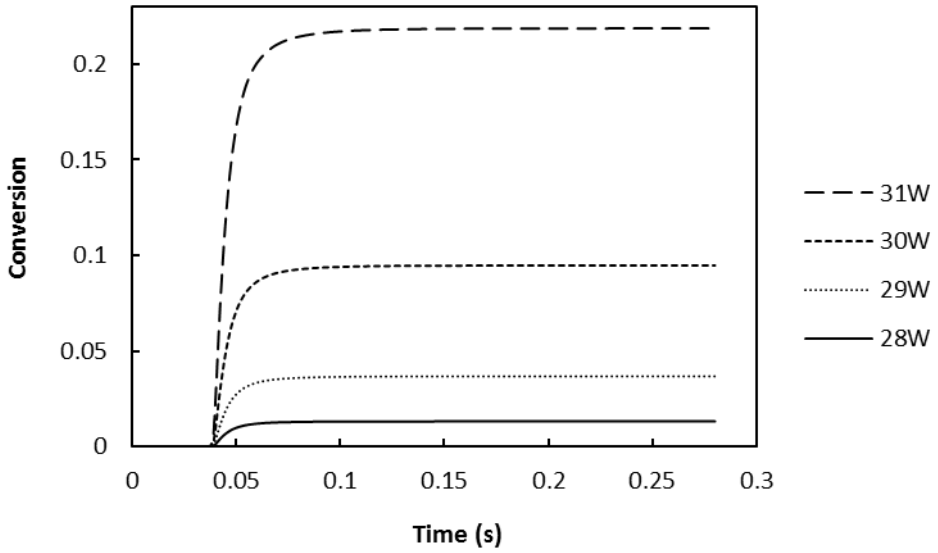

Figure E.3 Predicted conversion vs time (PC 0.025wt% CB, 25mm/s, contact weld)

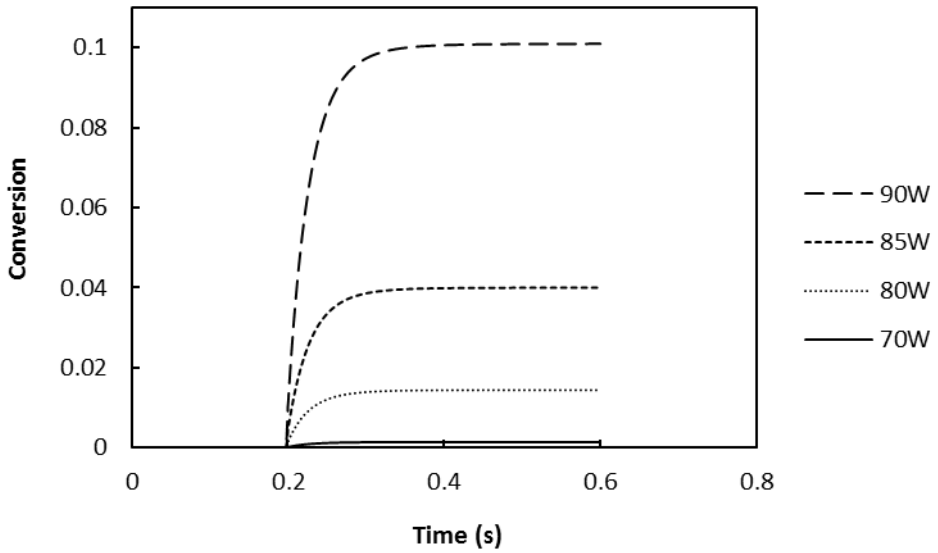

Figure E.4 Predicted conversion vs time (PA6 0.05wt% CB, 25mm/s, contact weld)

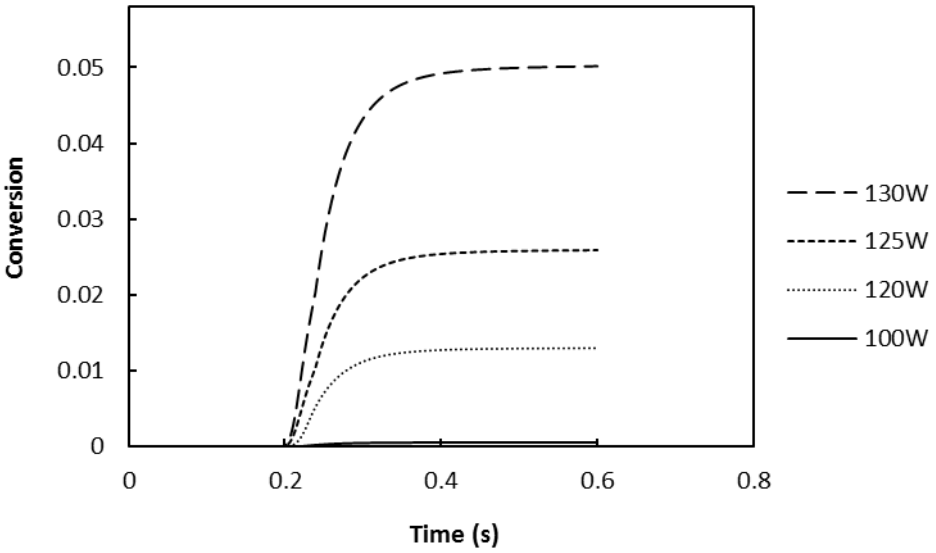

Figure E.5 Predicted conversion vs time (PA6 0.025wt% CB, 25mm/s, contact weld

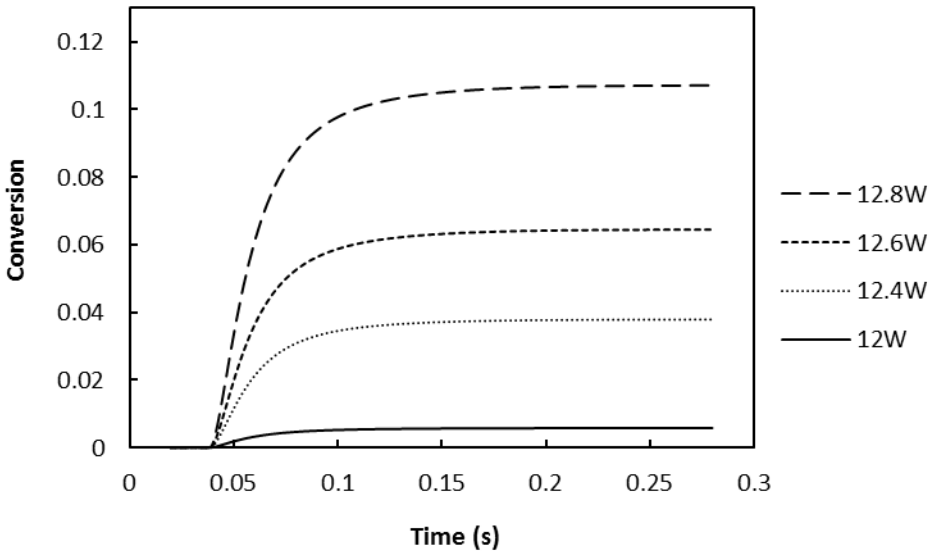

Figure E.6 Predicted conversion vs time (PC 0.05wt% CB, 25mm/s, non-contact weld).

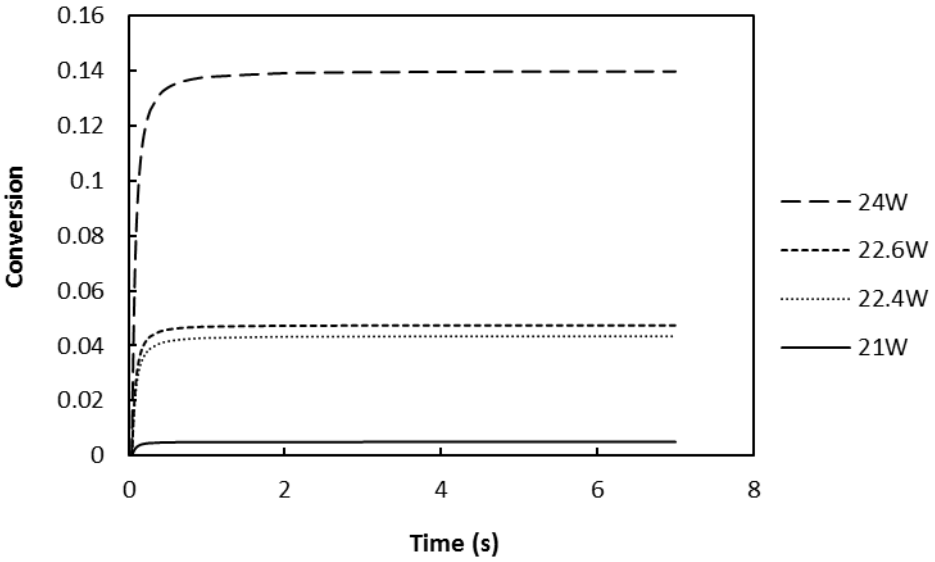

Figure E.7 Predicted conversion vs time (PC 0.025wt% CB, 25mm/s, non-contact weld).

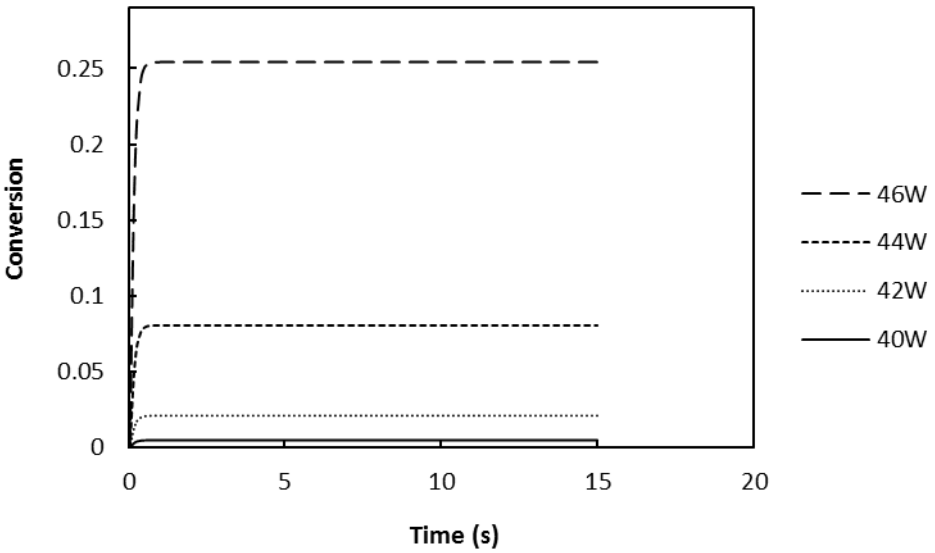

Figure E.8 Predicted conversion vs time (PC 0.0125wt% CB, 25mm/s, non-contact weld).

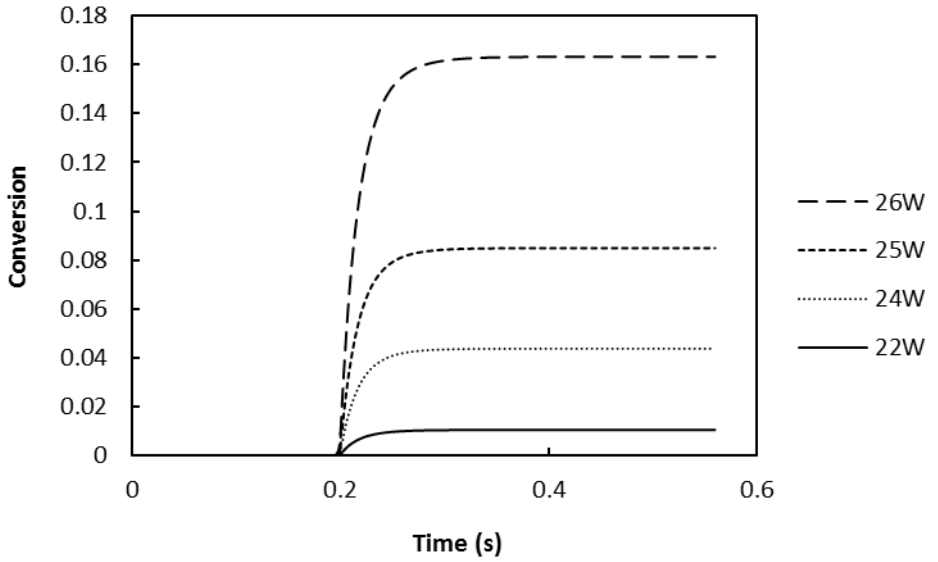

Figure E.9 Predicted conversion vs time (PA6 0.2wt% CB, 25mm/s, non-contact weld)

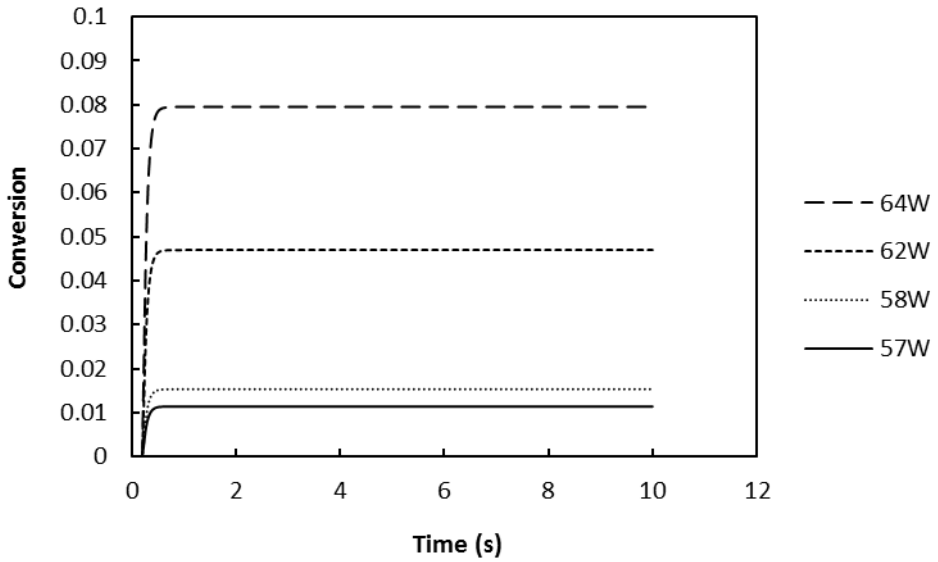

Figure E.10 Predicted conversion vs time (PA6 0.05wt% CB, 25mm/s, non-contact weld)

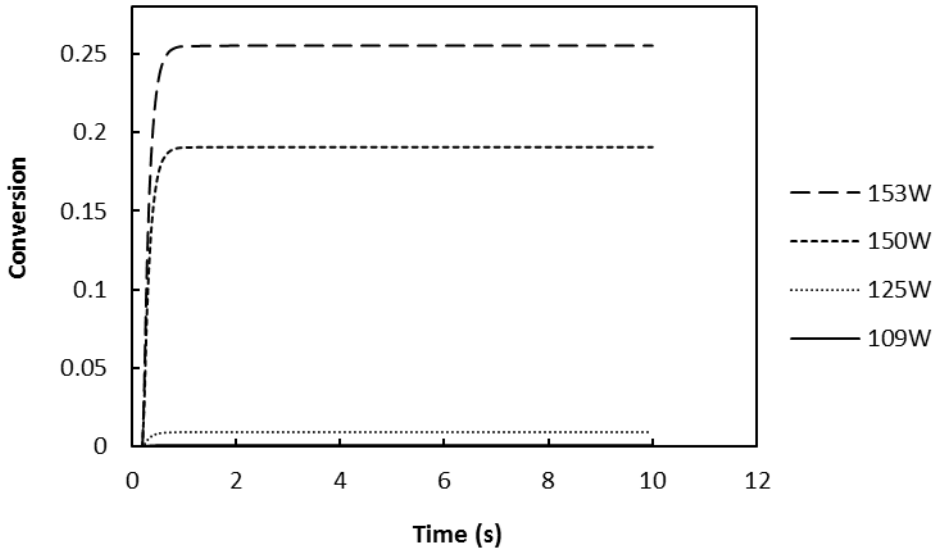

Figure E.11 Predicted conversion vs time (PA6 0.0167wt% CB, 25mm/s, non-contact weld)

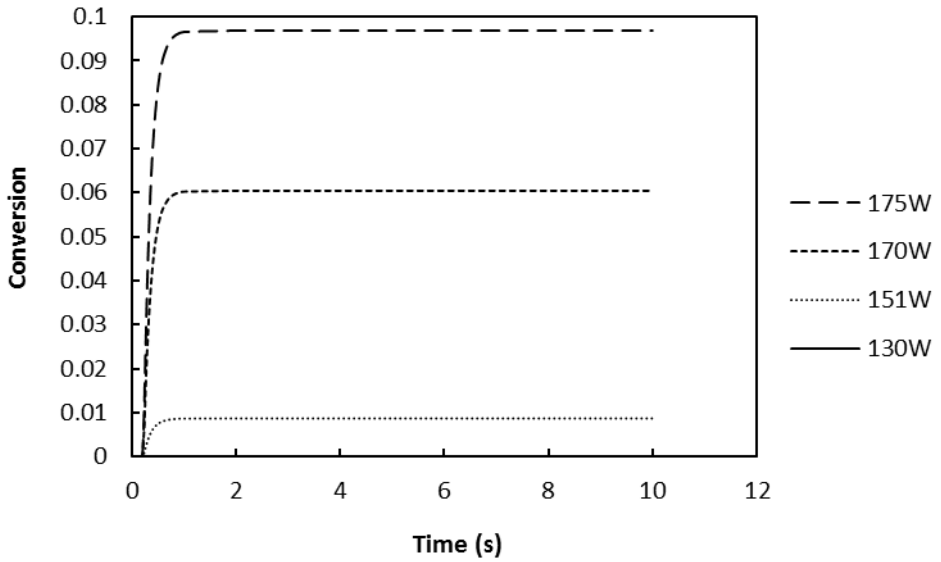

Figure E.12 Predicted conversion vs time (PA6 0.0125wt% CB, 25mm/s, non-contact weld)

Appendix F

Matlab code used to estimate the material conversion as a result of thermal degradation during LTW

```
%Reads time data from excel file
time = xlsread('PC.xls',1, 'A4:A404')';

%separates the heating and cooling time
t_heating_start = 25;
t_heating_end = 58;

t_heating = time (t_heating_start:t_heating_end);
t_cooling = time (t_heating_end:end);

t_1 = t_heating;
t_2 =t_cooling;

%Kinetic parameters

x= [(5.9E+14)/60, 225,1.281831723 0.384535698];

%Gas constant
R =0.0083144621;




%Solve ODE with Matlab ODE 45


%Obtaining material conversion for the heating phase (y1).

dy = @(t_1,y1)(x(1).*exp(-(x(2)./(R*(f(t))))).*((1-y1).^x(3))).*(y1.^x(4));


%Initial conversion at time =0. Set to a very small value;
y0 =0.000000001;

     [t_1,y1]= ode45 (dy,t_1,y0);


%Obtaining material conversion for the cooling phase (y2)
dy = @(t_2,y2)(x(1).*exp(-(x(2)./(R*(f(t))))).*((1-y2).^x(3))).*(y2.^x(4));


y0 =y1(end);
```

```
    [t_2,y2]= ode45(dy,t_2,y0);


 %concatenate the heating and cooling material conversion to obtain y
   y= [y1' y2'];

   t = [t_1' t_2'];




% plotting conversion vs time

 figure (1)

   plot (t,y,'+')

ylabel('Conversion')
xlabel ('Time (s)')
```